



Validation report of the CAMS near-real time global atmospheric composition service

Period March – May 2020

Issued by: KNMI

Date: 24 September 2020

Ref: CAMS84_2018SC2_D1.1.1_MAM2020

This document has been produced in the context of the Copernicus Atmosphere Monitoring Service (CAMS). The activities leading to these results have been contracted by the European Centre for Medium-Range Weather Forecasts, operator of CAMS on behalf of the European Union (Delegation Agreement signed on 11/11/2014). All information in this document is provided "as is" and no guarantee or warranty is given that the information is fit for any particular purpose. The user thereof uses the information at its sole risk and liability. For the avoidance of all doubts, the European Commission and the European Centre for Medium-Range Weather Forecasts has no liability in respect of this document, which is merely representing the authors view.



Validation report of the CAMS near-real-time global atmospheric composition service: Period March - May 2020

EDITORS:

Y. Christophe (BIRA-IASB), M. Ramonet (LSCE), A. Wagner (MPG),
M. Schulz (MetNo), H.J. Eskes (KNMI)

AUTHORS:

S. Basart (BSC), A. Benedictow (MetNo), Y. Bennouna (CNRS-LA),
A.-M. Blechschmidt (IUP-UB), S. Chabrillat (BIRA-IASB), E. Cuevas (AEMET),
A. El-Yazidi (LSCE), H. Flentje (DWD), P. Fritzsche (DWD), K. M. Hansen (AU),
U. Im (AU), J. Kapsomenakis (AA), B. Langerock (BIRA-IASB),
A. Richter (IUP-UB), N. Sudarchikova (MPG), V. Thouret (CNRS-LA),
T. Warneke (UBC), C. Zerefos (AA)

REPORT OF THE COPERNICUS ATMOSPHERE MONITORING SERVICE, VALIDATION SUBPROJECT.

AVAILABLE AT:

http://atmosphere.copernicus.eu/quarterly_validation_reports

CITATION:

Christophe, Y., M. Ramonet, A. Wagner, M. Schulz, H. J. Eskes, S. Basart, A. Benedictow, Y. Bennouna, A.-M. Blechschmidt, S. Chabrillat, E. Cuevas, A. El-Yazidi, H. Flentje, P. Fritzsche, K.M. Hansen, U. Im, J. Kapsomenakis, B. Langerock, A. Richter, N. Sudarchikova, V. Thouret, T. Warneke, C. Zerefos, Validation report of the CAMS near-real-time global atmospheric composition service: Period March - May 2020, Copernicus Atmosphere Monitoring Service (CAMS) report, CAMS84_2018SC2_D1.1.1_MAM2020.pdf, September 2020.

STATUS:

Version 1, final

DATE:

24 September 2020



Executive Summary

The Copernicus Atmosphere Monitoring Service (<http://atmosphere.copernicus.eu>, CAMS) is a component of the European Earth Observation programme Copernicus. The CAMS global near-real time (NRT) service provides daily analyses and forecasts of reactive trace gases, greenhouse gases and aerosol concentrations. This document presents the validation statistics and system evolution of the CAMS NRT service for the period up to 1 June 2020, with a focus on March to May 2020 (MAM-2020). Updates of this document appear every 3 months, e.g. Schulz et al. (2020). A detailed description of the measurement datasets used is provided in Eskes et al. (2019). Automated verification plots are made available through the CAMS global evaluation server, <https://global-evaluation.atmosphere.copernicus.eu>.

This summary is split according to service themes as introduced on the CAMS website: air quality & atmospheric composition, climate forcing, ozone layer and UV. Specific attention is given to the ability of the CAMS system to capture recent events. We focus on the 'o-suite' composition fields, which are the daily analyses and forecasts produced by the IFS (Integrated Forecast System) modelling system at ECMWF, using the available meteorological and atmospheric composition observations which are ingested in the ECMWF 4D-Var assimilation system. The model and assimilation configurations are summarised in section 2. We furthermore assess the impact of the composition observations by comparing the validation results from the 'o-suite' to a 'control' configuration without atmospheric composition data assimilation. Also, the pre-operational delayed-mode analyses and high-resolution forecasts of CO₂ and CH₄ are assessed in this report.

The o-suite data delivery for the period March, April and May 2020 was excellent, with an on-time percentage of 100%.

Air quality and atmospheric composition

Tropospheric ozone (O₃)

The CAMS o-suite ozone is validated with surface and free tropospheric ozone observations from the GAW and ESRL networks, IAGOS airborne data, ozone sondes and IASI tropospheric ozone retrievals. For free tropospheric ozone against ozone sondes, the o-suite modified normalized mean biases (MNMBs) are on average small, $\pm 10\%$ over the Northern Hemisphere (NH), between $\pm 30\%$ for stations in the Tropics, and $\pm 20\%$ for the Arctic in more recent years (Fig. S.1). Over Antarctica o-suite biases are observed between 0% and $\pm 20\%$ for recent years, whereas the control run shows larger negative biases. For MAM 2020, good agreement is found over the NH mid latitudes, Arctic (MNMBs of o-suite and control within $\pm 10\%$) and Antarctica (MNMBs between -3 and -14%) in the free troposphere.

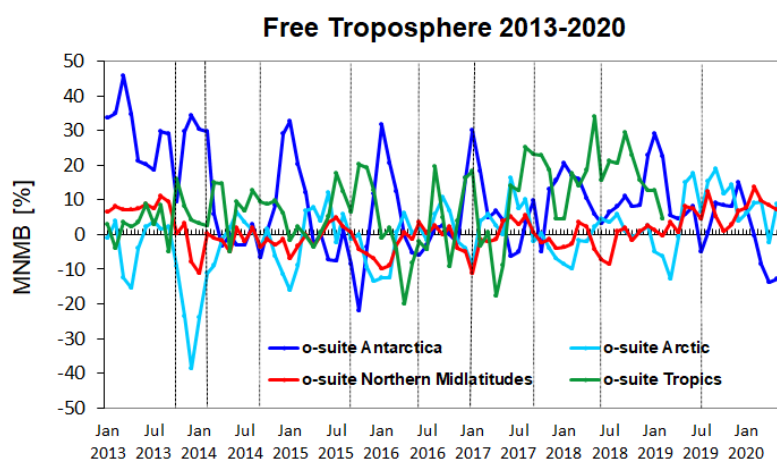


Figure S.1: Time series of MNMB of ozone in the o-suite, compared against ozone sondes, averaged over different latitude bands. The free troposphere is defined here as the layer between 750 and 300 hPa. Model upgrades are indicated in black vertical lines.

Due to the COVID-19 pandemic, air travel was largely reduced during MAM. Ozone data over Frankfurt are available only in the first half of March, and for most of the month in May. Ozone is well represented in the low troposphere by both runs with on average a positive MNMB of less than 20% and a correlation of more than 90%. In the UTLS region the bias is larger, ozone is mostly overestimated by the o-suite with MNMBs of around 40%.

The comparison with GAW surface stations shows that O_3 surface mixing ratios in MAM are overestimated with MNMBs within 15% for Europe and up to 20% for Asian stations. Correlation coefficients for European stations are between 0.53 and 0.75 and between 0.56 and 0.96 for Asian stations. The timeseries of modelled surface ozone show in general a good correspondence with the observations.

Tropospheric Nitrogen dioxide (NO_2)

Model validation with respect to GOME-2/MetOp-A and Sentinel-5P TROPOMI NO_2 data shows that tropospheric NO_2 columns are well reproduced by the NRT model runs, indicating that emission patterns and NO_x photochemistry are generally well represented, although modelled shipping signals are more pronounced than in the satellite retrievals. Tropospheric NO_2 columns over some local emission hotspots (e.g. Moscow, and Red Basin in China) are overestimated, while wintertime and springtime values over Europe around Benelux are underestimated. The long-term development over East-Asia (and Europe) for previous years (Fig. S.2), associated with the development of emissions, is not in agreement with the observations. Between spring and autumn, the models regularly show an overestimation over several regions with boreal forest fire activity (Canada, Alaska, Siberia). With respect to months affected by COVID-19 lockdown time periods, the o-suite generally fails to reproduce observed reductions in tropospheric NO_2 for large areas over China and South Asia, but performs better for Europe.

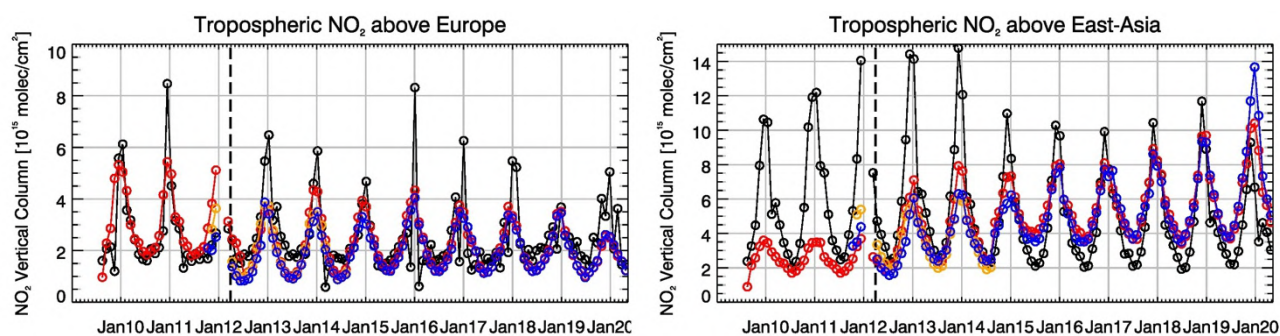


Figure S.2: Time series of tropospheric NO₂ columns from SCIAMACHY (up to March 2012) and GOME-2 (from April 2012 onwards) compared to model results for Europe and East-Asia. Black lines show the observations, red shows the o-suite, blue lines show CAMS control results including older configurations from the MACC projects before September 2014, orange shows the forecast from the MACC project, based on the Mozart-IFS model.

Tropospheric Carbon Monoxide (CO)

Model validation with respect to GAW network surface observations, European surface observations, IAGOS airborne data, FTIR observations (NDACC and TCCON) and MOPITT / IASI satellite retrievals reveals that the absolute values, latitude dependence and seasonality, as well as day-to-day variability of CO can be reproduced well by the CAMS-global analyses and forecasts. Biases for the o-suite are within -10% for European and Asian GAW stations and within $\pm 20\%$ for stations located in the Southern Hemisphere. The control run shows larger negative biases (up to -20%) for European and Asian stations. The comparisons with EEA AirBase surface observations in Europe shows high temporal correlations, small biases over Spain, Belgium and Germany, and larger biases over Switzerland (up to 40%), Poland and the Czech Republic (down to -40%).

The comparison with NDACC data shows, that the model upgrade (60 to 137 levels) implemented in July 2019 changes the overall biases in both the troposphere and stratosphere. The bias for the tropospheric columns becomes -7.5% in MAM (-8.5% in DJF, -7% in SON) and is larger than the reported measurement uncertainty (Fig. S.3). The bias in the stratosphere is reduced to -13% in MAM 2020 (-12% in DJF, +10% SON) and just exceeds the measurement's uncertainty.

For TCCON data, sites with available data are Nicosia and Orleans. The comparisons show that all models capture the seasonality well and the agreement is within 5-10 ppb.

According to IAGOS observations, CO is mostly underestimated over Frankfurt by both, the o-suite and the control run. Largest biases appear in the lowest layers, while upper layers show a better agreement in general. Between April and May 2020, the results from the o-suite and the control run notably differ, with the control run showing large negative biases. From the surface to the lower troposphere, MNMBs range between -20% and -10% for the o-suite and between -40% and -20% for the control run. The large differences are presumably reflecting the changes in emissions during the Covid-19 lockdowns in Europe, which are not captured by the control run.

The relative difference between the model runs and MOPITT shows that the o-suite performs better than the control run without data assimilation. The o-suite generally underestimates the satellite data by about 10% with some regional exceptions where the negative bias reaches 20% (mostly over land).

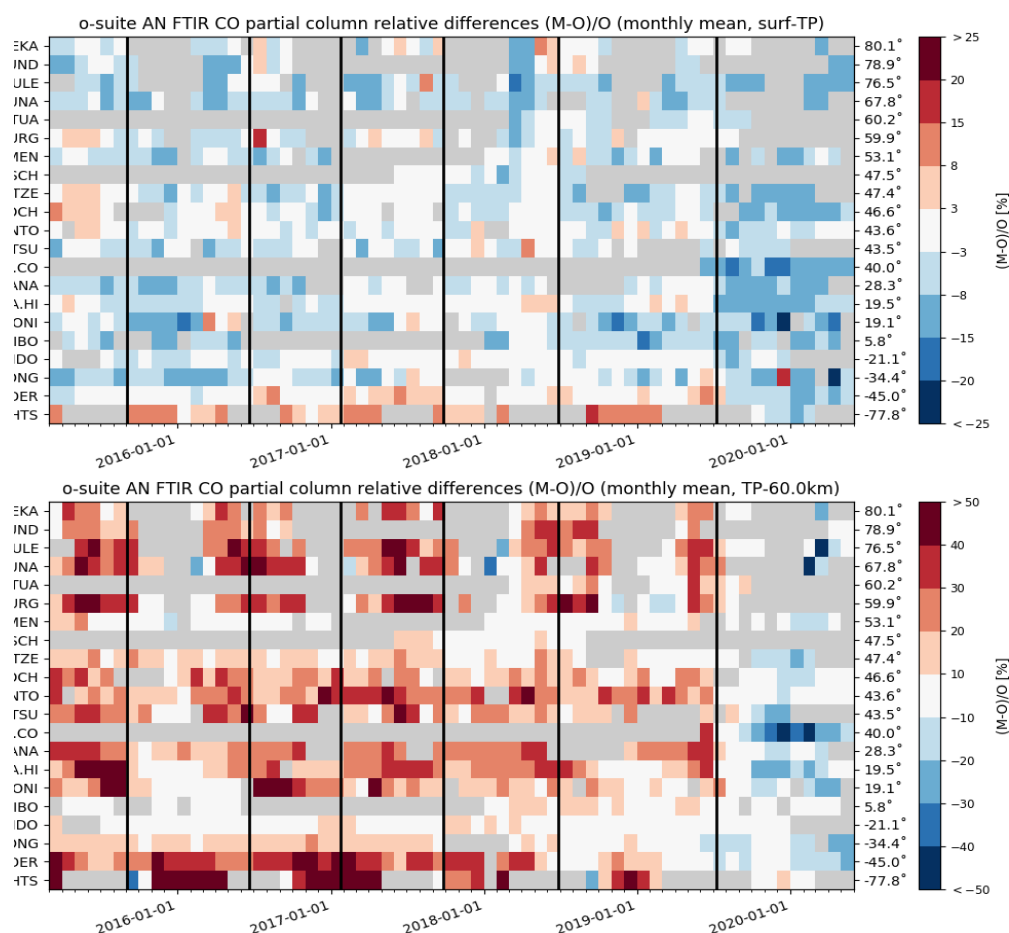


Figure S.3: Monthly mean biases for a 5-year period for the tropospheric CO columns (top) and stratospheric CO columns (bottom) from comparisons with NDACC FTIR observations. The o-suite upgrades are indicated in black vertical lines, stations are sorted by latitude. The overall uncertainty for the CO measurements is approximately 3% on the tropospheric columns and 10% for the stratospheric columns. The o-suite analysis averaged bias in tropospheric columns increased to -7.5% for MAM compared to the bias before the model update in 2019. The bias in the stratosphere reduced to -12% and just exceeds the measurement's uncertainty.

After the update from 60 to 137 levels in the second half of the year 2019, we see the following changes:

- Enhanced negative biases over the US and Europe in the o-suite run and more pronounced underestimations in the control run.
- Improvement of the o-suite results over East and South Asia (bias is almost zero).
- General change of bias sign in the control run from positive to negative during the second half of 2019 over the Siberian fire region and enhanced negative biases in the o-suite run.
- Strong increase of negative bias for the control run over the Alaskan region.
- Stronger underestimation over South Africa in both, the o-suite and control run and stronger underestimation over North Africa for the o-suite.

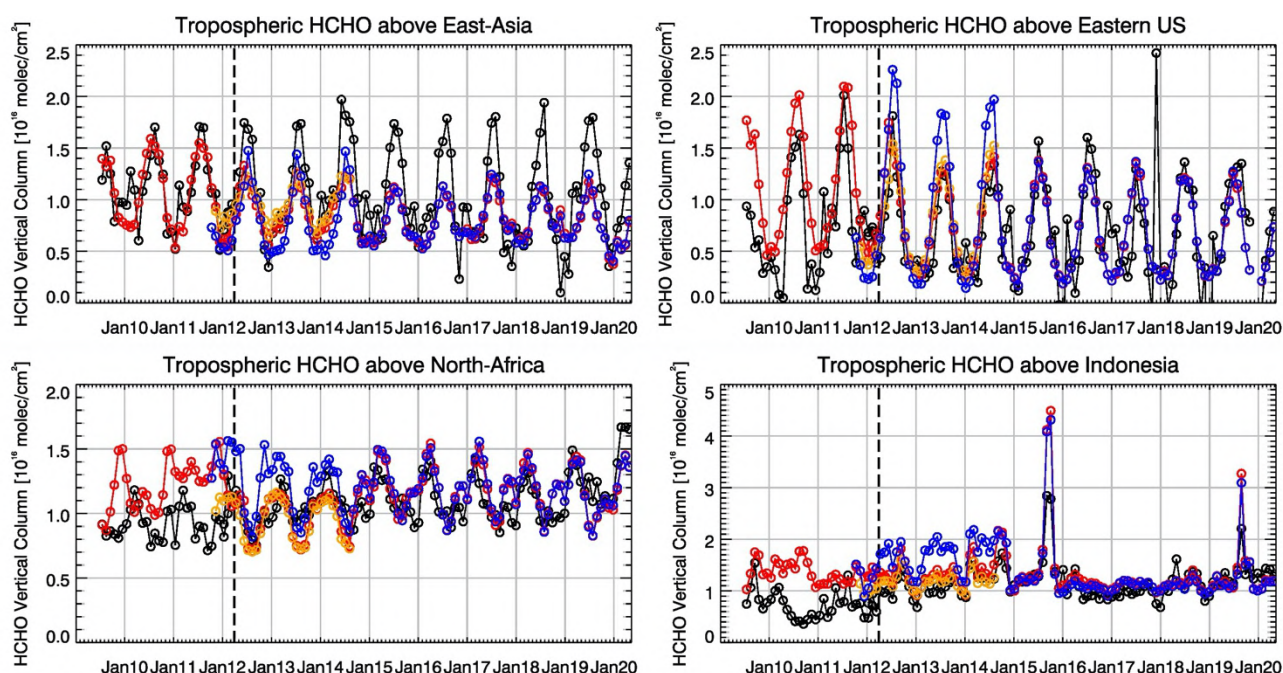


Figure S.4: Time series of average tropospheric HCHO columns [10^{16} molec cm^{-2}] from SCIAMACHY (up to March 2012) and GOME-2 (from April 2012 onwards) compared to model results for different regions. Black lines show the observations, red shows the o-suite, blue lines show CAMS control results including older configurations from the MACC projects before September 2014, orange shows forecasts from the MACC projects. The regions are: East-Asia ($25\text{--}40^{\circ}\text{N}$, $110\text{--}125^{\circ}\text{E}$), Eastern US ($30\text{--}40^{\circ}\text{N}$, $75\text{--}90^{\circ}\text{W}$), Northern Africa ($0\text{--}15^{\circ}\text{N}$, $15^{\circ}\text{W}\text{--}25^{\circ}\text{E}$) and Indonesia ($5^{\circ}\text{S}\text{--}5^{\circ}\text{N}$, $100\text{--}120^{\circ}\text{E}$). Vertical dashed black lines mark the change from SCIAMACHY to GOME-2 based comparisons in April 2012.

Formaldehyde

Model validation, with respect to SCIAMACHY/Envisat HCHO data (before April 2012), GOME-2/MetOp-A and Sentinel-5P TROPOMI HCHO data, shows that modelled monthly HCHO columns represent well the magnitude of oceanic and continental background values and the overall spatial distribution in comparison with mean satellite HCHO columns (Fig. S.4). Compared to GOME-2 satellite retrievals, an overestimation of values regularly occurs over Australia and Central Africa, which could be both related to biogenic emissions and fire emissions. For time series over East-Asia and the Eastern US, both regions where HCHO columns are probably dominated by biogenic emissions, models and retrievals agree rather well, but the yearly cycle over East-Asia is underestimated by the models.

Tropospheric Water Vapour (H_2O)

Overall, water vapour values and variability are well represented by the two runs in the low troposphere over Frankfurt with small positive biases (smaller than 10%) and high correlation values (higher than 90%). Some differences between the two runs are found in the upper layers as the control run presents slightly smaller biases and higher correlation especially in the mid-troposphere.

The agreement is worse in the upper layers, with larger biases and smaller correlation and mostly negative biases in the UTLS (up to -40%).

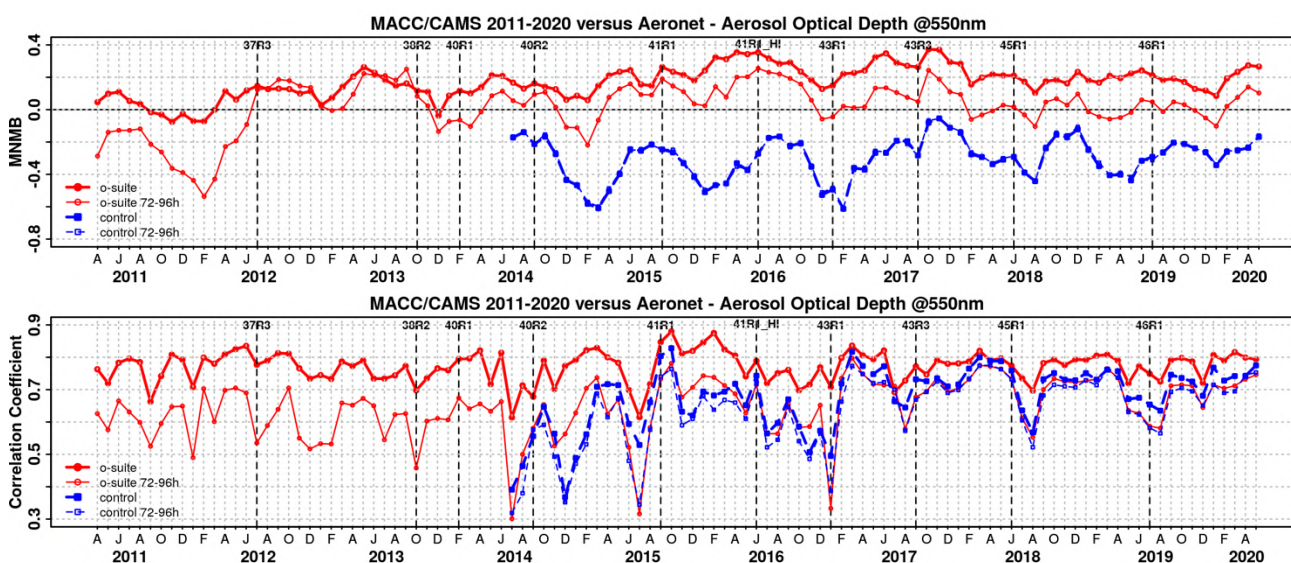


Figure S.5. Aerosol optical depth at 550nm in IFS 00Z model simulations for April 2011 – May 2020 against daily matching Aeronet Version3 level 1.5 data. a) Modified normalized mean bias (MNMB); o-suite (thick red curve); o-suite at last forecast day (light red curve); Control (blue dashed); Control at last forecast day (light blue dashed); b) Corresponding correlation coefficient. Model version changes are marked as vertical bars.

Aerosol

We estimate that the o-suite aerosol optical depth showed an average positive bias in the latest three months of +26%, measured as modified normalized mean bias against daily Aeronet (V3 level 1.5) sun photometer data. The 3-day forecasted aerosol distribution shows 19% less aerosol optical depth (AOD) than that from the initial forecast day, as shown in Fig. S.5-a. Spatiotemporal correlation, shown in Fig. S.5-b, shows month-to-month variation in MAM-2020 similar to spring 2019, indicating the simulation reproduces approximately 42% of the day to day AOD variability across all Aeronet stations. The o-suite forecast at +3 days shows slightly lower correlation, as a consequence of imperfect forecasted meteorology and fading impact of the initial assimilation of MODIS AOD and MODIS fire info on model performance. The o-suite forecast running each day at 12UTC shows almost identical performance as the forecast starting at 00UTC.

The AOD performance of the o-suite with respect to the AERONET data exhibits no pronounced seasonal cycle but somewhat less correlation in late summer. Since the latest upgrade, the largest contributions to global AOD come from organics, sulphate and sea salt. All species AOD decreased due to the model upgrade in July 2019 with nitrate now contributing to AOD. With the coupling of chemistry and aerosol schemes for sulphur in the latest upgrade in July 2019, first there was an increase of SO₄ especially in the northern hemisphere, but then in the beginning of 2020, an increase is seen in the southern hemisphere.

The aerosol Ångström exponent (AE) contains information about the size distribution of the aerosol, and implicitly about composition. The o-suite AE became more positive indicating a change to slightly more fine particles since the model upgrade to version 45R1 in June 2018.

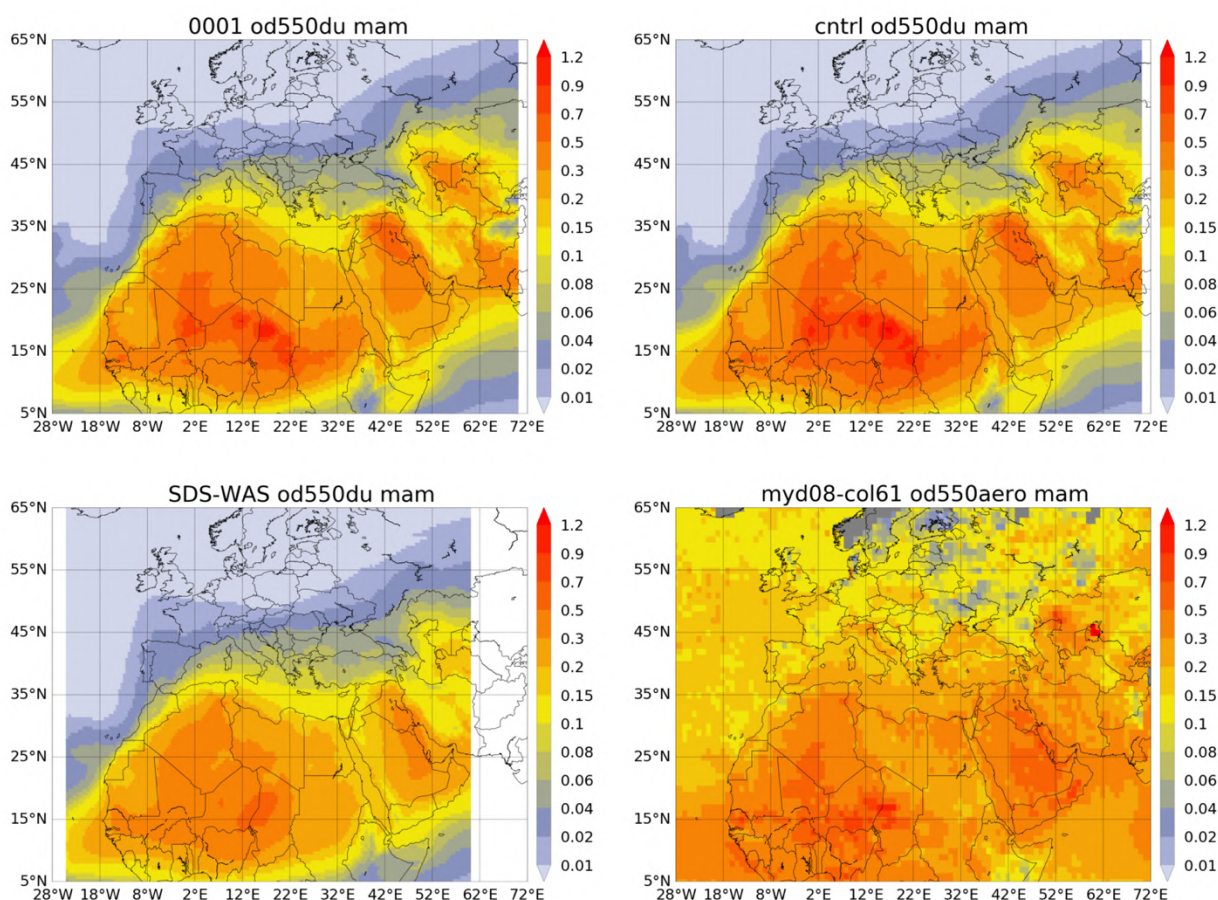


Figure S.6: Averaged DOD 24h forecast from o-suite (top left) and control (top right), DOD of the multi-model SDS-WAS Median product (bottom left) as well as AOD from MODIS/Aqua Collection 6.1 Level 3 combined Dark Target and Deep Blue product (bottom right) for the study period.

PM₁₀ and PM₂₅, as defined by the IFS aerosol model, are evaluated against an average from rural and background site data in the period 2000-2009 at 160 sites in North America and Europe. This indicates that PM₁₀ concentrations exhibit on average in the latest period an underestimation with MNMB bias of -46% in Europe and a smaller underestimation of -11% in North America. PM₂₅ concentrations are underestimated with -50% in Europe and overestimated with 18% in North America. Consistent with this finding a higher positive bias is also found for AOD in North America than in Europe. The fraction of PM simulated data within a factor 2 of observed values stayed similar since September 2017 for both PM₁₀ and PM₂₅. PM₂₅ seems to have deteriorated compared to periods before mid-2017, while PM₁₀ shows an improvement. However, with the latest model version upgrade in July 2019, the PM₂₅ has improved significantly.

Anthropogenic black carbon and organic aerosol (OA) emissions were found to be shifted by 180 degrees in longitude from January 2020 onwards. This resulted in particular in erroneous, shifted black carbon fields, possibly also BC absorption fields. OA results are less affected, since secondary aerosol formation and biomass burning sources are more important for OA fields. PM and Optical depth is also not impacted to a large extent, mainly because BC is a very small fraction of these parameters.



During this season, satellites (see MODIS in Figure S.6) show that significant dust activity in Northern Africa (seasonal AOD above 0.5) is concentrated in latitudes between 10 and 25°N with maximum seasonal AOD values over 0.9 in Bodélé (Chad). Meanwhile, in the Middle East, high AOD values up to 0.7 are observed in Iraq and Saudi Arabia. Overall, o-suite shows lower season values than the control run, which are in general higher than the SDS-WAS multi-median product. Both CAMS runs reproduce high DOD dust activity in the region of Chad, Mali, Niger and Algeria, despite they overestimate in Eastern Sahara in Sudan. Seasonal DOD over Iraq and in the Mediterranean Basin appears overestimated in comparison with MODIS and the SDS-WAS multi-model. On the contrary, CAMS run can reproduce the dust transport over the North Atlantic region, but this is underestimated.

From March to May, CAMS runs reproduce the daily variability of AERONET dust-filtered observations, with a correlation coefficient around averaged over all AERONET sites, which is lower than the SDS-WAS multi-model product which has a correlation coefficient of 0.82. o-suite tends to slightly overestimate the AERONET observations with an MB of 0.02 for o-suite and 0 for control in comparison with the SDS-WAS multi-model that presents higher underestimations (MB of -0.03). The comparison of 1 to 3-day forecasts shows that the prediction is stable during the 3-days forecasts in comparison with AERONET direct-sun observations.

The vertical profiles of backscatter are evaluated in Germany. The changes due to the model upgrades in July 2019 and the unusual warm Winter 2019/2020 have an impact on model performance. Notable is the low positive bias of the model backscatter with better correlation. The step at the top of the PBL is captured notably better with 137 levels than with 60 levels (51L instead of 27L <8 km altitude), same for o-suite and control. The amplitude of the model vertical profile is now very close to the observation (reference). Foehn situations over the alps have been observed including some transport of Saharan dust into Germany, leading to slightly higher bias in mean profiles. Based on three-hourly data Pearson's correlation coefficients in Dec/Jan (run g7h4) have improved and cluster around $r = 0.2-0.8$ for the 137L model in contrast to $r = 0.0-0.6$ for the 60L version (Winter 2018/19) before.

System performance in the Arctic

The CAMS simulations are validated using surface ozone measurements from the ESRL-GMD and the IASOA networks (5 sites) and ozone concentrations in the free troposphere and UTLS are evaluated using balloon sonde measurement data.

Both simulations strongly overestimates surface ozone values at most of the Arctic stations with MNMB ranging from +16% to +24% for the o-suite and from +16% to +90% for the control simulation in March – May 2020. This large positive model offset is related to the chemistry scheme in the CAMS global system, which does not contain the halogen reactions to capture the ozone depletion events (ODE) that occur in spring. An exception from this pattern is the results from Summit (MNMB = 14% for the o-suite and 16% for the control run), at the centre of the Greenland ice sheet, where ODE does not occur. In other seasons, the CAMS ozone simulations are generally in good agreement with the observations.

During March – May 2020 there is on average an overestimation of ozone concentrations in the Arctic free troposphere for the o-suite (MNMB = -2% – 10%) and for the control run (MNMB = 4% – 8%) as well as in the UTLS (MNMB up to 10% for the o-suite).

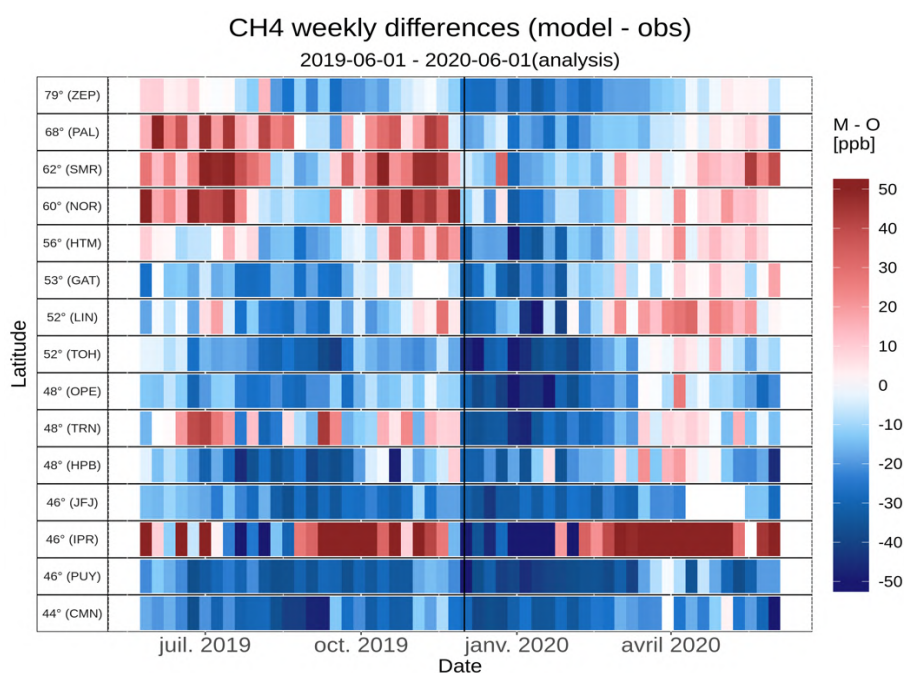


Figure S.7: Mosaic plot of CH₄ biases (in ppb) of the CAMS analysis, compared to surface station observations. Each vertical coloured line represents a weekly mean.

Comparison with FTIR observations from the NDACC network shows that the CO tropospheric columns are in good agreements at the arctic sites with bias between 1% and +5% for both the o-suite and the control run, while the bias for the stratospheric column is larger with bias between 4% and 17%. Comparison with MOPITT versions 7 shows that modeled CO total columns are in good agreement with the satellite retrievals with low bias in the Arctic ($\pm 10\%$).

System performance in the Mediterranean

During spring, both CAMS runs do reproduce the daily variability of AERONET AOD observations, although present general overestimation in the whole Mediterranean Basin. Overestimations are linked to an excess of dust transport over this region during this season. The correlation coefficient increases from (0.53, 0.63 and 0.65) for control to (0.59, 0.74 and 0.71) and MB decreases from (0.14, 0.15 and 0.11) for control to (0.09, 0.10 and 0.12) for o-suite respectively for Western, Central and Eastern Mediterranean.

At surface levels, both CAMS runs show a higher correlation coefficient in Northern Europe (above 0.6) than Southern Europe (under 0.4) in comparison with the EEA PM₁₀ and PM_{2.5} observations. For PM₁₀, both CAMS runs show larger underestimations in Northern Europe (MB under $-8 \mu\text{g}/\text{m}^3$) meanwhile Central and Southern Europe appear overestimated (MB above $6 \mu\text{g}/\text{m}^3$). On the contrary, both CAMS runs underestimated PM_{2.5} EEA observations with larger underestimations in northern European and North Atlantic regions. Frequent desert dust episodes were observed in Southern Europe during this season. The upgrade of the CAMS o-suite during July 2019 led to an increase of the coarse particles at the surface that increase the PM₁₀ levels in Southern Europe. In particular coastal sites, CAMS runs show systematic high PM₁₀ concentrations ($25 \mu\text{g}/\text{m}^3$).

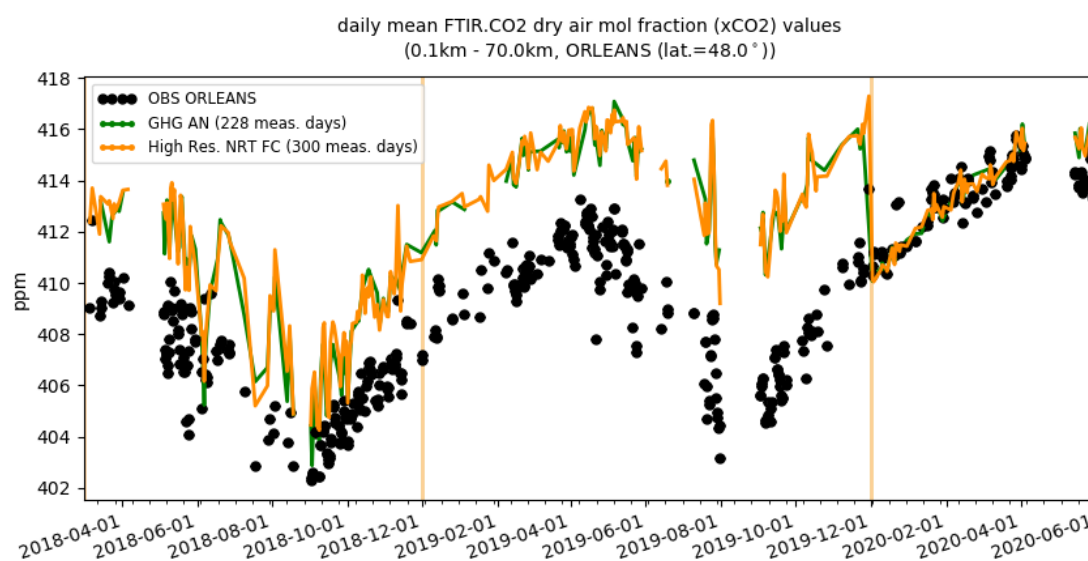


Figure S.8: Comparison of the CO₂ CAMS configurations with TCCON CO₂ at Orleans.

The model is compared to surface O₃ observations from the AirBase network. Our analysis shows that model MNMBs vary between -14% and 30% depending on the station. Temporal correlation coefficients between simulated and observed surface ozone for both the o-suite and control runs are highly significant over the entire Mediterranean from Gibraltar to Cyprus.

Climate forcing

Greenhouse gases

CO₂ and CH₄ surface concentrations from ICOS network, and total or partial columns from TCCON and NDACC stations have been used to validate the analysis and high resolution forecast experiments.

With new experiments started in December 2019 both ICOS (surface) and TCCON (total columns) observations showed CH₄ negative biases ranging from -10 to -50 ppb. However, since mid-March this bias is turning positive at high and mid latitude ICOS sites (Fig. S.7). NDACC partial columns indicate also negative biases in the troposphere, but slight positive biases in the stratosphere.

The surface and total column measurements were showing with the previous experiments an overestimation of the amplitude of the CO₂ seasonal cycle in the northern hemisphere by $\pm 1\%$. The new experiments started on December 2019 indicate a step change with a clear improvement in the CO₂ concentrations at the surface and in total columns (Fig S.8). However, since then the CO₂ bias is increasing at most ICOS and TCCON sites.

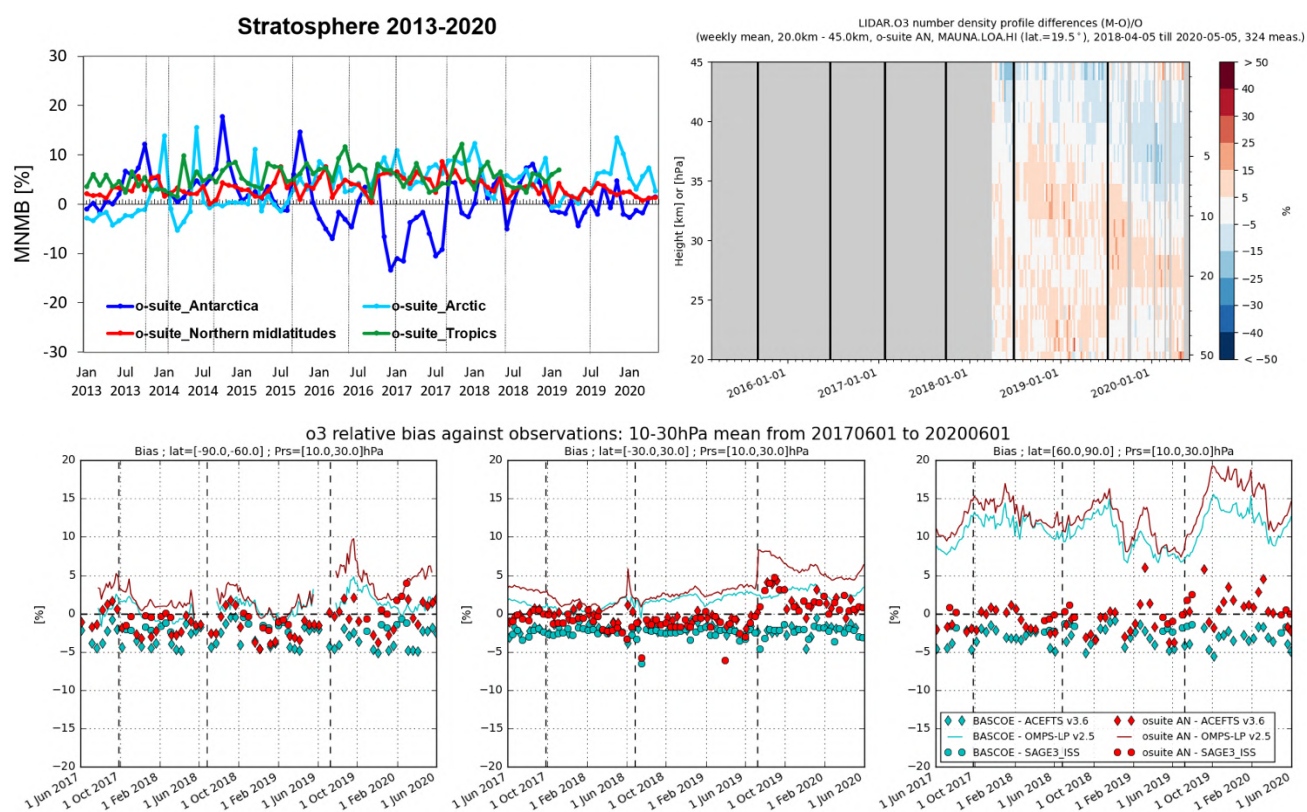


Figure S.9: Top: MNMBs (%) of ozone in the stratosphere from the o-suite against aggregated ozonesonde data in the Arctic (light blue), Antarctic (dark blue) northern midlatitudes (red) and tropics (green) from 2013 to May 2020. The stratosphere is defined as the altitude region between 60 and 10 hPa in the tropics and between 90 and 10 hPa elsewhere. Center: Comparison of the weekly mean profile bias between the O₃ mixing ratios of the 1-d forecast and the NDACC LIDAR at Mauna Loa. Bottom: Time series comparing model runs to observations for the period 2017-06-01 to 2020-06-01 in the upper stratosphere (10-30hPa averages): o-suite analyses (red) and BASCOE (cyan) vs OMPS-LP (solid), ACE-FTS (diamonds) and SAGE-III (bullets). Shown is the normalized mean bias (model-obs)/obs (%).

Ozone layer and UV

Ozone partial columns and vertical profiles

Ozone columns and profiles have been compared with the following observations: vertical profiles from balloon-borne ozonesondes; ground-based remote-sensing observations from the NDACC (Network for the Detection of Atmospheric Composition Change, <http://www.ndacc.org>); and satellite observations by 3 instruments (OMPS-LP, ACE-FTS and SAGE-III). Furthermore, the o-suite analyses are compared with those delivered by the independent assimilation system BASCOE.

Compared to ozone sondes (Fig. S.9) the o-suite O₃ partial pressures are slightly overestimated in all latitude bands (MNMB between -1 and +14%) except above the Antarctic. For the current period, the control run was not able to forecast the exceptional ozone hole above the Arctic.

Comparisons with the NDACC network include several stations for FTIR and UVVIS stratospheric columns, as well as microwave profiles for Ny Alesund (78.9°N) and Bern (47°N) and LIDAR profiles at Hohenpeissenberg (47.8°N) and Observatoire Haute Provence (OHP), France (43°N) and Mauna



Loa, Hawaii (19.5°N). The comparisons show a general good agreement with the o-suite, with small performance differences between AN and 1d forecasts. At the tropical sites the 1d FC performs significantly worse since the June 2016 update of the o-suite. This is confirmed by FTIR and the Mauna Loa LIDAR measurements (Fig. S.9).

The comparison with independent satellite observations is generally in good agreement for the considered period: for ACE-FTS, the NMB is mainly within 10% between 8km and 40km, and mostly within 5% between 15km and 35km except in the tropics; for SAGE-III, the NMB is mainly within 10% between 15km and 40km. OMPS-LP has less regular profiles, but the NMB still remain within 15% for most parts of the 20-40 km range. Since the upgrade to cycle 46R1 and the new vertical grid of 137 levels on July 9th 2019, a systematic overestimation of up to 10% around 30km (20hPa) is present in the NMB profiles (Fig. S.9).

Other stratospheric trace gases

Due to the lack of stratospheric chemistry in the C-IFS-CB05 scheme, the only useful product in the stratosphere is ozone. Other species, like NO₂, have also been evaluated but the results are only indicative.

Events

Ozone depletion over the Arctic in spring 2020: During spring of this year, an exceptionally strong and stable polar vortex and cold temperatures in the Arctic stratosphere lasting for several months, enabled the formation of PSCs, which resulted in large ozone losses over the Arctic. The Copernicus Atmosphere Monitoring Service tracked the ozone hole in near-real time (<https://atmosphere.copernicus.eu/cams-tracks-record-breaking-arctic-ozone-hole>).

The performance of the CAMS system to describe the event was investigated using ozone sonde data and the independent BASCOE stratospheric ozone analysis system. This study shows that the CAMS o-suite was able to reproduce ozone vertical distributions in much detail during the formation and break up of the ozone hole in the Arctic stratosphere during March and April 2020.

Dust event in Eastern Mediterranean in May 2020: From early May, satellites and ground-based observations detected several African dust outbreaks into Europe. Predicted AOD values above 0.7 and PM₁₀ values above 100 µg/m³ are observed in the whole Mediterranean with achieving maximum values up to 700 µg/m³ in Sardinia on 17th May. The comparison with observations show how the o-suite did timely reproduce the spatial distribution of the two dust plumes despite the model tending to overestimate the observed maximum values.

The impact of covid-19 on NO₂: Drastic reductions in NO₂ have been reported during the lockdowns in China, India and Europe during February-April 2020. The ability of the model simulations to reproduce observed tropospheric NO₂ columns during time periods with COVID-19 lockdown is investigated based on GOME-2/MetOp-A and TROPOMI/Sentinel-5P data satellite retrievals. The results show that both the o-suite and control run do not quantitatively reproduce the observed reductions in NO₂ when comparing 2020 with 2019. The emission inventory used is not aware of the changes related to the lockdown situations. The o-suite analysis compares slightly better with the satellite observations than the control run, but generally remains close to the control.



Table of Contents

Executive Summary	4
Air quality and atmospheric composition	4
Climate forcing	13
Ozone layer and UV	14
Events	15
1. Introduction	18
2. System summary and model background information	22
2.1 System based on the ECMWF IFS model (the o-suite and control run)	22
2.1.1 The CAMS o-suite	24
2.1.2 Short description of the latest CAMS upgrade (46r1)	25
2.1.3 Control	27
2.1.4 High-resolution CO ₂ and CH ₄ forecasts and delayed-mode analyses	27
2.2 Other systems	28
2.2.1 BASCOE	28
2.2.2 SDS-WAS multimodel ensemble	29
2.3 CAMS products	29
2.4 Availability and timing of CAMS products	29
3. Tropospheric Ozone	31
3.1 Validation with sonde data in the free troposphere	31
3.2 Ozone validation with IAGOS data	34
3.3 Validation with GAW and ESRL-GMD surface observations	41
3.4 Validation with AirBase observations in Mediterranean	45
3.5 Validation with AirBase observations over Europe	47
3.6 Validation with IASOA surface observations	49
3.7 Validation with IASI data	50
4. Carbon monoxide	51
4.1 Validation with Global Atmosphere Watch (GAW) Surface Observations	51
4.2 Validation with IAGOS Data	53
4.3 Validation against FTIR observations from the NDACC network	64
4.4 Validation against FTIR observations from the TCCON network	67
4.5 Evaluation with MOPITT and IASI data	71
4.6 Evaluation with CO surface observations over Europe	75
5. Tropospheric nitrogen dioxide	77
5.1 Evaluation against GOME-2 and TROPOMI retrievals	77
5.2 Evaluation against ground-based DOAS observations	82



6. Formaldehyde	85
6.1 Validation against satellite data	85
6.2 Evaluation against ground-based DOAS observations	90
7. Water vapour	92
8. Aerosol	99
8.1 Global comparisons with Aeronet and EMEP	99
8.2 Validation of dust optical depth against AERONET, and comparisons with the Multi-model Median from SDS-WAS	105
8.3 Ceilometer backscatter profiles	111
8.4 Aerosol validation over Europe and the Mediterranean	115
9. Stratosphere	122
9.1 Validation against ozone sondes	122
9.2 Validation against observations from the NDACC network	123
9.3 Comparison with dedicated systems and with observations by limb-scanning satellites	131
9.4 Stratospheric NO ₂	137
10. Validation results for greenhouse gases	140
10.1 CH ₄ and CO ₂ validation against ICOS observations	140
10.2 CH ₄ and CO ₂ validation against TCCON observations	145
10.3 Validation against FTIR observations from the NDACC network	150
11. Event studies	154
11.1 Ozone hole over the Arctic in spring 2020	154
11.2 Dust event in the Eastern Mediterranean in May 2020	160
11.3 Impact of COVID-19 on tropospheric NO ₂	162
12. References	169
Annex 1: Acknowledgements	175



1. Introduction

The Copernicus Atmosphere Monitoring Service (CAMS, <http://atmosphere.copernicus.eu/>) is a component of the European Earth Observation programme Copernicus. The CAMS global near-real time (NRT) service provides daily analyses and forecasts of trace gas and aerosol concentrations. The CAMS near-real time services consist of daily analysis and forecasts with the ECMWF IFS system with data assimilation of trace gas concentrations and aerosol properties. This document presents the system evolution and the validation statistics of the CAMS NRT global atmospheric composition analyses and forecasts. The validation methodology and measurement datasets are discussed in Eskes et al. (2015).

In this report the performance of the system is assessed in two ways: both the longer-term mean performance (seasonality) as well as its ability to capture recent events are documented. Table 1.1 provides an overview of the trace gas species and aerosol aspects discussed in this CAMS near-real time validation report. This document is updated every 3 months to report the recent status of the near-real time service. The report covers results for a period of at least one year to document the seasonality of the biases. Sometimes reference is made to other model versions or the reanalysis to highlight aspects of the near-real time products.

This validation report is accompanied by the "Observations characterization and validation methods" report, Eskes et al. (2019), which describes the observations used in the comparisons, and the validation methodology. This report can also be found on the global validation page, <http://atmosphere.copernicus.eu/user-support/validation/verification-global-services>.

Key CAMS NRT products and their users are: Boundary conditions for regional air quality models (e.g. AQMEII, air quality models not participating in CAMS); Long range transport of air pollution (e.g. LRTAP); Stratospheric ozone column and UV (e.g. WMO, DWD); 3D ozone fields (e.g. SPARC). As outlined in the MACC-II Atmospheric Service Validation Protocol (2013) and MACC O-INT document (2011), relevant user requirements are quick looks of validation scores, and quality flags and uncertainty information along with the actual data. This is further stimulated by QA4EO (Quality Assurance Framework for Earth Observation, <http://www.qa4eo.org>) who write that "all earth observation data and derived products is associated with it a documented and fully traceable quality indicator (QI)". It is our long-term aim to provide such background information. The user is seen as the driver for any specific quality requirements and should assess if any supplied information, as characterised by its associated QI, are "fit for purpose" (QA4EO task team, 2010).

CAMS data are made available to users as data products (grib or netcdf files) and graphical products from ECMWF, accessible through the catalogue on <http://atmosphere.copernicus.eu/>.

A summary of the system and its recent changes is given in section 2. Subsequent sections give an overview of the performance of the system for various species, and during recent events. Routine validation results can be found online via regularly updated verification pages,

<http://atmosphere.copernicus.eu/user-support/validation/verification-global-services>.

Table 1.2 lists all specific validation websites that can also be found through this link.



Table 1.1: Overview of the trace gas species and aerosol aspects discussed in this CAMS near-real time validation report. Shown are the datasets assimilated in the CAMS analysis (second column) and the datasets used for validation, as shown in this report (third column). Green colours indicate that substantial data is available to either constrain the species in the analysis, or substantial data is available to assess the quality of the analysis. Yellow boxes indicate that measurements are available, but that the impact on the analysis is not very strong or indirect (second column), or that only certain aspects are validated (third column).

Species, vertical range	Assimilation	Validation
Aerosol, optical properties	MODIS Aqua/Terra AOD PMAp AOD	AOD, Ångström: AERONET, GAW, Skynet, MISR, OMI, lidar, ceilometer
Aerosol mass (PM10, PM2.5)	MODIS Aqua/Terra	European AirBase stations
O ₃ , stratosphere	MLS, GOME-2, OMI, SBUV-2, TROPOMI	Sonde, lidar, MWR, FTIR, OMPS, ACE-FTS, SAGE3-ISS and BASCOE analyses
O ₃ , UT/LS	MLS	IAGOS, ozone sonde
O ₃ , free troposphere	Indirectly constrained by limb and nadir sounders	IAGOS, ozone sonde, IASI
O ₃ , PBL / surface		Surface ozone: WMO/GAW, NOAA/ESRL-GMD, AIRBASE
CO, UT/LS	IASI, MOPITT	IAGOS
CO, free troposphere	IASI, MOPITT	IAGOS, MOPITT, IASI, TCCON
CO, PBL / surface	IASI, MOPITT	Surface CO: WMO/GAW, NOAA/ESRL
NO ₂ , troposphere	OMI, GOME-2, partially constrained due to short lifetime	TROPOMI, SCIAMACHY, GOME-2, MAX-DOAS
HCHO		TROPOMI, GOME-2, MAX-DOAS
SO ₂	GOME-2 (Volcanic eruptions)	
Stratosphere, other than O ₃		NO ₂ column only: SCIAMACHY, GOME-2
CO ₂ , surface, PBL		ICOS
CO ₂ , column	GOSAT	TCCON
CH ₄ , surface, PBL		ICOS
CH ₄ , column	GOSAT, IASI	TCCON



Table 1.2: Overview of quick-look validation websites of the CAMS system.

<i>The CAMS global evaluation server</i>
https://global-evaluation.atmosphere.copernicus.eu
<i>Reactive gases – Troposphere</i>
<p>IAGOS tropospheric ozone and carbon monoxide: http://www.iagos.fr/cams/</p> <p>Surface ozone from EMEP (Europe) and NOAA-ESRL (USA): http://www.academyofathens.gr/cams</p> <p>Tropospheric nitrogen dioxide and formaldehyde columns against satellite retrievals: http://www.doas-bremen.de/macc/macc_veri_iup_home.html</p> <p>Tropospheric CO columns against satellite retrievals: http://www.mpimet-cams.de</p> <p>GAW surface ozone and carbon monoxide: https://atmosphere.copernicus.eu/charts/cams_gaw_ver/v0d_gaw_oper_operfc_nrt_sites?facets=undefined&time=2018060100,0,2018060100&fieldpair=CO&site=cmn644n00</p>
<i>Reactive gases - Stratosphere</i>
<p>Stratospheric composition: http://www.copernicus-stratosphere.eu</p> <p>NDACC evaluation in stratosphere and troposphere (the NORS server) http://nors-server.aeronomie.be</p>
<i>Aerosol</i>
<p>Evaluation against Aeronet stations: http://aerocom.met.no/cams-aerocom-evaluation/</p> <p>More in-depth evaluations are available from the Aerocom website.</p> <p>WMO Sand and Dust Storm Warning Advisory and Assessment System (SDS-WAS) model intercomparison and evaluation: http://sds-was.aemet.es/forecast-products/models</p> <p>Aeronet verification of CAMS NRT forecasts: https://atmosphere.copernicus.eu/charts/cams_aeronet_ver/?facets=undefined&time=2019020100,0,2019020100&site=ARM_Graciosa</p>
<i>Satellite data monitoring</i>
<p>Monitoring of satellite data usage in the Near-Real-Time production: https://atmosphere.copernicus.eu/charts/cams/cams_satmon?facets=undefined&time=2016071800&Parameter=AURA_MLS_profile_Ozone_1_GLOBE</p>

The CAMS global evaluation server, <https://global-evaluation.atmosphere.copernicus.eu>, became available in Summer 2019. This server combines many of the individual verification results shown on the other CAMS web pages listed in Table 1.2, and presents the comparisons through a uniform interface.



Naming and color-coding conventions in this report follow the scheme as given in Table 1.3.

Table 1.3. Naming and colour conventions as adopted in this report.

Name in figs	experiment	Colour
{obs name}	{obs}	black
o-suite D+0 FC	0001	red
control	gsyg	blue
GHG high-resolution run	gqpe / ghqy	orange
GHG global analysis	gqiq	green



2. System summary and model background information

The specifics of the different CAMS model versions are given below (section 2.1) including an overview of model changes. Other systems used in CAMS are listed in section 2.2. An overview of products derived from this system is given in section 2.3. Timeliness and availability of the CAMS products is given in section 2.4.

2.1 System based on the ECMWF IFS model (the o-suite and control run)

Key model information is given on the CAMS data-assimilation and forecast run o-suite and its control experiment, used to assess the performance of the assimilation. The forecast products are listed in Table 2.1. Table 2.2 provides information on the satellite data used in the o-suite. Further details on the different model runs and their data usage can be found at <http://atmosphere.copernicus.eu/documentation-global-systems>.

Table 2.1: Overview of model runs assessed in this validation report.

Forecast system	Exp. ID	Brief description	Upgrades (e-suite ID)	Cycle
O-suite	0001	Operational CAMS DA/FC run	20190709-present 20180626-20190708 20170926-20180625 20170124-20170926 20160621-20170124 20150903-20160620 20140918-20150902	46R1 45R1 43R3 43R1 41R1 41R1 40R2
Control	h7c4 gzhy gsyg gnhb gjhh geuh g4o2	control FC run without DA	20190709-present 20180626-20190708 20170926-20180625 20170124-20170926 20160621-20170124 20150901-20160620 20140701-20150902	46R1 45R1 43R3 43R1 41R1 41R1 40R2
GHG run	h72g	Tco399L137 NRT CO ₂ , CH ₄ analyses (~25km)	20191201-present	46R1
	h9sp	High resolution Tco1279 (~9km) NRT CO ₂ , CH ₄ forecast	20191201-present	46R1
	gwx3 gqiq	GHG analysis Tco399 (~25km)	20181201-20191130 20170101-20181130	45R1 43R1
	gznv gqpe	High resolution Tco1279 (~9km) NRT CO ₂ , CH ₄ forecast	20181201-20191130 20170101-20181130	45R1 43R1
	ghqy gf39	High resolution T1279, NRT CO ₂ and CH ₄ without DA	20160301-20170621 20150101-20160229	



Table 2.2: Satellite retrievals of reactive gases and aerosol optical depth that are actively assimilated in the suite.

Instrument	Satellite	Provider	Version	Type	Status
MLS	AURA	NASA	V4	O3 Profiles	20130107 -
OMI	AURA	NASA	V883	O3 Total column	20090901 -
GOME-2	Metop-A	Eumetsat	GDP 4.8	O3 Total column	20131007 - 20181231
GOME-2	Metop-B	Eumetsat	GDP 4.8	O3 Total column	20140512 -
GOME-2	Metop-C	Eumetsat	GDP 4.9	O3 Total column	20200505 -
SBUV-2	NOAA-19	NOAA	V8	O3 21 layer profiles	20121007 -
OMPS	Suomi-NPP	NOAA / EUMETSAT		O3 Profiles	20170124 - 20190409
TROPOMI	Sentinel-5P	ESA		O3 column	20181204-
IASI	MetOp-A	LATMOS/ULB Eumetsat	-	CO Total column	20090901 - 20180621 20180622 - 20191118
IASI	MetOp-B	LATMOS/ULB Eumetsat	-	CO Total column	20140918 - 20180621 20180622 -
IASI	MetOp-C	Eumetsat		CO total column	20191119 -
MOPITT	TERRA	NCAR	V5-TIR V7-TIR V7-TIR Lance V8-TIR	CO Total column	20130129 - 20160124 - 20180626 20180626 20190702
OMI	AURA	KNMI	DOMINO V2.0	NO2 Tropospheric column	20120705 -
GOME-2	MetOp-A	Eumetsat	GDP 4.8	NO2 Tropospheric column	20180626 - 20200504
GOME-2	MetOp-B	Eumetsat	GDP 4.8	NO2 Tropospheric column	20180626 -
GOME-2	MetOp-C	Eumetsat	GDP 4.9	NO2 Tropospheric column	20200505-
GOME-2	MetOp-A	Eumetsat	GDP 4.8	SO2 Total column	20150902 -
GOME-2	MetOp-B	Eumetsat	GDP 4.8	SO2 Total column	20150902-
GOME-2	MetOp-C	Eumetsat	GDP 4.9	SO2 Total column	20200505-
MODIS	AQUA / TERRA	NASA	Col. 5 Deep Blue Col. 6, 6.1	Aerosol total optical depth, fire radiative power	20090901 - 20150902 - 20170124 -
PMAp	METOP-A METOP-B	EUMETSAT		AOD	20170124 - 20170926 -

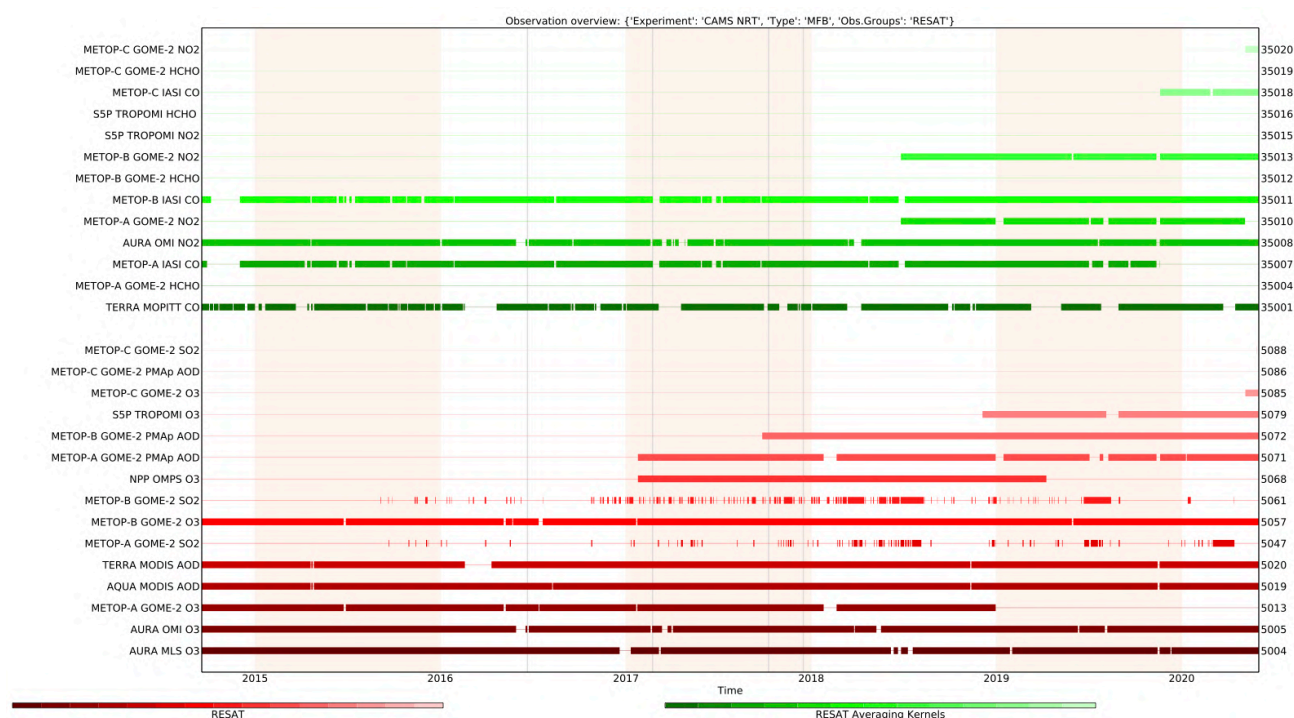


Figure 2.1: Satellite observation usage in the real-time analysis, for ozone, CO, aerosol AOD and NO₂, from October 2014 onwards. Top rows (in green): products assimilated using averaging kernels. Sentinel-5P TROPOMI ozone is assimilated since Dec. 2018 and other products from TROPOMI are monitored.

2.1.1 The CAMS o-suite

The o-suite consists of the IFS-CB05 chemistry combined with the CAMS bulk aerosol model. The chemistry is described in Flemming et al. (2015) and Flemming et al. (2017), aerosol is described in Morcrette et al. (2009). The forecast length is 120 h. The o-suite data is stored under **expver '0001'** of **class 'MC'**. On 21 June 2016 the model resolution has seen an upgrade from T255 to T511, and forecasts are produced twice per day.

A short summary of the main model specifications:

- The modified CB05 tropospheric chemistry is used (Williams et al., 2013), originally taken from the TM5 chemistry transport model (Huijnen et al., 2010)
- Stratospheric ozone during the forecast is computed from the Cariolle scheme (Cariolle and Teyss  re, 2007) as already available in IFS, while stratospheric NO_x is constrained through a climatological ratio of HNO₃/O₃ at 10 hPa.
- Monthly mean dry deposition velocities are based on the SUMO model provided by the MOCAGE team.
- Data assimilation is described in Inness et al. (2015) and Benedetti et al. (2009) for chemical trace gases and aerosol, respectively. Satellite data assimilated is listed in Table 2.2 and Fig. 2.1.
- Anthropogenic and biogenic emissions are based on MACCity (Granier et al., 2011) and a climatology of the MEGAN-MACC emission inventories (Sindelarova et al., 2014). Anthropogenic emissions changed to CAMS_GLOB v2.1 with the July 2019 update.
- NRT fire emissions are taken from GFASv1.2 (Kaiser et al. 2012).



The aerosol model includes 14 prognostic variables (Remy et al., 2019).

- 3 size bins each for sea-salt and desert dust
- 2 bins (hydrophilic and hydrophobic) each for organic matter and black carbon
- 1 bin for sulphate
- 2 bins (fine and coarse) for nitrate (New since 46R1)
- 1 bin for ammonium (New since 46R1)

The SO₂ precursor for sulphate aerosol no longer exists as a separate prognostic in the aerosol scheme, which since 46R1 couples directly to the SO₂ in the chemistry scheme instead. Likewise, the precursors for the new nitrate and ammonium aerosol (nitric acid and ammonia) are also part of the chemistry scheme rather than the aerosol scheme.

Aerosol total mass is constrained by the assimilation of MODIS and PMAp AOD (Benedetti et al. 2009). A variational bias correction is currently applied for the PMAp AOD based on the approach used also elsewhere in the IFS (Dee and Uppala, 2009).

A history of updates of the o-suite is given in Table 2.3, and is documented in earlier MACC-VAL and CAMS reports: <https://atmosphere.copernicus.eu/node/326>. This includes a list with changes concerning the assimilation system.

The CAMS o-suite system is upgraded regularly, following updates to the ECMWF meteorological model as well as CAMS-specific updates such as changes in chemical data assimilation. These changes are documented in e-suite validation reports, as can be found from the link above. Essential model upgrades are also documented in Table 2.3.

The penultimate upgrade of the system (45r1) took place on 26 June 2018. This upgrade is also relevant for this report (for the period up to 8 July), and the validation for this upgrade is described in Eskes et al., 2018b/2018c.

2.1.2 Short description of the latest CAMS upgrade (46r1)

The latest upgrade of the system took place on 9 July 2019 and is based on IFS version cy46r1_CAMS and involves the move from 60 to 137 vertical levels, see <https://atmosphere.copernicus.eu/cycle-46r1> or <https://confluence.ecmwf.int/display/COPSRV/Current+global+production+suites>.

The validation for this 46r1 upgrade is described in Basart et al. 2019: https://atmosphere.copernicus.eu/sites/default/files/2019-07/CAMS84_2018SC1_D3.2.1-201907_esuite_v1.pdf

The meteorological changes can be found on the ECMWF-IFS CY46R1 page, <https://confluence.ecmwf.int/display/FCST/Implementation+of+IFS+cycle+46R1>.



Table 2.3: Long-term o-suite system updates.

Date	o-suite update
2009.08.01	Start of first NRT experiment f7kn with coupled MOZART chemistry, without aerosol. Also without data assimilation.
2009.09.01	Start of first MACC NRT experiment f93i, based on meteo cy36r1, MOZART v3.0 chemistry, MACC aerosol model, RETRO/REAS and GFEDv2 climatological emissions, T159L60 (IFS) and $1.875^{\circ} \times 1.875^{\circ}$ (MOZART) resolution.
2012.07.05	Update to experiment fnyp: based on meteo cy37r3, MOZART v3.5 chemistry, where changes mostly affect the stratosphere, MACCity (gas-phase), GFASv1 emissions (gas phase and aerosol), T255L60 (IFS) and $1.125^{\circ} \times 1.125^{\circ}$ (MOZART) resolution. Rebalancing aerosol model, affecting dust.
2013.10.07	Update of experiment fnyp from e-suite experiment fwu0: based on meteo cy38r2, no changes to chemistry, but significant rebalancing aerosol model. Assimilation of 21 layer SBUV/2 ozone product
2014.02.24	Update of experiment fnyp from e-suite experiment fzpr: based on meteo cy40r1. No significant changes to chemistry and aerosol models.
2014.09.18	Update to experiment g4e2: based on meteo cy40r2. In this model version IFS-CB05 is introduced to model atmospheric chemistry.
2015.09.03	Update to experiment g9rr: based on meteo cy41r1.
2016.06.21	Update to experiment 0067: based on meteo cy41r1, but a resolution increase from T255 to T511, and two production runs per day
2017.01.24	Update to cycle 43R1_CAMS, T511L60
2017.09.26	Update to cycle 43R3_CAMS, T511L60
2018.06.26	Update to cycle 45R1_CAMS, T511L60
2019-07-09	Update to cycle 46R1_CAMS, T511L137

The atmospheric composition content of the new cycle includes the following aspects:

Assimilation:

- New model-error covariance matrices for aerosol and chemistry at 137 levels.

Observations:

- No new atmospheric composition observations compared to Cycle 45r1.

Emissions:

- New emissions inventories: CAMS_GLOB_ANT v2.1 (anthropogenic) and CAMS_GLOB_BIO v1.1 (biogenic), in place of previous MACCity and MEGAN_MACC inventories.
- Biomass-burning injection heights from GFAS and updated diurnal cycle. In particular, this reduces the overestimation of near-surface PM_{2.5} during fire events.



- Anthropogenic SOA production was updated with a diurnal cycle and a regionally-varying ratio to CO emissions. This has a small impact on AOD, but significantly reduces night-time near-surface PM_{2.5} in polluted regions.
- New online dust emission scheme (Nabat et al., 2012). This increases total dust emissions and shifts them towards larger particle sizes, in line with recent literature. An updated dust source function improves the selection of source regions, reducing "gaps" in dust emissions.
- Sea-salt production over freshwater lakes eliminated. This corrects an issue that was particularly noticeable over the Great Lakes.

Other model changes:

- Vertical resolution increased from 60 levels to 137 levels, matching that used at ECMWF for NWP. This includes moving the model top from 0.1 hPa to 0.01 hPa.
- New nitrate and ammonium aerosol species are included and are coupled to the gas-phase nitrogen chemistry. This is a major expansion of the aerosol species represented in the model, giving a more complete representation of the species which contribute to e.g. PM_{2.5} over Europe.
- Sulphur species (SO₂ and SO₄) coupled between chemistry and aerosol schemes. See discontinued parameters below. This brings a greater consistency between the chemistry and aerosol products related to the sulphur cycle.
- Online calculation of dry deposition velocities for trace gases. This was already in place for aerosols in 45r1 and allows the deposition scheme to better account for variations in surface properties.
- Updates to wet deposition parameterisations. This brings improvements in the distinction between scavenging by liquid and ice and harmonises the treatment for aerosols and trace gases.
- Updates to chemical reaction rates following latest recommendations by JPL/IUPAC.

2.1.3 Control

The control run (relevant expver = **gzhy**, since 26/06/2018; expver = **h7c4** since 09/07/2019) applies the same settings as the respective o-suites, based on the coupled IFS-CB05 system with CAMS aerosol for cy54r1, except that data assimilation is not switched on. The meteorology in the control run is initialized with the meteorological fields from the o-suite.

2.1.4 High-resolution CO₂ and CH₄ forecasts and delayed-mode analyses

The pre-operational forecasts of CO₂ and CH₄ use an independent setup of the IFS at a resolution of TL1279, i.e. ~16 km horizontal, and with 137 levels. This system runs in real time and does not apply data assimilation for the greenhouse gases.

The land vegetation fluxes for CO₂ are modelled on-line by the CTESSEL carbon module (Boussetta et al., 2013). A biogenic flux adjustment scheme is used in order to reduce large-scale biases in the net ecosystem fluxes (Agusti-Panareda, 2015). The anthropogenic fluxes are based on the annual



mean EDGARv4.2 inventory using the most recent year available (i.e. 2008) with estimated and climatological trends to extrapolate to the current year. The fire fluxes are from GFAS (Kaiser et al., 2012). Methane fluxes are prescribed in the IFS using inventory and climatological data sets, consistent with those used as prior information in the CH₄ flux inversions from Bergamaschi et al. (2009). The anthropogenic fluxes are from the EDGAR 4.2 database (Janssens-Maenhout et al., 2012) valid for the year 2008. The biomass burning emissions are from GFAS v1.2 (Kaiser et al., 2012). The high-resolution forecast experiments also included a linear CO scheme (Massart et al., 2015).

The experiments analysed in this report are:

- **“h72g”** NRT CO₂, CH₄ analyses from 1 December 2019, with a resolution Tco399 (~25km) and 137 vertical levels. Cycle 46R1.
- **“h9sp”** NRT CO₂, CH₄ forecasts from 1 December 2019, with high resolution Tco1279 (~9km) and 137 vertical levels. Cycle 46R1.
- **“gqpe”** (43R1) from January 2017, and **“gznv”** (45R1) from 1 December 2018 to present. It runs with a TCO1279 Gaussian cubic octahedral grid (equivalent to approximately 9km horizontal resolution). Note that the CO₂, CH₄ and linear CO tracers are initialized with the GHG analysis (gqiq) for CO₂ and CH₄ and the CAMS operational analysis for CO.
- The greenhouse gas analysis experiment runs on a TCO399 grid (equivalent to around 25km) and 137 vertical levels and is available from January 2017 (**“gqiq”**, 43R1) and 1 December 2018 (**“gwx3”**, 45R1). This experiment runs in delayed mode (4 days behind real time) and makes use of observations from TANSO-GOSAT (methane and CO₂) and MetOp-IASI (methane).
- **“ghqy”** from March 2016. The initial conditions used in ghqy on 1st of March 2016 are from the GHG analysis (experiment gg5m). Furthermore, the meteorological analysis used to initialize the ghqy forecast changed resolution and model grid in March 2016. Note that the CO₂, CH₄ and linear CO tracers are free-running.

2.2 Other systems

2.2.1 BASCOE

The NRT analyses and forecasts of ozone and related species for the stratosphere, as delivered by the Belgian Assimilation System for Chemical Observations (BASCOE) of BIRA-IASB (Lefever et al., 2014; Errera et al., 2008), are used as an independent model evaluation of the CAMS products. The NRT BASCOE product is the ozone analysis of Aura/MLS-SCI level 2 standard products, run in the following configuration (version 05.07):

- The following species are assimilated: O₃, H₂O, HNO₃, HCl, HOCl, N₂O and ClO.
- It lags by typically 4 days, due to latency time of 4 days for arrival of non-ozone data from Aura/MLS-SCI (i.e. the scientific offline Aura/MLS dataset).
- Global horizontal grid with a 3.75° longitude by 2.5° latitude resolution.
- Vertical grid is hybrid-pressure and consists in 86 levels extending from 0.01 hPa to the surface.
- Winds, temperature and surface pressure are interpolated in the ECMWF operational 6-hourly analyses.



- Time steps of 20 minutes, output every 3 hours

See the stratospheric ozone service at <http://www.copernicus-stratosphere.eu/>. It delivers graphical products dedicated to stratospheric composition and allows easy comparison between the results of o-suite, BASCOE and TM3DAM. The BASCOE data products (HDF4 files) are also distributed from this webpage. Other details and bibliographic references on BASCOE can be found at <http://bascoe.oma.be/>. A detailed change log for BASCOE can be found at http://www.copernicus-stratosphere.eu/4_NRT_products/3_Models_changelogs/BASCOE.php.

2.2.2 SDS-WAS multimodel ensemble

The World Meteorological Organization's Sand and Dust Storm Warning Advisory and Assessment System (WMO SDS-WAS) for Northern Africa, Middle East and Europe (NAMEE) Regional Center (<http://sds-was.aemet.es/>) has established a protocol to routinely exchange products from dust forecast models as the basis for both near-real-time and delayed common model evaluation. Currently, twelve regional and global models (see the complete list in the following link https://sds-was.aemet.es/forecast-products/forecast-evaluation/model-inter-comparison-and-forecast-evaluation/at_download/file) provides daily operational dust forecasts (i.e. dust optical depth, DOD, and dust surface concentration).

Different multi-model products are generated from the different prediction models. Two products describing centrality (multi-model median and mean) and two products describing spread (standard deviation and range of variation) are daily computed. In order to generate them, the model outputs are bi-linearly interpolated to a common grid mesh of $0.5^\circ \times 0.5^\circ$. The multi-model dust optical depth (DOD at 550 nm) median from nine dust prediction models participating in the SDS-WAS Regional Center is used for the validation of the CAMS NRT streams.

2.3 CAMS products

An extended list of output products from the NRT stream o-suite are available as 3-hourly instantaneous values up to five forecast days. These are available from ECMWF (through ftp in grib2 and netcdf format, <https://atmosphere.copernicus.eu/data>).

2.4 Availability and timing of CAMS products

The availability statistics provided in Table 2.6 are computed for the end of the 5-day forecast run. The CAMS production KPI is defined as the percentage of cycles in which all the general data dissemination tasks are completed before the deadlines: 10 UTC for the 00:00 and 22 UTC for the 12:00 UTC run. This was in part based on requirements from the regional models. We note that at present most regional models can still provide their forecasts even if the global forecast is available a bit later. Note that since 21 June 2016 two CAMS forecasts are produced each day.

The o-suite data delivery for the period March - May 2020 (MAM-2020) was excellent, with an on-time delivery percentage of 100%.

See table 2.6 for detailed statistics from 2014 to MAM-2020.



Table 2.6: Timeliness of the o-suite from December 2014. From June 2016 onwards CAMS has produced two forecasts per day.

Months	On time, 10 & 22 utc	80th perc	90th perc	95th perc
Dec-Feb '14-'15	97%	D+0, 19:43	D+0, 20:28	D+0, 21:13
Mar-May 2015	96%	D+0, 19:38	D+0, 21:03	D+0, 21:40
Jun-Aug 2015	95%	D+0, 20:24	D+0, 20:53	D+0, 21:54
Sept-Nov 2015	95%	D+0, 19:44	D+0, 20:55	D+0, 21:51
Dec-Feb '15-'16	100%	D+0, 18:39	D+0, 18:57	D+0, 19:43
Mar-May 2016	98%	D+0, 19:32	D+0, 19:47	D+0, 20:00
Jun-Aug 2016 (00 and 12 cycle)	100%	D+0, 08:53 D+0, 20:55	D+0, 09:04 D+0, 21:01	D+0, 09:18 D+0, 21:18
Sep-Nov 2016	98.9%	D+0, 08:44 D+0, 20:44	D+0, 08:51 D+0, 20:48	D+0, 08:52 D+0, 20:51
Dec 2016 - Feb 2017	99.4%	D+0, 09:02 D+0, 21:01	D+0, 09:11 D+0, 21:02	D+0, 09:18 D+0, 21:04
Mar-May 2017	100%	D+0, 09:08 D+0, 21:07	D+0, 09:14 D+0, 21:09	D+0, 09:19 D+0, 21:11
Jun-Aug 2017	100%	D+0, 09:05 D+0, 21:05	D+0, 09:07 D+0, 21:08	D+0, 9:09 D+0, 21:10
Sep-Nov 2017	100%	D+0, 09:02 D+0, 21:00	D+0, 09:05 D+0, 21:04	D+0, 9:09 D+0, 21:07
Dec 2017 - Feb 2018	98.33%	D+0, 08:55 D+0, 20:54	D+0, 08:59 D+0, 20:59	D+0, 09:01 D+0, 21:02
Mar-May 2018	98.9%	D+0, 09:00 D+0, 21:00	D+0, 09:06 D+0, 21:03	D+0, 09:08 D+0, 21:06
Jun-Aug 2018	100%	D+0, 09:11 D+0, 21:07	D+0, 09:14 D+0, 21:09	D+0, 09:20 D+0, 21:11
Sep-Nov 2018	100%	D+0, 09:05 D+0, 21:03	D+0, 09:09 D+0, 21:07	D+0, 09:13 D+0, 21:10
Dec 2018 - Feb 2019	98.9%	D+0, 09:03 D+0, 21:04	D+0, 09:06 D+0, 21:06	D+0, 09:08 D+0, 21:10
Mar-May 2019	100%	D+0, 09:07 D+0, 21:05	D+0, 09:10 D+0, 21:09	D+0, 09:12 D+0, 21:11
Jun-Aug 2019	99.5%	D+0, 09:19 D+0, 21:14	D+0, 09:22 D+0, 21:17	D+0, 09:27 D+0, 21:19
Sep-Nov 2019	98.9%	D+0, 09:14 D+0, 21:07	D+0, 09:23 D+0, 21:20	D+0, 09:26 D+0, 21:24
Dec 2019 - Feb 2020	99.4%	D+0, 09:00 D+0, 20:58	D+0, 09:03 D+0, 21:02	D+0, 09:12 D+0, 21:08
Mar-May 2020	100%	D+0, 08:55 D+0, 20:57	D+0, 08:58 D+0, 21:01	D+0, 09:00 D+0, 21:05



3. Tropospheric Ozone

3.1 Validation with sonde data in the free troposphere

Model profiles of the CAMS runs were compared to free tropospheric balloon sonde measurement data of 38 stations taken from the NDACC, WUODC, NILU and SHADOZ databases for January 2013 to February 2020 (see Fig. 3.1.1 - 3.1.2). Towards the end of the period, the number of available soundings decreases, which implies that the evaluation results may become less representative. The figures contain the number of profiles in each month that are available for the evaluation. The methodology for model comparison against the observations is described in Douros et al., 2017. The free troposphere is defined as the altitude range between 750 and 200hPa in the tropics and between 750 and 300hPa elsewhere.

Please note that recent scientific findings (<https://tropo.gsfc.nasa.gov/shadoz/Archive.html>, Thompson et al., 2017; Witte et al., 2017; 2018, Stauffer, et al. in preparation 2020) show a drop-off in Total Ozone at various global ozone stations in comparison with satellite instruments. This drop-off amounts between 5-10% for stratospheric ozone. Changes in the ECC ozone instrument are associated with the drop-off, but no single factor has been identified as cause yet. For tropospheric ozone (<50 hPa) no alternations are reported, but cannot be ruled out. Data availability is thus recently limited.

MNMBs for the o-suite are mostly within the range $\pm 20\%$, for all months, in all zonal bands, except for the Tropics and Antarctica, where larger positive MNMBs up to $\pm 45\%$ appear, see Fig. 3.1.4. During the last year (May 2019 to May 2020) MNMBs are within -2% and 20% over the Arctic, $\pm 15\%$ over the Northern Midlatitudes and Antarctica, see Fig. 3.1.1.-3.1.4.

Over the Arctic, the o-suite mostly shows smaller and partly slightly negative MNMBs during winter and spring season 2019 and 2020 (MNMBs between -2% and up to 14%) and positive biases during the rest of the period (MNMBs up to 20%) see, Fig. 3.1.1.

Over the NH mid-latitudes MNMBs for the o-suite are on average close to zero and only during the summer season maxima up to 14% appear. In the UTLS (Fig 3.1.3 on the right), MNMBs are positive over all regions and range within 20% .

Over Antarctica, the o-suite shows mostly positive MNMBs up to 15% , and negative biases from March to May 2020 (MNMBs up to -14%). The control run has mostly negative biases (up to -15%). For MAM, biases improve compared to the o-suite.

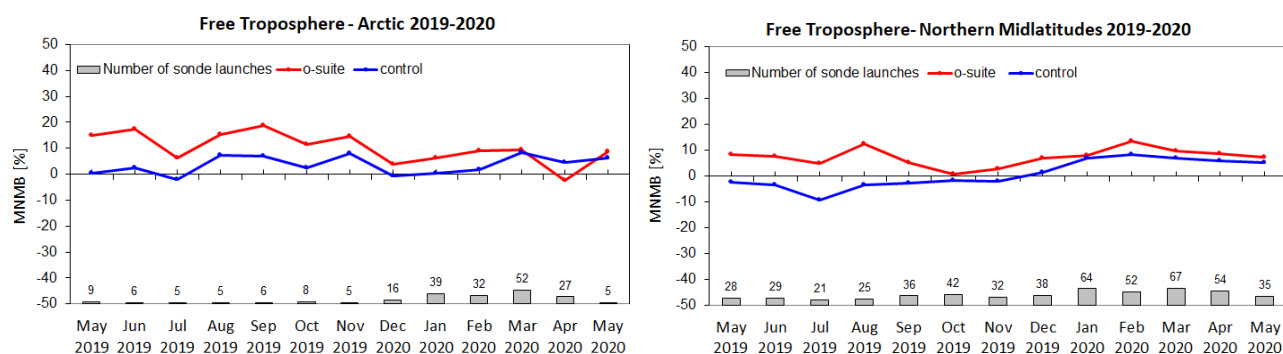


Figure 3.1.1: MNMBs (%) of ozone in the free troposphere (between 750 and 300 hPa) from the IFS model runs against aggregated sonde data over the Arctic (left) and the Northern mid latitudes (right). The numbers indicate the amount of individual number of sondes.

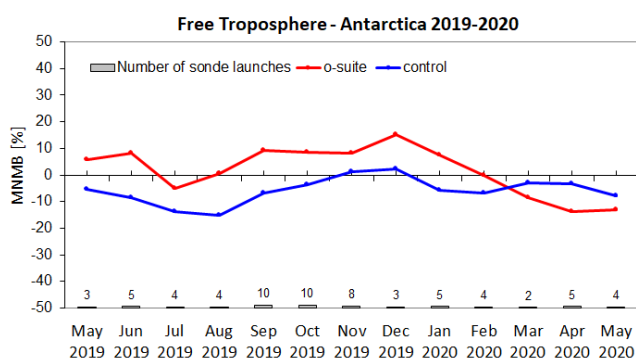


Figure 3.1.2: MNMBs (%) of ozone in the free troposphere (between 750 and 200hPa (Tropics) / 300hPa) from the IFS model runs against aggregated sonde data over Antarctica. The numbers indicate the amount of individual number of sondes.

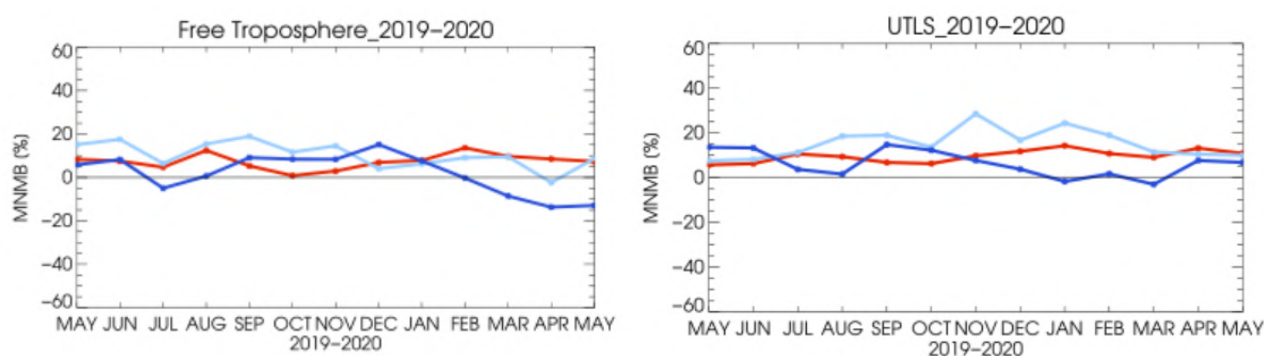


Figure 3.1.3: MNMBs (%) of ozone in the free troposphere (left, between 750 and 200hPa (Tropics) / 300hPa) and UTLS (right, between 300 and 100hPa (Tropics) / 60hPa) from the IFS model runs against aggregated sonde data over Antarctica (blue), Arctic (light blue) and Northern Midlatitudes (red).

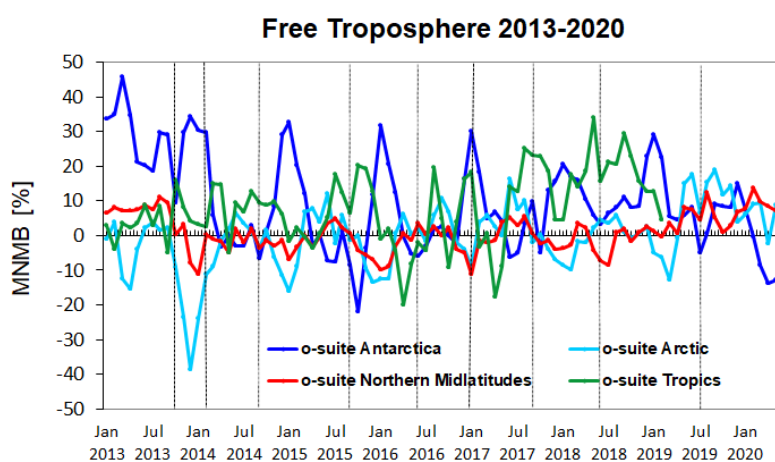


Figure 3.1.4: Time series of MNMB of ozone in the o-suite, compared against ozone sondes, averaged over different latitude bands. The free troposphere is defined here as the layer between 750 and 300 hPa.

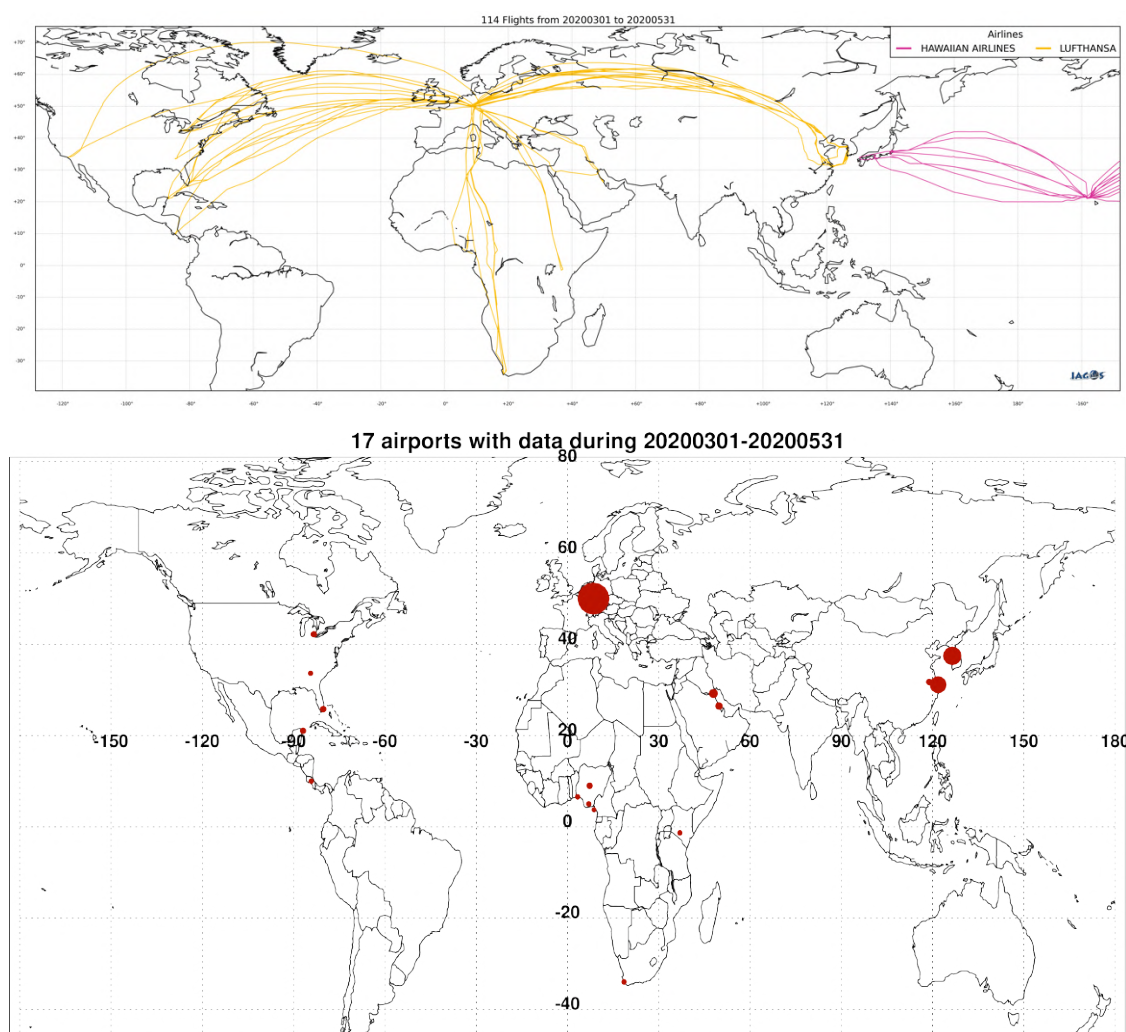


Figure 3.2.1: Map of the flights (top) and the visited airports (bottom) during the period March 2020 - May 2020, by the IAGOS-equipped aircraft. The size of the plotting circle represents the number of profiles available.

3.2 Ozone validation with IAGOS data

The daily profiles of ozone measured at airports around the world are shown on the CAMS website at http://www.iagos-data.fr/cams/nrt_profiles.php. For the period from March-May 2020, the data displayed on the web pages and in this report include only the data as validated by the instrument PI. The available flights and available airports are shown in Fig. 3.2.1 top and bottom respectively. Performance indicators have been calculated for different parts of the IAGOS operations.

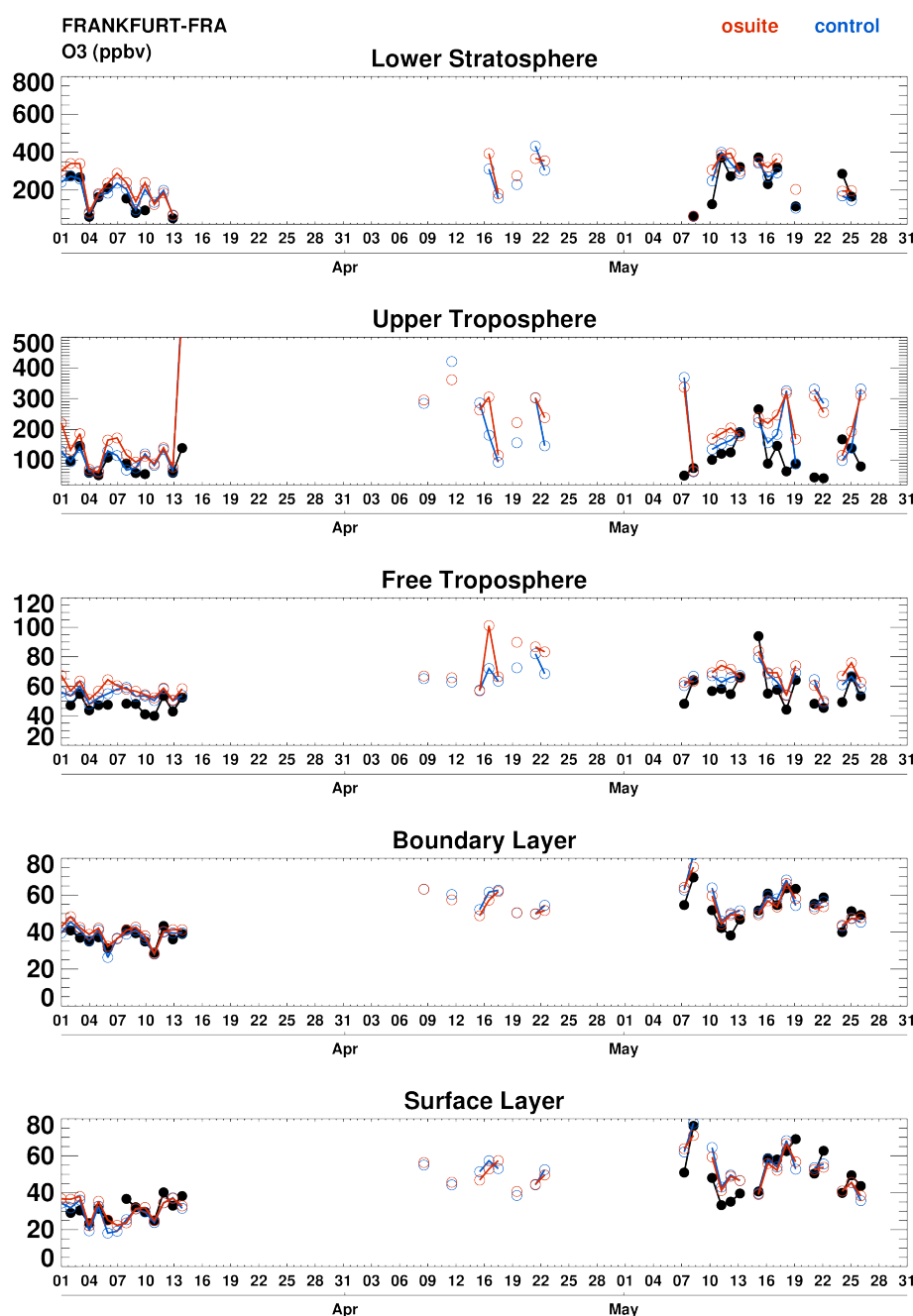


Figure 3.2.2: Time series of daily mean ozone over Frankfurt during MAM 2020 for 5 layers: Surface Layer, Boundary Layer, Free Troposphere, Upper Troposphere and Lower Stratosphere. IAGOS is shown in black, the o-suite in red and associated control run in blue. Units: ppbv.

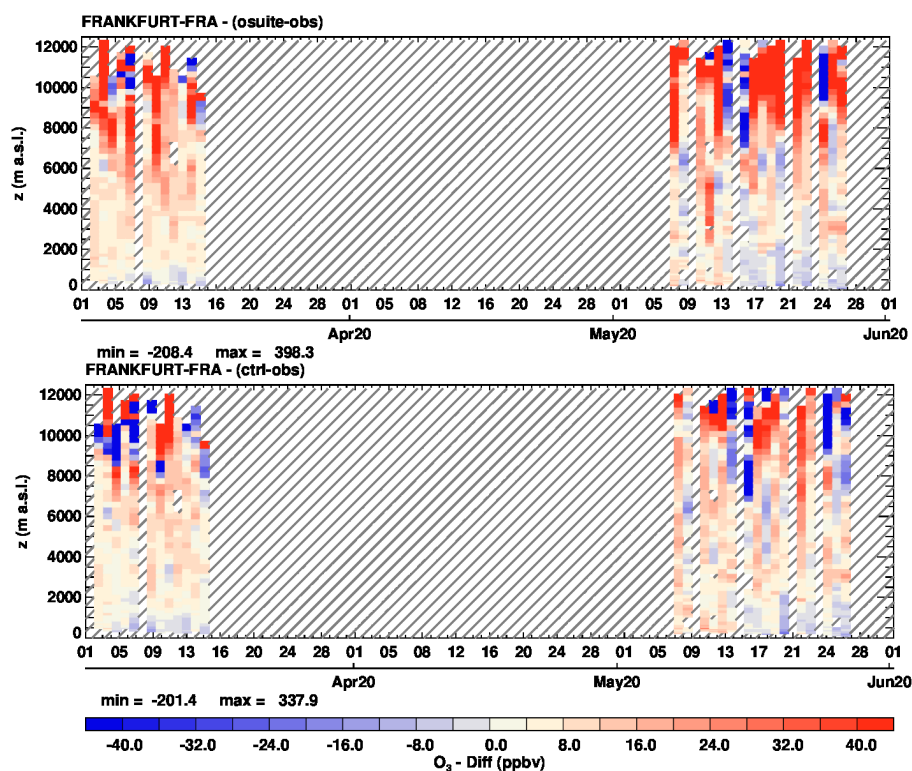


Figure 3.2.3: Time series of the absolute differences (model – IAGOS observations) in daily profiles for ozone over Frankfurt during MAM 2020. The top panel corresponds to o-suite the bottom panel to control run. Units: ppbv.

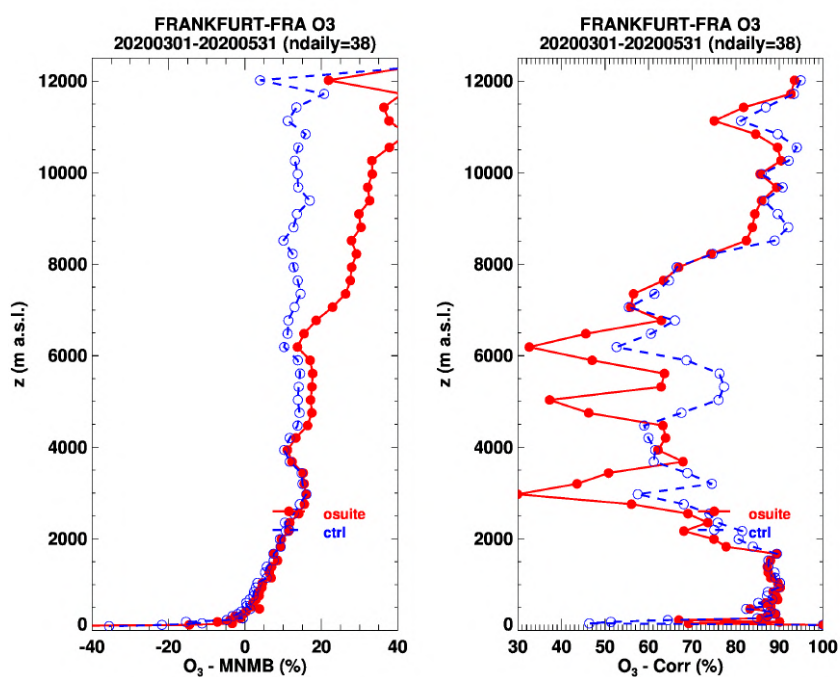


Figure 3.2.4: Model scores (MNMB and Correlation coefficient) for ozone at Frankfurt calculated over the period MAM 2020. The left panel corresponds to MNMB and the right panel to Correlation coefficient. The o-suite is shown in red and associated control run in blue. Units: %.



Six aircraft are equipped with the IAGOS system during this period. With these aircrafts, operating fully over the three-month period, we can expect a total of about 1260 flights. The actual number of flights within the period was 114 (228 profiles) giving a performance of 9%. These flights are shown in Fig. 3.2.1 (top). The low performance is mainly due to the unprecedented reduction of air traffic related with COVID-19 lockdowns. Despite this context, one of the Lufthansa airplanes was transformed into a cargo carrier which allowed to operate throughout the lockdown period. In total for the MAM period, fifty three percent (53%) of the operational flights had usable measurements of ozone and 88% of the flights had usable CO.

Ozone and CO data are only delivered by the two aircrafts from Lufthansa operating from Frankfurt. Only one aircraft from Lufthansa is delivering O₃ data, while CO data are delivered by both Lufthansa aircrafts. Fig. 3.2.1 (bottom) shows the available airports, with a plotting circle scaled to the highest number of flights at an airport. Fig. 3.2.1 (bottom) shows the available airports, with a plotting circle scaled to the highest number of flights at an airport.

Europe

Figure 3.2.2 presents ozone time series at Frankfurt during the full period March – May 2020 for 5 atmospheric layers. Time series of the profile differences (in ppbv) are also presented in Fig. 3.2.3. In the low to mid-troposphere the two runs behave similarly. Ozone data are available only at the beginning of the period in the first half of March, and most of the month in May. Ozone is well represented in the low troposphere by both runs with on average a positive MNMB of less than 20% and a correlation of more than 90% (Fig. 3.2.3 and 3.2.4). In the mid troposphere the MNMB of the models remain close to 20% but the correlation coefficient is much smaller (Fig. 3.2.3 and 3.2.4). In the UTLS region the bias is larger and the results from the two runs differ, ozone is mostly overestimated by the o-suite with an MNMB of 40% (Fig. 3.2.3 and 3.2.4), whereas control run does not present a systematic behaviour with frequent underestimations (Fig. 3.2.3) with an absolute values of the bias often smaller than that of the o-suite.

According to observations, in the surface and boundary layer, ozone values are small in the first half of March (20-40 ppbv), while they are relatively large in the second half of May (40-80 ppbv) especially around the 8 and 19 of May where a peak of 80 ppbv and 70 ppbv is reached in the surface layer respectively (Fig. 3.2.2). This can also be seen in the examples of individual profiles at Frankfurt presented in Fig. 3.2.5 for days 8, 18 and 19. The comparison with the climatological variability of observations (see regional report MAM2020) shows that these increases in ozone lead to a positive anomaly in the low troposphere. This effect might be related to the reduction in emissions during COVID-19 lockdowns leading to less chemical titration of ozone. However, this effect could also be attributed to particular meteorological conditions during the month of May that have to be further investigated. These high ozone values in the surface and boundary layer are well represented by the two runs with small underestimations (Fig. 3.2.3 and 3.2.5). In the free troposphere and UTLS large bias are found especially during the month of May with often a slightly better performance from control run as shown on time series of the bias (Fig. 3.2.3) individual profiles of 11, 15 and 21 May (Fig. 3.2.5).

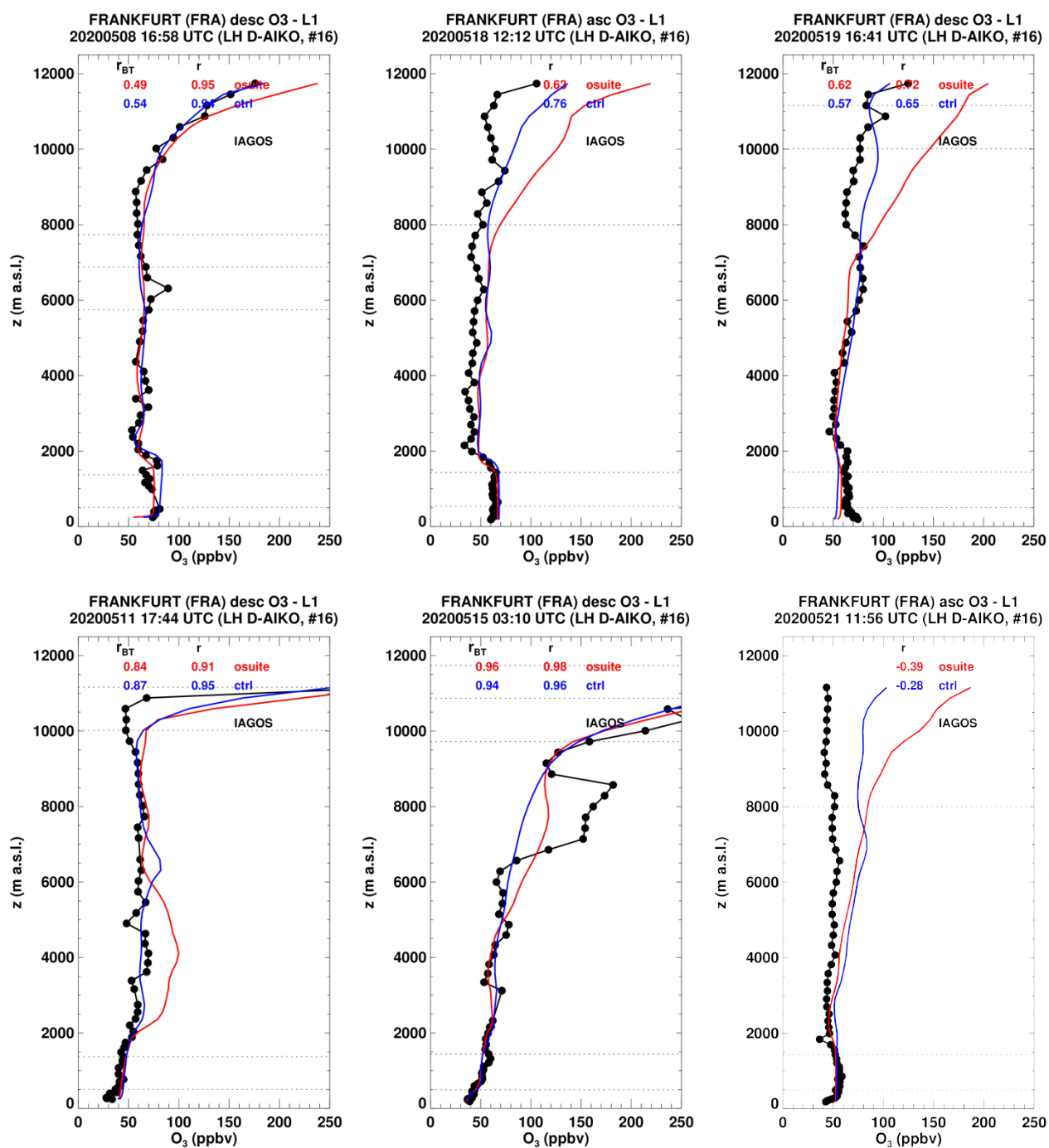


Figure 3.2.5: Selection of individual profiles for ozone from IAGOS (black) and the two NRT runs (o-suite: red, control: blue) over Europe during MAM 2020. Units: ppbv.

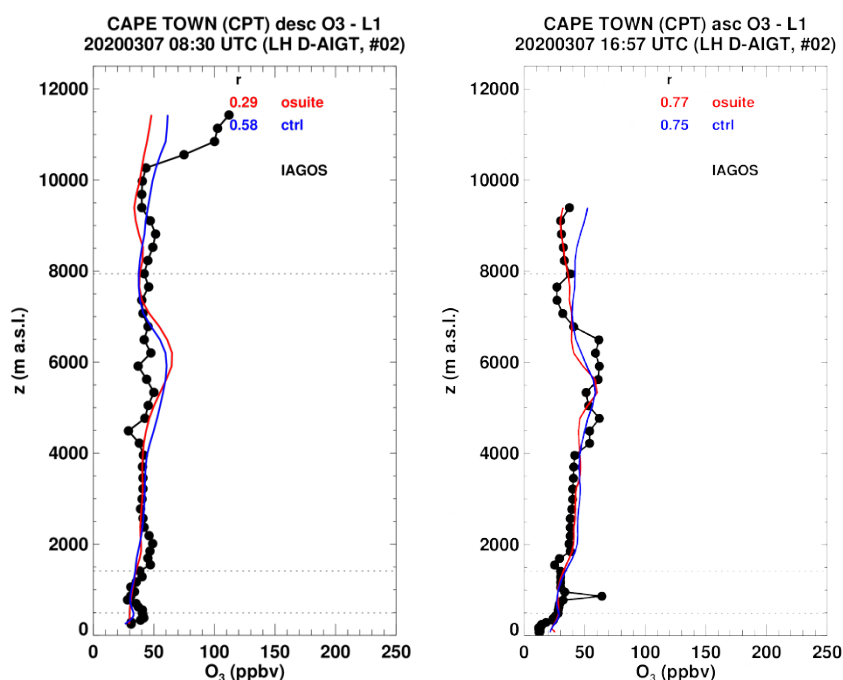


Figure 3.2.6: Selection of individual profiles for ozone from IAGOS (black) and the two NRT runs (o-suite: red, control: blue) over South Africa during MAM 2020. Units: ppbv.

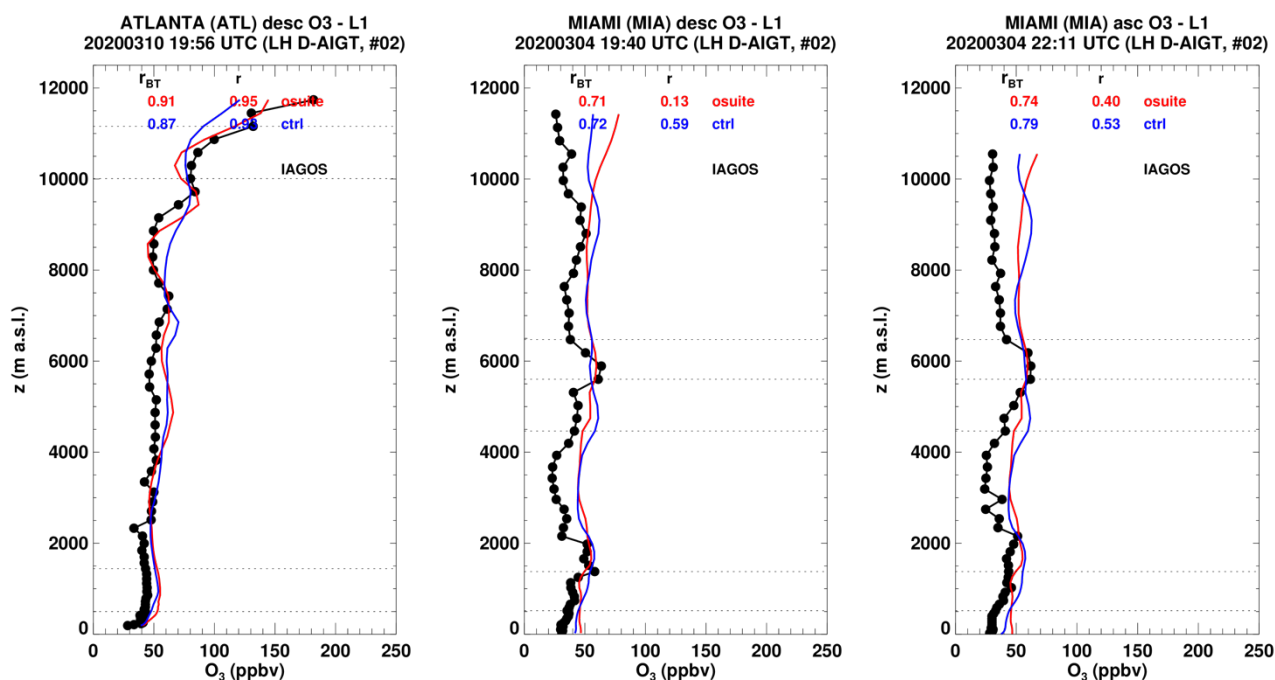


Figure 3.2.7: Selection of individual profiles for ozone from IAGOS (black) and the two NRT runs (o-suite: red, control: blue) over North America during MAM 2020. Units: ppbv.

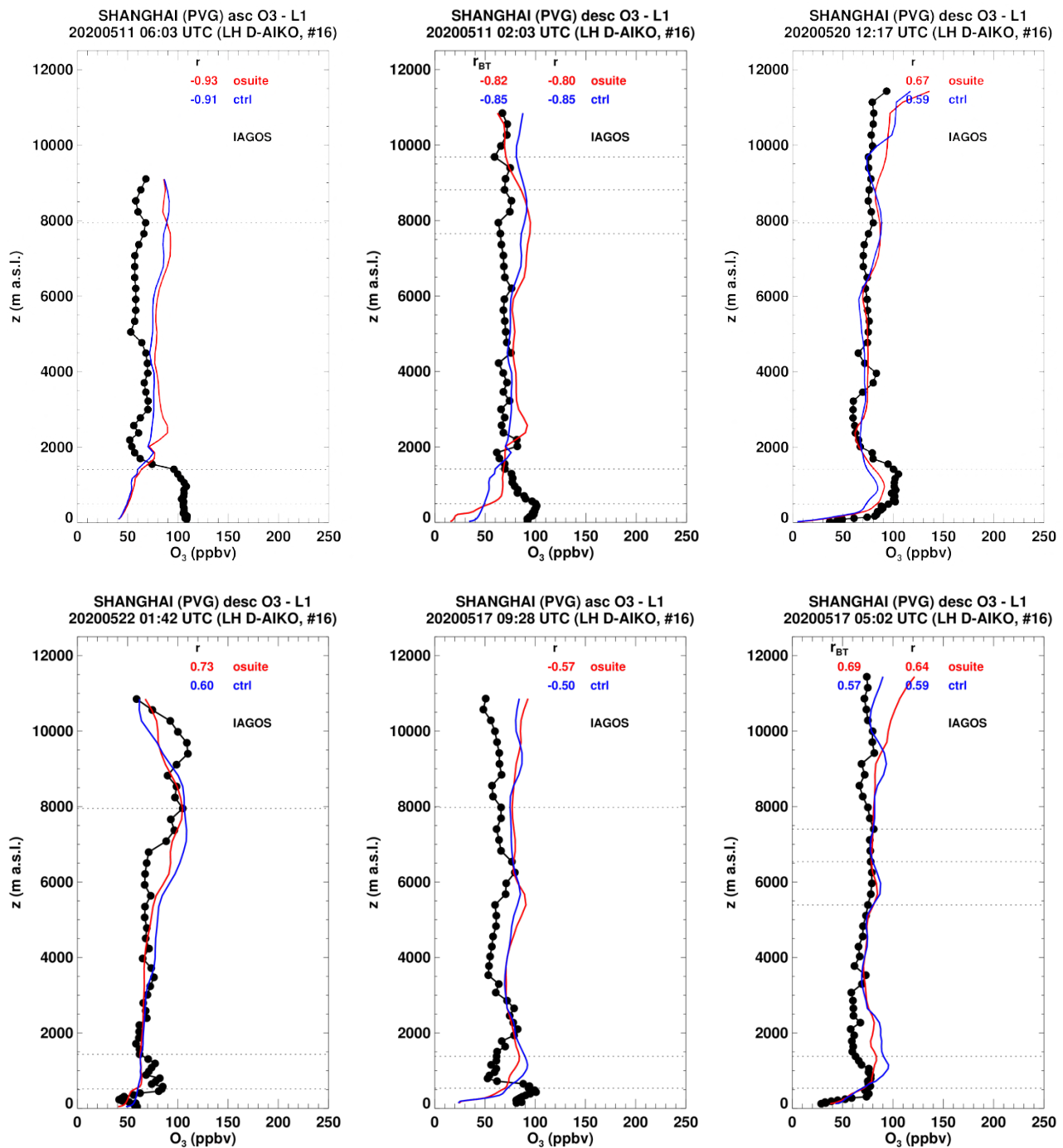


Figure 3.2.8: Selection of individual profiles for ozone from IAGOS (black) and the two NRT runs (o-suite: red, control: blue) over East Asia during MAM 2020. Units: ppbv.

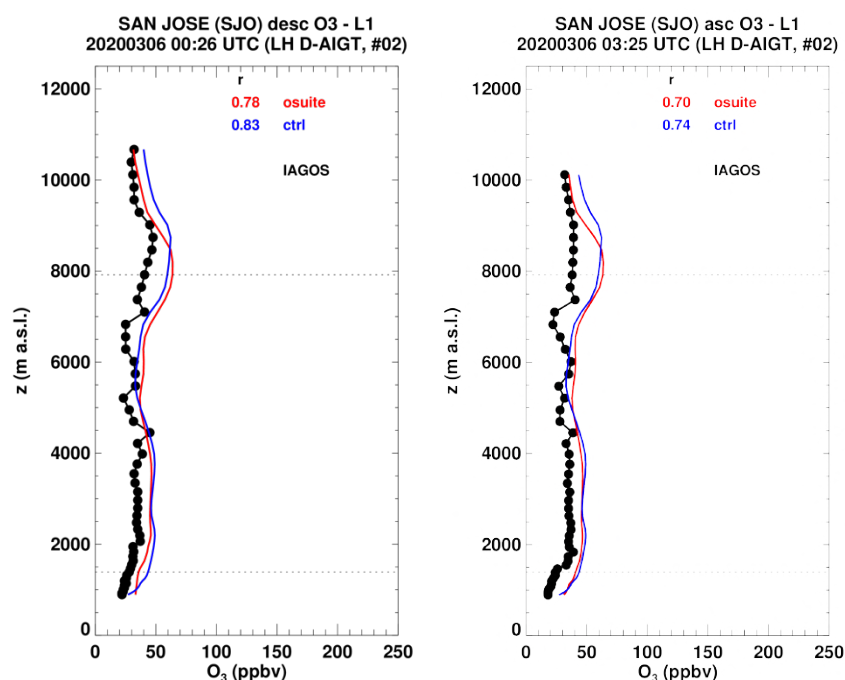


Figure 3.2.9: Selection of individual profiles for ozone from IAGOS (black) and the two NRT runs (o-suite: red, control: blue) over Central America during MAM 2020. Units: ppbv.

South Africa

Two ozone profiles are available at the airport of Cape Town (Fig. 3.2.6). The results from the two models are similar in all layers. The models agree well with observations from the surface to the free troposphere, while in the UTLS large positive biases are found for both models.

North America

Over North America's airports, ozone profiles are available at: Atlanta and Miami (Fig. 3.2.7). For all profiles, ozone values are generally close to or below 50 ppbv from the lowest layers to the free troposphere. The behaviour of the two runs is similar. Ozone is well represented at Atlanta and overestimations are found at Miami in the free troposphere and above.

East Asia

Over East Asia, ozone profiles are available only at the airport of Shanghai (Fig. 3.2.8). The two runs behave similarly in all layers. The largest biases are found near the surface and in the boundary layer where the models often underestimate in particular when ozone reaches values close to 100 ppbv. The agreement is better in the free troposphere for both models while in the upper layers the agreement is often worse.

Central America

Over Central America, two ozone profiles are available at the airport of San Jose (Costa Rica) as shown on Fig. 3.2.9. The results from both runs are similar, and ozone is slightly overestimated in all layers.

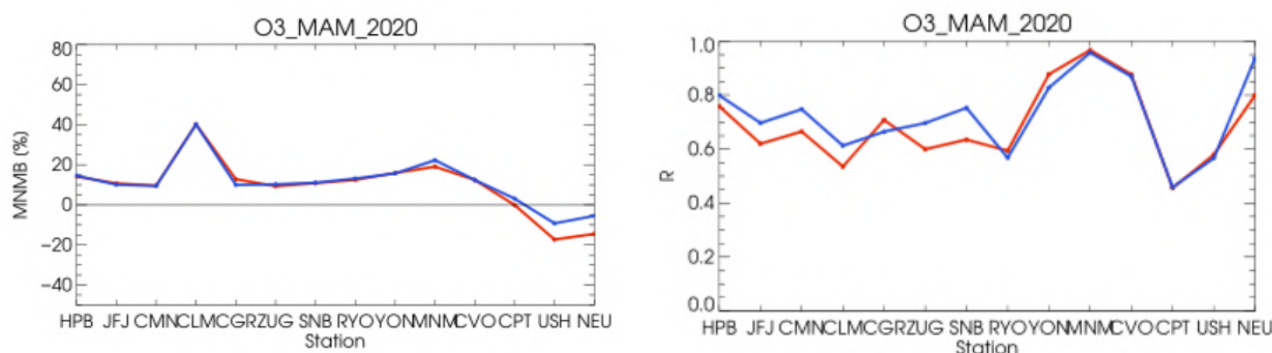


Figure 3.3.1: Modified normalized mean bias in % (left) and correlation coefficient (right) of the NRT forecast runs compared to observational GAW data in the period March-May 2020 (o-suite: red, control: blue).

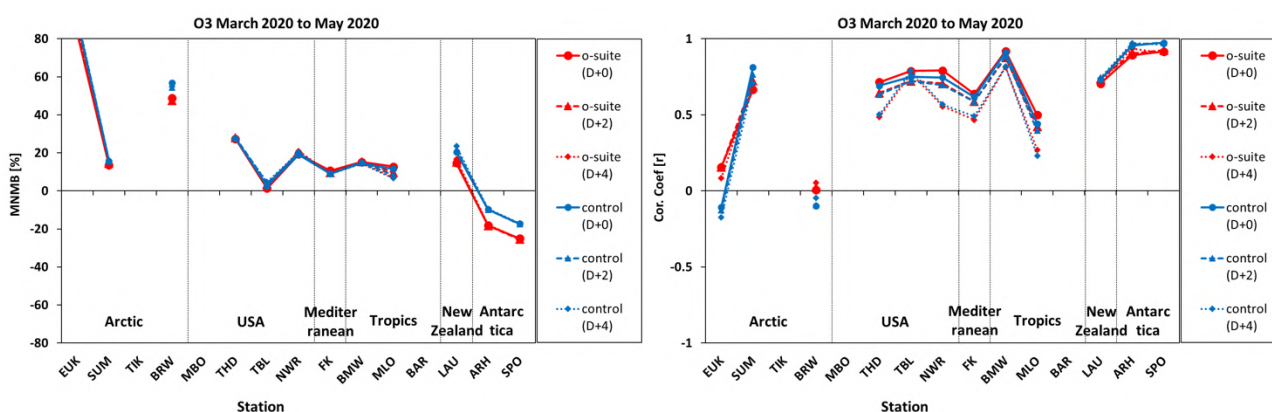


Figure 3.3.2: Modified normalized mean bias in % (left) and correlation coefficient (right) of the NRT forecast runs compared to observational ESRL data in the period March-May 2020. Circles correspond to D+0, triangles to D+2 and rhombs to D+4 metrics respectively.

3.3 Validation with GAW and ESRL-GMD surface observations

For the Near Real Time (NRT) validation, 13 GAW stations and 14 ESRL stations are currently delivering O₃ surface concentrations in NRT, and the data are compared to model results. In the following, a seasonal evaluation of model performance for the 2 NRT runs (o-suite and control) has been carried out for the period from March to May 2020. The latest validation results based on GAW stations and based on ESRL observations can be found on the CAMS website, see section 1, Table 1.2.

Modified normalized mean biases in % (left panel) and correlation coefficients (right panel) for different forecasts days (D+2, red-dashed and D+4, red-pointed) with respect to GAW and ESRL observations are shown in Figs. 3.3.1 and 3.3.2. It indicates that MNMBs for both o-suite and control run mostly remain stable up to D+4 (forecast run from 96h to 120h). Correlations between simulated and observed surface ozone values remain almost stable up to D+2 (forecast run from 48h to 72h), but then drop (correlations for D+4 are lower than correlations for D+2 and D+0), see Fig. 3.3.1 and 3.3.2, right graph).

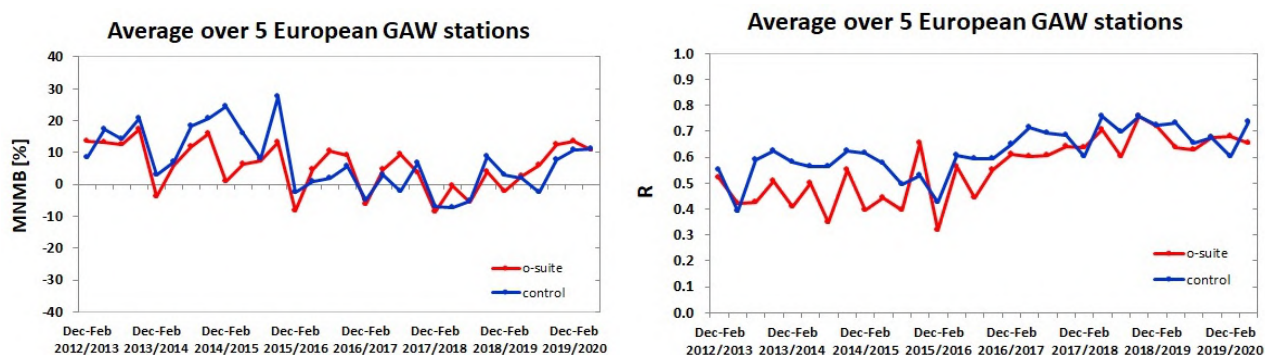


Figure 3.3.3: Long term (Dec. 2012 – May 2020) evolution of seasonal mean MNMB (left) and correlation (right), as averaged over 5 GAW stations in Europe, for o-suite (red) and control (blue).

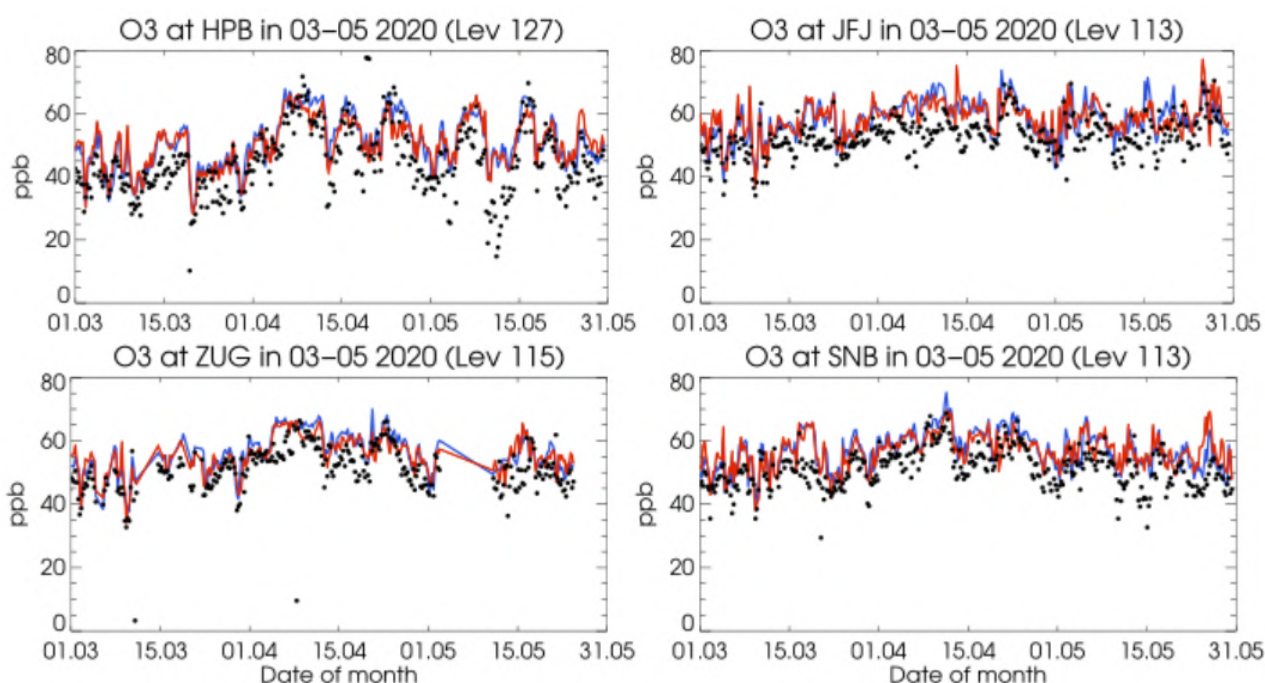


Figure 3.3.4: Time series for the o-suite (red) and control (blue) compared to GAW observations for Hohenpeissenberg (47.05°N, 11.02°E) and Jungfrauoch (46.55°N, 7.99°E) (upper panel), Zugspitze (47.4°N, 10.9°E) and Sonnblick (47.05°N, 12.96°E) (lower panel).

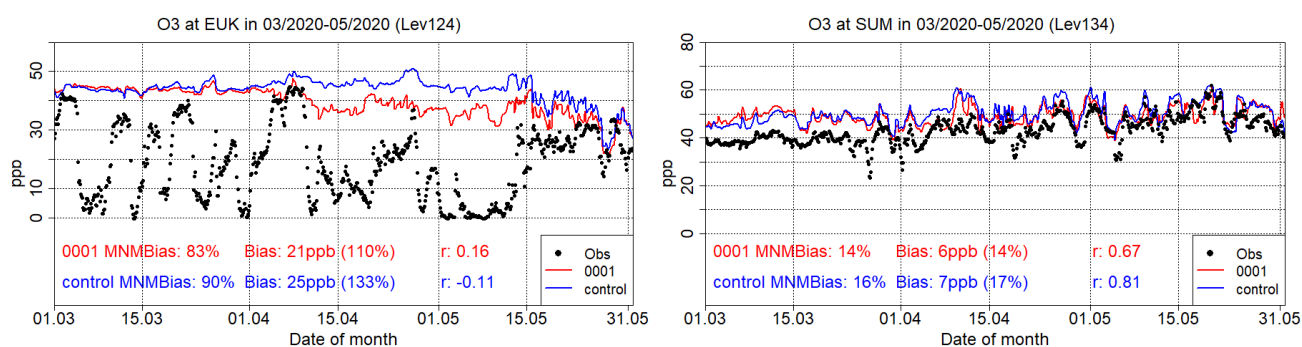


Figure 3.3.5: Time series for the o-suite (red) and control (blue) compared to ESRL observations at Eureka Canada station (80.05°N, 86.42°W, left) and at Summit, Greenland station (72.57°N, 38.48°W, right)

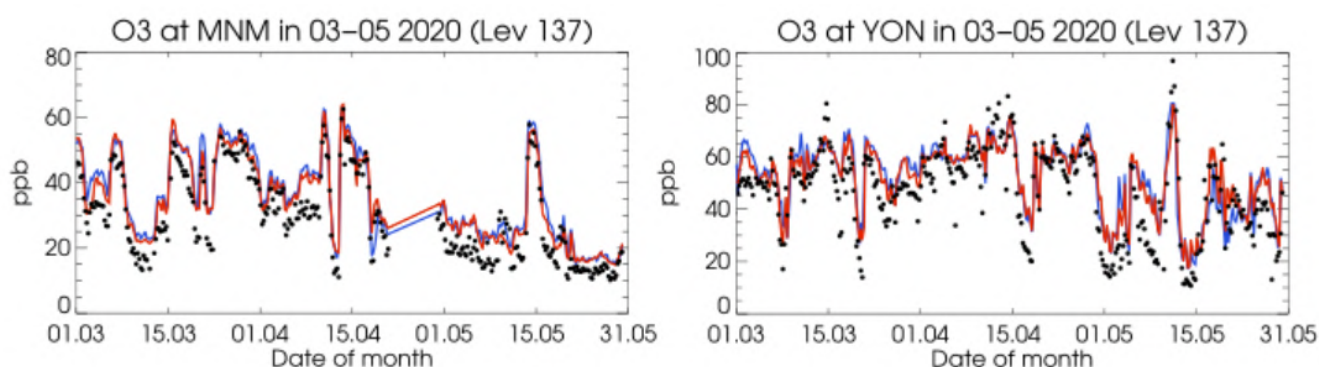


Figure 3.3.6: Time series for the o-suite (red) and control (blue) compared to GAW observations for Minamitorishima (24.29°N, 153.98°E, right panel) and Yonagunijima (24.47°N, 123.02°E, right panel).

A comparison of the seasonal-mean MNMB over Europe (Fig. 3.3.3) from December 2012 to present shows minimal MNMBs during the winter season and larger biases in other months. Also, on average the MNMB for the o-suite and control shows an improvement over the years. The temporal correlation is consistently better for the control run than for the o-suite, but the o-suite shows strong improvements recently. The GAW results are summarized in Figs 3.3.1 and 3.3.3.

Looking at different regions, for European stations (HPB, JFJ, ZUG, SNB, CMN, CLM, CGR), observed O₃ surface mixing ratios are overestimated with MNMBs within 15% for o-suite and control (Fig. 3.3.4) (exception: CLM with a bias of 40% due to exceptionally low observations during MAM). Correlations for European stations are between 0.53 and 0.75 for the o-suite and between 0.61 and 0.79 for the control run, see Fig. 3.3.1.

Over Point Barrow (BRW) and Eureka (EUK) Arctic stations, due to ozone depletion events from March to May, the CAMS NRT simulations strongly overestimate measured ozone concentrations (March-May MNMBs 50% at BRW and 80% at EUK), except for the few days without depletion events, where the predicted model levels are in a fair agreement with observations. CAMS NRT MNMBs are closer to zero (MNMB=15%) at Summit due to absence of depletion events (see also Fig 3.3.5). Correlations between modelled and observed ozone values are 0.67 and 0.81 for the o-suite and the control run respectively over SUM station while for BRW and EUK are almost zero mainly because both runs cannot reproduce the ozone depletion events.

Concerning USA stations (THD, TBL and NWR), the observed ozone mixing ratios are overestimated by both the o-suite and the control run by 25% and 15% at THD and NRW respectively, while in the TBL station both models MNMBs are almost zero. Correlations between o-suite and observations vary between 0.71 (at THD) and 0.80 (at NWR) for the o-suite and between 0.69 (at THD) and 0.75 (at NWR and at TBL) for the control run.

Ozone mixing ratios for Asian stations (RYO, MNM, YON) are overestimated by up to 20% by both runs. Correlation coefficients range between 0.56 and 0.96, with higher correlation for the o-suite.

At CVO station, the model corresponds very well to the observations with MNMB of 12% for both runs and correlation of 0.87.

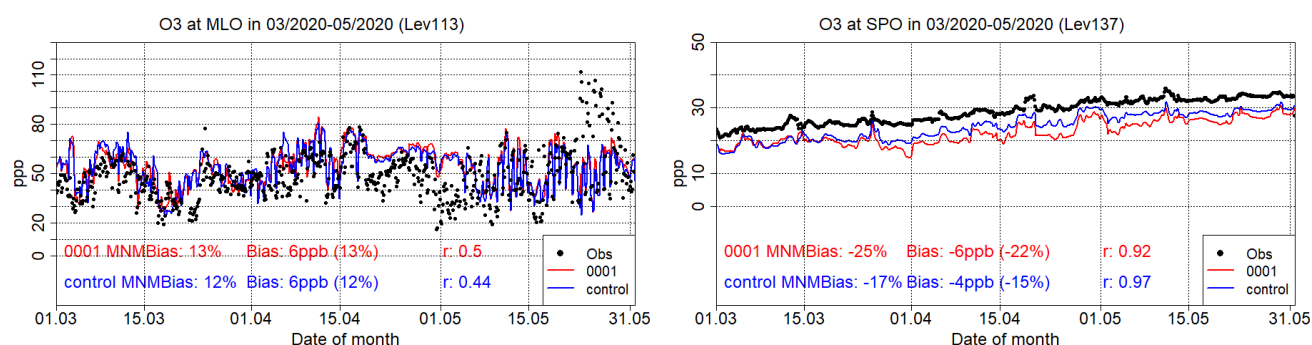


Figure 3.3.7: Time series for the o-suite (red) and control (blue) compared to ESRL observations (black dots) at Mauna Loa, Hawaii station (19.54°N, 155.58°W) and at South Pole, Antarctica station (90.00°S, 24.80°W).

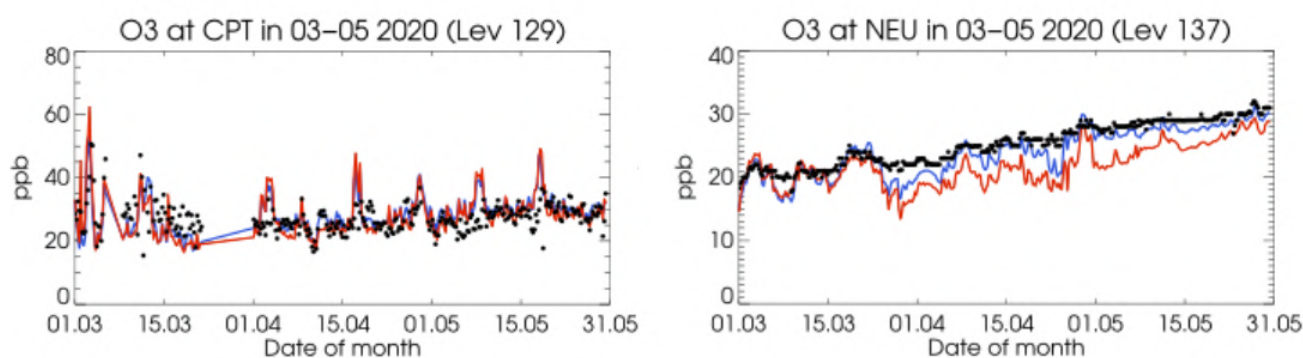


Figure 3.3.8: Time series for the o-suite (red) and control (blue) compared to GAW observations (black dots) at Cape Point (34.55°S, 18.48°W) and GAW observations at Neumayer (70.65°S, 8.25°W).

The O₃ mixing ratios of the southern hemispheric stations (CPT, USH) show MNMBs between 0 and -17% for the o-suite. The control run shows lower underestimations for USH (-9%) and a slight overestimation for CPT (3%), see Fig 3.3.8.

At Lauder (LDR) station in New Zealand the o-suite overestimates O₃ mixing ratios by 14% while the control run by 20%. Correlations between simulated and observed surface ozone values for the o-suite and the control run are 0.71 and 0.73, respectively.

Both CAMS NRT runs underestimate surface ozone values at Arrival Height (ARH) and at South Pole station in Antarctica (SPO) stations in Antarctica. More specifically at ARH the MNMB is -18% for the o-suite and -10% for the control run. At South SPO, the MNMB is -25% for the o-suite and -17% for the control run. It is interesting to note that till 2019 the control run negative MNMBs are significantly greater than the o-suite MNMBs. Correlation coefficients are 0.9 for both runs at Antarctica stations.

For Neumayer station (NEU) the MNMB is -14% for the o-suite and -5% for the control run. Correlation coefficients are 0.79 for the o-suite and 0.93 for the control run, Fig. 3.3.8.



Table 3.4.1: Coordinates, elevation, corresponding model level (level 137 is the surface level), as well as validation scores (MNMBs and correlations for the period MAM 2020) obtained with the 2 forecast runs (o-suite and control), for each one of the selected Mediterranean stations. MNMBs and correlations with blue denote stations where control run performs better while with red are denoted stations where o-suite performs better.

Station Name	Stat_ID	Lon	Lat	Alt (m)	Level	Distance from the shore (km)	MNMB		Cor. Coef	
							o-suite	control	o-suite	control
Al Cornocales	ES1648A	-5.66	36.23	189	133	16	29.0	27.4	0.67	0.67
Caravaka	ES1882A	-1.87	38.12	1	137	73	31.4	29.9	0.59	0.58
Zarra	ES0012R	-1.10	39.08	885	130	70	17.1	15.3	0.63	0.68
Villar Del Arzobispo	ES1671A	-0.83	39.71	430	137	48	7.0	5.8	0.51	0.52
Cirat	ES1689A	-0.47	40.05	466	137	37	27.1	26.0	0.52	0.55
Bujaraloz	ES1400A	-0.15	41.51	327	137	60	20.6	19.3	0.45	0.45
Morella	ES1441A	-0.09	40.64	1150	128	51	NA	NA	NA	NA
Bc-La Senia	ES1754A	0.29	40.64	428	137	21	-9.3	-10.6	0.36	0.36
Ay-Gandesá	ES1379A	0.44	41.06	368	136	15	18.7	17.3	0.56	0.57
Ak-Pardines	ES1310A	2.21	42.31	1226	135	81	27.0	26.1	0.74	0.75
Hospital Joan March	ES1827A	2.69	39.68	172	133	3	13.7	11.6	0.69	0.70
Al-Agullana	ES1201A	2.84	42.39	214	137	25	15.0	14.6	0.46	0.48
Av-Begur	ES1311A	3.21	41.96	200	132	9	24.9	23.8	0.70	0.71
Plan Aups/Ste Baume	FR03027	5.73	43.34	675	124	21	17.0	16.0	0.75	0.78
Montemonaco	IT1842A	13.34	42.90	1000	127	46	18.3	17.3	0.59	0.69
Gharb	MT00007	14.20	36.07	114	132	31	3.4	1.5	0.58	0.67
Aliartos	GR0001R	23.11	38.37	110	59	18				
NEO	-	21.67	37.00	50	60	2				
Finokalia	GR0002R	25.67	35.32	250	57	4	10.7	9.1	0.64	0.62
Agia Marina	CY0002R	33.06	35.04	532	55	14	9.5	8.4	0.69	0.70

3.4 Validation with AirBase observations in Mediterranean

The surface ozone validation analysis over the Mediterranean is based on an evaluation against station observations from the Airbase Network (<http://acm.eionet.europa.eu/databases/airbase/>). In addition, 1 station from the Department of Labour Inspection - Ministry of Labour and Social Insurance, of Cyprus (<http://www.airquality.dli.mlsi.gov.cy/>) is used in the validation analysis. For the validation analysis, stations in the Mediterranean located within about 100 km from the shoreline of the Mediterranean shore are used. Table 3.4.1 shows the names, coordinates, elevation and the MNMBs and correlations obtained with the 2 forecast runs (o-suite and control). It indicates that the variance explained by each station of both the o-suite and control is high and correlations are highly significant over Western, Central and Eastern Mediterranean. It should be noted that the o-suite run reproduces slightly better than the control run the surface ozone day to day variability over most of the Mediterranean stations (see Table 3.4.1).

In terms of biases, o-suite overestimates surface ozone values (with the exception of Bc-La Senia station) and its MNMBs vary between 7% and 32% depending on the stations over the Mediterranean shore of Spain (average MNMB for the 13 Spain Mediterranean station is 18.5%). The Control MNMBs are on average 1.2% lower than those of the o-suite and are closer to zero. Over the stations Plan Aups/Ste Baume in France and Montemonaco in Italy the o-suite overestimates surface ozone concentrations by 17% and 18% respectively. Again, the Control MNMBs are lower by 1% than the o-suite MNMBs and are closer to zero compared to the o-suite. Over Gharb station in Malta the o-suite overestimates surface ozone values by 3.4% and the control

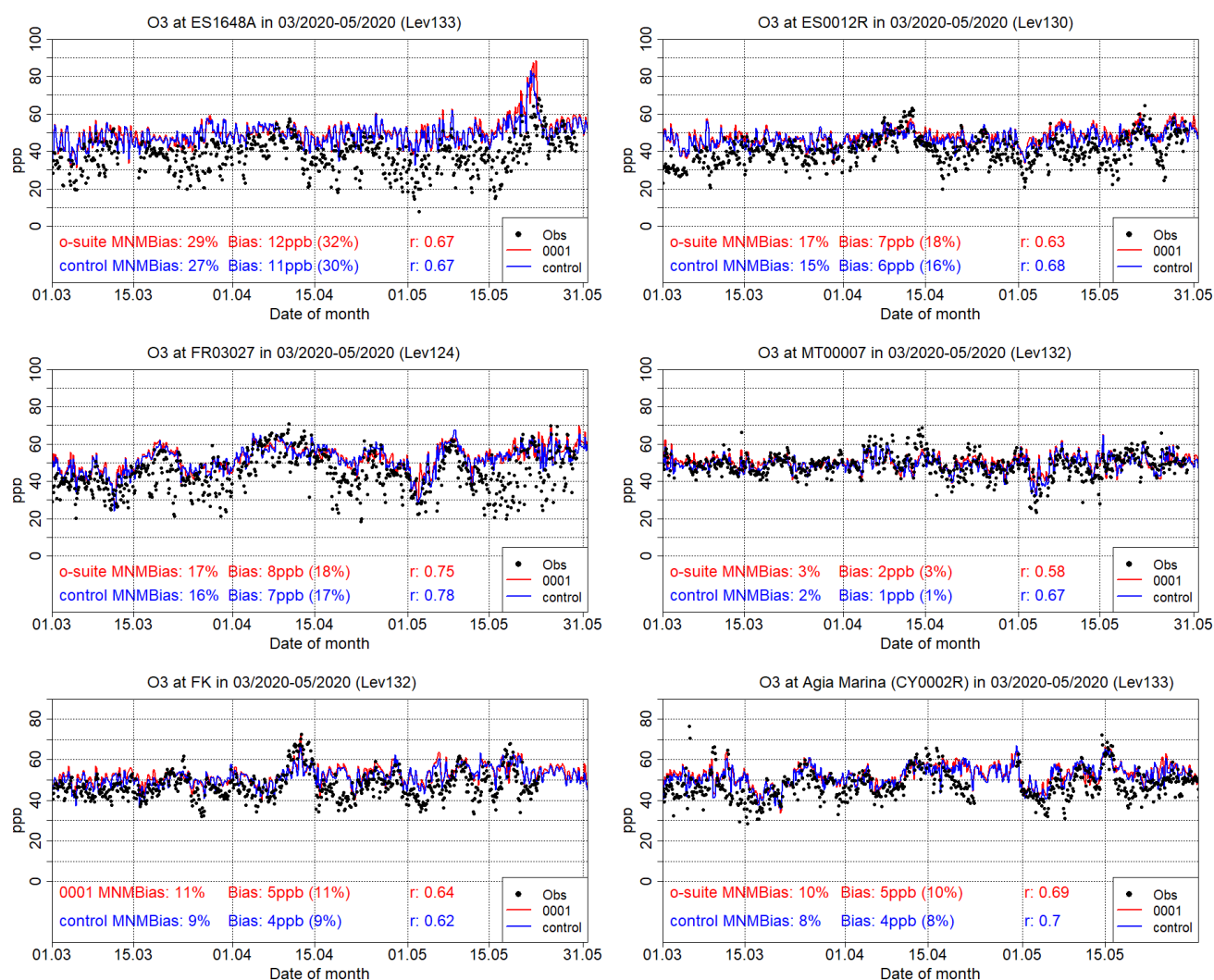


Figure 3.4.1: Time series for the o-suite (red) and Control (blue) compared to Airbase observations at Al Cornocales, Spain station (36.23°N, 5.66 °W, top left), at Zarra, Spain station (39.08°N, 1.10°W, top right), at Plan Aups/Ste Baume, France station (43.34°N, 5.73°E, center left), at Gharb, Malta station (36.07°N, 14.20°E, center right at Finokalia, Crete Greece station (35.32°N, 25.67°E, bottom left) and compared to observations provided by the Department of Labour Inspection - Ministry of Labour and Social Insurance of Cyprus) at Agia Marina, Cyprus station (35.04°N, 33.06 °E, low right).

run by 1.5%. Over Finokalia station in Crete and Agia Marina in Cyprus the o-suite overestimates surface ozone by 10.7% and 9.5. Again, the Control MNMBs are lower 1.5% than o-suite MNMBs and are closer to zero compared to o-suite MNMB.

The spatial distribution of MNMBs and the correlation coefficients of the o-suite over the Mediterranean are shown in 3.4.2, where it is evident that correlations over the entire Mediterranean from Gibraltar to Cyprus are highly significant. It is also evident that the CAMS NRT run overestimate surface ozone values over the entire Mediterranean from Gibraltar to Cyprus and that CAMS NRT have a better performance over Central and eastern Mediterranean compared to the Mediterranean shore of Spain in terms of biases.

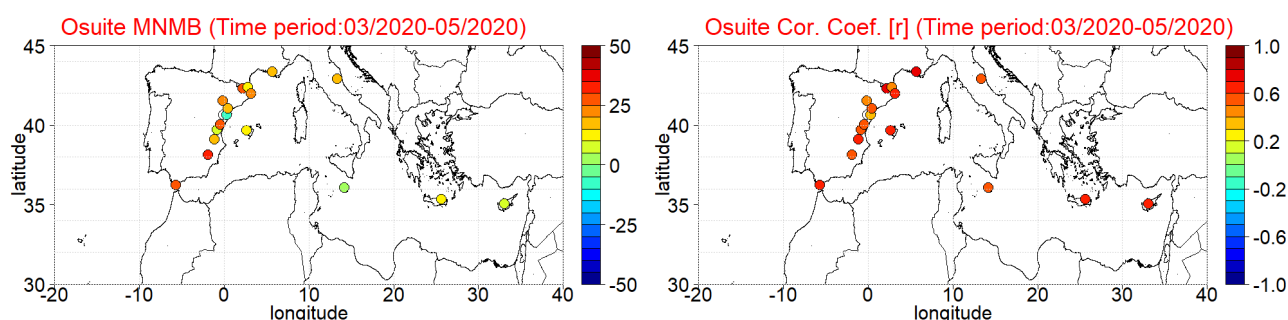


Figure 3.4.2: Spatial distribution of MNMB in % (left) and correlation coefficient (right) of the o-suite run compared to observational data during the period from 1 March 2020 to 31 May 2020.

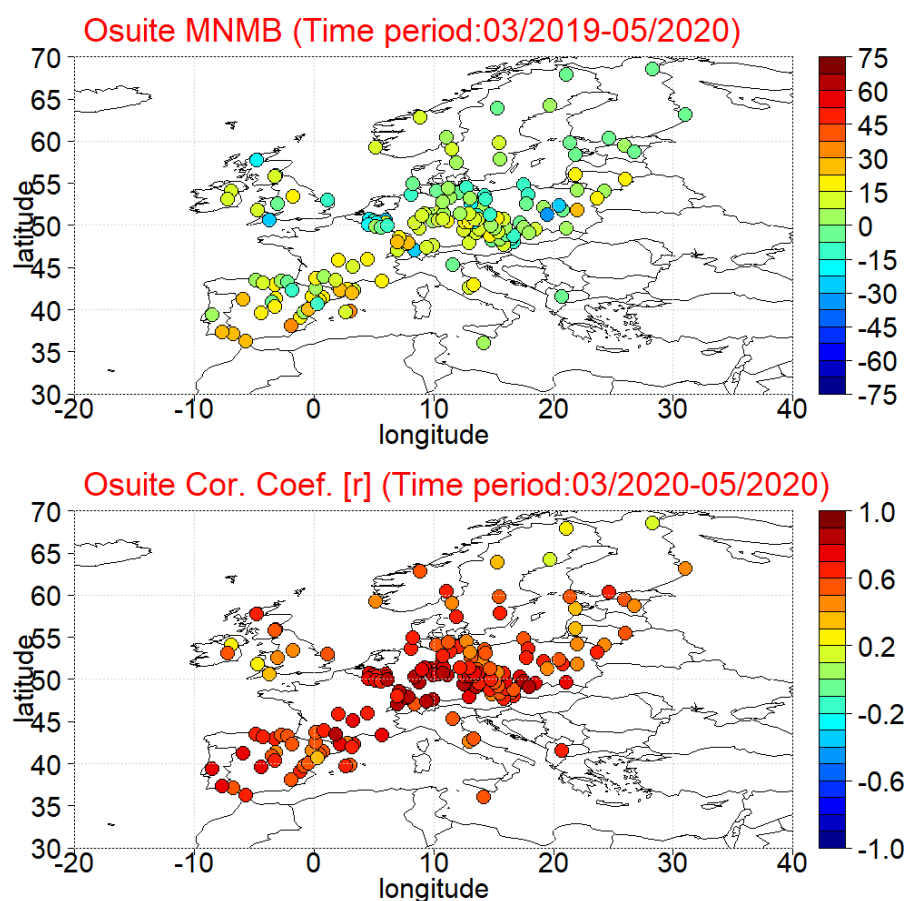


Figure 3.5.1: Spatial distribution of MNMB in % (left) and correlation coefficient (right) of the o-suite run compared to observational data during the period from 1 March 2020 to 31 May 2020.

3.5 Validation with AirBase observations over Europe

The surface ozone validation analysis over Europe is based on an evaluation against Background rural Classes 1-2 O₃ Joly-Peuch classification (Joly and Peuch, 2012) station observations from Airbase Network (<http://acm.eionet.europa.eu/databases/airbase/>). The spatial distribution of MNMBs and the correlation coefficients of the o-suite over Europe are shown in 3.5.1, where it is evident that correlations over most European AirBase stations in southern and central Europe (with

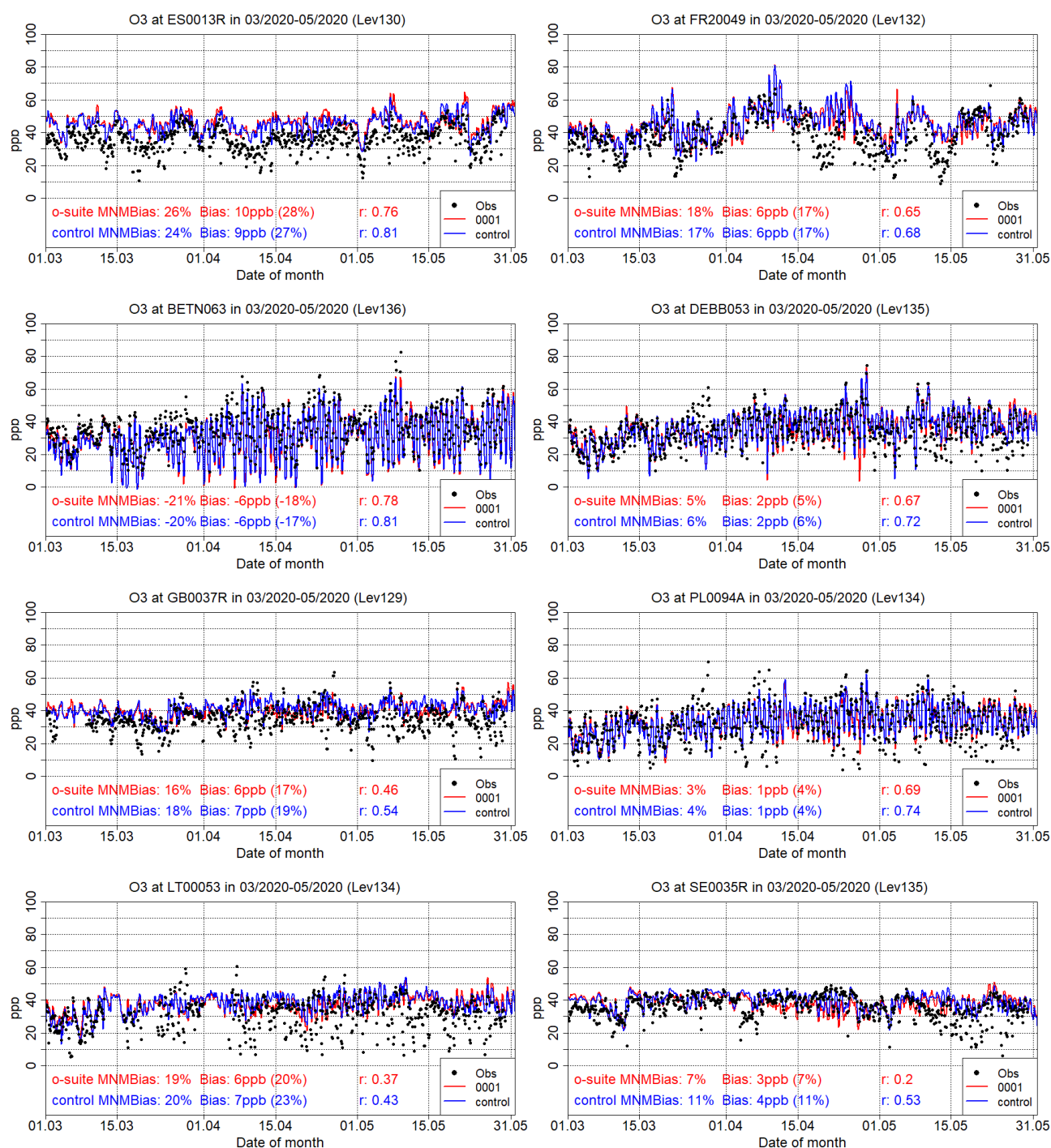


Figure 3.5.2: Time series for the o-suite (red) and Control (blue) compared to Airbase observations at Al Penausende, Spain station (41.24°N, 5.90 °W, 1st row left), at Haut Beaujolais, France station (45.96°N, 4.47°E, 1st row right), at Corroy L.G., Belgium Station (50.67°N, 4.67°E, 2nd row left), at Hasenholz, Germany (52.56°N, 14.02°E, 2nd row right), at Ladybower, Great Britain station (53.40°N, 1.75°W, 3rd row left), at LdGajewWIOSAGajew, Poland station (52.14°N, 19.23°E 3rd row right), at Zemaitija, Lithuania station (56.01°N, 21.89°E, 4th row left) and at Vindeln, Sweden station (64.25°N, 19.77°E, 4th row right).

a very few exceptions) are highly significant ($0.5 < r < 0.95$). Correlations are lower in the northern part of Sweden and Finland ($0.1 < r < 0.3$). CAMS NRT runs MNMBs varies from -30% to +30% over Europe depending on the station. More specifically, CAMS NRT represent well the surface ozone mean concentrations over Sweden, Finland and Estonian, and Finland (depending on the station MNMBs vary from -5% to +5%). It is also evident that over France Spain and Italy the o-suite mostly overestimates surface ozone values up to 30%, underestimate it over Belgium and Poland down to -20% while in the rest of Central Europe o-suite MNMBs varies between -10% and 20%. The above-mentioned findings concerning CAMS NRT runs biases and correlations are also observed in individual time series at selected stations plotted in Figure 3.5.2. From this time series and the plotted validation metrics is also evident that the control run surface ozone mean spring concentrations are almost identical with the o-suite values and that the control run shows slightly higher correlations with the observed ozone values than the o-suite.

3.6 Validation with IASOA surface observations

CAMS results were compared to surface O₃ observations from the Villum Research Station, Station Nord in north Greenland (81.6°N 16.7°W) Eureka, Nunavut, Canada (80.1°N 86.4°W), and Zeppelin Mountain, Svalbard (78.9°N 11.9°E) from the IASOA network (Fig. 3.5.1).

The data from Svalbard and VRS are covering the period from December 2014 to May 2020. Data from Eureka covers the period August 2016 – May 2020. The CAMS simulations do not capture ozone depletion events in March – June in 2015 – 2020 during spring at any of the sites. These events are related to halogen chemistry reactions that are not represented in the CAMS simulations. The simulations are on average in good agreement with the observations apart from the spring depletion events.

For the period March – May 2020 the measurements are not quality controlled. Due to the ozone depletion events the CAMS simulations overestimate measured concentrations, except for the few days without depletion events, where the predicted levels are in a fair agreement with observations at the sites. This results in large positive bias and low correlation coefficients for the period (Table 3.5.1).

Table 3.6.1. Modified Normalised Mean Bias (MNMB) and correlation coefficient (r) of the o-suite and the control simulations for the sites Eureka, Svalbard and Villum Research Station (VRS) for the period March – May 2020.

		MNMB	R
Eureka	o-suite	0.63	-0.02
	control	0.70	-0.16
Svalbard	o-suite	0.16	0.04
	control	0.24	-0.05
VRS	o-suite	0.24	0.46
	control	0.31	0.31

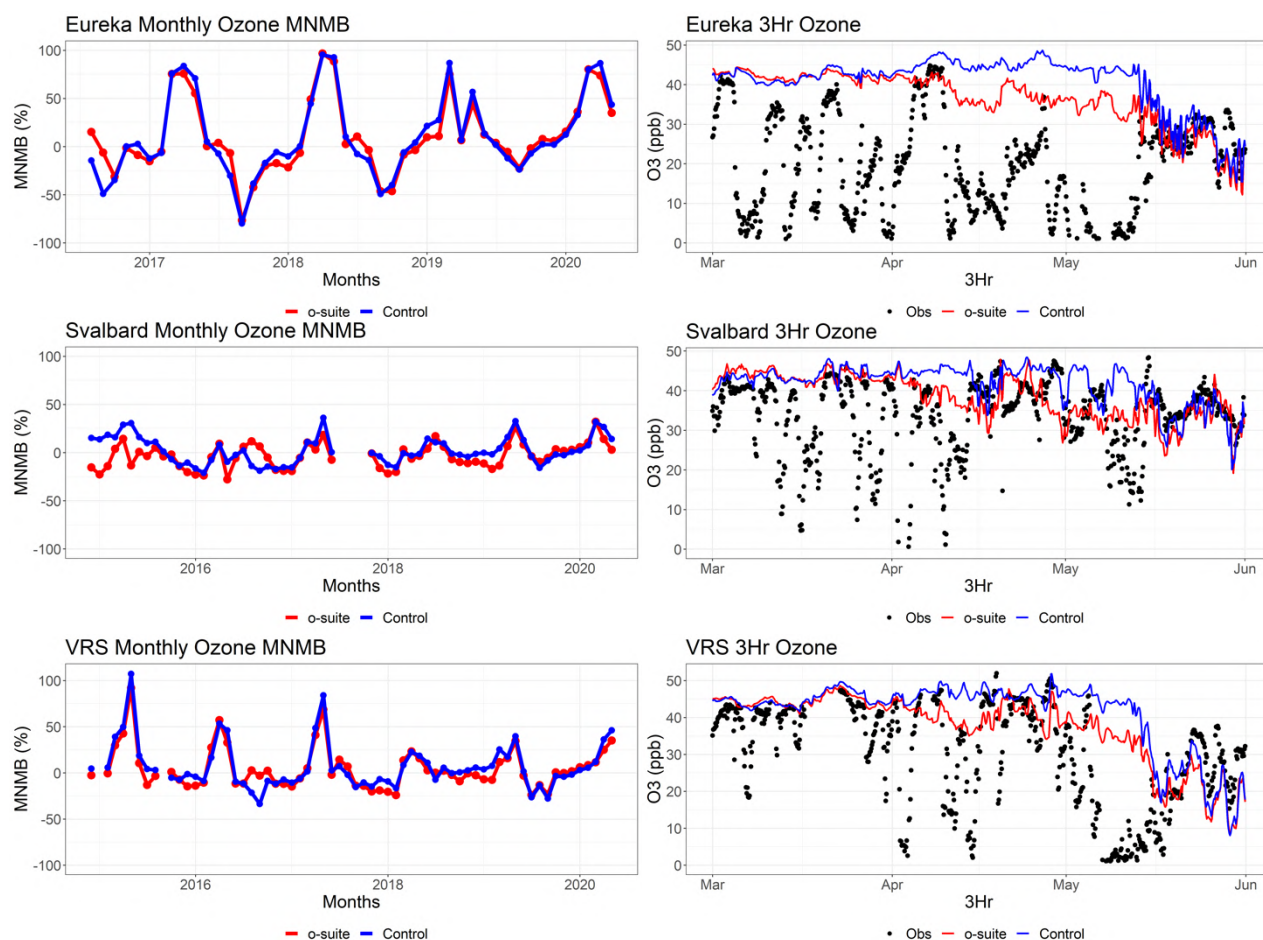


Figure 3.6.1: Time series for o-suite (red) and control (blue) compared to observations (black dots) at Eureka (top row), Svalbard (middle row) and the Villum Research Station, Station Nord, Greenland (bottom row) MNMB for the full period (left) and concentrations for March-May (right).

3.7 Validation with IASI data

Unfortunately the IASI ozone data for March-May 2020 was not available to us at the time this document was written.

4. Carbon monoxide

4.1 Validation with Global Atmosphere Watch (GAW) Surface Observations

For the Near-Real-Time (NRT) validation, 10 GAW stations have delivered CO surface mixing ratios in NRT and data is compared to model results as described in Eskes et al. (2019) and is used for CAMS model evaluation for March to May 2020. The latest validation results can be found on the CAMS website, see section 1.

For stations in the Northern Hemisphere, both runs mostly show slightly negative MNMBs for stations in Europe (Fig. 4.1.1).

A comparison of the seasonal-mean MNMB over Europe (Fig. 4.1.2) from December 2012 to present shows a slowly improving MNMB from about -20% in 2013 to less than -10% for more recent periods. Temporal correlation remains relatively constant at $r=0.6$ on average, except for the quarter JJA in 2018, where the correlation of the control run drops to 0.24.

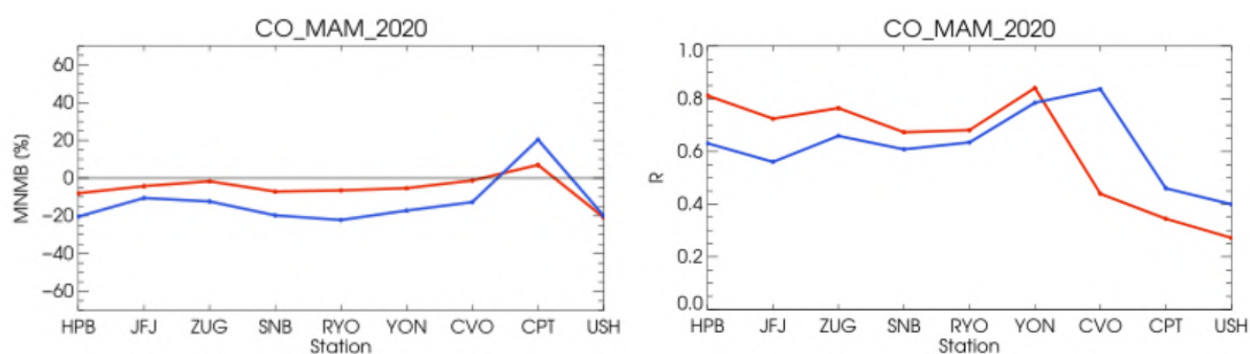


Figure 4.1.1: Modified normalized mean bias in % (left) and correlation coefficient (bottom right) of the NRT model runs compared to observational GAW data in the period March to May 2020 (o-suite: solid red, and control: blue).

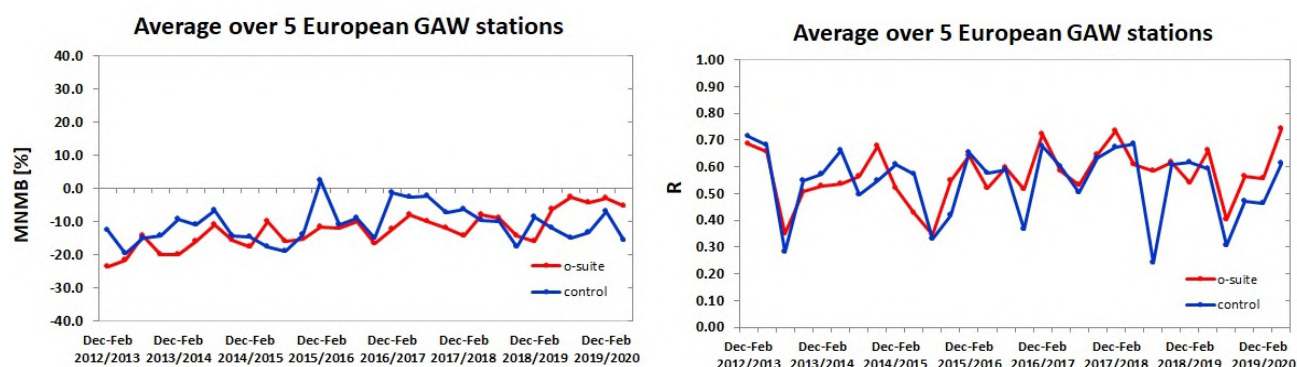


Figure 4.1.2: Long term (Dec. 2012 – May 2020) evolution of seasonal mean MNMB (left) and correlation (right), as averaged over 5 GAW stations in Europe, for o-suite (red) and control (blue).

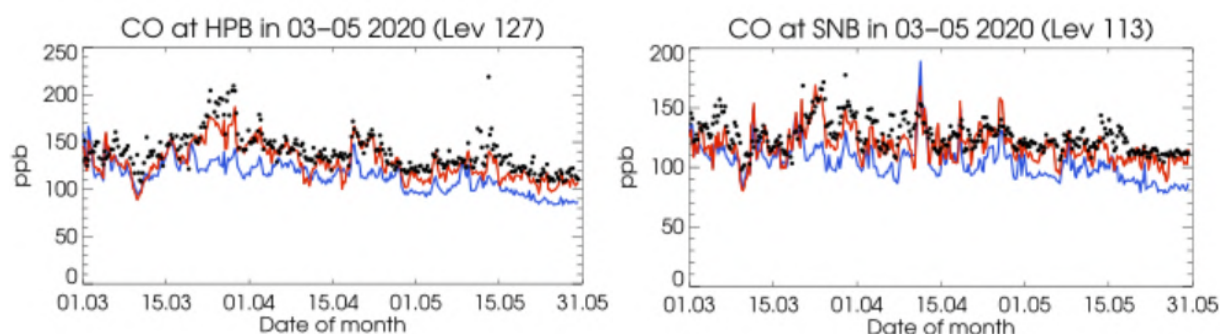


Figure 4.1.3: Time series for the o-suite (red) and control (blue) compared to GAW observations at Hohenpeissenberg (47.8°N, 11.02°E) and Sonnblick (47.05°N, 12.96°E).

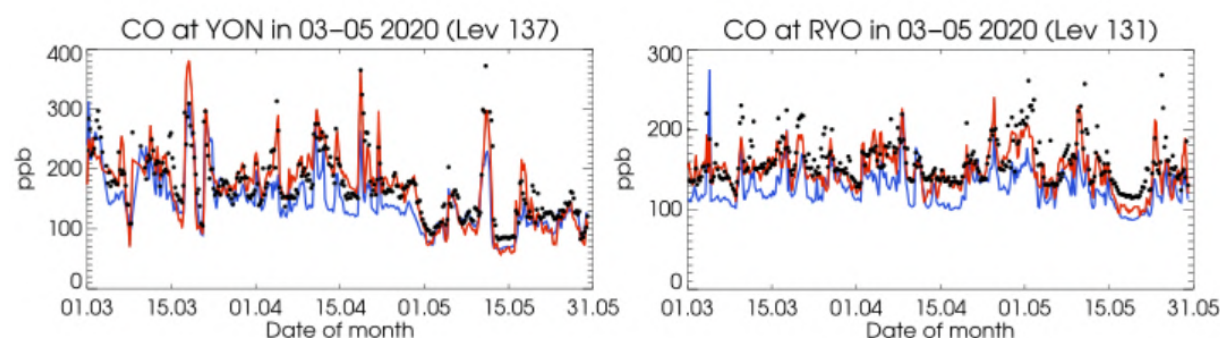


Figure 4.1.4: Time series for the o-suite (red) and control (blue) compared to GAW observations at Yonagunijima (24.47°N, 123.02°E) and Ryori (39.03°N, 141.82°E).

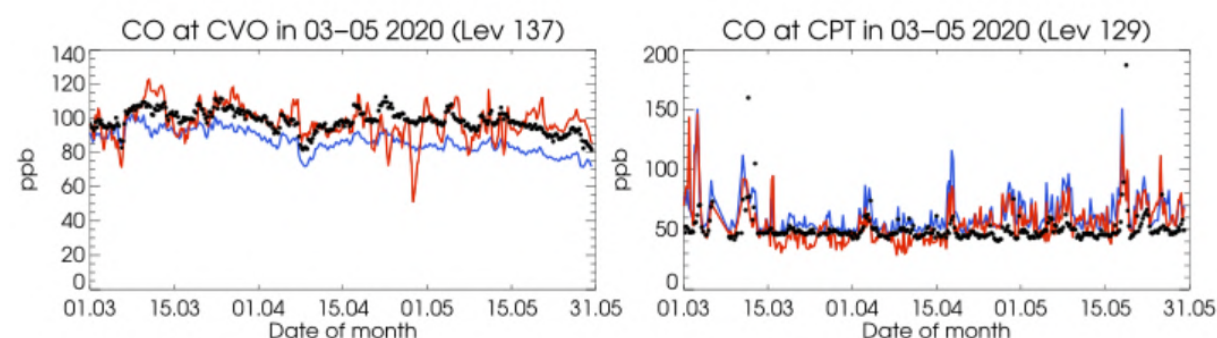


Figure 4.1.5: Time series for the o-suite (red) and control (blue) compared to GAW observations at Ushuaia (54.85°S, -68.32°W) and Cape Point (34.35°S, 18.5°E).

For European stations (Fig. 4.1.3), the o-suite shows only a slight underestimation of CO with MNMBs within 10%, whereas the control run underestimates the observations with MNMBs up to -20%. Correlation coefficients are between 0.67 and 0.81 for the o-suite and between 0.56 and 0.65 for the control run.

For Asian stations, the o-suite corresponds well to the observations with only minimal underestimations (-6%). The control run shows a stronger negative offset with MNMBs up to -22% (Fig. 4.1.4).



For CVO, MNMBs are almost zero for o-suite and -12% for the control. Correlation is high with 0.83 for the control, but lower for the o-suite (0.43) due to larger peaks in the model in April and May (Fig.4.1.5).

For the two stations in the Southern mid-latitudes (CPT and USH), MNMBs vary between 6% and -20% for the o-suite and between 20% and -20% for the control (Fig.4.1.5). Correlation coefficients are low for both runs (for the o-suite 0.27 (USH) and 0.34 (CPT) and for the control 0.39 (USH) and 0.45 (CPT).

4.2 Validation with IAGOS Data

Like for ozone, CO time series at Frankfurt are discontinuous during the MAM 2020 period, however, several CO observations are also available in the month of April, which was not the case for ozone (Fig. 4.2.1).

During the entire MAM 2020 period, low CO values are observed at Frankfurt in the surface and boundary layer with values always below 200 ppbv (Fig.4.2.1). CO is mostly underestimated by the o-suite, and the largest biases are generally found in the low troposphere, while in upper layers the agreement is often better (Fig.4.2.1 and 4.2.2). A number of overestimations are also found but rarely, especially in the mid and upper troposphere during the month of May (Fig. 4.2.2). The behaviour of the control run is rather similar to that of the o-suite during the month of March with a slightly worse performance for the control run. For the month of April and May, the results from the two runs notably differ (Fig.4.2.1 and 4.2.2). While in the first two weeks of data the bias is large in the lowest layers, for the April-May periods large negative bias extend to upper layers for the control run in particular during April. In April, the performance of the o-suite appears less degraded than that of control although some large underestimations are also found in the mid-troposphere. In May, some large overestimations are found in the mid and upper troposphere for the o-suite. On average, from the surface to the upper troposphere, MNMBs are roughly between -40 and -20% for the control run, against a range of -20 to -10 % for the o-suite (Fig. 4.2.3). For both runs the correlation coefficient is highest in the low troposphere and in the upper troposphere, with about 50 and 80 % respectively (Fig. 4.2.3). For the control run the correlation coefficient in the mid-troposphere remains close to 50%, while for the o-suite it presents much smaller values in the mid-troposphere (Fig. 4.2.3).

As it was the case for ozone, the comparison with the climatological variability exhibit an anomaly, but negative in the case of CO and at all levels (see regional report MAM 2020). This might be attributed to the reduction of both regional and global emissions during the COVID-19 pandemic lockdowns. It should be noted that during this period the o-suite presents significantly better results than control run from the low to the mid-troposphere.

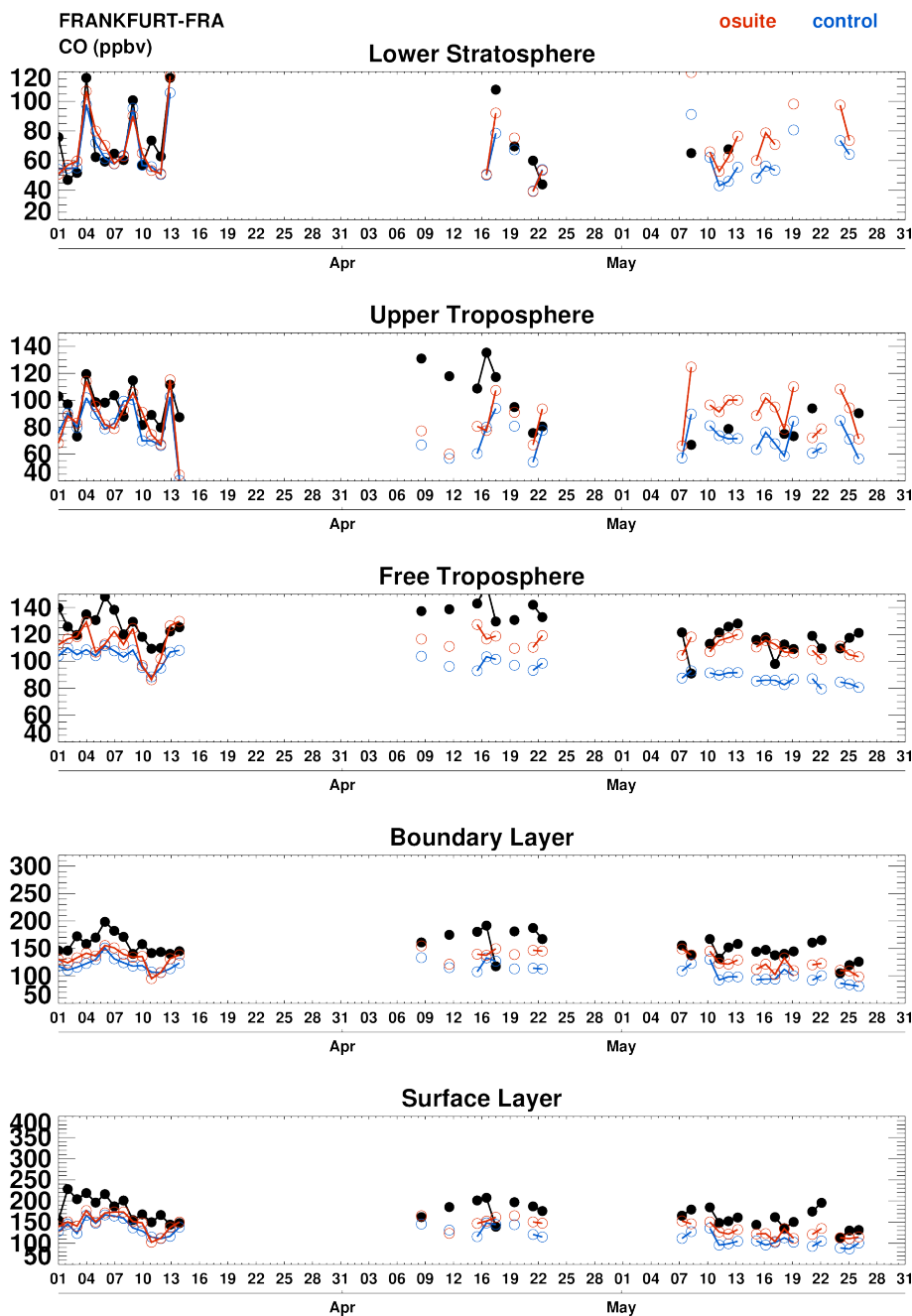


Figure 4.2.1: Time series of daily mean CO over Frankfurt during MAM 2020 for 5 layers: Surface Layer, Boundary Layer, Free Troposphere, Upper Troposphere and Lower Stratosphere. IAGOS is shown in black, the o-suite in red and associated control run in blue. Units: ppbv.

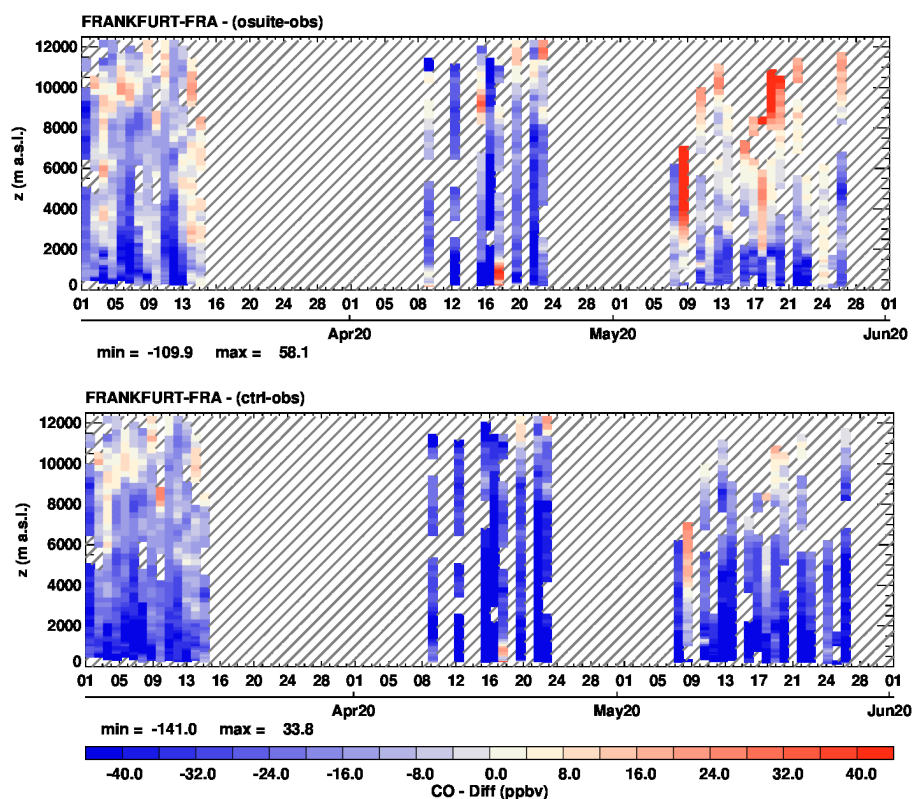


Figure 4.2.2: Time series of the absolute differences (model – IAGOS aircraft observations) in daily profiles for CO over Frankfurt during MAM 2020. The top panel corresponds to o-suite, the bottom panel to control run. Units: ppbv.

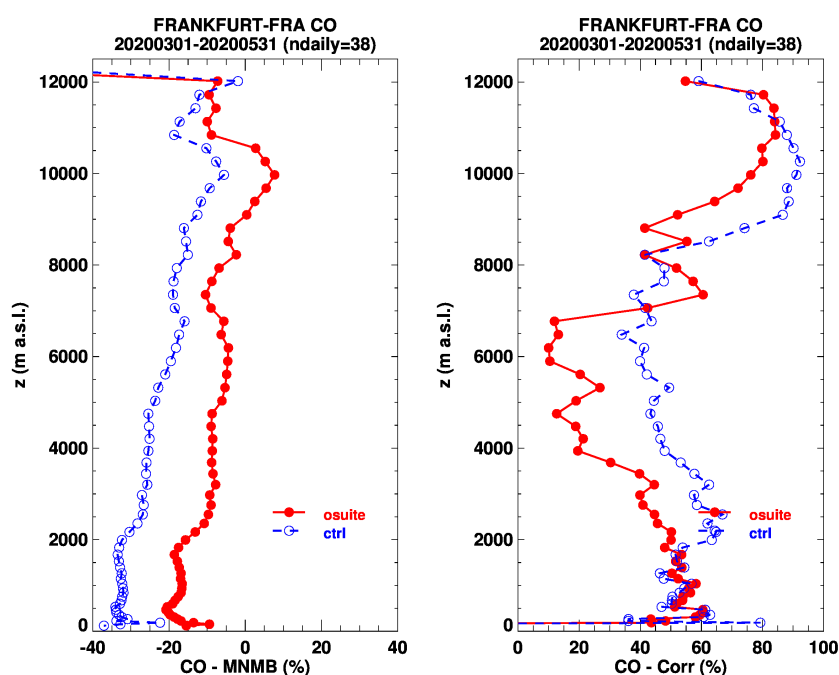


Figure 4.2.3: Model scores (MNMB and Correlation coefficient) for CO at Frankfurt calculated over the period MAM 2020. The left panel corresponds to MNMB and the right panel to Correlation coefficient. The o-suite is shown in red and associated control run in blue. Units: %.

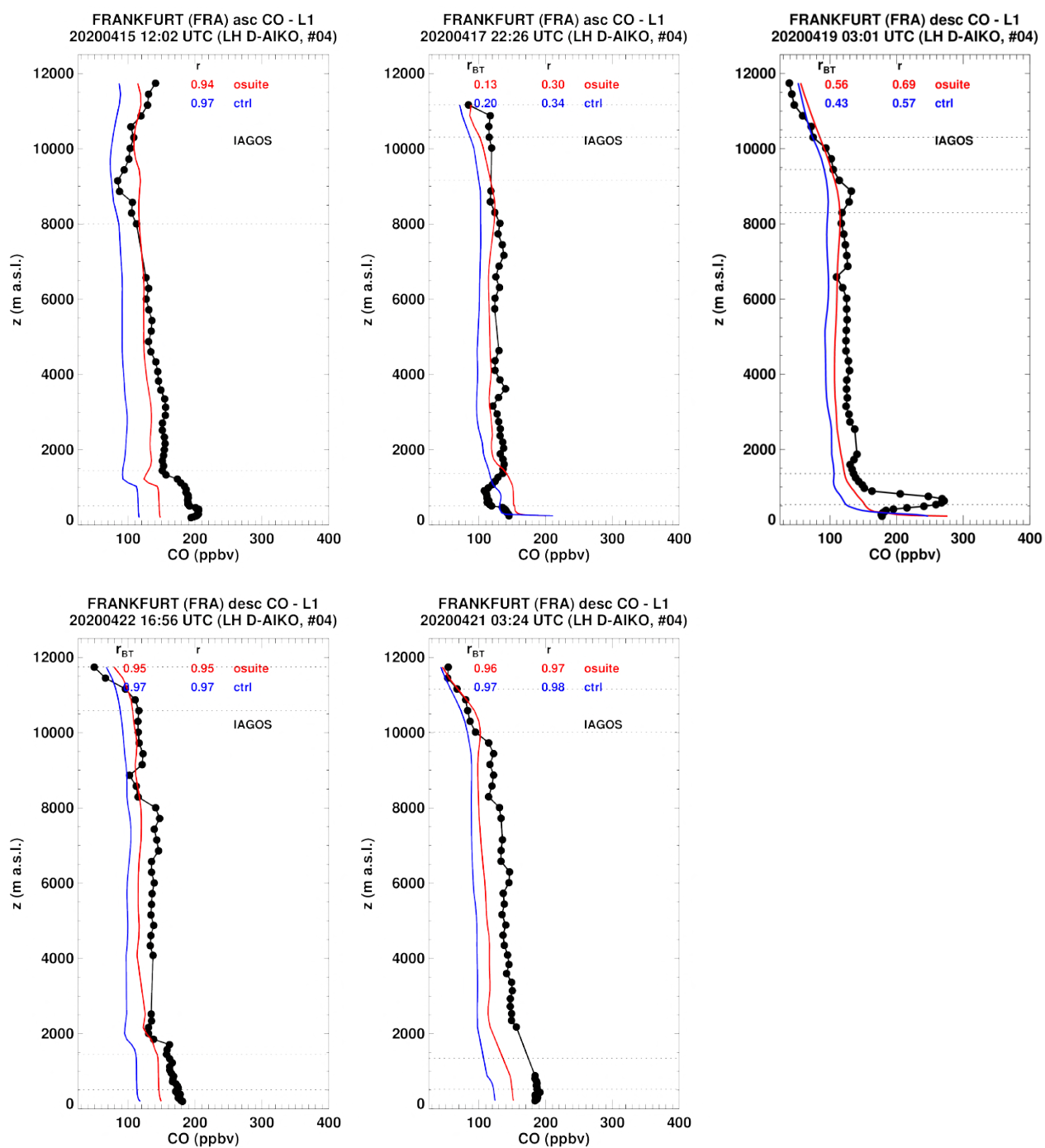


Figure 4.2.4.a: Selection of individual profiles for CO from IAGOS (black) and the two NRT runs (o-suite: red, control: blue) over Europe during MAM 2020. Units: ppbv.

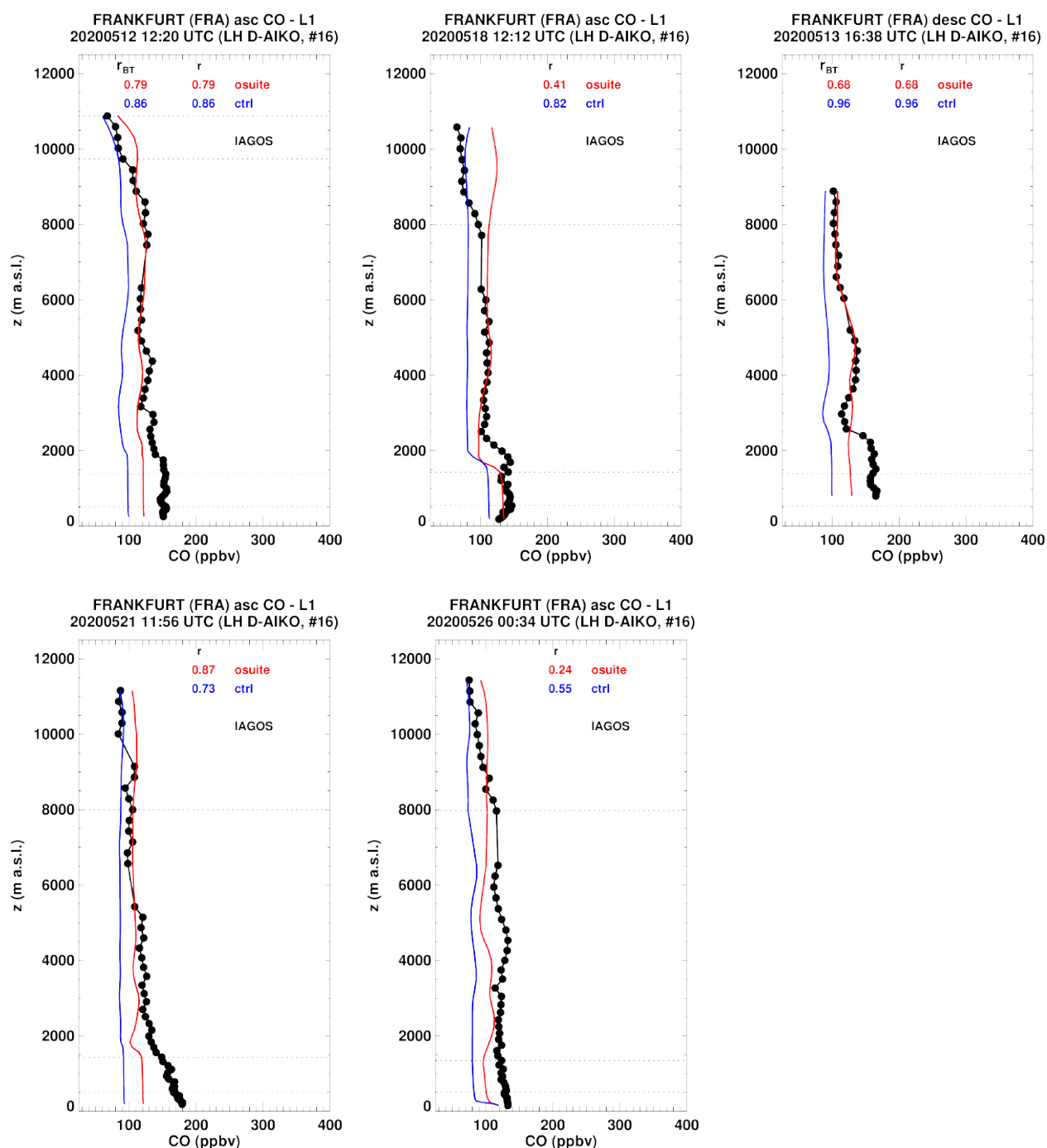


Figure 4.2.4.b: Selection of individual profiles for CO from IAGOS (black) and the two NRT runs (o-suite: red, control: blue) over Europe during MAM 2020. Units: ppbv.

A number of individual profiles are shown in Fig. 4.2.4.a-b for April and May respectively. On most of these profiles the differences between the two runs as well as the best performance from the run with assimilation can be clearly seen, as already mentioned above. The relatively low correlation found in Fig. 4.2.3 for the o-suite is mainly due to the variability observed in the profiles in March and May (see Fig. 4.2.2).

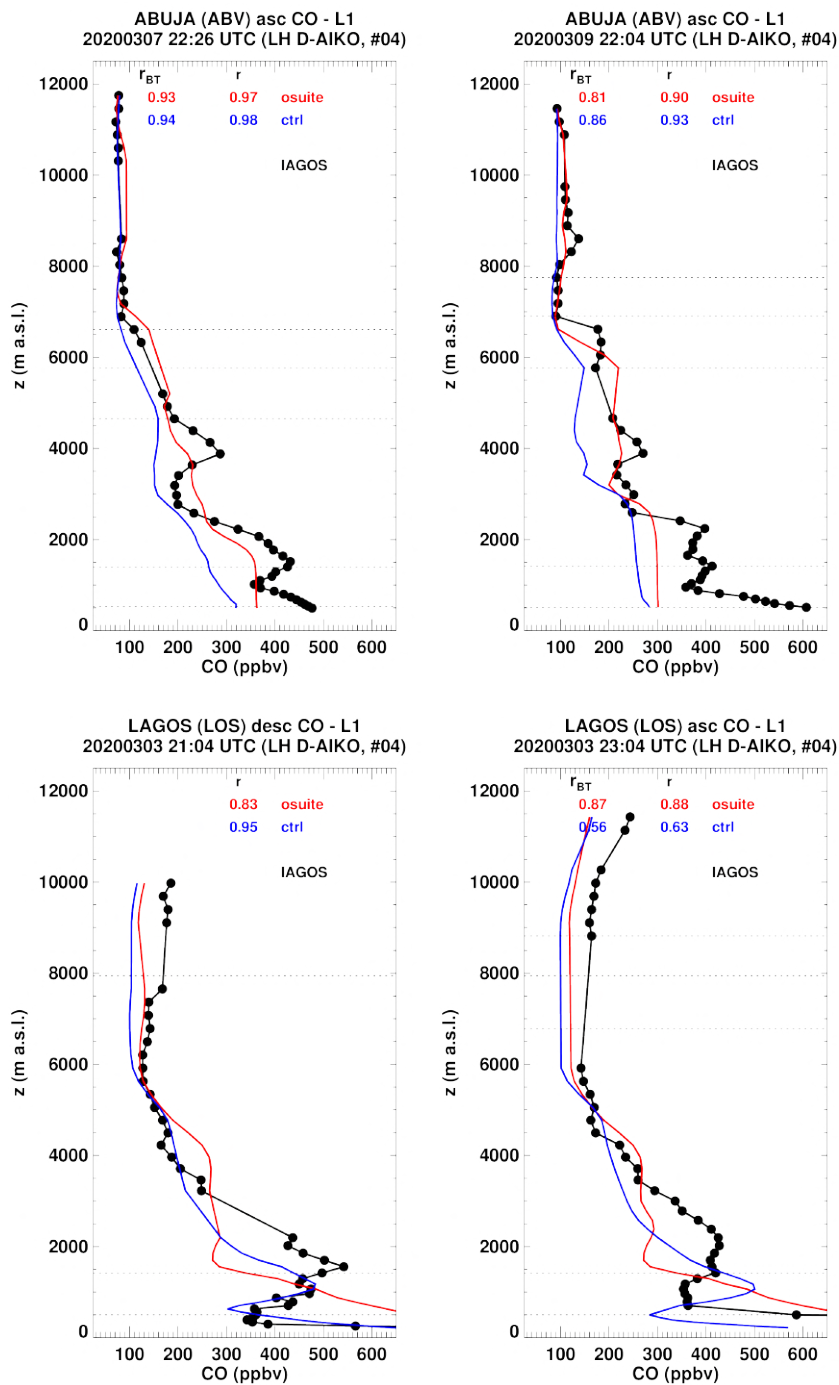


Figure 4.2.5: Selection of individual profiles for CO from IAGOS (black) and the two NRT runs (o-suite: red, control: blue) over Western Africa during MAM 2020. Units: ppbv.

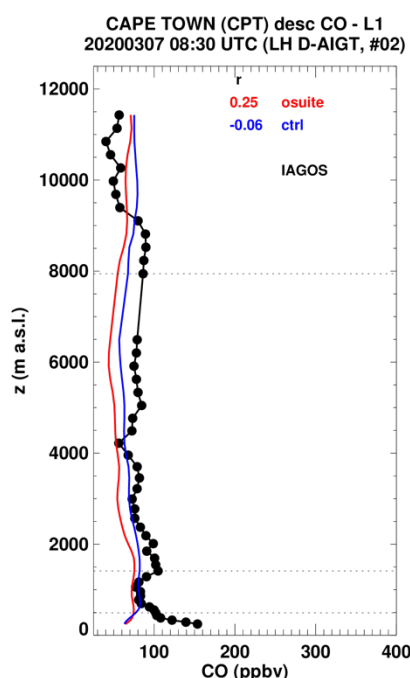


Figure 4.2.6: Selection of individual profiles for CO from IAGOS (black) and the two NRT runs (o-suite: red, control: blue) over South Africa during MAM 2020. Units: ppbv.

Western Africa

Over Western Africa a few profiles are available at Abuja airport and two at Lagos airport (Fig. 4.2.5). The complex shapes of the profiles are not always well reproduced by the two runs. At Abuja the run with assimilation performs clearly better than the control run, especially although large underestimations are found in the low troposphere for the two runs. At Lagos, the shape of the profile is better reproduced by the control run. The maxima in the low troposphere are reproduced only by the control run, but at a lower altitude than observations. In the UTLS the results of the two runs are similar, and a good agreement with observations is found at Abuja while at Lagos the bias (negative) is larger.

South Africa

Over South Africa, only two CO profiles are available at the airport of Cape Town, but only one is presented here for the other is not complete (Fig. 4.2.6). For this profile, the results of the two runs are very similar for this period. In the low troposphere, values are underestimated. In the free troposphere and UTLS, o-suite and control run behave similarly and agree well with observations.

North America

CO profiles are available at the airport of Atlanta, Detroit and Miami during MAM 2020 (Fig. 4.2.7). For this period, in the available profiles, CO observed values are roughly in the range 100-200 ppbv in the low troposphere. These values are underestimated similarly by both runs at the three locations. In the free troposphere and UTLS both runs agree better with observations, with a slightly better performance from control run at Miami.

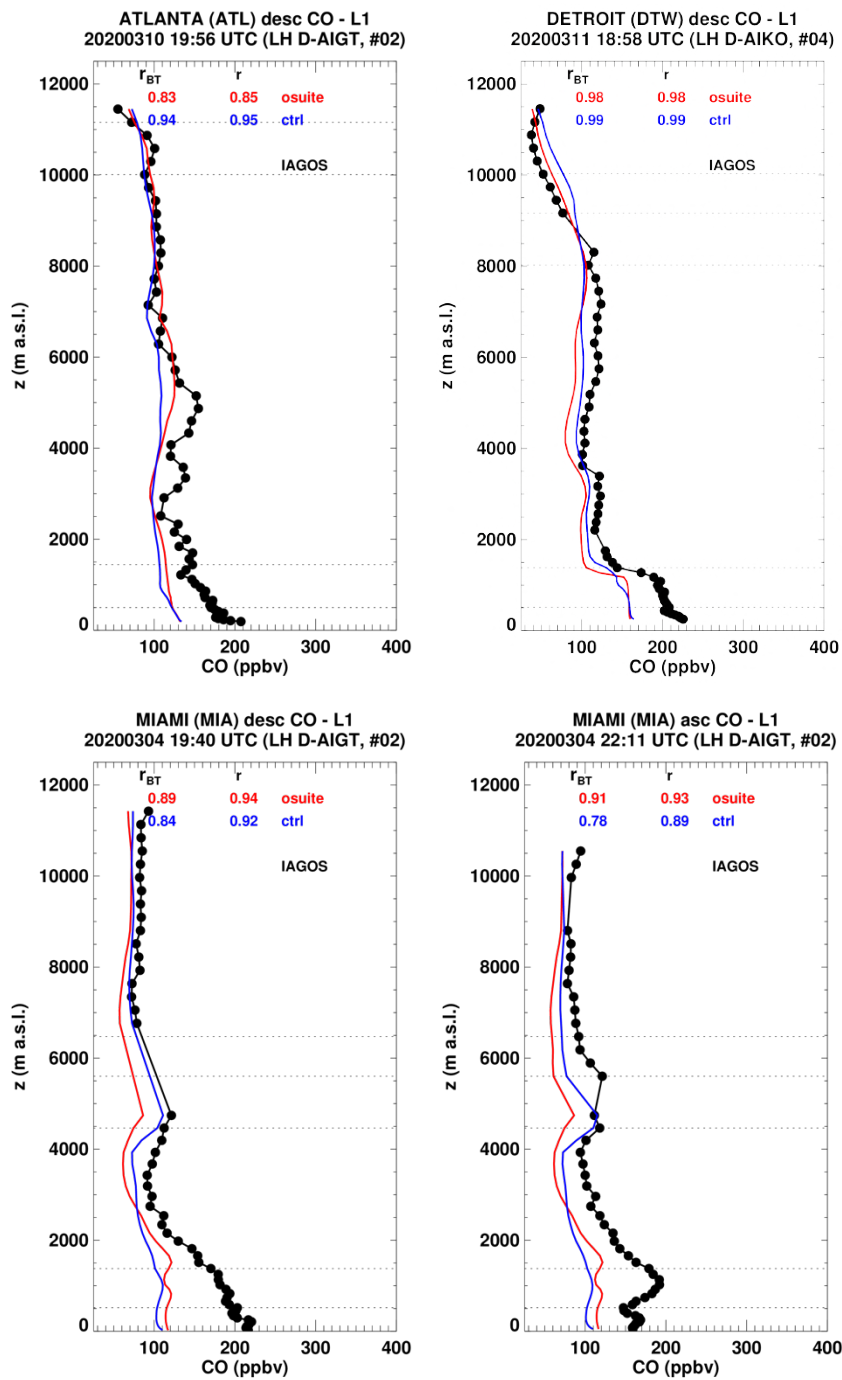


Figure 4.2.7: Selection of individual profiles for CO from IAGOS (black) and the two NRT runs (o-suite: red, control: blue) over North America during MAM 2020. Units: ppbv.

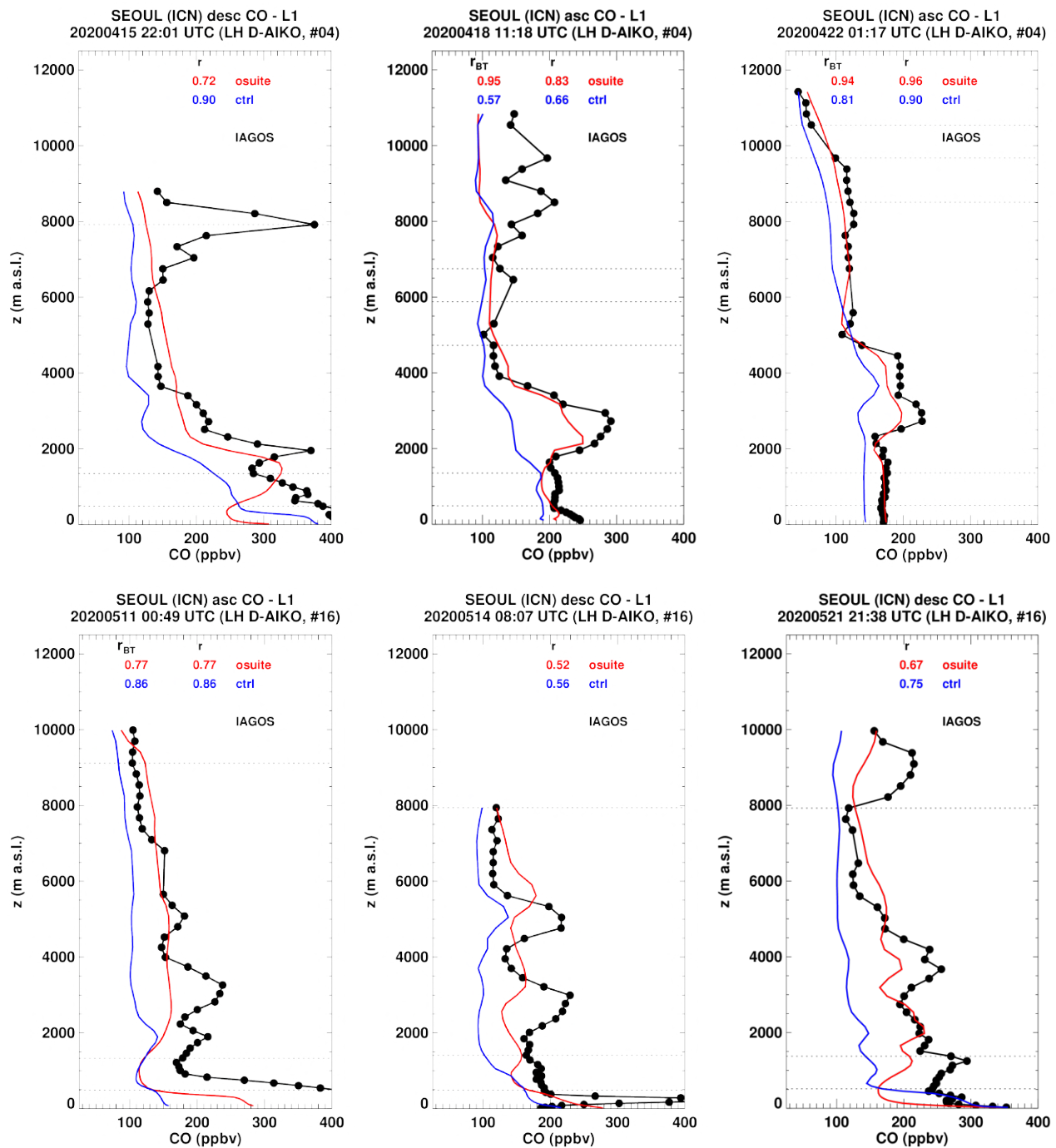


Figure 4.2.8.a: Selection of individual profiles for CO from IAGOS (black) and the two NRT runs (o-suite: red, control: blue) over East Asia during MAM 2020. Units: ppbv.

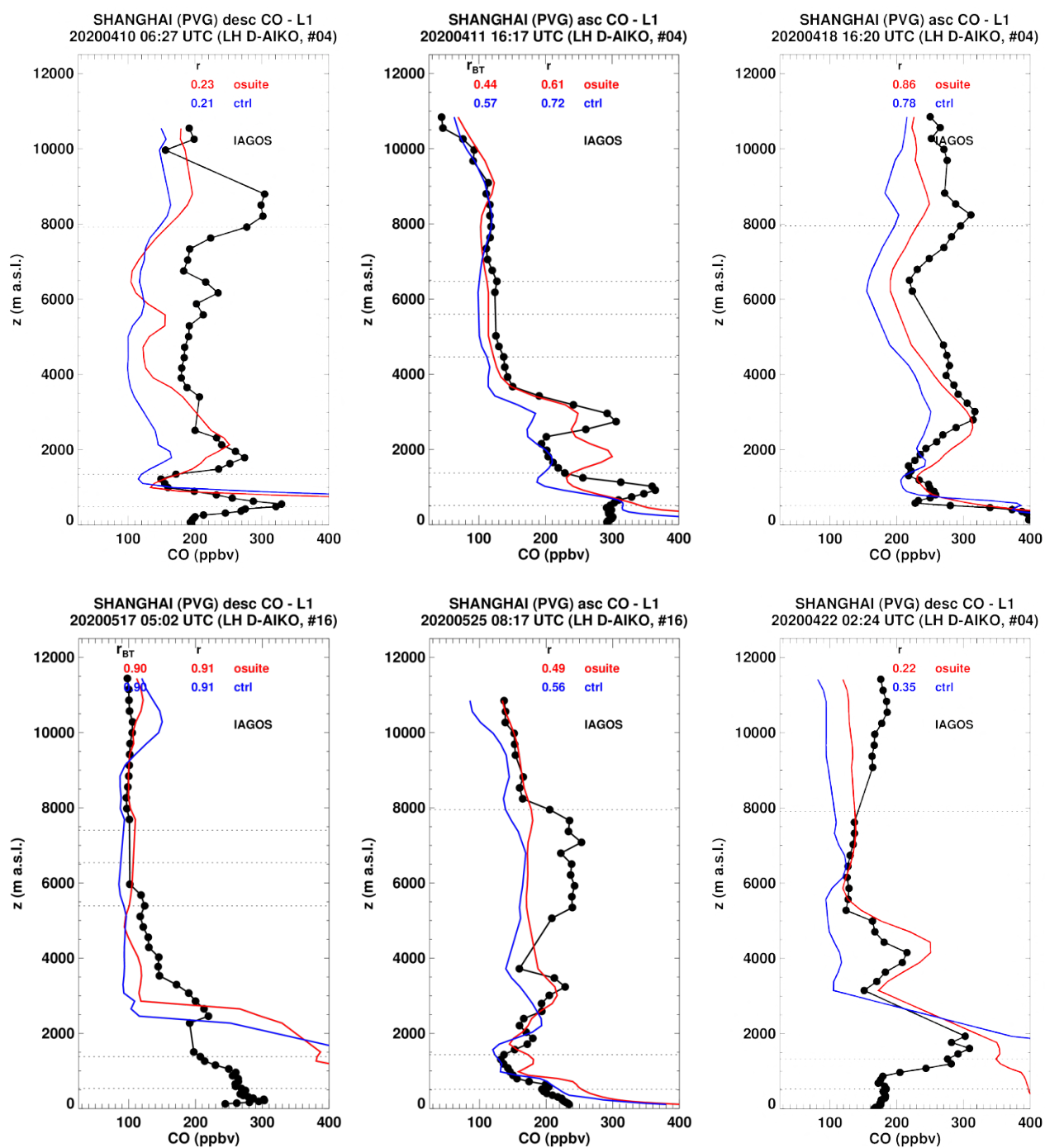


Figure 4.2.8.b: Selection of individual profiles for CO from IAGOS (black) and the two NRT runs (o-suite: red, control: blue) over East Asia during MAM 2020. Units: ppbv.

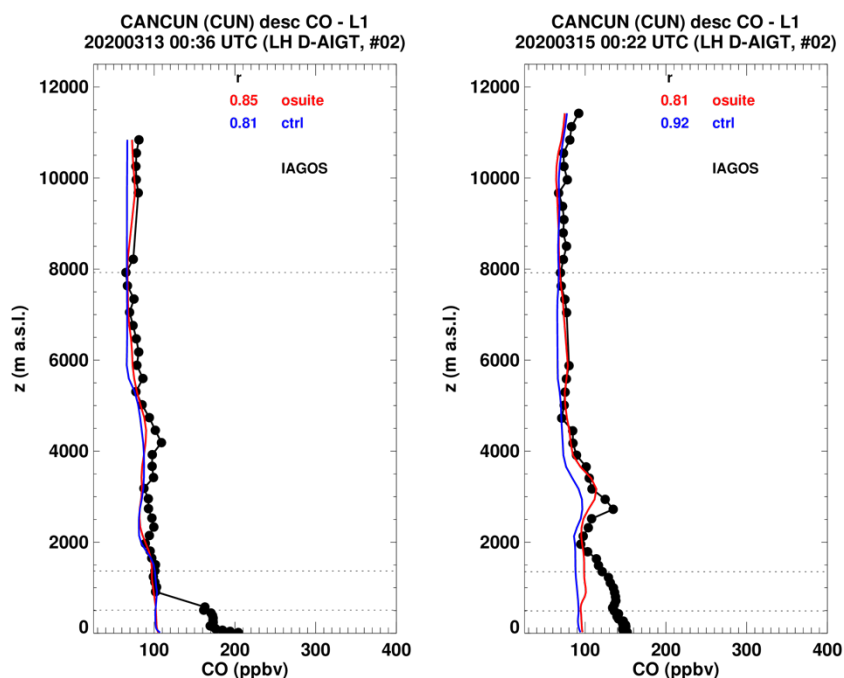


Figure 4.2.9: Selection of individual profiles for CO from IAGOS (black) and the two NRT runs (o-suite: red, control: blue) over South America during MAM 2020.

Eastern Asia

Over East Asia, several profiles of CO are available at the airports Seoul (Fig. 4.2.8.a) and Shanghai (Fig. 4.2.8.b) in April and May 2020. All these profiles present complex shapes with often high CO values in the low troposphere as well as several maxima in the free troposphere. In the lowest layers the results of the two runs are in general similar with underestimations in Seoul and overestimations in Shanghai. The shape of the profiles is not always well reproduced by the models (amplitude and altitude of the maxima) but for all profiles at these airports, the run with assimilation is clearly providing better results than the control run, which generally presents much smoother profiles and fails to reproduce the maxima in the free troposphere. In the UTLS, the agreement is better than in the lowest layers and the performances of the two runs are similar.

Central America

During MAM 2020, three profiles of CO are available at Cancun in Mexico (Fig. 4.2.9). The performance of the two runs are similar. CO values are underestimated in the surface and boundary layer by both runs. In the free troposphere and UTLS the bias is small, CAMS global and control run perform similarly well.

4.3 Validation against FTIR observations from the NDACC network

In this section, we compare the CO profiles of the CAMS products with FTIR measurements at 21 FTIR stations within the NDACC network. These ground-based, remote-sensing instruments are sensitive to the CO abundance in the troposphere and lower stratosphere, i.e. between the surface and up to 20 km altitude. Tropospheric and stratospheric CO partial columns are validated. A description of the instruments and applied methodologies can be found at <http://nors.aeronomie.be>.

Figure 4.3.1 show that the o-suite tropospheric columns of CO agree well. The model upgrade (60 to 137 levels) implemented in July 2019 changes the overall biases in both the troposphere and stratosphere. The negative bias for the tropospheric columns increased to -7.5% in MAM, -8.5% in DJF, -7% in SON (compared to -4% in JJA 2019) and is larger than the reported measurement uncertainty. The stratospheric column bias also changed to -13% in MAM 2020 compared to +10% in SON and +6% in JJA. There are no large differences between the o-suite AN and 1d FC, except at Boulder where the o-suite AN performs significantly worse than the o-suite 1d forecast.

Figure 4.3.2 shows a trend in the tropospheric CO column at Jungfraujoch (4km – TP) of about 1.5% per year. A similar trend is observed at Zugspitze (3km above sea level), but not at other non-mountain sites like St Petersburg. The trend at the o-suite 1dFC at both mountain stations is much lower (around -0.5%/y), which suggests the trend is located in the upper tropospheric column and is related to the assimilation.

Table 4.3.1: Detailed statistics for tropospheric CO column comparisons for FTIR measurements during MAM 2020. Both analysis and 1d FC o-suite behave similar, except at Boulder where the bias is significantly lower for the o-suite AN.

FTIR site	o-suite AN tropospheric column					o-suite 1d FC tropospheric column					lat
	#	rel. std	corr	rel diff (%)	rel diff std(%)	#	rel. std	corr	rel diff (%)	rel diff std(%)	
EUREKA	6	0.7	0.93	-7.61	4.25	6	0.6	0.92	-7.57	4.56	80.1
NY.ALESUND	6	1.3	0.86	-8.79	3.23	6	1.2	0.85	-8.69	3.32	78.9
THULE	41	1.1	0.95	-9.59	3.8	41	1.1	0.96	-9.39	3.62	76.5
BREMEN	13	0.9	0.79	-1.81	3.84	13	0.8	0.88	-4.51	3.39	53.1
JUNGFRAUJOCH	30	0.8	0.83	-9.4	4.78	30	0.8	0.87	-2.58	4.36	46.6
TORONTO	44	0.8	0.75	-1.17	5.77	44	0.9	0.85	-2.91	4.15	43.6
BOULDER.CO	38	1	0.89	-11.14	3.14	38	0.8	0.83	-1.22	4.71	40
MAUNA.LOA.HI	26	1.1	0.98	-6.09	3.03	26	1.3	0.98	-7.41	3.45	19.5
ALTZOMONI	4	1	0.89	-14.7	6.17	4	0.7	0.83	-13.25	10.64	19.1
PARAMARIBO	3	1.2	0.95	-8.89	2.49	3	1	0.94	-7.19	3.17	5.8
WOLLONGONG	13	1.6	0.36	-5.95	10.67	13	2.1	0.34	-4.62	10.65	-34.4
LAUDER	41	1	0.91	-5.76	4.68	41	1	0.91	-3.65	4.6	-45
		1	0.84	-7.58	4.65		1	0.85	-6.08	5.05	

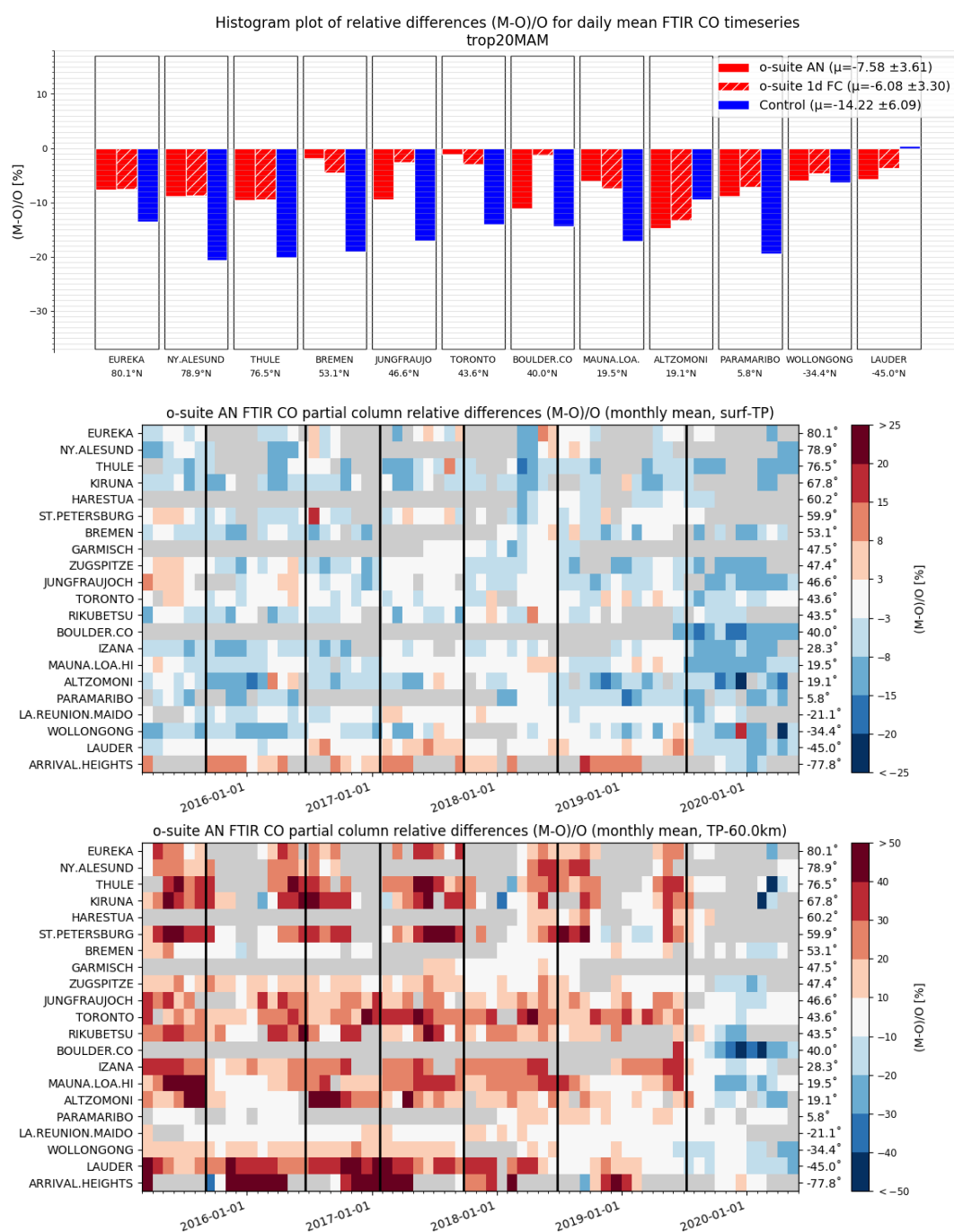


Figure 4.3.1: Seasonal relative mean bias for tropospheric CO columns (MB, %) for the considered period MAM 2020 (top) and monthly mean biases for a longer time period for the tropospheric CO columns (middle) and stratospheric CO columns (bottom) (o-suite upgrades are indicated in black vertical lines, stations are sorted by latitude). The overall uncertainty for the CO measurements is approximately 3% on the tropospheric columns and 10% for the stratospheric columns. The o-suite analysis averaged bias in tropospheric columns increased to -7.5% for MAM compared to the bias before the model update in 2019. The bias in the stratosphere reduced to -12% and just exceeds the measurement's uncertainty.

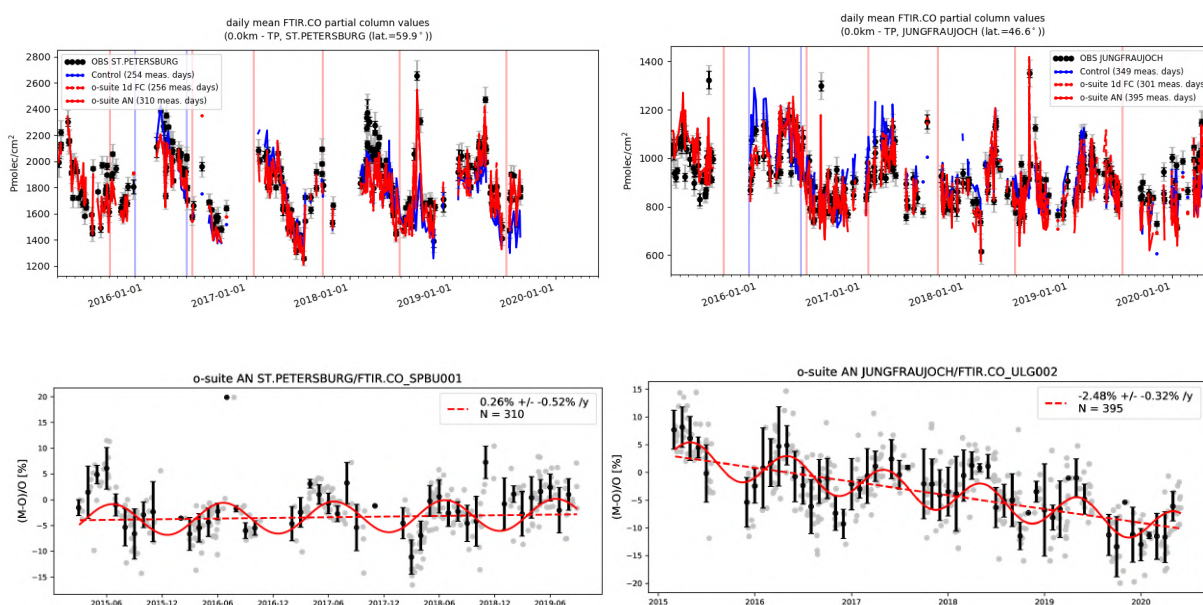


Figure 4.3.2: Top: daily mean values of tropospheric CO columns by the o-suite (AN and 1d FC, red) and the control run (blue) compared to NDACC FTIR data at St Petersburg and Jungfraujoch for the period March 2015-May 2020. During March 2018 the o-suite underestimated the CO columns at St. Petersburg. Bottom row contains a linear fit and seasonal cycle fit through the relative differences for the o-suite AN. An underestimation is observed during the local autumn/winter months. The negative trend at Jungfraujoch is -1%/y in the o-suite 1dFC and 2.5% in the o-suite AN.

The Taylor diagrams in Figure 4.3.3 provide information on the correlation of all three CAMS products under consideration with the FTIR time series. Leaving out the sites with few measurements, the assimilation has a positive effect on the correlation coefficient. Looking at the correlation values for the period 2019 SON, the o-suite 1d FC (averaged correlation for all sites is 0.78) is comparable to the o-suite AN (averaged correlation for all sites is 0.79).

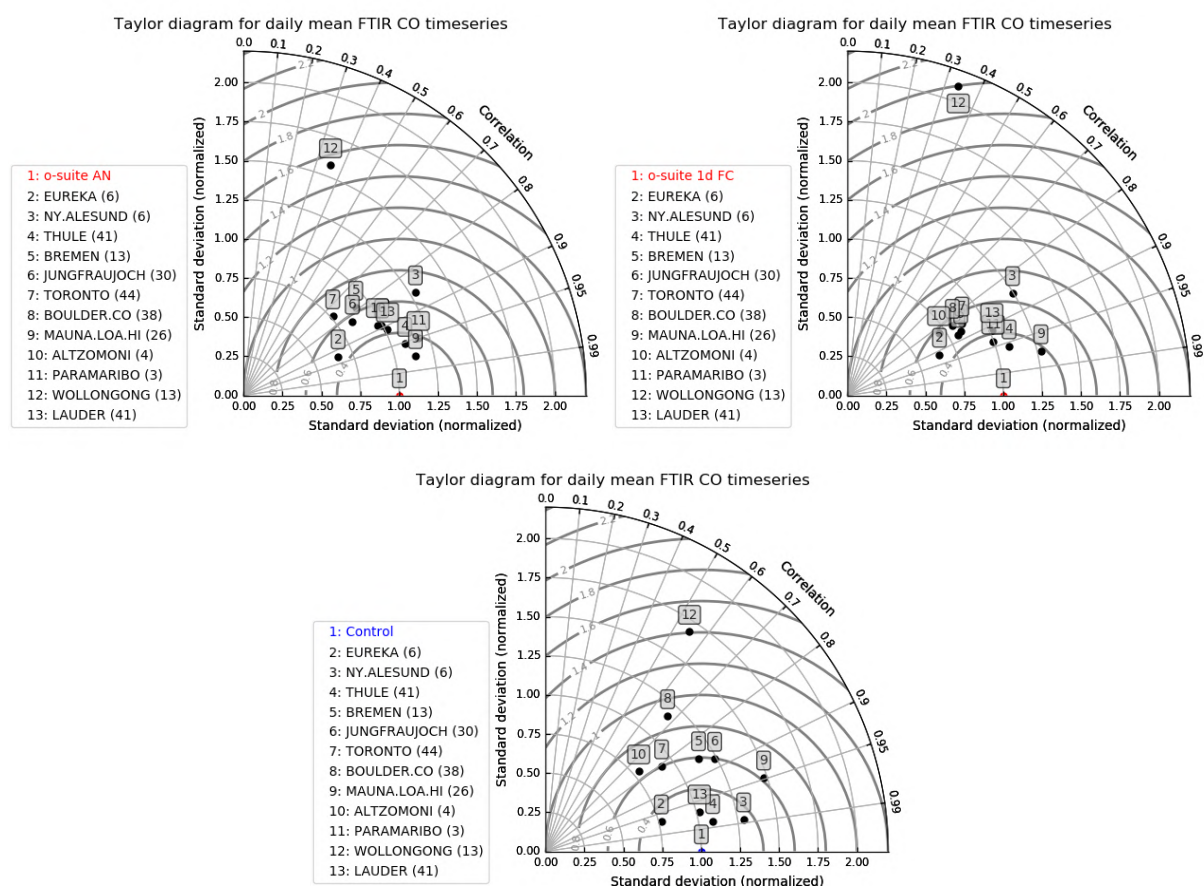


Figure 4.3.3: Taylor diagrams relating the standard deviations for the model /GB time series of tropospheric CO column data and their correlation. All time-series are normalised such that the std of the model is 1. Wollongong has low correlation in this quarter because the number of measurements is low and because background values are measured.

4.4 Validation against FTIR observations from the TCCON network

The CO column averaged mole fractions of the CAMS models are compared with data from the Total Carbon Column Observing Network (TCCON). Column averaged mole fractions provide different information content than the in situ measurements and are therefore complementary to the in situ data. In this section, we compare column averaged mole fractions of CO of the CAMS models with TCCON retrievals. Data from the following TCCON sites has been used:

Izana (Blumenstock et al., 2017), Reunion (De Mazière et al., 2017), Bialystok (Deutscher et al., 2017), Manaus (Dubey et al., 2017), Four Corners (Dubey et al., 2017), Ascension (Feist et al., 2017), Anmeyondo (Goo et al., 2017), Darwin (Griffith et al., 2017), Wollongong (Griffith et al., 2017), Karlsruhe (Hase et al., 2017), Edwards (Iraci et al., 2017), Indianapolis (Iraci et al., 2017), Saga (Kawakami et al., 2017), Sodankyla (Kivi et al., 2017), Hefei (Liu et al., 2018), Tsukuba (Morino et al., 2017), Burgos (Morino et al., 2018), Rikubetsu (Morino et al., 2017), Bremen (Notholt et al., 2017), Spitsbergen (Notholt et al., 2017), Lauder (Sherlock et al., 2017, Pollard et al., 2019), Eureka (Strong et al., 2018), Garmisch (Sussmann et al., 2017), Zugspitze (Sussmann et al., 2018), Paris (Te et al.,

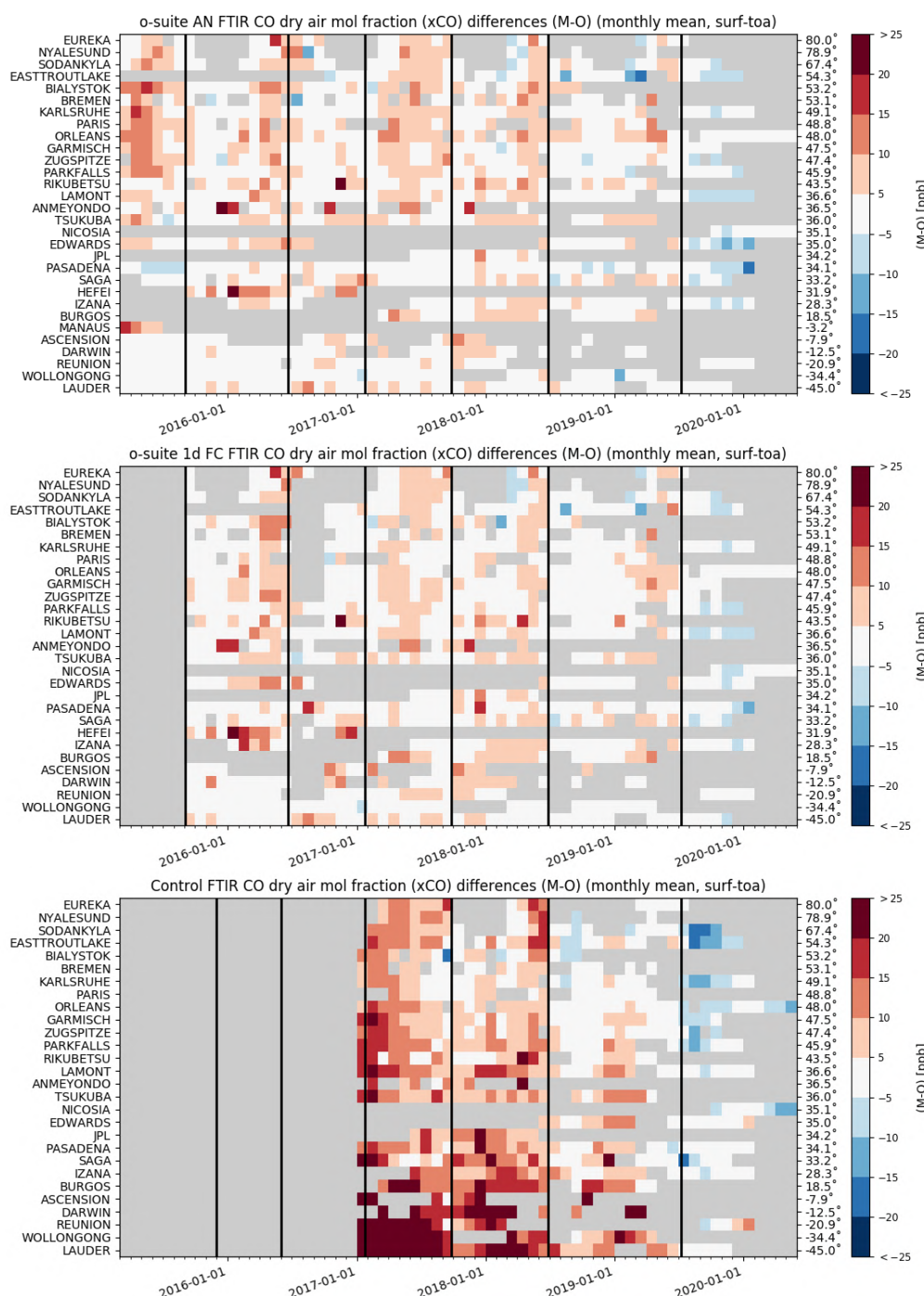


Figure 4.4.1: Monthly differences for the last 4 years. The stations are sorted by latitude (northern to southern hemisphere).

2017), Orleans (Warneke et al., 2017), Park Falls (Wennberg et al., 2017), Caltech (Wennberg et al., 2017), Lamont (Wennberg et al., 2017), Jet Propulsion Laboratory (Wennberg et al., 2017), East Trout Lake (Wunch et al., 2017), Nicosia (Petri et al., 2020)

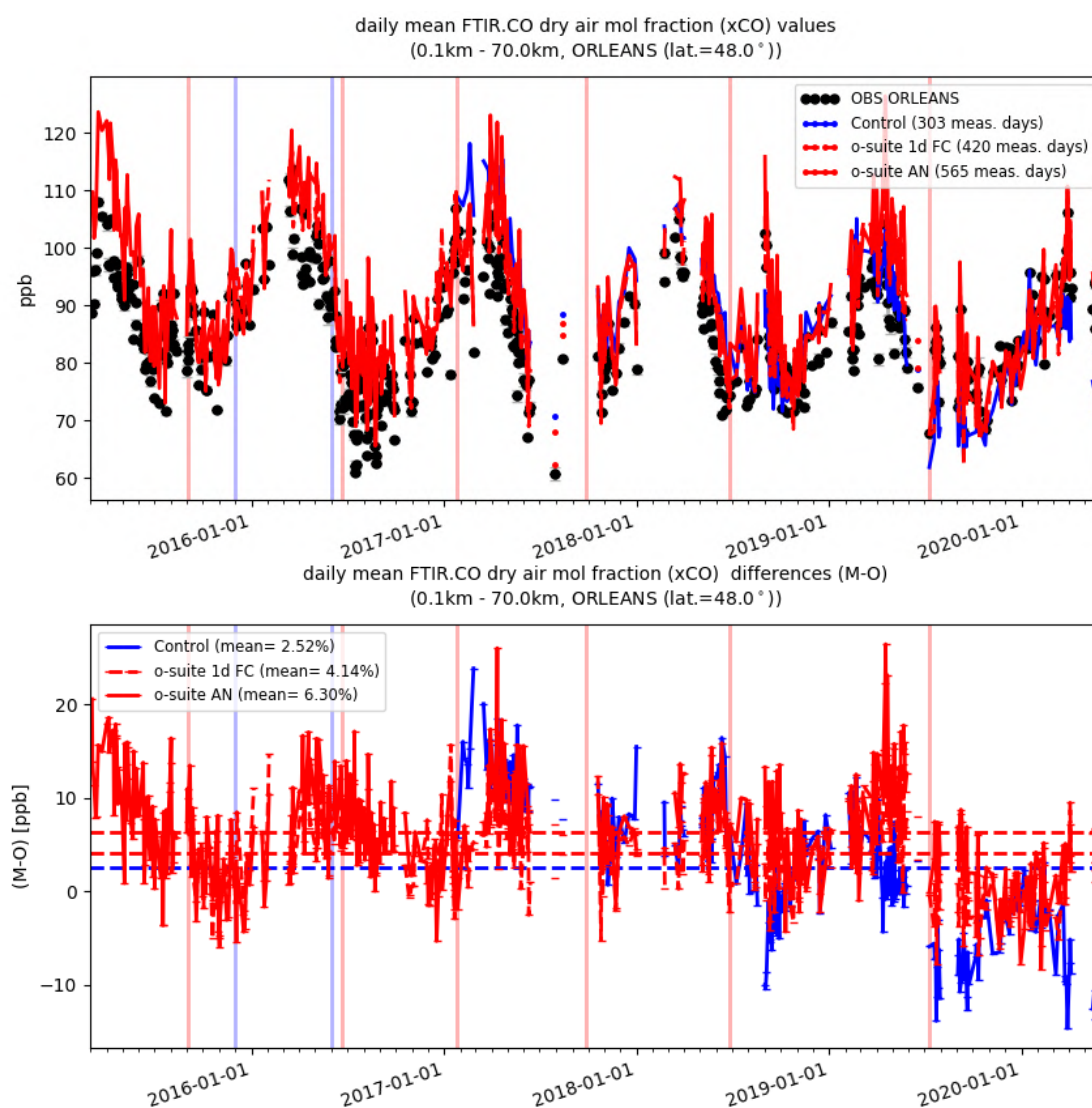


Figure 4.4.2: Comparison of the CO model data with TCCON CO at Orleans.

For the validation of the models in March, April and May the sites that made data available were Nicosia and Orleans.

For the comparison period the o-suite analysis and the o-suite forecast simulations compare very well with the measurements (Fig 4.4.1). These two models overestimate the CO slightly (< 5%) at Orleans (Fig. 4.4.2) and at Nicosia the agreement is within 1% (Fig. 4.4.3). The control model underestimates the CO by about 8% (Fig. 4.4.3).

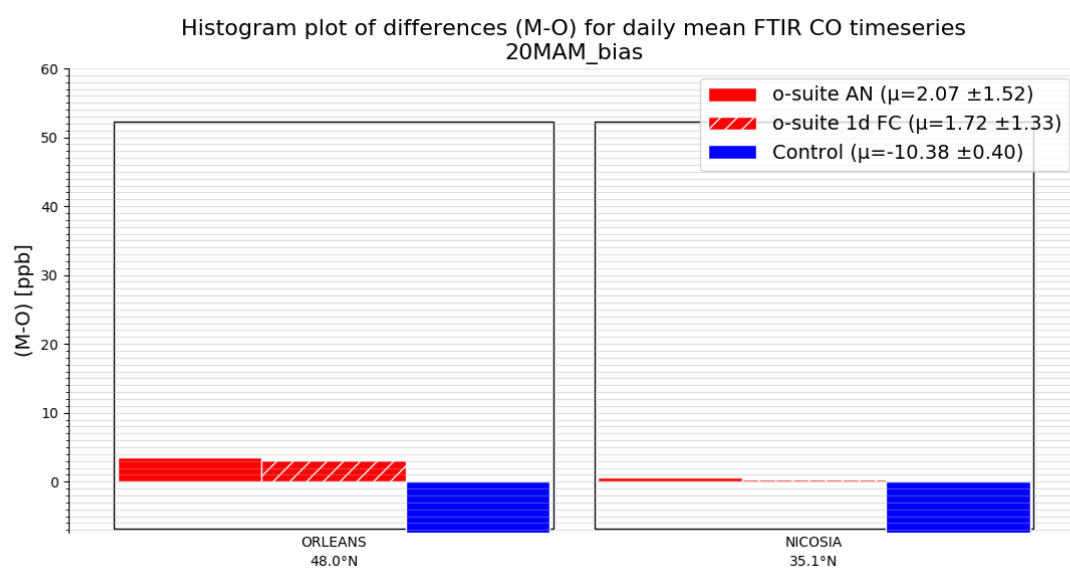


Figure 4.4.3: Differences during the reporting period. The different sites cover different periods of the comparison period.

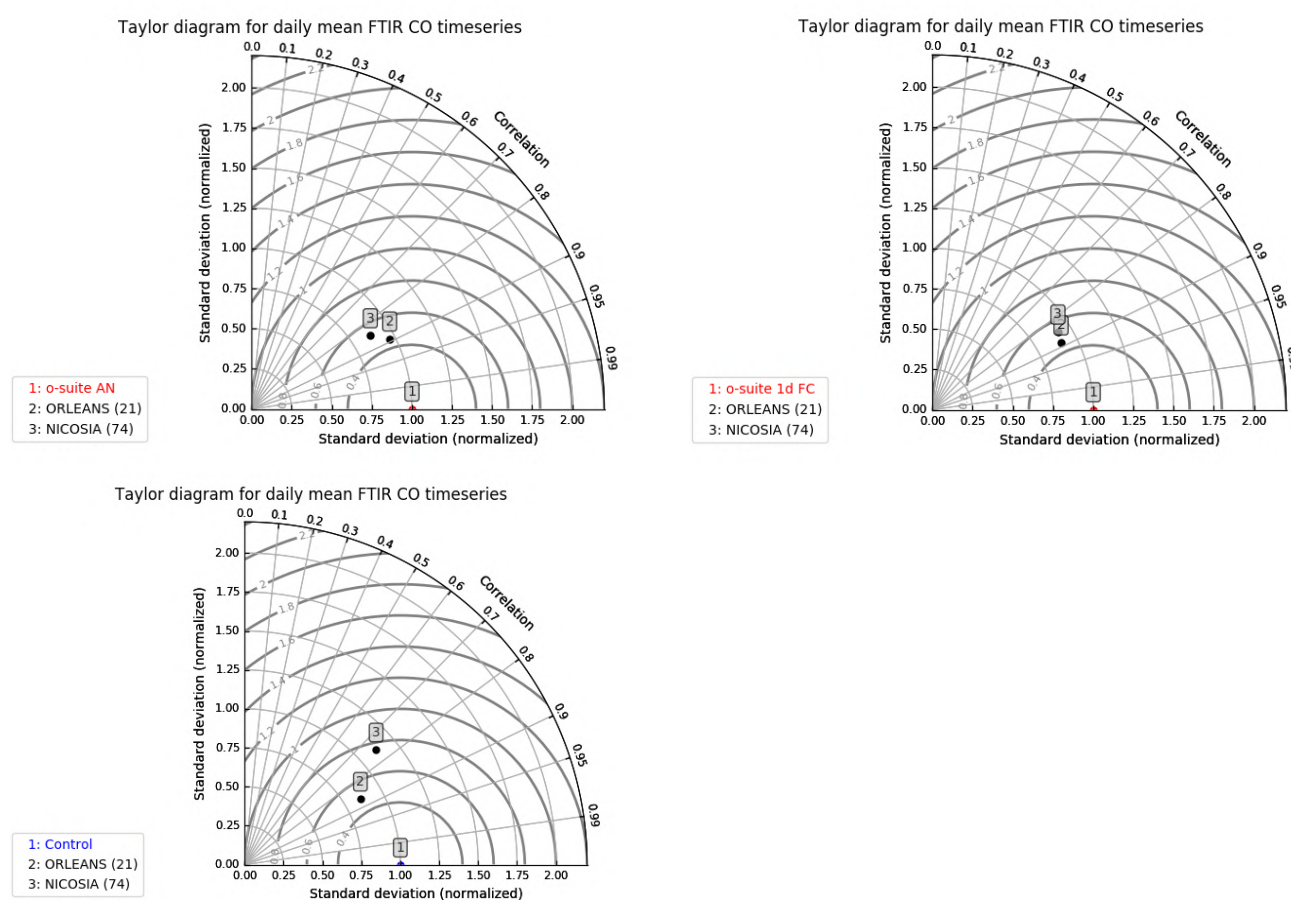


Figure 4.4.4: Taylor diagrams for the comparison period.



4.5 Evaluation with MOPITT and IASI data

In this section, modelled CO total columns are compared to MOPITT version 8 (thermal infrared radiances) (Emmons et al., 2009, Deeter et al., 2010) and IASI satellite retrievals (Clerbaux et al., 2009). Figure 4.5.1 shows the global distribution of CO total columns retrieved from MOPITT V8 (top left) and the relative biases of the model runs with respect to MOPITT V8 for April 2020.

MOPITT shows high values mainly over Mainmar (Birma), Thailand and east of China and associated parts of the Pacific Ocean. The modelled CO geographical distribution and magnitude of values show that the model performs reasonably well. The relative difference between the model runs and MOPITT shows that the o-suite performs better than the control run without data assimilation. The o-suite shows negative biases within 10-20 % over the Southern Hemisphere and biases within +/- 10% over the Northern Hemisphere. The high CO values over Indonesia and east of China are captured relatively well, showing light overestimation (within 10%) over the eastern part of China and associated part of the ocean and underestimation within 20% over Mainmar (Birma) and Thailand. The control run shows negative biases up to 30% over the Northern Hemisphere land and within 20% over the Northern Hemisphere ocean. The values over the abovementioned high CO regions are underestimated by about 20-30%. The biases over the Southern Hemisphere are within +/- 10% with some exceptions (e.g. over Australia and Indonesia where biases reach 20%). The o-suite run shows a growing biases, both, positive and negative, on the 4th forecast day.

Figure 4.5.2 shows time series of CO total column for MOPITT V8, IASI and the model runs over the eight selected regions. For the comparison with MOPITT, the modelled CO concentrations were transformed using MOPITT V8 averaging kernels (Deeter, 2004). Both, MOPITT and IASI CO total columns are assimilated in the o-suite run, while a bias correction scheme is applied to IASI data to bring it in line with MOPITT. MOPITT and IASI CO total columns show a relatively similar variability over different regions. IASI CO values are lower than MOPITT over most regions with some seasonal exceptions till the year 2016. Since then IASI and MOPITT are more consistent with each other over Europe, the US and East Asia. Significant difference between MOPITT and IASI are observed over the Alaskan and Siberian fire regions in winter seasons, with IASI CO total column values being lower up to 30%. In North and South Africa, deviations become larger since 2016 with IASI values being higher than MOPITT by up to 20%. The modelled seasonality of CO total columns is in relatively good agreement with the retrievals. In general, the comparison between the o-suite and control run shows that the assimilation of satellite CO has a more positive, pronounced impact on model results over East and South Asia, South Africa, and since the end of 2016, over the US in winter and spring seasons, and smaller impact over the other regions. Since June 2016, the o-suite shows very good agreement with the satellite retrievals over Europe and the US with biases less than 5%.

A general reduction of CO values from the year 2015 to the year 2018 can be seen over Europe, the US and East Asian regions. The South African region shows a slight increase of the seasonal minimum compared to previous springs. Summer 2019 was characterised by a strong fire events in Siberia. This can be seen in IASI data (peak in August), but it is not reflected in the MOPITT data partly due to only few days of observations available in August.

The modified normalized mean bias (MNMB) of the model runs compared to MOPITT V8 (Fig. 4.5.3) allows quantifying the impact of the assimilation on the model performance. The o-suite model run shows negative biases over Europe, the US and Alaskan fire regions with some seasonal exceptions.

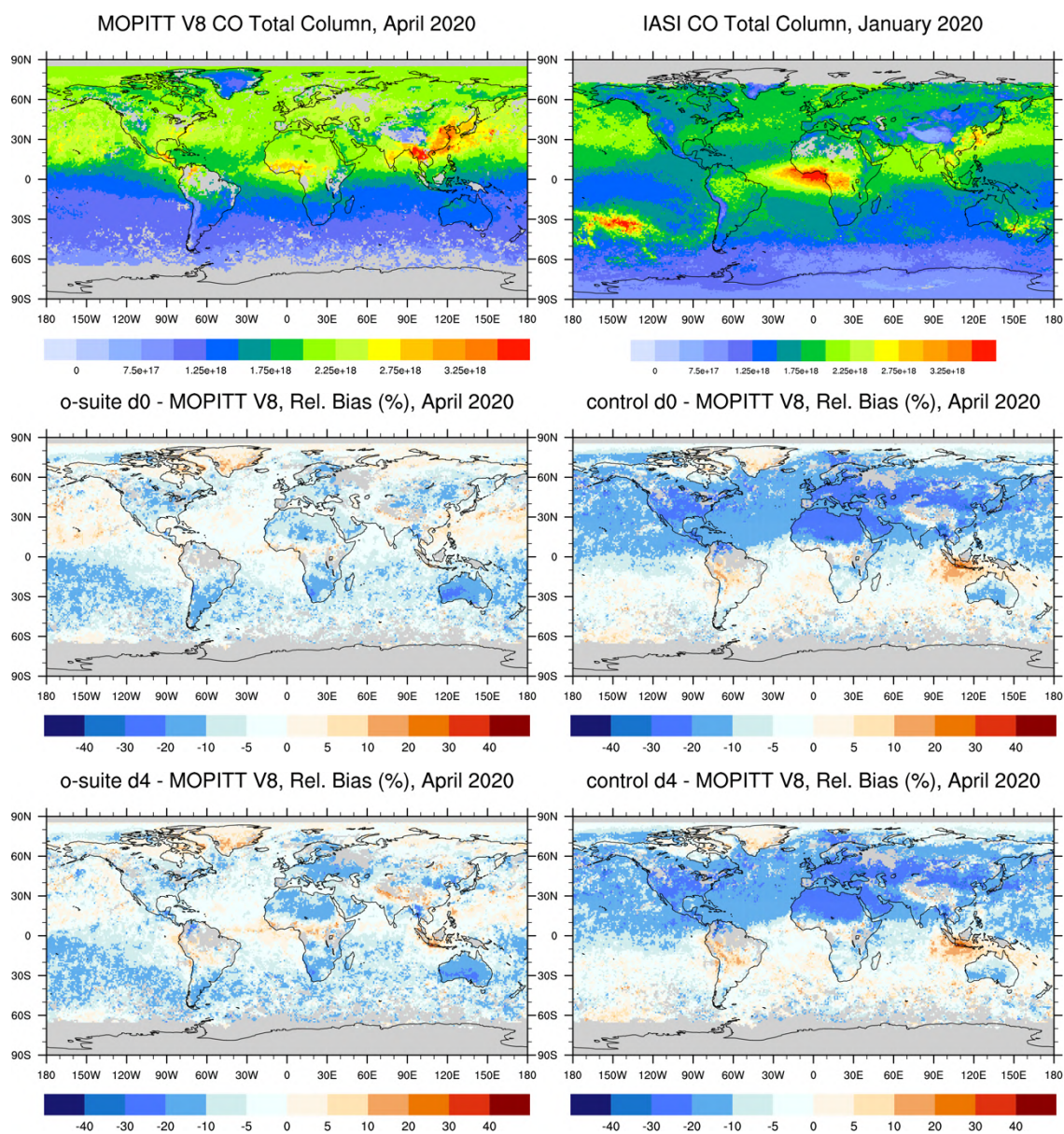


Fig. 4.5.1: CO total columns for MOPITT V8 (top left) and IASI (top right) satellite retrievals and relative difference between the model runs and MOPITT for April 2020: o-suite (middle left), control run (middle right), o-suite 4th forecast day (bottom left), o-suite 4th forecast day (bottom right). Grey colour indicates missing values.

The control run shows a systematic positive bias up to 20% over South Asia in November-December 2014, 2015, 2016, and 2017. Over southern Africa the control run overestimates satellite retrieved values by up to 25% in winter and spring 2015, 2016, and 2017. In general, the o-suite is within +/- 10% in all regions, while the control run shows larger biases over East and South Asia and North and South Africa, as well as stronger seasonal cycles.

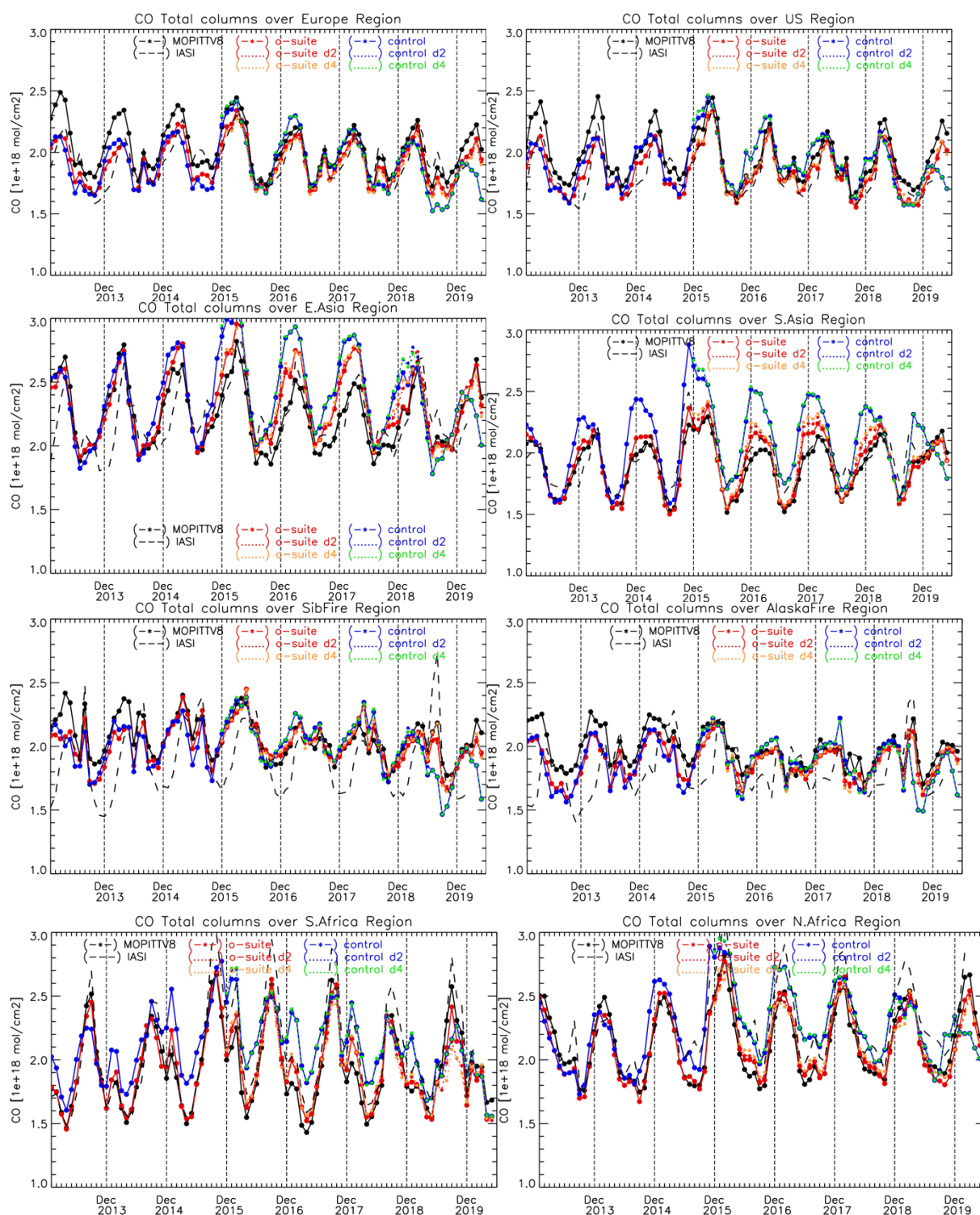


Fig. 4.5.2: Time series of CO total columns for satellite retrievals MOPITT V8, IASI (black) and the model runs over the selected regions: o-suite (red, solid), control (blue, solid), o-suite 2nd forecast day (red, dotted), o-suite 4th forecast day (orange, dotted), control 2nd forecast day (blue, dotted), control 4th forecast day (green, dotted). Period: January 2013 to May 2020.

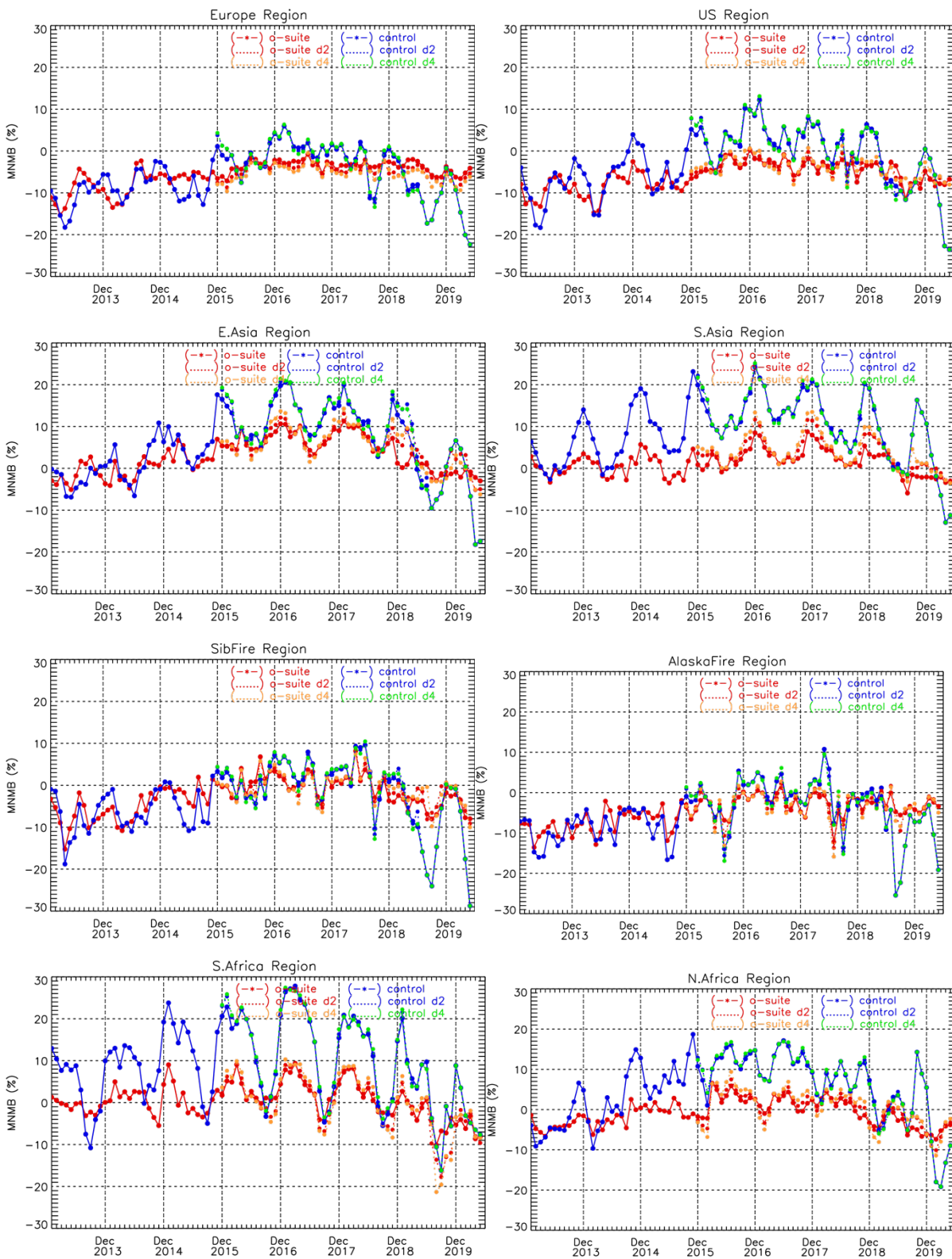


Fig. 4.5.3: Timeseries of modified normalized mean bias (%) for CO total columns from the model simulations vs MOPITT V8 retrievals over selected regions. O-suite (red, solid), control run (blue, solid), o-suite 2nd forecast day (red, dotted), o-suite 4th forecast day (orange, dotted), control 2nd forecast day (blue, dotted), control 4th forecast day (green, dotted). Period: January 2013 to May 2020.

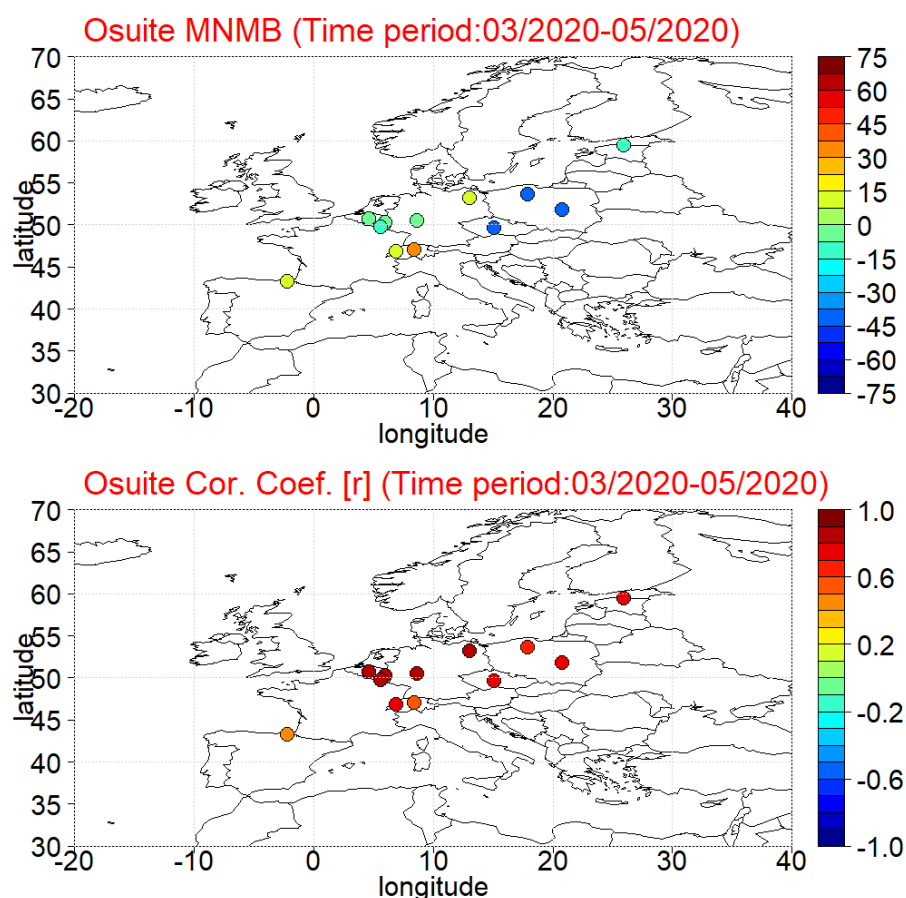


Figure 4.6.1: Spatial distribution of MNMB in % (left) and correlation coefficient (right) of the o-suite run compared to observational data during the period from 1 June 2020 to 31 August 2020.

Starting from the second half of the year 2019, the negative biases over Europe and US increase for both runs (from $\sim 5\%$ to $\sim 10\%$ for o-suite). The o-suite results over Asian regions improved and are very close to the observations, especially over East Asia. The control runs also show strong reduction of biases. Change of bias sign from positive to negative and/or increase of the negative bias can be seen over the Siberian and Alaskan fire regions and African regions for both runs. A non-systematic underestimation of 20% can be seen in the control run in February 2020 over North Africa.

For the MAM the o-suite results over Europe, US, Siberian fire region, African regions are in relatively good agreement with the observations with the negative bias within 10%. Asian regions show results that are very similar to observations. The control run shows underestimation of CO over Europe, US, East Asia, Alaska fire region and north Africa up to 25%, over Siberian fire region – up to 30% (in May) and over south Asia and south Africa – within 10%. Please note that on time of writing this report, the IASI data were not available for MAM 2020.

4.6 Evaluation with CO surface observations over Europe

The surface carbon monoxide validation analysis over Europe is based on an evaluation against background rural classes 1 to 5 of the Joly-Peuch classification (Joly and Peuch, 2012). The station

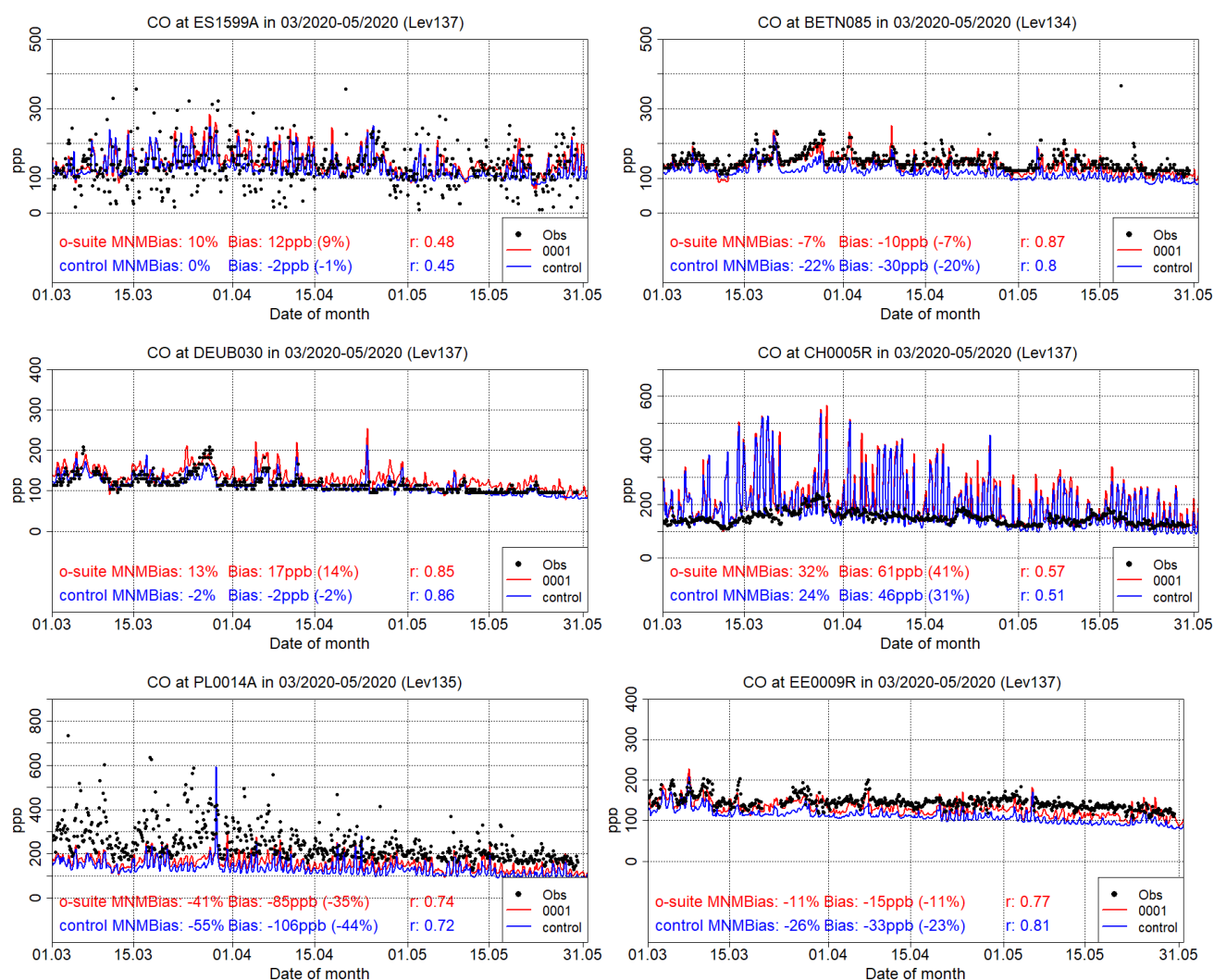


Figure 4.6.2: Time series for the o-suite (red) and control run (blue) compared to Airbase observations at Pagoeta, Spain station (43.25°N, 2.15°W, 1st row left), at Vielsalm, Belgium station (50.30°N, 6.02°E, 1st row right), at Neuglobsow, Germany (53.14°N, 14.02°E, 2nd row left), at Dübendorf, Swiss station (47.06°N, 8.46°W, 2nd row right), at Belsk, Poland station (51.84°N, 20.79°E 3rd row left), and at Lahemaa, Estonia (59.49°N, 25.93°E, 3rd row right)

observations are taken from the Airbase Network database at EEA (<http://acm.eionet.europa.eu/databases/airbase/>). The spatial distribution of bias and correlation coefficients of the o-suite over Europe are shown in Fig. 4.6.1. The results show that correlations over all CO European AirBase stations are highly significant ($0.5 < r < 0.9$). It is also evident that the CAMS NRT runs reproduce well the surface carbon monoxide mean concentrations over Spain, Belgium and Germany (depending on the station MNMBs vary from -10% to +10%), overestimate it over Switzerland (up to 40%) and underestimate it over Estonia (-10%), over Poland and the Czech Republic (down to -40%). These findings are further illustrated in time series at selected stations plotted in Figure 4.6.2. The control run surface carbon monoxide concentrations are 15-20 ppb (10%-15%) lower than the o-suite, resulting in a smaller bias over Spain, Switzerland and Germany, but a stronger negative bias over Poland, Estonia and the Czech Republic.



5. Tropospheric nitrogen dioxide

5.1 Evaluation against GOME-2 and TROPOMI retrievals

In this section, model columns of tropospheric NO₂ are compared to SCIAMACHY/Envisat NO₂ satellite retrievals (IUP-UB v0.7) [Richter et al., 2005] for model data before April 2012, and to GOME-2/MetOp-A NO₂ satellite retrievals (IUP-UB v1.0) [Richter et al., 2011] for simulations after April 2012. First comparisons (for model data from Jan 2019 onwards) to TROPOMI/Sentinel-5P data (IUP-UB v0.9, preliminary) and to GOME-2/MetOp-C (IUP v0.9, preliminary) are provided, using the CAMS o-suite as a-priori in these retrievals only. The satellite data provides excellent coverage in space and time and very good statistics. However, only integrated tropospheric columns are available, and the satellite data is always taken at the same local time, roughly 09:30 LT for the GOME-2 instruments, 10:00 LT for SCIAMACHY and 13:30 LT for TROPOMI and at clear sky only. Therefore, model data are vertically integrated, interpolated in time and then sampled to match the satellite data. The satellite data were gridded to model resolution (currently 0.4° x 0.4° degree). Model data were treated with the same reference sector subtraction approach as the satellite data for all SCIAMACHY/GOME-2A comparisons. For all comparisons to TROPOMI and GOME-2C satellite data, the stratospheric contribution has been removed from the measurements using STREAM-B which is a IUP-Bremen version of the STREAM algorithm by Beirle et al. (2016). In the current version of STREAM-B, the free tropospheric contribution is not yet well accounted for, which leads to a negative offset in the current preliminary TROPOMI and GOME-2C data versions and will be improved by addition of tropospheric background values in the near future. Uncertainties in NO₂ satellite retrievals are large and depend on the region and season. Winter values in mid and high latitudes are usually associated with larger error margins. Systematic uncertainties in regions with significant pollution are on the order of 20% – 30%.

Figure 5.1.1 shows global maps of GOME-2A and model monthly mean tropospheric NO₂ columns as well as differences between retrievals and simulations for April 2020 as an example for the last spring. The overall spatial distribution and magnitude of tropospheric NO₂ is well reproduced by both CAMS runs, indicating that emission patterns and NO_x photochemistry are reasonably well represented. Some differences are apparent between observations and simulations, with generally larger shipping signals simulated by the models. For example, shipping signals are much more pronounced in model simulations to the south of India. Emissions over Europe and especially the pollution hotspots around the Benelux countries are regularly underestimated, especially during winter. However, other local maxima of tropospheric NO₂ observed over anthropogenic emission hotspots in East Asia (e.g. over the heavily populated Sichuan Basin; 30°N, 105°E), India and others such as Teheran, Mecca and Moscow and over boreal forest fires (mainly during summer) are regularly overestimated. Likewise, values over the Persian Gulf and the Red Sea are regularly overestimated (mainly summer and autumn). A systematic overestimation over pollution hotspots is visible in the TROPOMI and GOME-2C based map comparisons (Figure 5.1.2).

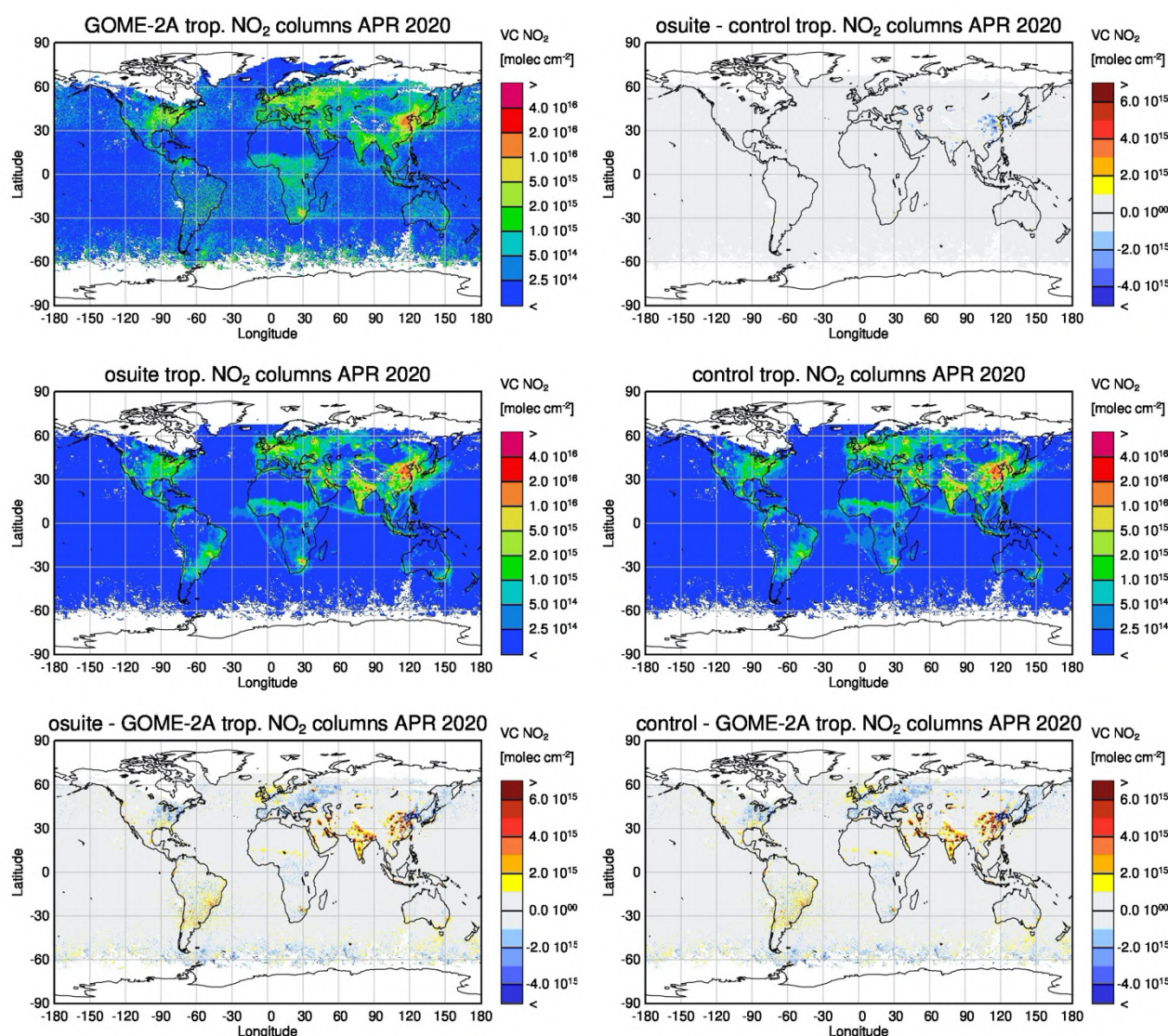


Figure 5.1.1: Global map comparisons of satellite retrieved and model simulated tropospheric NO₂ columns [molecules cm⁻²] for April 2020. The top row shows monthly mean tropospheric NO₂ columns retrieved from GOME-2A as well as the difference between o-suite and control, the second row shows the corresponding tropospheric NO₂ columns for model simulated averages. The third row shows differences of monthly means between models and GOME-2A. GOME-2A data were gridded to model resolution (i.e. 0.4° x 0.4° degree). Model data were treated using the same stratospheric correction method as for the satellite data.

The o-suite also strongly overestimates values over pollution hotspots compared to the TROPOMI operational offline retrieval product (van Geffen et al., 2020). The TROPOMI IUP Bremen data product shows lower values compared to the operational offline product, this is expected to be reduced with the next data version of the Bremen product (see data description above).. Differences in comparison results between the sensors are in principal due to differences in observation time and the retrieval products. Note that the standard IUP-UB GOME-2A retrievals use different a priori profiles, different Air Mass Factors (AMF) and different stratospheric correction method compared to the GOME-2C product.

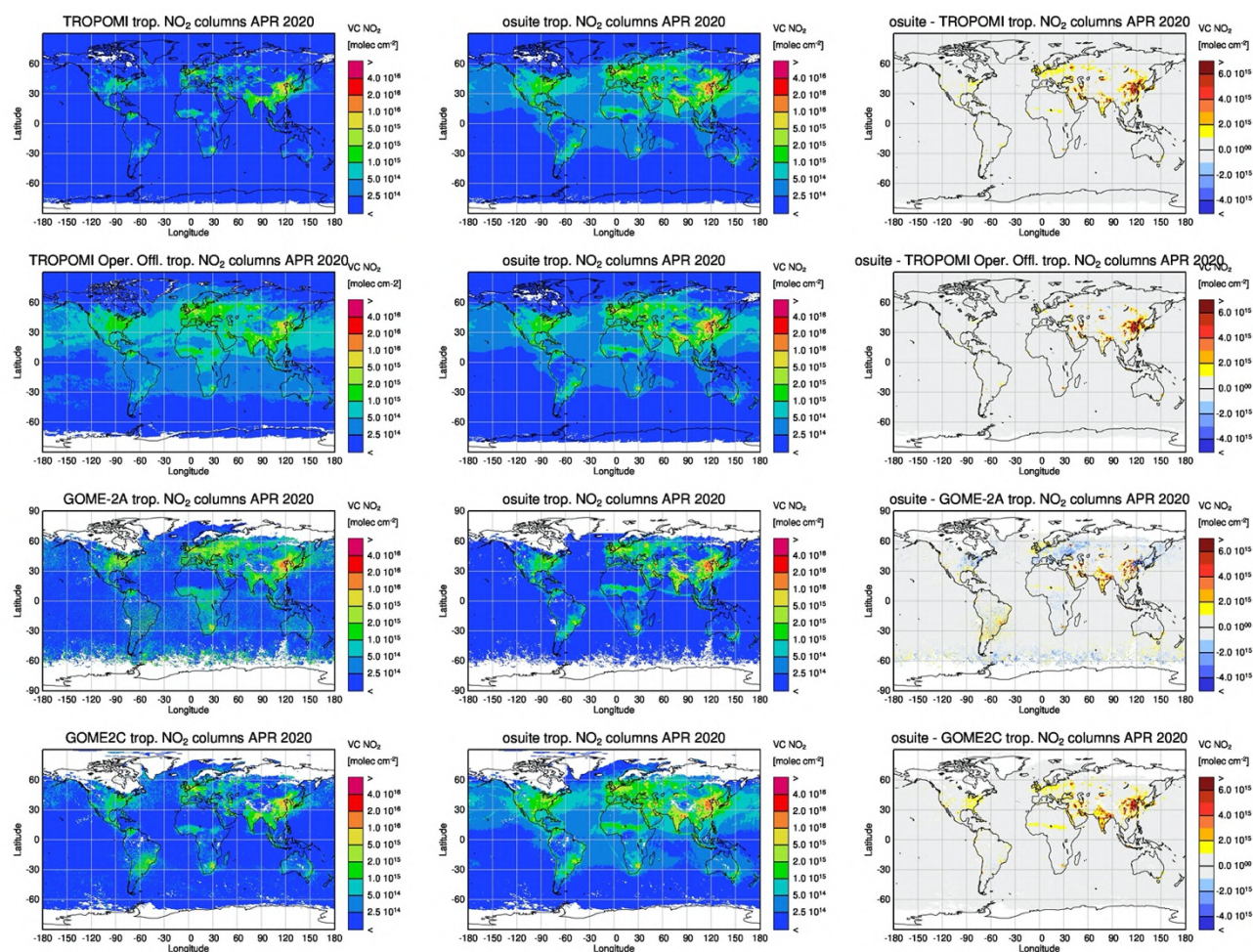


Figure 5.1.2: Global map comparisons of satellite retrieved and model simulated tropospheric NO₂ columns [molecules cm⁻²] for April 2020 based on (from top to bottom) TROPOMI, TROPOMI operational offline, GOME-2A and GOME-2C. The columns show (from left to right) satellite observations, o-suite simulations and the difference between o-suite and satellite observations. The satellite data were gridded to model resolution (i.e. 0.4° x 0.4° degree) and the CAMS o-suite was used as a-priori in the GOME-2C and TROPOMI IUP-Bremen retrievals only. Comparisons to the control are not available for this report.

Closer inspection of the seasonal variation of tropospheric NO₂ in some selected regions (Fig. 5.1.3) reveals significant differences between GOME-2A measurements and model results and points to some simulation problems. Over regions where anthropogenic emissions are major contributors to NO_x emissions, models correctly simulate the occurrence of maxima and minima in seasonality in time, but fail to reproduce the inter-annual variability observed by GOME-2A. Over East-Asia, absolute values and seasonality were strongly underestimated before 2014 by all model runs (most likely due to an underestimation of anthropogenic emissions) for all seasons apart from summertime minima, with the o-suite showing the best results since an upgrade in July 2012. As wintertime NO₂ column retrievals decreased significantly in 2014, model simulated wintertime maxima previously have been in better agreement with the satellite retrieved ones for recent years.



However, the observed NO₂ decrease was not reproduced by the simulations and therefore the better agreement for more recent years could not be attributed to model improvements. Moreover, summertime model minima increased in 2015 compared to previous years, which is in contrast to the satellite retrievals, so that the simulated values for the summers since 2015 are about 50% larger than satellite retrieved ones. For the first time in the time series, model results for the latest winter season (DJF 2019/2020) overestimate the peak in seasonality, with the control showing a significantly larger overestimation compared to the o-suite. Note that the overestimation occurs already for Dec 2019, in advance of the COVID-19 pandemic in China. The long-term development of model simulated tropospheric NO₂ columns over East-Asia points to inadequate scenarios of emission development.

As for East-Asia, a decrease in satellite retrieved values also occurred in 2015 over Europe where a peak is usually found around January, which was, as a result, only slightly underestimated by the models for January 2015. The underestimation of tropospheric NO₂ columns over Europe may be caused to some extent by a change of emission inventories in 2012. However, the situation changed for the three winter periods between 2015 and 2017, for which GOME-2A shows (compared to previous years) a strong increase in January peak values, combined with a decrease in values for December and February that is not reproduced by the models. It is not clear if the GOME-2A observations are realistic here, although an inspection of daily GOME-2A satellite images did not point to problems regarding the retrieval. The simulations show the same pattern as the retrievals however for winter 2018/2019 but strongly underestimate the retrievals again for the last winter (DJF 2019/2020).

Over regions where biomass burning is the major contributor to NO_x emissions, seasonality and amplitude of model columns are determined by fire emissions. The seasonality for the two regions in Africa was simulated reasonably well for 2010 and after October 2011. In the time period in between, a bug in reading fire emissions lead to simulation errors for all MOZART runs. Over North-Africa, the o-suite shows improved results since an update in July 2012 and the change to IFS-CB05 in September 2014. However, tropospheric NO₂ columns around December are still overestimated by the models. Summer to autumn NO₂ columns over North-Africa are underestimated compared to the satellite data from 2015 onwards and especially for 2019. The models (especially the o-suite) generally overestimate the seasonal cycle for South-Africa, particularly for 2014-2016 with an overestimation of the seasonal maximum, which usually occurs around August (e.g. by a factor of 1.4 larger compared to GOME-2A retrievals in 2016). However, August maxima are in better agreement since the upgrade of the o-suite in 2017, but minima during SH summer remain underestimated.

Time series comparisons between the o-suite and TROPOMI as well as GOME-2C are shown in Figure 5.1.4 for data since January 2019. They show differences with respect to the GOME-2A based ones: the o-suite is in general positively biased compared to the TROPOMI and GOME-2C retrievals, only over North- and South-Africa the o-suite shows smaller values than the TROPOMI operational offline product. As described above, differences in comparison results are in principal due to differences in observation time or differences in the retrieval products.

With respect to months affected by COVID-19 lockdown time periods, the o-suite generally fails to reproduce observed reductions in tropospheric NO₂ for large areas over China and South Asia, but performs better for Europe (see section 11.3).

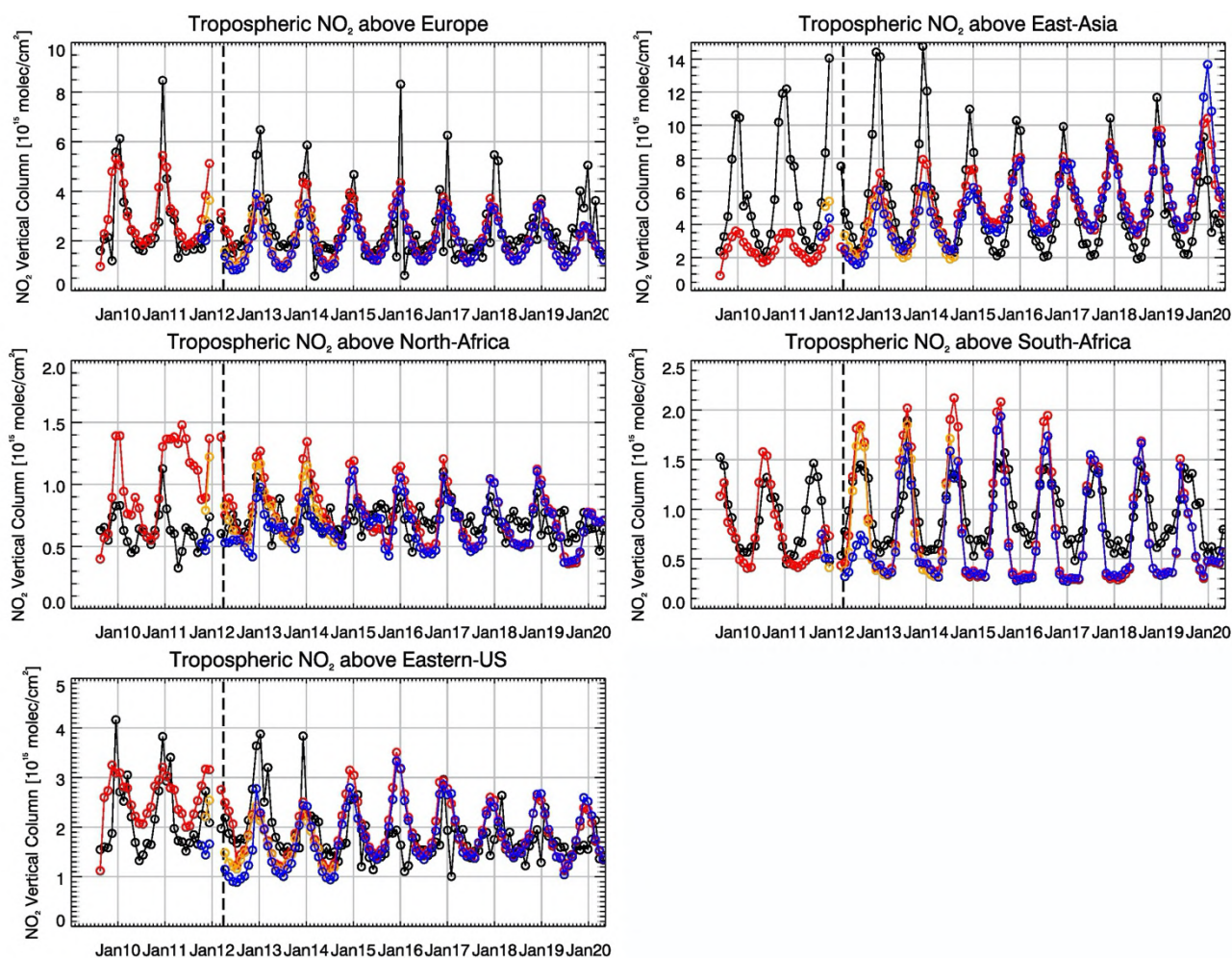


Figure 5.1.3: Time series of average tropospheric NO₂ columns [10¹⁵ molec cm⁻²] from SCIAMACHY (up to March 2012, black) and GOME-2A (from April 2012 onwards, black) compared to model results (red: o-suite; blue: MACC-TM5 forecast, MACC-CIFS forecast or control; orange: MACC-MOZART forecasts) for different regions (see Annex 2). The upper panels and lower panel represent regions dominated by anthropogenic emissions, and the panels for Africa represent those dominated by biomass burning. Vertical dashed black lines mark the change from SCIAMACHY to GOME-2A based comparisons in April 2012.

More NO₂ evaluation plots can be found on the CAMS website, see table 1.2.

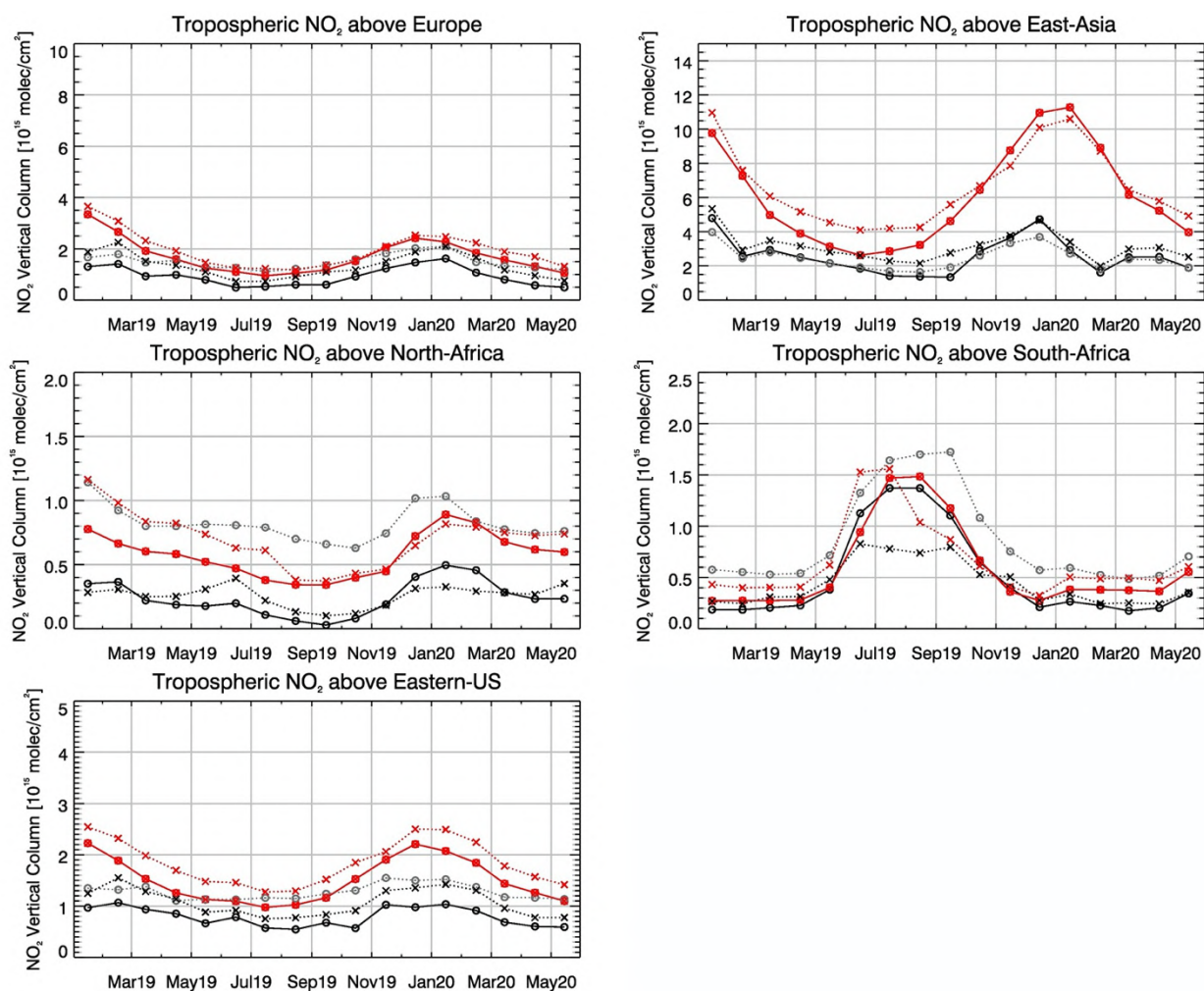


Figure 5.1.4: Time series of average tropospheric NO₂ columns [10^{15} molec cm⁻²] from (black and grey) satellite retrievals and (red) o-suite model results since Jan 2019 (see Annex 2 for definition of regions). The solid lines with circles show comparisons based on TROPOMI (in black the IUP-Bremen product and in grey the operational offline product), the dotted lines with crosses show comparisons for GOME-2C. The upper panels represent regions dominated by anthropogenic emissions, and the lower panels represent those dominated by biomass burning.

5.2 Evaluation against ground-based DOAS observations

In this section, we compare the NO₂ columns of the CAMS products with UVVIS DOAS profile measurements at Uccle and column data from the other stations.¹ This ground-based, remote-sensing instrument is sensitive to the NO₂ abundance in the lower troposphere, up to 1km altitude with an estimated uncertainty of 8%. Tropospheric NO₂ profiles and columns are validated (up to 3.5km or 10km). A description of the instruments and applied methodologies is the same for all DOAS OFFAXIS measurements, see <http://nors.aeronomie.be>. It is important to mention here that the model partial column values are calculated from the smoothed model profiles. This guarantees

¹ No contribution from Xianghe, Reunion and OHP due to instrument failure.

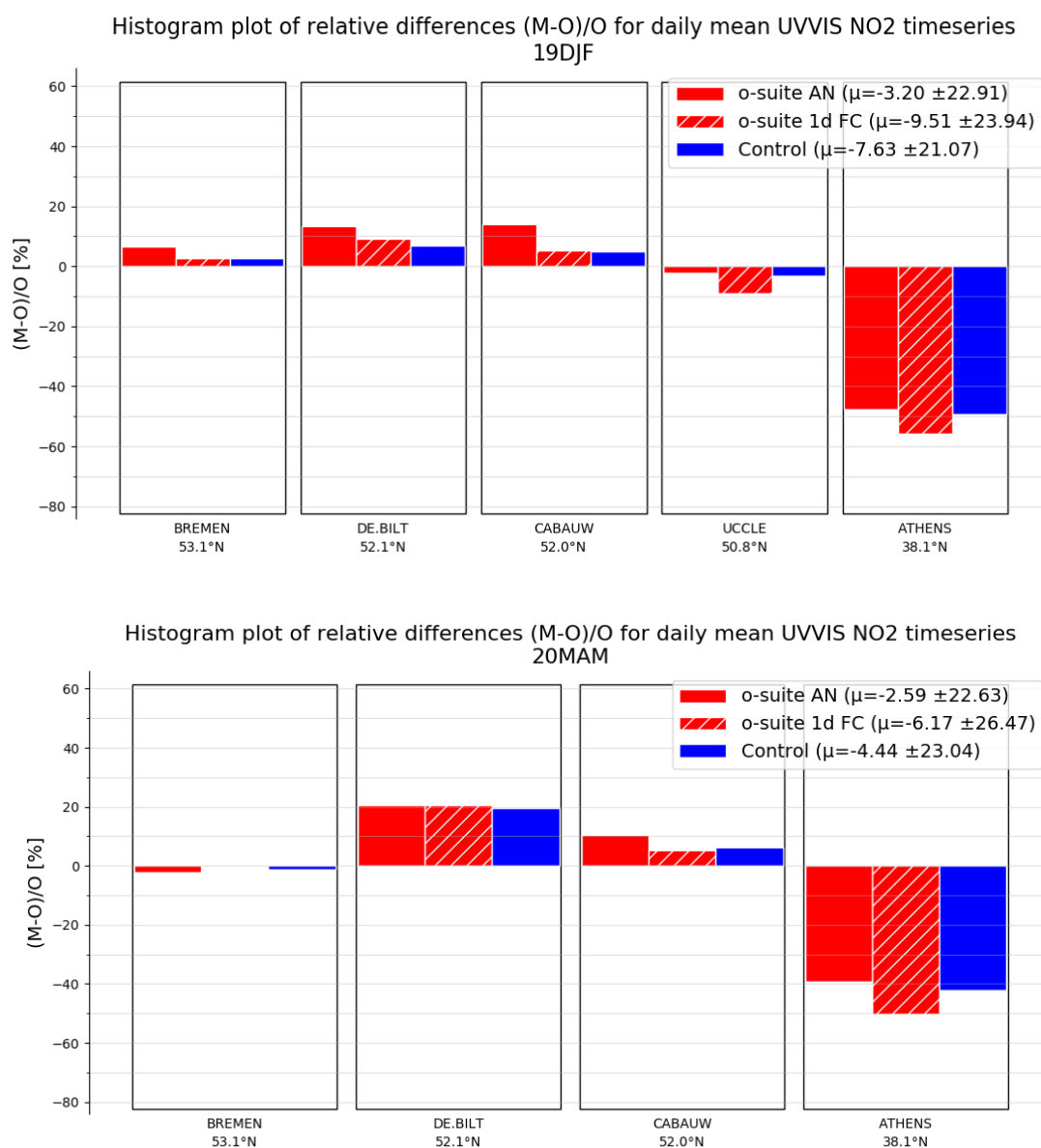


Figure 5.2.1: Table diagram showing the seasonal bias Dec-Feb 2020 (top) and March-May 2020 (bottom) for five stations, sorted by latitude. Compared to the previous validation period DJF, the relative biases in MAM did not change significantly.

that the model levels where the measurement is not sensitive do not contribute to the observed bias. We should mention that the measurement data is still catalogued as rapid delivery and not in the consolidated NDACC database.

Figure 5.2.1 shows the biases for the latest validation periods Dec-Feb 2020 and March-May 2020 at the different sites. The corresponding time series are shown in Fig. 5.2.2. At the urban sites at Uccle and Athens an underestimation is observed. For the other sites (Bremen, De Bilt and Cabauw) the o-suite is able to capture only few of the high pollution events.

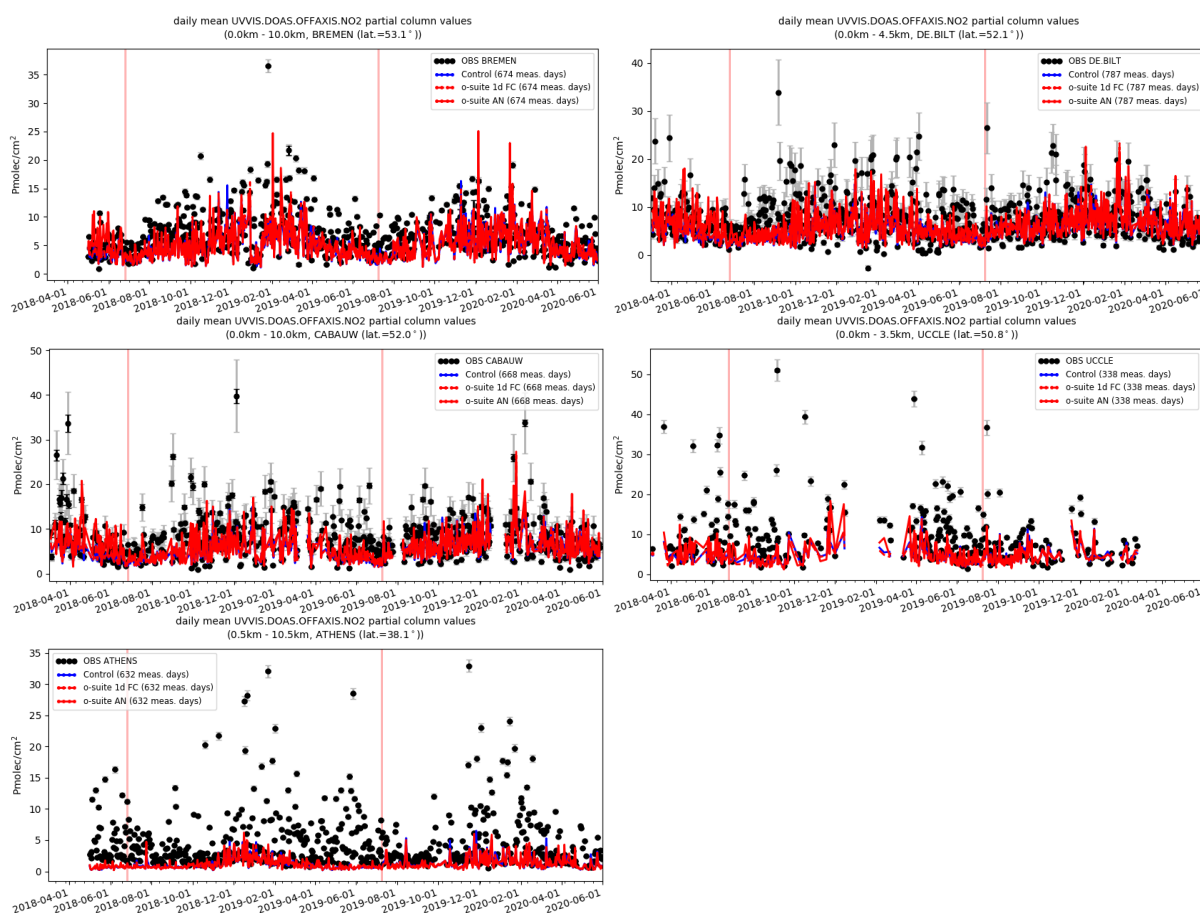


Figure 5.2.2: Time series of NO₂ partial columns at the five different sites. For all sites except Athens, background concentrations are well captured by the CAMS products. The o-suite and control runs show little difference.

with an estimated uncertainty of 8%. Tropospheric NO₂ profiles and columns are validated (up to 3.5km or 10km). A description of the instruments and applied methodologies is the same for all DOAS OFFAXIS measurements, see <http://nors.aeronomie.be>. It is important to mention here that the model partial column values are calculated from the smoothed model profiles. This guarantees that the model levels where the measurement is not sensitive do not contribute to the observed bias. We should mention that the measurement data is still catalogued as rapid delivery and not in the consolidated NDACC database.

Figure 5.2.1 shows the biases for the latest validation periods Dec-Feb 2020 and March-May 2020 at the different sites. The corresponding time series are shown in Fig. 5.2.2. At the urban sites at Uccle and Athens an underestimation is observed. For the other sites (Bremen, De Bilt and Cabauw) the o-suite is able to capture only few of the high pollution events.



6. Formaldehyde

6.1 Validation against satellite data

In this section, simulations of tropospheric formaldehyde are compared to SCIAMACHY/Envisat HCHO satellite retrievals (IUP-UB v1.0) [Wittrock et al., 2006] for model data before April 2012 and to GOME-2/MetOp-A HCHO data (IUP-UB v1.0) [Vrekoussis et al., 2010] afterwards. First comparisons to TROPOMI/Sentinel-5P data (IUP-UB v1.0) and to GOME-2/MetOp-B (IUP v0.9, preliminary) are provided, using the CAMS o-suite as a-priori in the TROPOMI retrievals. The HCHO retrievals are described in Alvarado et al. (2019). The satellite data (tropospheric columns only) is always taken at approximately the same local time, roughly 09:30 LT for the GOME-2 instruments, 10:00 LT for SCIAMACHY and 13:30 LT for TROPOMI and at clear sky only. The satellite data were gridded to model resolution (currently $0.4^\circ \times 0.4^\circ$ degree). As the retrieval is performed in the UV part of the spectrum where less light is available and the HCHO absorption signal is smaller than that of NO₂, the uncertainty of monthly mean HCHO columns is relatively large (20% – 40%) and both noise and systematic offsets have an influence on the results. However, absolute values and seasonality are retrieved more accurately over HCHO hotspots.

In Figure 6.1.1, monthly mean satellite HCHO columns from GOME-2A are compared to model results for April 2020 as an example for the last spring. The magnitude of oceanic and continental background values and the overall spatial distribution are well represented by the o-suite and control. The models regularly overestimate values over regions in Central Africa, which could be due to fire or biogenic emissions. This appears less pronounced for autumn 2019 compared to recent years. Moreover, HCHO columns over regions with fire and biogenic emissions in Northern Australia were regularly overestimated mainly during SON and DJF, but this appears much less pronounced since 2019. The comparison to TROPOMI based map comparisons (see Figure 6.1.2 for Apr 2020) shows a very good agreement for Apr 2020, while comparison to GOME-2B shows a positive bias over main emission regions of HCHO and over the ocean to the east of Greenland (GIN sea) and the north of Norway (Barents Sea) as well as over the ocean at a higher southern latitudes. Differences in comparison results between the sensors are in principal due to differences in observation time and the retrieval products. Note that the standard IUP-UB GOME-2A retrievals use different a priori profiles and different Air-Mass Factors (AMF) compared to the GOME-2B product.

Time series comparisons based on GOME-2A in Fig. 6.1.3 highlight three cases:

- East-Asia and the Eastern US, where HCHO is dominated by biogenic emissions. Model results and GOME-2A retrievals generally agree rather well. However, all model runs underestimate the yearly cycle over East-Asia since 2012. In contrast to MOZART runs, MACC_CIFS_TM5 overestimated satellite values for the Eastern US since the middle of 2013. However, the newer IFS-CB05 runs perform well for Eastern US since 2015. For recent years and both regions, there is virtually no difference between the most recent o-suite run with IFS-CB05 chemistry and the corresponding control run without data assimilation. The variability or “ups and downs” in HCHO columns observed by GOME-2A since December 2014 is due to the lack of data (caused by instrument degradation) for these regions during winter in the Northern Hemisphere, leading to e.g. the negative values in the GOME-2A time



series for Eastern US since December 2015. Summertime maxima are still underestimated over East-Asia despite of the higher resolution of the model runs since 2019.

- North-Africa, where biomass burning as well as biogenic sources largely contribute to HCHO and its precursors. GOME-2A satellite observations over North-Africa tend to be slightly overestimated by IFS-CB05 chemistry model runs since 2014 and also the latest higher resolution model versions since July 2016. However, GOME-2A values are higher, and model values a bit lower for summer 2019 compared to previous years, resulting in a pronounced underestimation with respect to the satellite observations. Moreover, the model simulated HCHO columns increase from summer 2019 to May 2020, though the satellite observed columns show seasonality (a decrease followed by an increase for this period). For spring 2020, models show a pronounced underestimation compared to GOME-2A, the satellite observed values are unusually high over North-Africa for last spring.
- Indonesia, where HCHO is also dominated by biogenic sources and biomass burning. Old MOZART based model versions generally overestimated satellite values here (by a factor of 3 – 4 in the second half of 2010) and failed to reproduce the observed seasonality. This may be due to the use of fire emissions including El Nino years, which experience much larger fire activities. MOZART simulations and observations agreed much better since late 2012. IFS-CB05 runs agree very well with satellite retrieved ones for December 2014 to August 2015. For September and October 2015, satellite retrieved HCHO columns show a pronounced maximum. 2015 was a strong El Nino year, which caused droughts and higher fire activity in Indonesia. Another pronounced, but by the models overestimated, increase in satellite observed values associated with comparatively weaker El Nino conditions occurs for Sep 2019. As for previous El Nino years, fire emissions used by IFS-CB05 seem to be largely overestimated, resulting in model-simulated HCHO columns, which are up to twice as large as those retrieved by GOME-2A. Further investigations (see previous reports) show that this is not caused by cloud flagging applied to the satellite and model data. Between the middle of 2016 and Sep 2019 there was mainly little variation from one month to another in both, satellite observations and model simulations and the magnitude of model and satellite values agreed overall well.

Time series comparisons between the o-suite and TROPOMI as well as GOME-2B are shown in Figure 6.1.4 for data since Jan 2019. They show differences with respect to the GOME-2A based ones: the peak over Indonesia for Sep 2019 is much less pronounced for both the o-suite and satellite observations, for North-Africa the development of values in time for Jan 2019 to May 2020 is in agreement and there is no pronounced underestimation for last spring, for East-Asia the seasonality is in good agreement between the satellite sensors and the o-suite. Apart from GOME-2B for North-Africa and Indonesia, differences between the satellite sensors and the o-suite are generally less pronounced. Differences in comparison results are in principal due to differences in observation time or differences in the retrieval products.

For details on the HCHO evaluation: http://www.doas-bremen.de/macc/macc_veri_iup_home.html

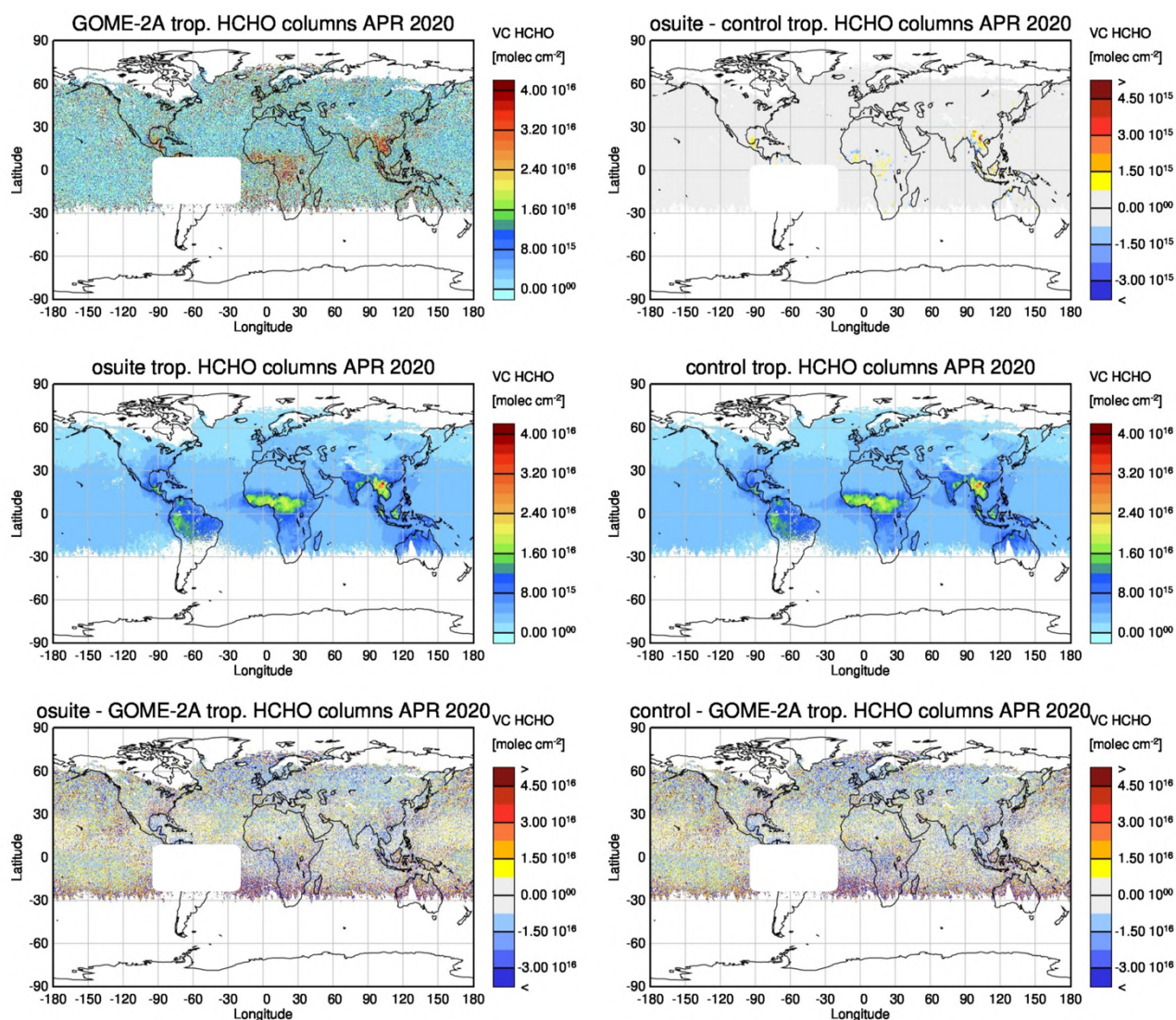


Figure 6.1.1: Global map comparisons of satellite-retrieved and model-simulated tropospheric HCHO columns [molec cm⁻²] for Apr 2020. The top row shows monthly mean tropospheric HCHO columns retrieved by GOME-2A, the second row shows the same but for model simulated averages. The third row shows differences of monthly means between models and GOME-2A. GOME-2A data were gridded to model resolution (i.e. 0.4° deg x 0.4° deg). Satellite retrieved values in the region of the South Atlantic anomaly are not valid and therefore masked out (white boxes in all images except those which show model results only).

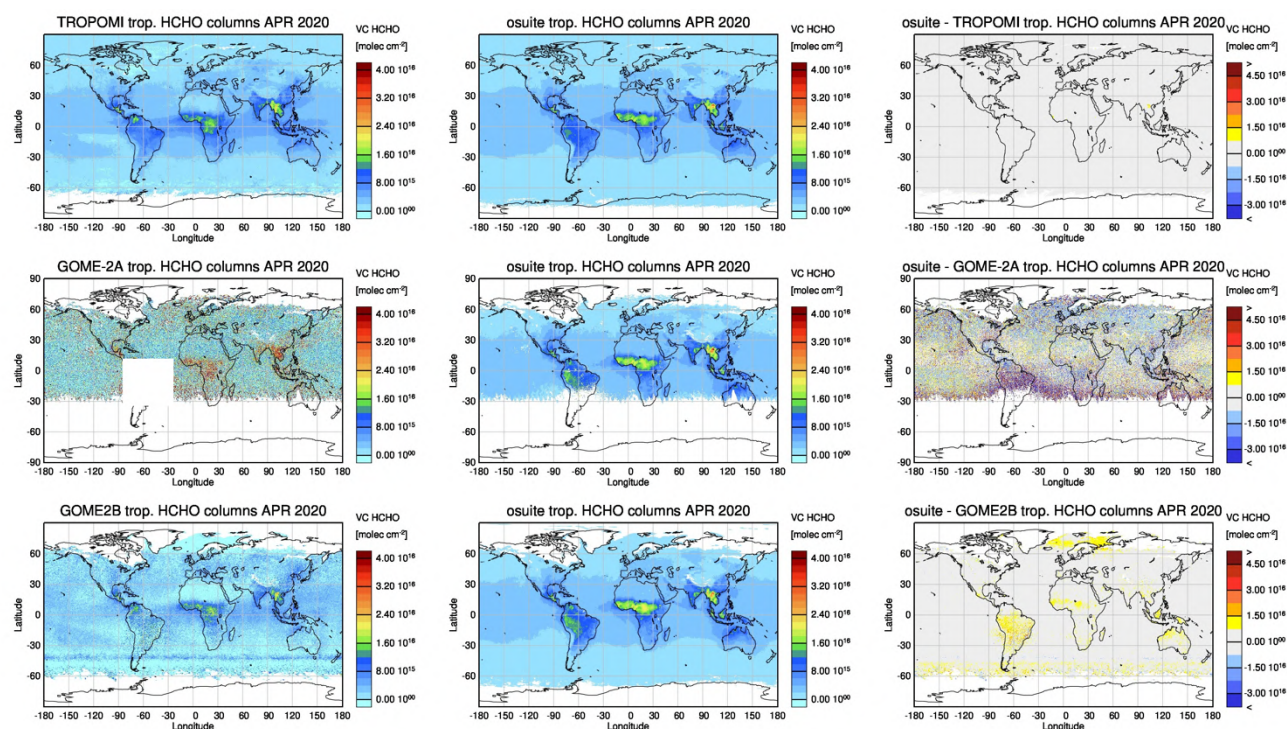


Figure 6.1.2: Global map comparisons of satellite retrieved, and model simulated tropospheric HCHO columns [molec cm⁻²] for Apr 2020 based on (from top to bottom) TROPOMI, TROPOMI operational offline, GOME-2A and GOME-2C. The columns show (from left to right) satellite observations, o-suite simulations and the difference between o-suite and satellite observations. The satellite data were gridded to model resolution (i.e. 0.4° x 0.4° degree) and the CAMS o-suite was used as a-priori in the TROPOMI IUP-Bremen retrievals only and not in the TROPOMI operational offline product.. Comparisons to the control are not available for this report.

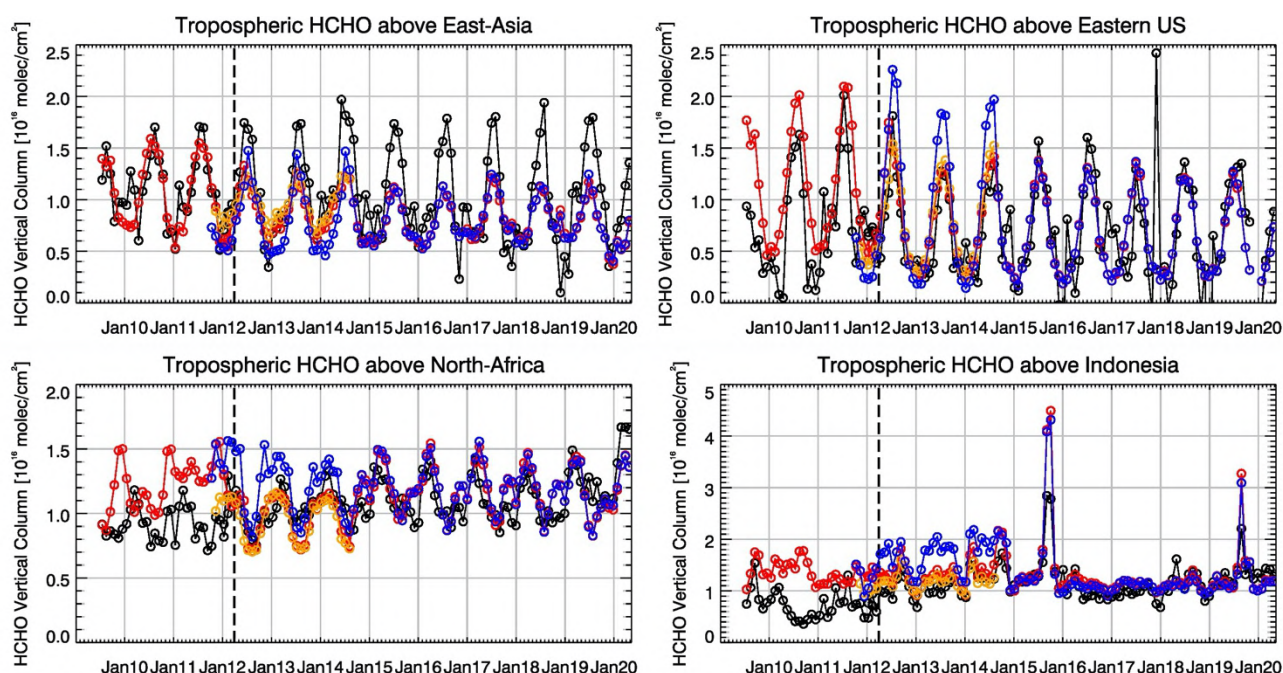


Figure 6.1.3: Time series of average tropospheric HCHO columns [10^{16} molec cm⁻²] from SCIAMACHY (up to March 2012, black) and GOME-2 (from April 2012 onwards, black) compared to model results (red – o-suite, blue - MACC_fnrt_TM5/MACC_CIFS_TM5/control, orange - MACC_fnrt_MOZ) for different regions. The blue line shows MACC_fnrt_TM5 from November 2011 to November 2012, MACC_CIFS_TM5 results from December 2012 to August 2014 and control results from September 2014 onwards (the model run without data assimilation is termed control since Sep 2014). The regions differ from those used for NO₂ to better focus on HCHO hotspots: East-Asia (25–40°N, 110–125°E), Eastern US (30–40°N, 75–90°W), Northern Africa (0–15°N, 15°W–25°E) and Indonesia (5°S–5°N, 100–120°E). Negative satellite retrieved values over Eastern US are due to a lack of data (caused by instrument degradation) during Northern Hemisphere winter months for this region. Vertical dashed black lines mark the change from SCIAMACHY to GOME-2A based comparisons in April 2012.

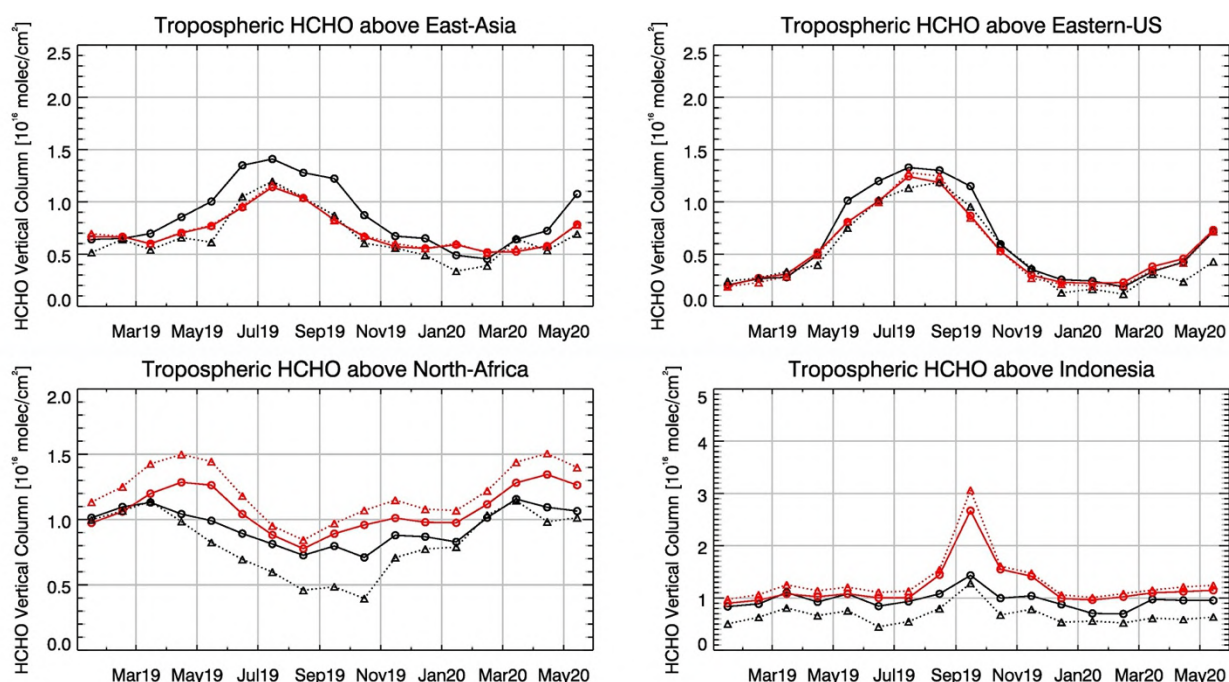


Figure 6.1.4: Time series of average tropospheric HCHO columns [10^{16} molec cm^{-2}] from (black and grey) satellite retrievals and (red) o-suite model results since Jan 2019. The solid lines with circles show comparisons based on TROPOMI the dotted lines with triangles show comparisons for GOME-2B. The regions differ from those used for NO_2 to better focus on HCHO hotspots: East-Asia ($25\text{--}40^\circ\text{N}$, $110\text{--}125^\circ\text{E}$), Eastern US ($30\text{--}40^\circ\text{N}$, $75\text{--}90^\circ\text{W}$), Northern Africa ($0\text{--}15^\circ\text{N}$, $15^\circ\text{W}\text{--}25^\circ\text{E}$) and Indonesia ($5^\circ\text{S}\text{--}5^\circ\text{N}$, $100\text{--}120^\circ\text{E}$).

6.2 Evaluation against ground-based DOAS observations

In this section, we compare the HCHO columns of the CAMS products with UVVIS DOAS measurements at Uccle, Cabauw and De Bilt.² These ground-based, remote-sensing instruments are sensitive to the HCHO abundance in the lower troposphere. Tropospheric HCHO profiles and columns are validated (up to 3.5km (Uccle) or 10km (Cabauw and De Bilt)). The validation methodology is the same as for the MWR O_3 and FTIR O_3 and CO validations see <http://nors.aeronomie.be>. It is important to mention here that the model partial column values are calculated for the smoothed model profiles. This guarantees that the model levels where the measurement is not sensitive do not contribute to the observed bias. We should mention that the measurement data is catalogued as rapid delivery and not in the consolidated NDACC database.

Figure 6.2.1 shows the absolute biases March – May 2020 at the different sites and indicates strongly reduced biases for the different sites. At all three sites high pollution events are not captured by the model and leads to a higher overall underestimation (Fig 6.2.2). From Fig. 6.2.1 and 6.2.2 we see little difference between the o-suite and the control run. Although the background column values are well captured by the products, the high emission events are not. Although a longer time series is required to analyze a seasonal dependence in the bias, at Cabauw and De Bilt, a seasonal dependence may be observed with an underestimation during summer and overestimation during winter months.

² No contribution from Reunion, Xianghe, Uccle and OHP due to instrument failure.

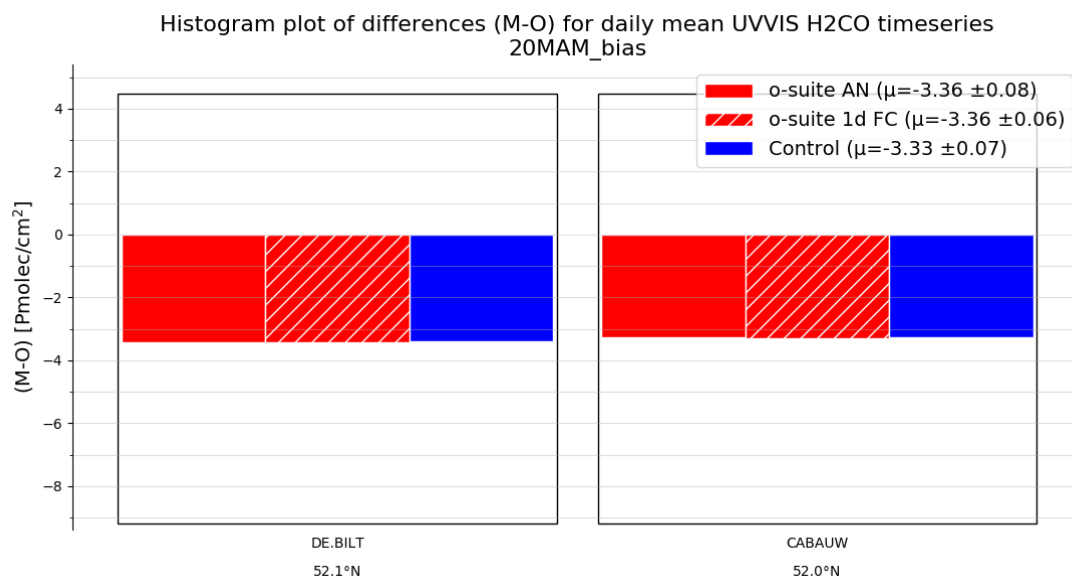


Figure 6.2.1: Table diagram showing the seasonal absolute bias in MAM-2020 for two stations, sorted by latitude

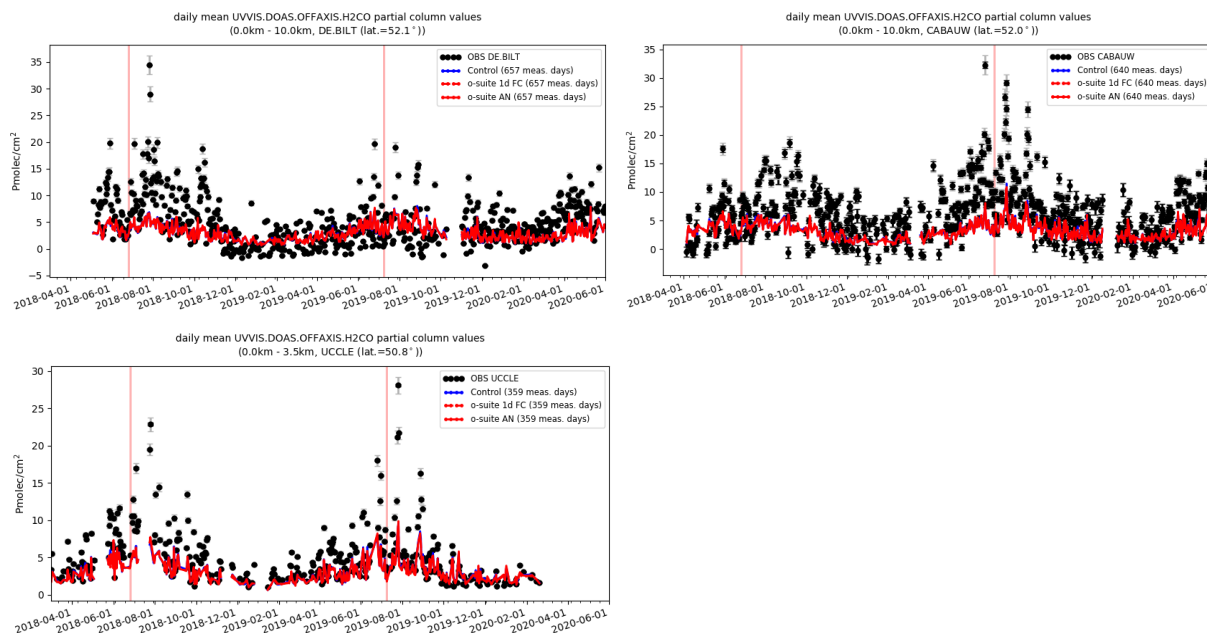


Figure 6.2.2: Time series of HCHO partial columns at the three different sites. All CAMS products underestimate the high peak HCHO concentrations. At Cabauw and De Bilt a seasonal dependence in the bias can be seen. At De Bilt the model overestimates during the winter months and at Cabauw the summer concentrations are underestimated.



7. Water vapour

During MAM 2020, water vapour has been sampled not only by the two Lufthansa but also by the Hawaiian Airlines aircraft (see Fig. 3.2.1 in IAGOS ozone section). The availability of water vapour data at Frankfurt is similar to that of CO (see IAGOS ozone and CO sections), with observations for each of the three months but with gaps. The results from the o-suite and control run are mostly similar (Fig. 7.1, Fig. 7.2) and the variability of water vapour during MAM 2020 is well represented by the models in all layers. The two runs agree well with the observations in the lowest layers with an MNMB smaller than 10% in absolute value (Fig. 7.3) and a correlation coefficient higher than 90% (Fig. 7.3). Some differences between the two runs are found in the upper layers as the control run presents slightly smaller biases in the upper troposphere and the correlation coefficient is higher for the o-suite at all levels especially in the mid-troposphere.

The agreement is worse in the upper layers, with larger biases and smaller correlation (Fig. 7.2 and Fig. 7.3). In the free troposphere, both large underestimations and overestimations are found (Fig. 7.2), and the correlation remains between 80% and 90% up to 8000 m (Fig. 7.3). In the UTLS, the bias of the models is mostly negative as shown on the time series (Fig. 7.2), with an MNMB of -40% (Fig. 7.3). However, sometimes large overestimations also occur in the UTLS, as it was the case in the free troposphere but less frequently. Note that the tropopause level may sometimes be inaccurate: the tropopause is determined from the IAGOS temperature profile, a procedure which sometimes fails, in which case a reference pressure level is used based on an international standard atmosphere.

Several examples of individual profiles at Frankfurt are shown on Fig. 7.4.a-b, which illustrate the aforementioned results. In the timeseries (Fig. 7.2), two peaks of water vapour are found during the months of May. These increase are correlated with high ozone values observed on the same days (see IAGOS ozone section). For these episodes, the models slightly underestimate water vapour values in the lowest layers. Related individual profiles for 10 and 22 May are also presented in Fig. 7.4.b.

As shown in some of these profiles, the models often fail to reproduce complex profile shapes (maxima/minima) in the free-troposphere. Individual profiles from other regions of the world are also presented in Fig. 7.5-10 for respectively: the Middle East, West and East Africa, South Africa, East Asia, North America and Central America. For all these regions the models present results similar to those observed over Europe at Frankfurt with the exception of the Pacific Region. Over the Pacific region, timeseries of water vapour are available almost for the whole month of March at the airport of Honolulu. The two runs behave very similarly and the bias is mostly negative in all layers and larger than at the European airport of Frankfurt (Fig. 7.11 and 7.12), with the larger values in the mid-troposphere of -70% against -30% in the low and upper troposphere. The correlation coefficient is small close to the surface (20%) but reaches a maximum of 80% between 1000 and 4000 m while it drops again above. Some individual profiles at Honolulu during the MAM 2020 period are also shown in Fig. 7.13.

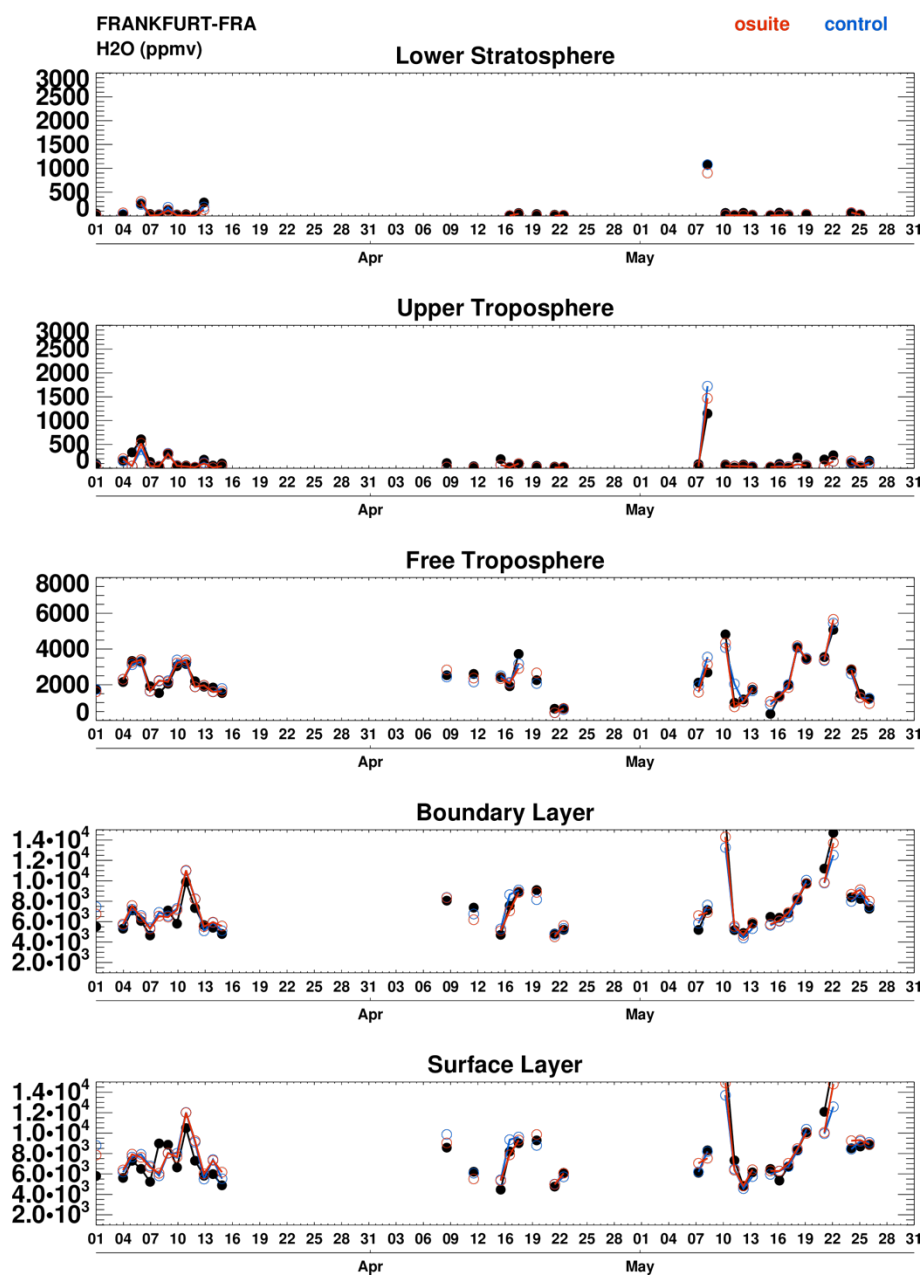


Figure 7.1: Time series of daily mean water vapour over Frankfurt during MAM 2020 for 5 layers: Surface Layer, Boundary Layer, Free Troposphere, Upper Troposphere and Lower Stratosphere. IAGOS is shown in black, the o-suite in red and associated control run in blue. Units: ppmv.

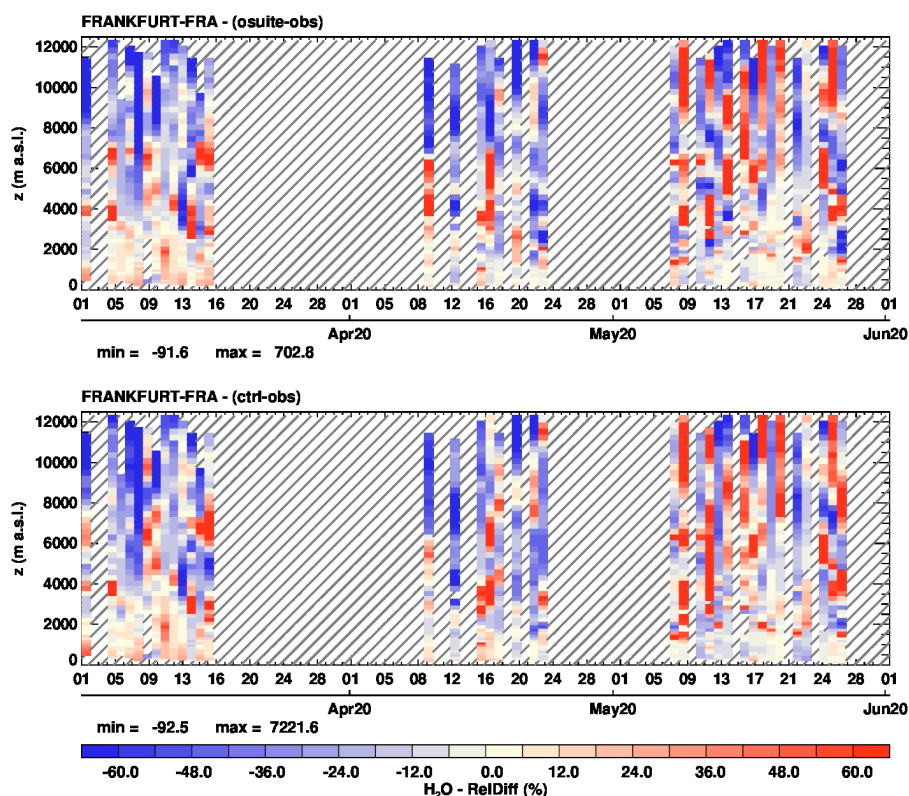


Figure 7.2: Time series of the relative differences ($[\text{model} - \text{observations}]/\text{observations}$) in daily profiles for water vapour over Frankfurt during MAM 2020. The top panel corresponds to o-suite the bottom panel to control run. Units: %.

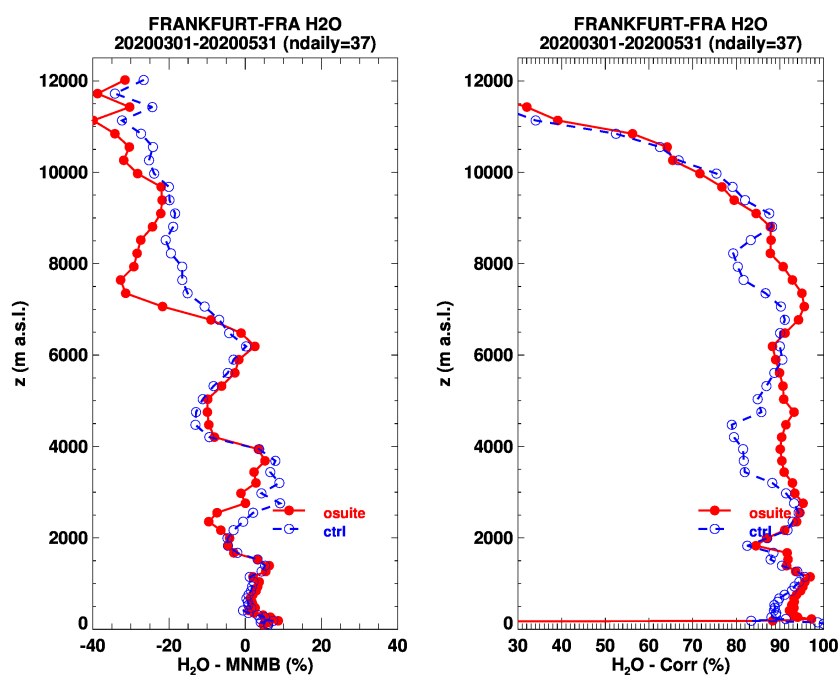


Figure 7.3: Model scores (MNMB and Correlation coefficient) for water vapour at Frankfurt calculated over the period MAM 2020. The left panel corresponds to MNMB and the right panel to Correlation coefficient. The o-suite is shown in red and associated control run in blue. Units: %.

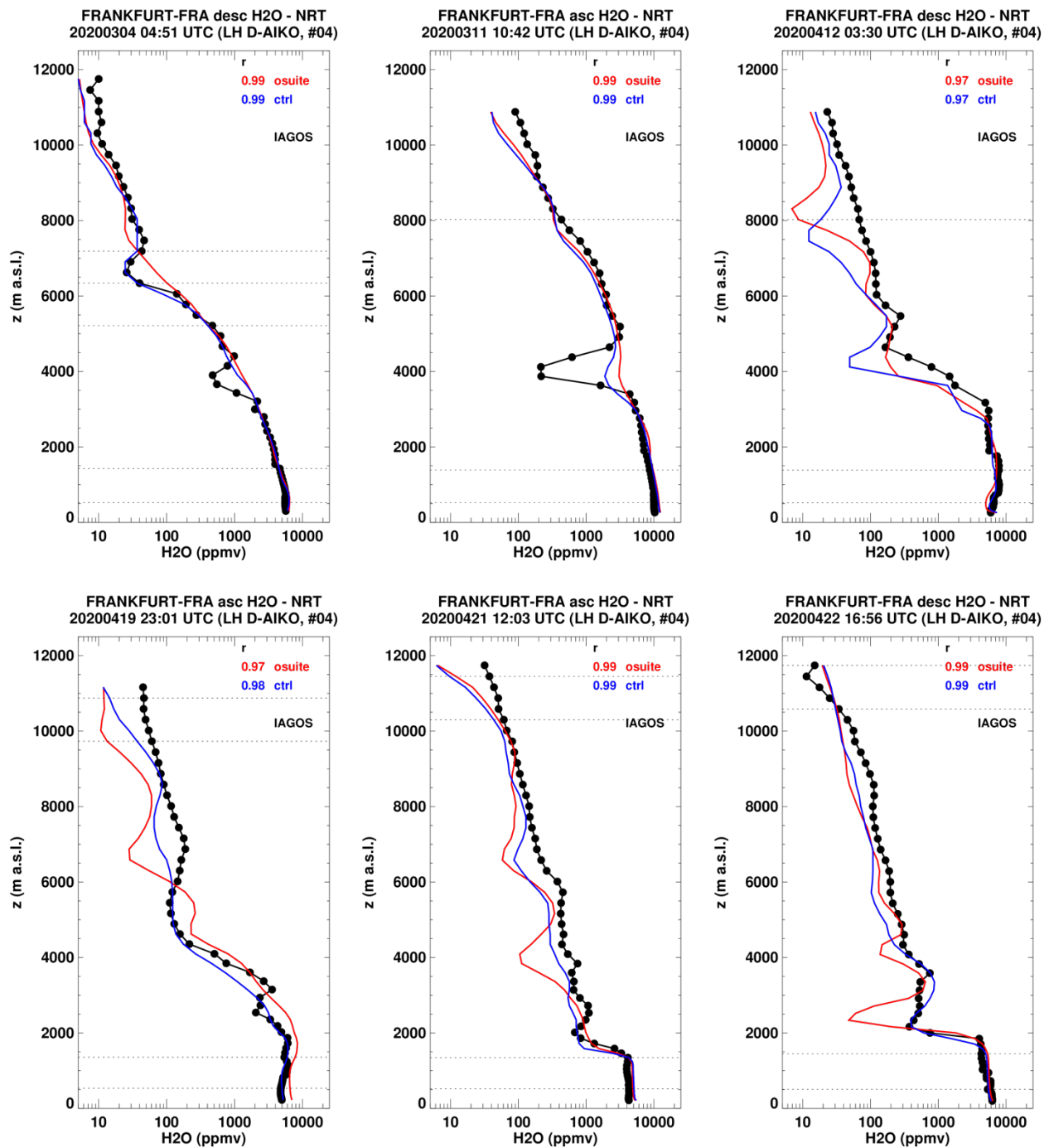


Figure 7.4.a: Selection of individual profiles for water vapour from IAGOS (black) and the two NRT runs (o-suite: red, control: blue) over Frankfurt during MAM 2020. Units: ppmv.

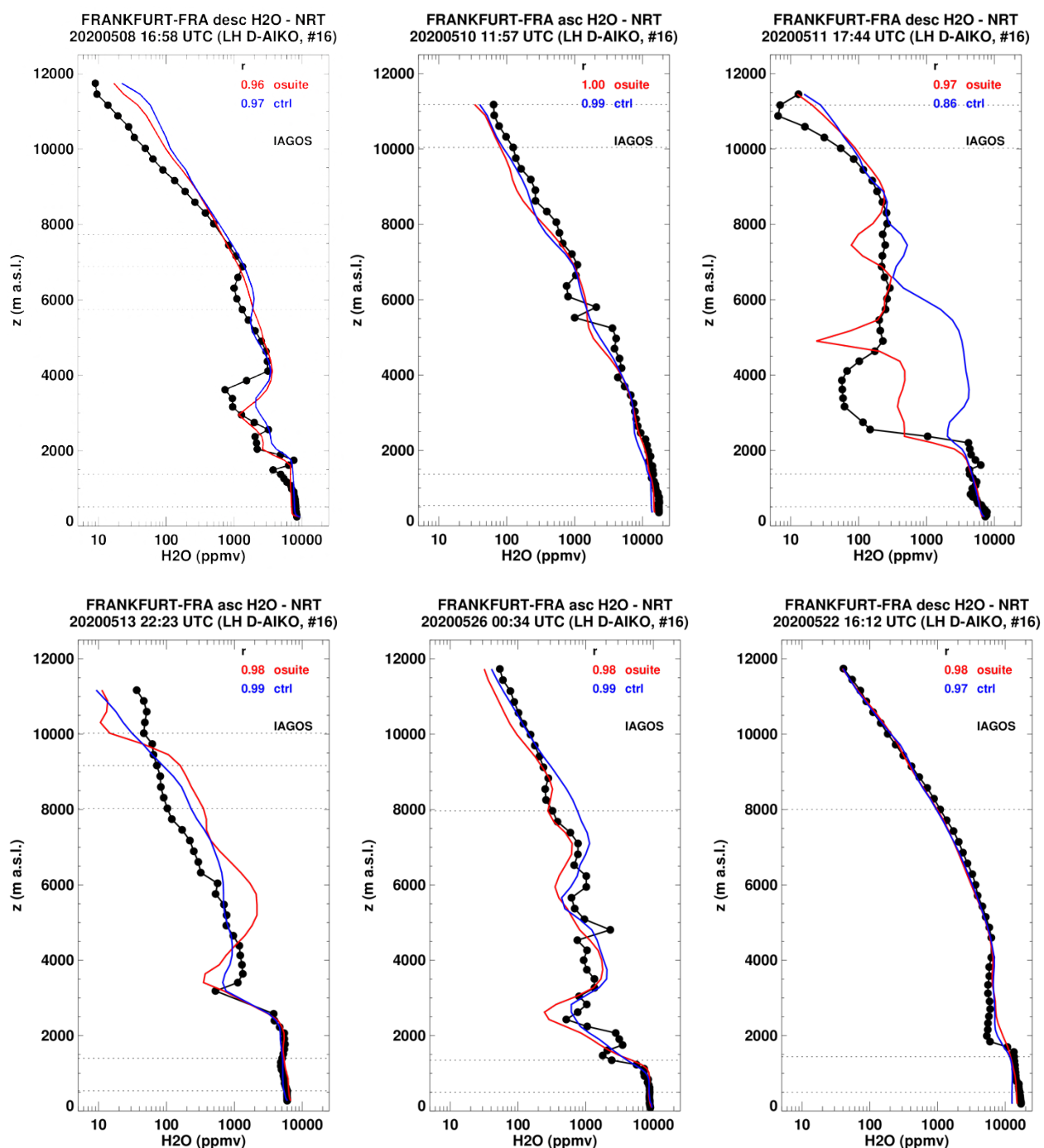


Figure 7.4.b: Selection of individual profiles for water vapour from IAGOS (black) and the two NRT runs (o-suite: red, control: blue) over Frankfurt during MAM 2020. Units: ppmv.

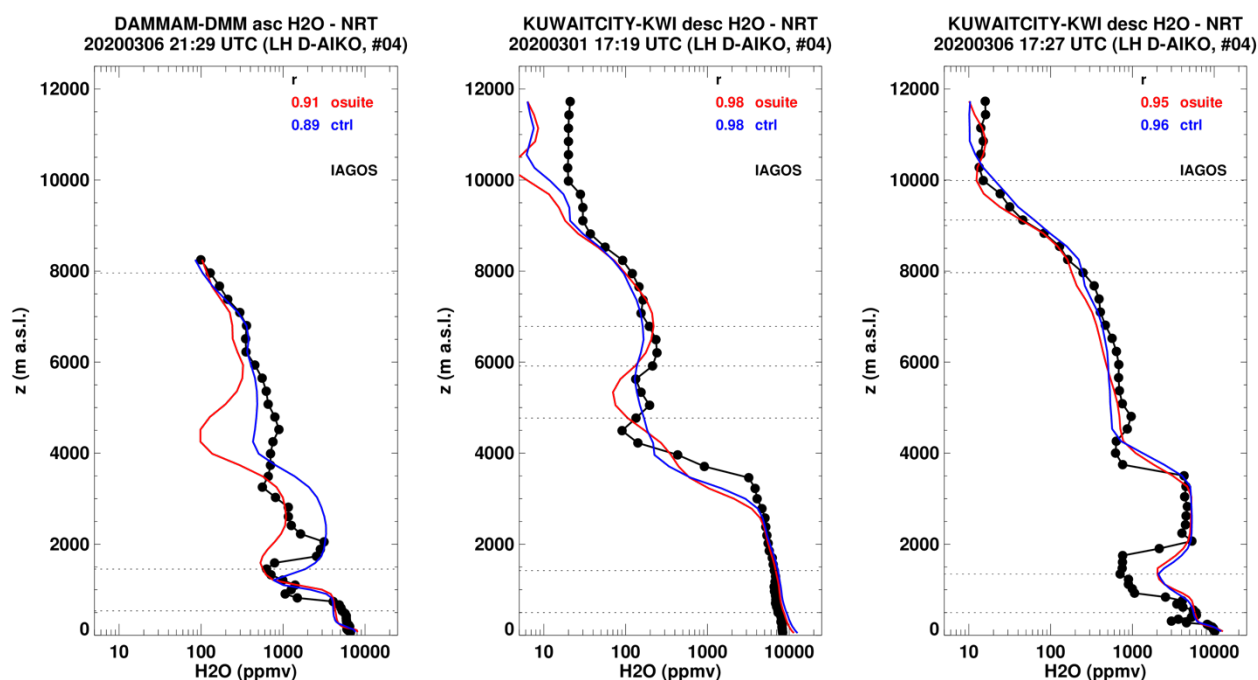


Figure 7.5: Selection of individual profiles for water vapour from IAGOS (black) and the two NRT runs (osuite: red, control: blue) over the Middle East during MAM 2020. Units: ppmv.

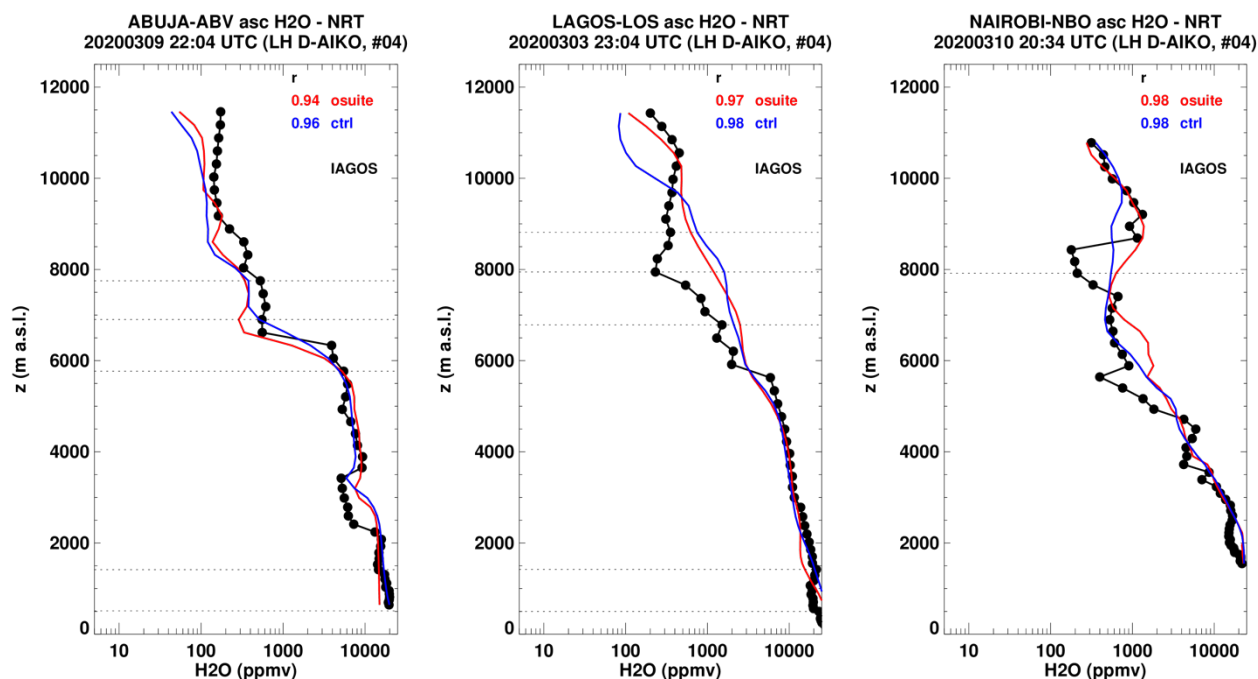


Figure 7.6: Selection of individual profiles for water vapour from IAGOS (black) and the two NRT runs (osuite: red, control: blue) over the West and East Africa during MAM 2020. Units: ppmv.

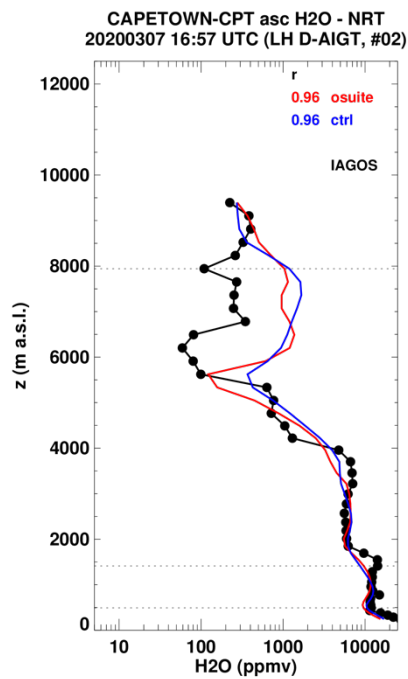


Figure 7.7: Selection of individual profiles for water vapour from IAGOS (black) and the two NRT runs (o-suite: red, control: blue) over the South Africa during MAM 2020. Units: ppmv.

8. Aerosol

8.1 Global comparisons with Aeronet and EMEP

The comparison of the CAMS simulation of time series of aerosol optical depth can be found for all Aeronet stations at: <http://aerocom.met.no/cams-aerocom-evaluation/>

More detailed evaluation including scores, maps, scatterplots, bias maps and histograms illustrating the performance of the aerosol simulation in the IFS system are made available through the [AeroCom web interface](#). The model run can be compared here to e.g. the CAMS interim reanalysis and other models, such as the AeroCom Median model.

Correlation, based on daily aerosol optical depth and NRT Aeronet observations, has been rather stable recently. The o-suite forecast at +3 days shows only slightly lower correlation. See figure S3.

Part of the month-to-month variation in correlation is due to the varying quality and coverage of the Aeronet network. This has been improved by the version 3 from Aeronet. We use therefore version 3 level 1.5 for all global comparison to Aeronet.

The performance of the o-suite model exhibits some seasonal variation in AOD depending on region (Fig. 8.1.1). Noteworthy is the persistent AOD overestimation over North America (Fig. 8.1.1-bottom), but also a long-term trend to overestimation in East Asia. The latitudinal display of model and Aeronet AOD in the period investigated here (Fig. 8.1.2) shows a small positive bias against Aeronet in the Southern Hemisphere.

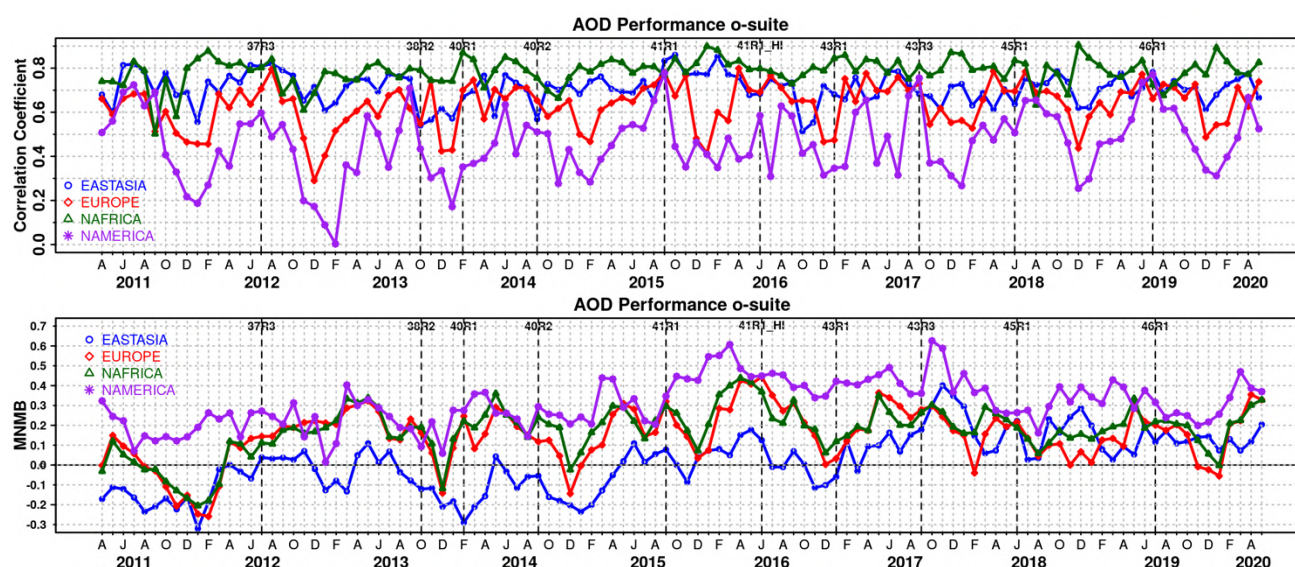


Figure 8.1.1. (top) Correlation coefficient and (bottom) modified normalized mean bias (MNMB) in AOD, since 2011, based on daily AOD comparison (Aeronet V3 level 1.5 data) in four world regions [East-Asia (blue); Europe (red); North Africa (green); North America (purple)] for the o-suite.

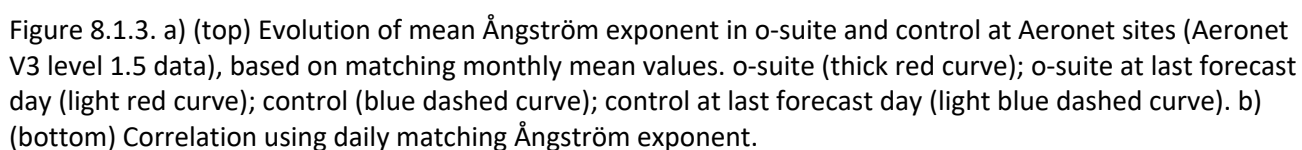
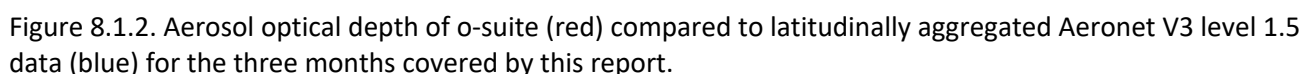


Table 8.1.1. Mean global total and speciated AOD in the o-suite for the last two periods covered by the VAL report and change after 3 forecast days.

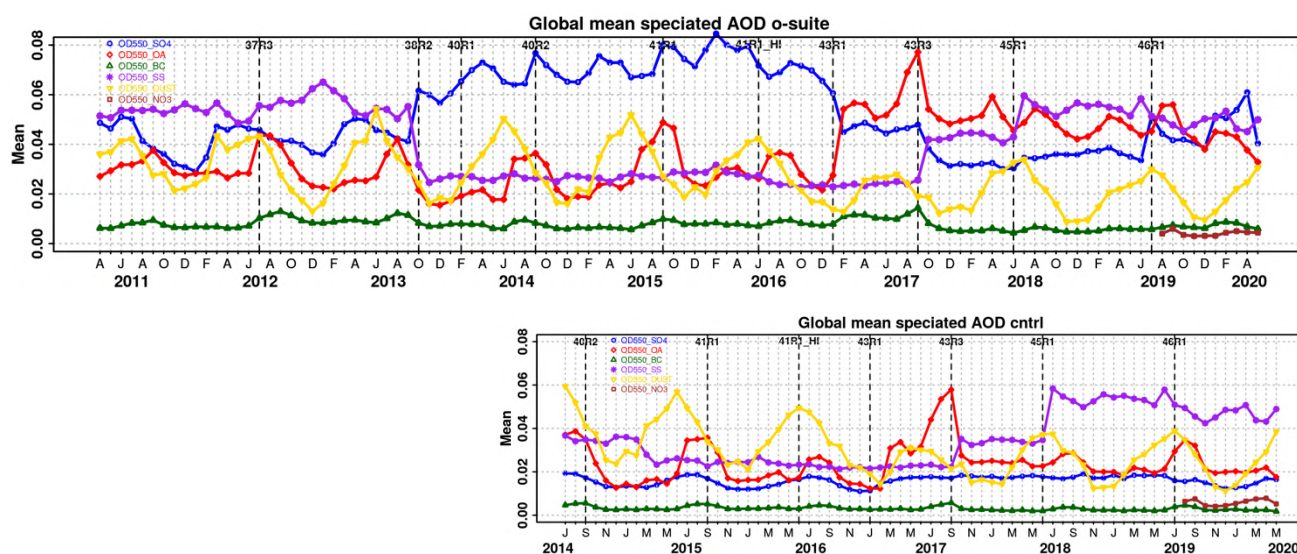


Figure 8.1.4. Evolution of the aerosol components of total AOD@550nm [OD550_SO4 = sulphate(blue); OD550_OA = organics(red); OD550_BC = black carbon(green); OD550_SS = sea salt(purple); OD550_DUST = dust(yellow); OD550_NO3 = nitrate(brown)] in o-suite and control simulation.

The simulated aerosol size distribution may be validated to first order using the wavelength-dependent variation in AOD, computed as Ångström exponent, with higher Ångström exponents indicative of smaller particles. We find in MAM 2020 a small bias (Figure 8.1.3-a). Temporal and spatial variability is difficult to capture, but correlation from all daily data is lower than for AOD (Figure 8.1.3-b and S3). Figure 8.1.4 shows that the Sep 2017 and Jun 2018 model changes are responsible for a shift in Ångström exponent. More organic matter seems to shift the size distribution to smaller sizes. The model upgrade in Feb 2017 with a bugfix for sea salt and improved parameterisations for SO4 lead to that sea salt increased with 45% while sulphate further decreased a bit. Sea salt has increased further due to a new sea salt emission scheme implemented in the Jun 2018 model upgrade and is back to earlier 2011-2013 levels. Since the latest model upgrade with the improvement to the sulphur cycle, the SO4 seem to have increased to same levels as before the Sep 2017 upgrade.

The o-suite uses data assimilation to obtain an analysis of the aerosol field. In the forecast period, however, a-priori model parameterisations and emissions (except fire emissions, which are kept in the forecast equal to the latest GFAS emission values) determine increasingly the aerosol fields. The performance of the day three forecasted AOD fields as compared to the first guess is shown in Figure S3 in the summary of this report. Table 8.1.1 shows an average global decrease in total aerosol optical depth during the first four forecast days, dominated by sulphate and organics. The control run with no assimilation shows somewhat less AOD (-39% compared to o-suite, see figure S3). All this supports the conclusion that either a-priori IFS aerosol and aerosol precursor sources are too small, or sinks are too effective in the IFS model.

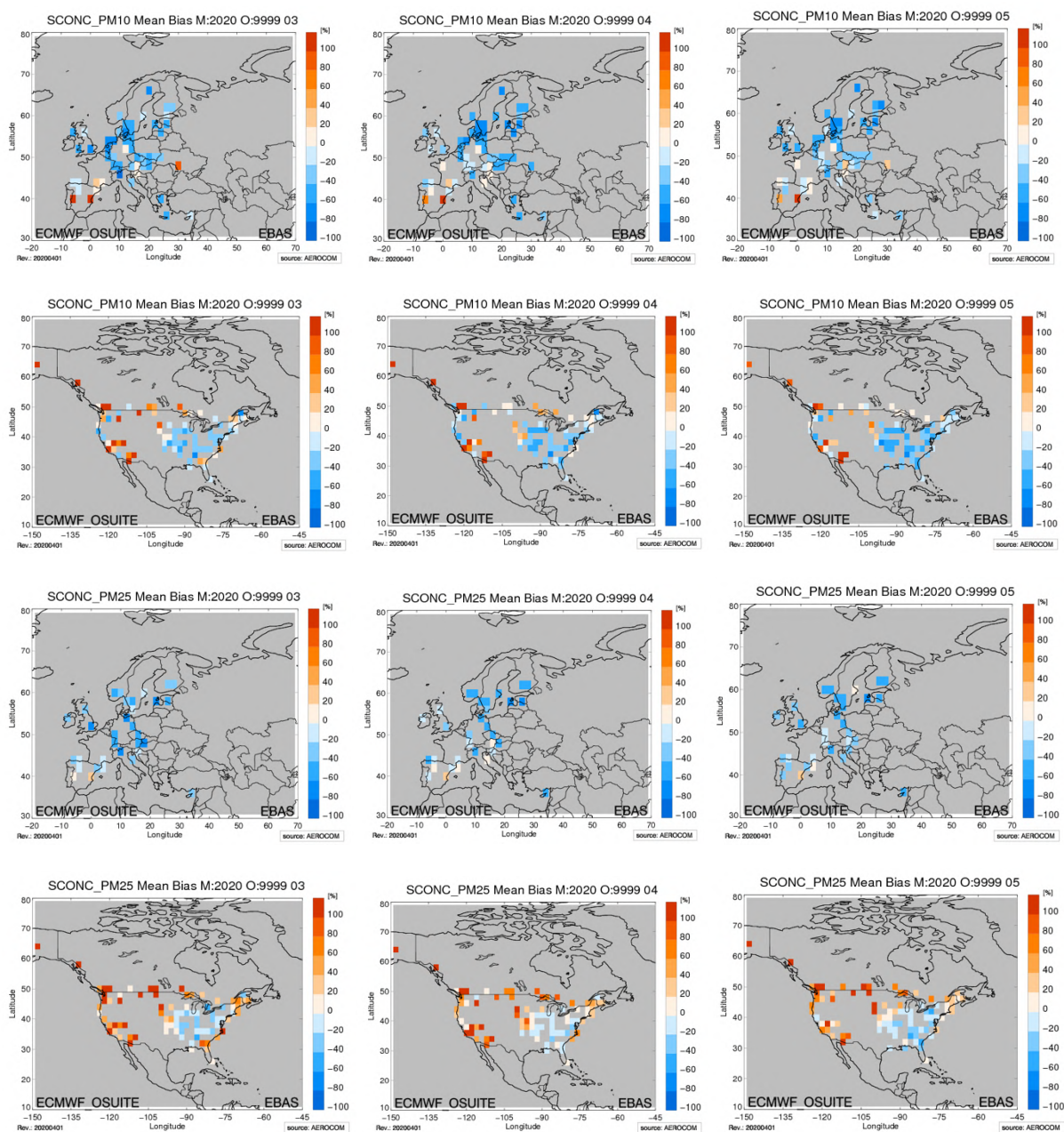


Figure 8.1.5. Bias [%] map of monthly mean PM₁₀ and PM_{2.5} concentrations at EMEP (Europe, first and third row) and IMPROVE sites (North America, second and fourth row) for March (left column), April (middle) and May 2020 (right); simulated o-suite versus EMEP/IMPROVE derived climatological average (2000-2009).

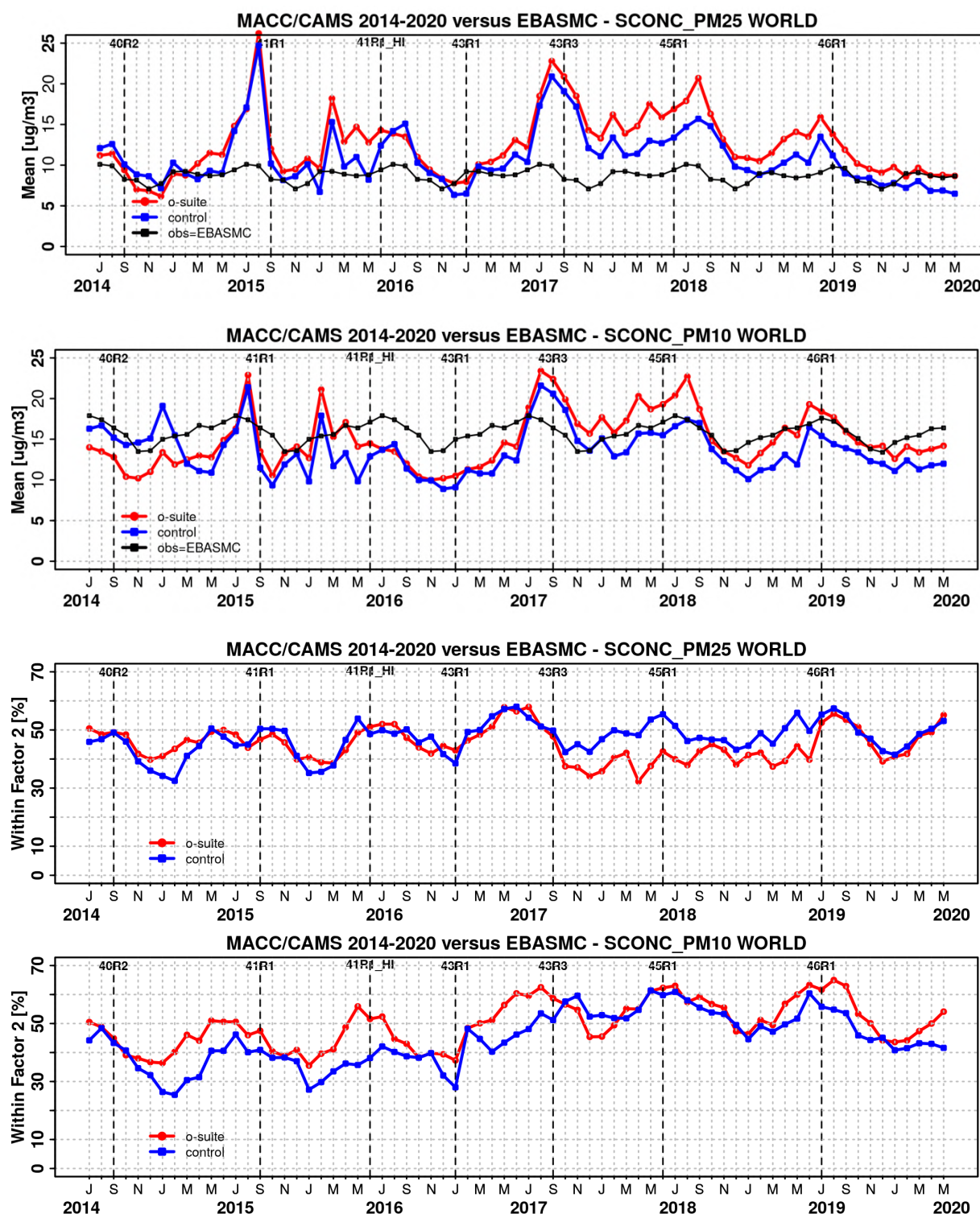


Figure 8.1.6. Temporal evolution of monthly mean average PM25 and PM 10 concentrations at EMEP (Europe) and IMPROVE sites (North America) and data fraction within a factor 2 of observed; ca 160 sites, observed data averaged from data available in EBAS from 2000-2009.

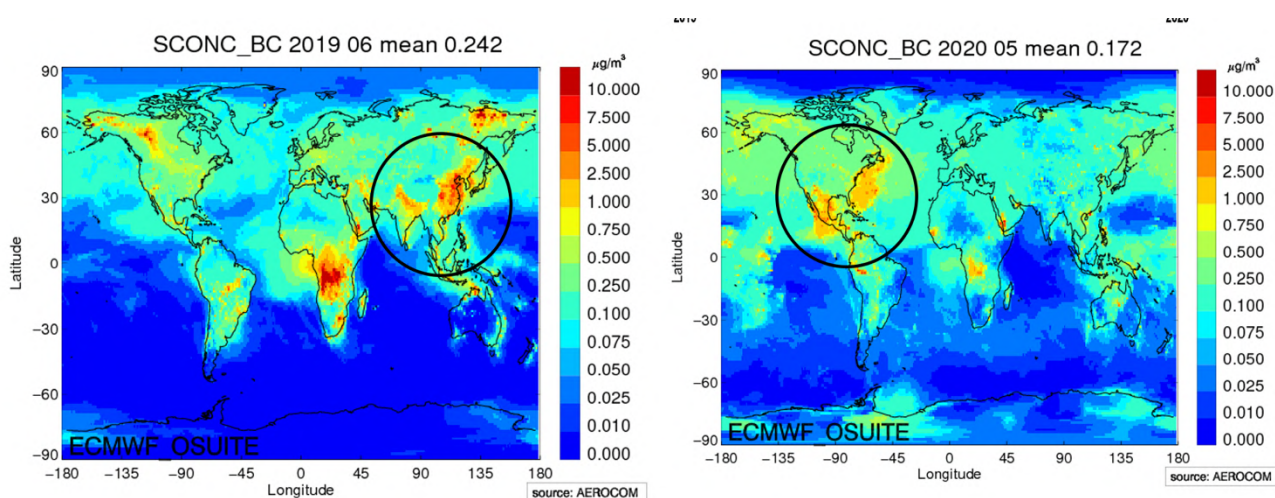


Figure 8.1.7. Surface concentration of black carbon in o-suite MAM 2019 (left) and MAM 2020 (right).

Surface concentration of particulate matter below 10 μm (PM₁₀) and below 2.5 μm (PM_{2.5}) from the o-suite experiment have been validated against data from 160 background IMPROVE and EMEP stations. A climatological average has been constructed from data in the period 2000-2009 as available in the EBAS database hold at NILU. The data availability is not the same at all stations, and sometimes covers only a few years.

A negative MNMB bias of PM₁₀ in Europe and an overestimate in North America PM_{2.5} appears (Fig. 8.1.5), consistent with the AOD bias in the two regions. Figure 8.1.6 shows the evolution of mean observed and simulated PM₁₀ and PM_{2.5}. The biggest change appeared in July 2017 with the bias of o-suite now becoming positive almost overall. Shown is also the statistics of being within factor 2, a more robust metrics for a comparison to climatological data. This statistical indicator has clearly improved over time, indicating best PM₁₀ and PM_{2.5} performance in summer months for the o-suite. O-suite is also better most of the times than the control simulation for PM₁₀. For PM_{2.5} the difference is less clear, but since September 2017 (upgrade to 43R3) the control is performing better than the o-suite, except since latest upgrade with a performance of o-suite as good as the control.

Anthropogenic black carbon and organic aerosol (OA) emissions were found to be shifted by 180 degrees in longitude from January 2020 onwards. This resulted in particular in erroneous, shifted black carbon fields, possibly also BC absorption fields (see figure 8.1.7). An analysis of the speciated surface concentration bias shows that the BC bias in Europe is becoming more negative from January 2020 onwards, because due the shift “pacific” BC emissions are effective over Europe (see figure 8.1.8).

OA results are less affected, since secondary aerosol formation and biomass burning sources are more important for OA fields. PM and Optical depth is also not impacted to a large extent, mainly because BC is a very small fraction of these parameters.

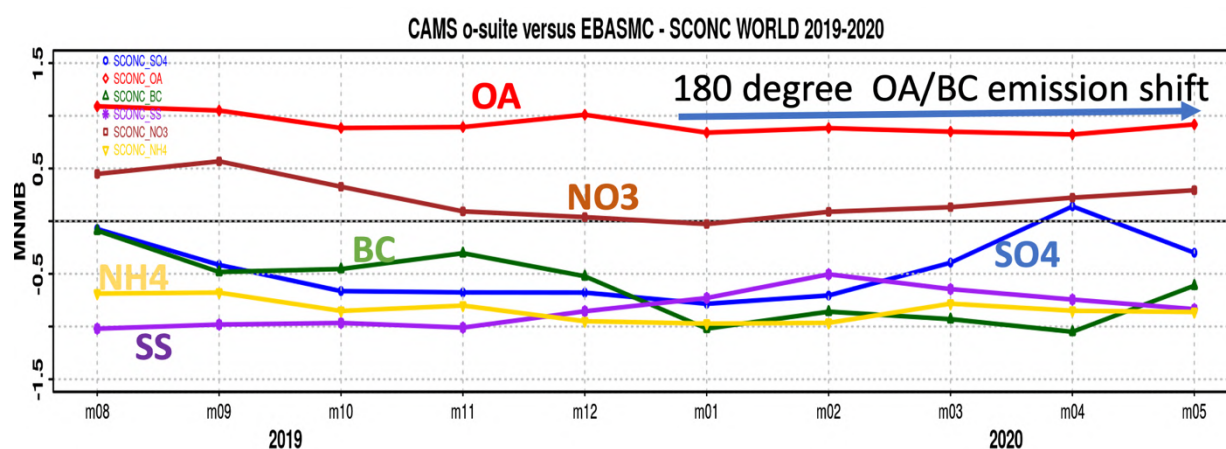


Figure 8.1.8. Evolution of MNMB Bias of simulated surface concentrations in o-suite against a climatology of speciated aerosol concentrations, mainly over Europe and North America.

8.2 Validation of dust optical depth against AERONET, and comparisons with the Multi-model Median from SDS-WAS

The 72-hour forecasts (on a 3-hourly basis) of dust aerosol optical depth (DOD) from CAMS o-suite and control have been validated for the period 1 December 2019 – 29 February 2020 against the AERONET Spectral Deconvolution Algorithm (SDA) cloud-screened observations, MODIS/Terra and Aqua Collection 6.1 Level 3 (1° x 1°) and SDS-WAS Multi-model Median DOD. The SDS-WAS Multi-model Median DOD is obtained from (currently) twelve dust prediction models participating in the Sand and Dust Storm Warning Advisory and Assessment System (SDS-WAS) Regional Center for Northern Africa, Middle East and Europe (<http://sds-was.aemet.es/>). At those sites where the SDA products are available, the dust AOD evaluation will be complemented with AOD-coarse, which is fundamentally associated with maritime/oceanic aerosols and desert dust. Since sea-salt is related to low AOD (< 0.03; Dubovik et al., 2002) and mainly affects coastal stations, high AOD-coarse values are mostly related to mineral dust.

During this season, satellites (see MODIS in Figure 8.2.1) show that significant dust activity in Northern Africa (seasonal AOD above 0.5) is concentrated in latitudes between 10 and 25°N with maximum seasonal AOD values over 0.9 in Bodélé (Chad). Meanwhile, in the Middle East, high AOD values up to 0.7 are observed in Iraq and Saudi Arabia.

Overall, o-suite shows lower season values than the control run, which are in general higher than the SDS-WAS multi-median product. Both CAMS runs reproduce high DOD dust activity in the region of Chad, Mali, Niger and Algeria, despite they overestimate in Eastern Sahara in Sudan. Seasonal DOD over Iraq and in the Mediterranean Basin appears overestimated in comparison with MODIS and the SDS-WAS multi-model ensemble (see Figure 8.2.1). On the contrary, CAMS run can reproduce the dust transport over the North Atlantic region, but this is underestimated.

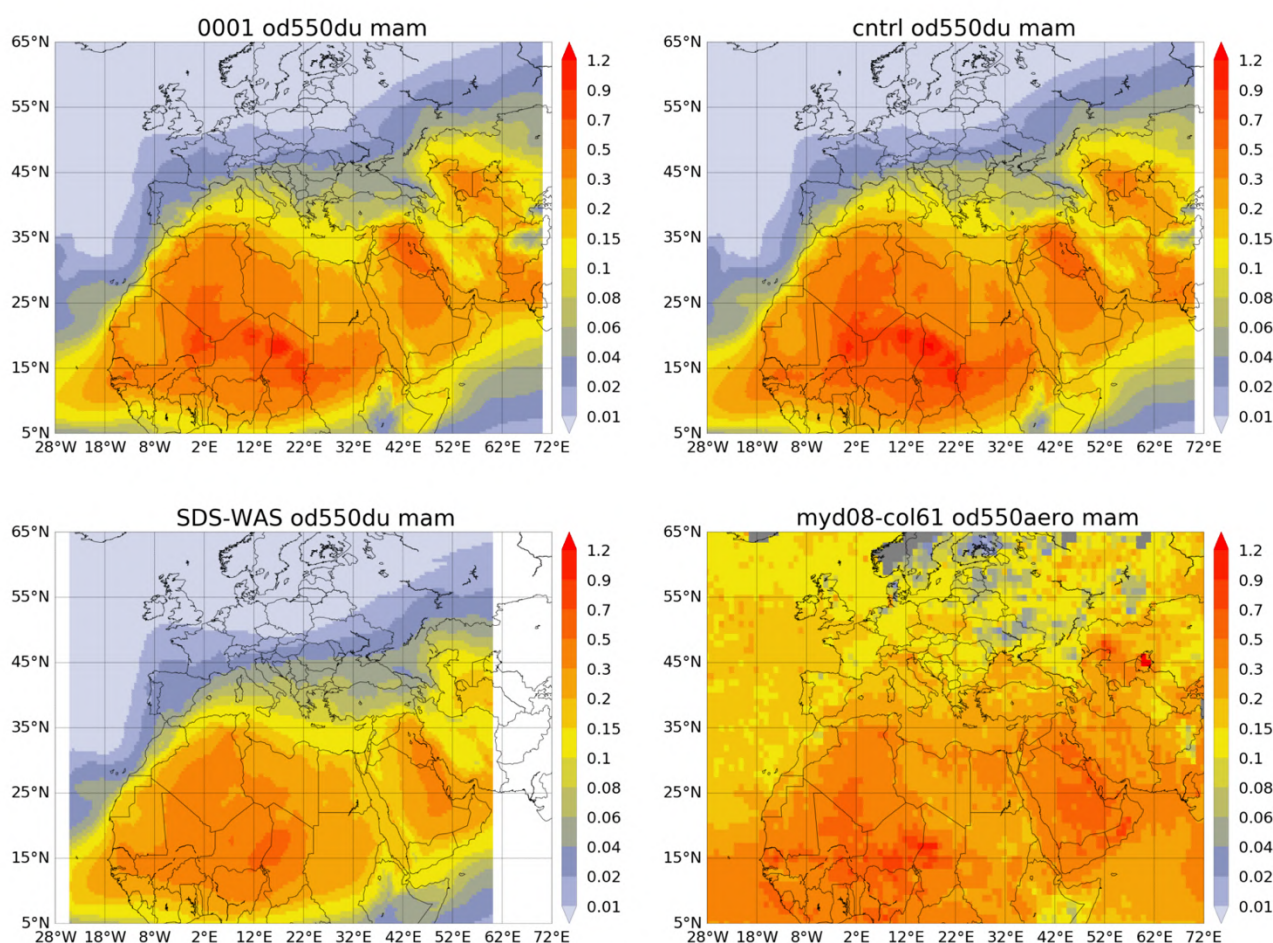


Figure 8.2.1: Averaged DOD 24h forecast from o-suite (top left) and control (top right), DOD of the multi-model SDS-WAS Median product (bottom left) as well as AOD from MODIS/Aqua Collection 6.1 Level 3 combined Dark Target and Deep Blue product (bottom right) for the study period.

From March to May, o-suite (control) reproduce the daily variability of AERONET dust-filtered observations (see Figure 8.2.2), with a correlation coefficient of 0.70 (0.73) averaged over all AERONET sites, which is lower than the SDS-WAS multi-model product which has a correlation coefficient of 0.82. Regarding mean bias (MB), o-suite tends to slightly overestimate the AERONET observations with an MB of 0.02 for o-suite and 0 for control in comparison with the SDS-WAS multi-model that presents higher underestimations (MB of -0.03).

Over desert dust sources in the Sahara (see Table 8.2.1 as well as Tamanrasset INM AERONET site in Figure 8.2.3a), CAMS runs do reproduce the daily variability with correlation coefficients 0.74. However, DOD is overestimated (MB of 0.24 for o-suite and 0.14 for control). As shown in Tamanrasset INM (Figure 8.2.3a), the overestimations observed in control are reduced in the o-suite experiment particularly since April. The SDS-WAS Multi-model results for Sahara shows better skills for this season (with a seasonal correlation of 0.82 and MB of 0.03). In the Middle East (see Kaust Campus in Figure 8.2.3a), the comparison with AERONET observations shows lower correlations

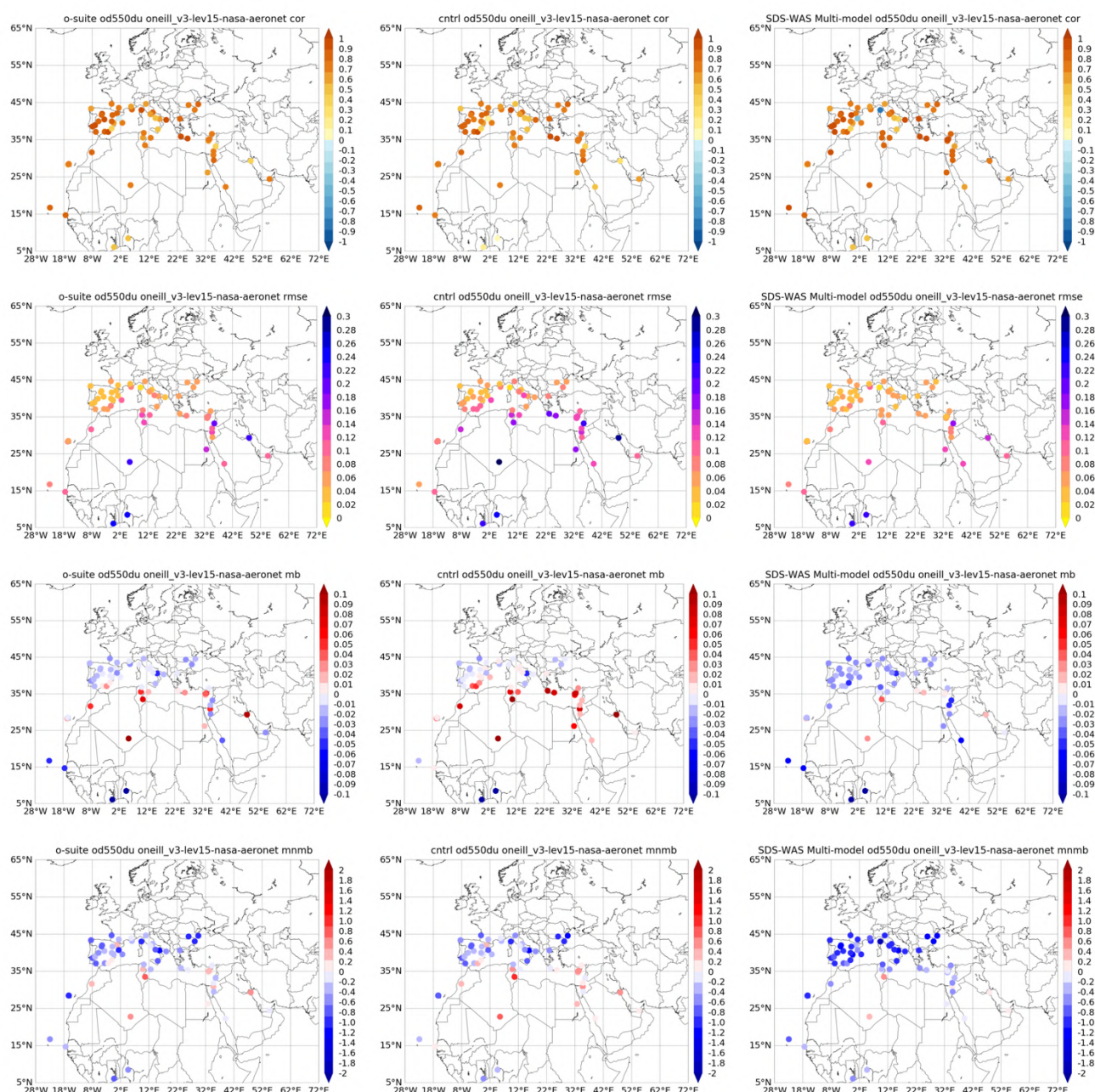


Figure 8.2.2: Skill scores (correlation coefficient, RMSE, MB and MNMB) for 24-hour forecasts of CAMS o-suite (left column), control (central column) and DOD Multi-model SDS-WAS Median (right column) for the study period. AOD-coarse from AERONET SDA is the reference.

coefficients (0.49 for o-suite and 0.65 for control) and smaller MB (MB of 0.02 for o-suite and -0.02 for control, see Table 8.2.1). These results in the Middle East are closer to the SDS-WAS Multi-model (with a seasonal correlation of 0.60 and MB of -0.03).



Table 8.2.1: Skill scores (MB, MNMB, RMSE and r) of 24h forecasts (on 3hourly basis) for CAMS o-suite, CAMS control and SDS-WAS Multi-model Median for the study period, and the number of data (NDATA) used. DOD (SDA AOD coarse product) from AERONET is the reference.

	NDATA	Control				o-suite DOD				SDS-WAS Median DOD			
		MB	MNMB	RMSE	r	MB	MNMB	RMSE	r	MB	MNMB	RMSE	r
Sahara	331	0.24	0.78	0.32	0.74	0.14	0.58	0.23	0.74	0.03	0.26	0.14	0.82
Sahel	247	-0.11	-0.23	0.24	0.10	-0.18	-0.48	0.25	0.46	-0.14	-0.35	0.22	0.45
Tropical North Atlantic	175	-0.02	-0.35	0.06	0.87	-0.05	-0.50	0.07	0.87	-0.06	-0.67	0.08	0.90
Subtropical North Atlantic	531	0.01	-0.62	0.09	0.50	-0.01	-0.68	0.06	0.51	-0.01	-0.85	0.06	0.49
North Western Maghreb	270	0.08	0.35	0.15	0.78	0.05	0.24	0.11	0.81	-0.03	-0.54	0.08	0.89
Western Iberian Peninsula	712	0.01	-0.29	0.07	0.76	-0.01	-0.36	0.04	0.84	-0.02	-0.82	0.04	0.88
Iberian Peninsula	1230	0.00	-0.53	0.06	0.78	-0.01	-0.61	0.04	0.87	-0.02	-1.02	0.04	0.88
Western Mediterranean	1138	0.00	-0.20	0.07	0.63	-0.01	-0.31	0.06	0.63	-0.03	-0.94	0.05	0.64
Central Mediterranean	1627	0.02	-0.12	0.10	0.70	0.01	-0.16	0.08	0.71	-0.01	-0.72	0.06	0.80
Eastern Mediterranean	2470	0.04	0.01	0.14	0.64	0.01	-0.13	0.11	0.64	-0.01	-0.44	0.08	0.76
Eastern Sahara													
Middle East	630	0.02	0.12	0.14	0.49	-0.02	-0.08	0.12	0.65	-0.03	-0.07	0.12	0.60
All sites	11334	0.02	-0.16	0.13	0.70	0.00	-0.27	0.10	0.73	-0.03	-0.65	0.08	0.82

In the Sahel (see Table 8.2.1), the o-suite reduces the high underestimations observed in the control run (MB of -0.11 for control and -0.18 for o-suite) despite control better reproduces the observed daily variability (with a correlation of 0.10 for o-suite in comparison to 0.46 for control). The underestimations observed in o-suite in the Sahel are also spread to the Tropical North Atlantic (MB of -0.02 for o-suite and -0.05 for control, see Table 8.2.1 and Capo Verde in Figure 8.2.3b) and sub-Tropical North Atlantic (MB of 0.01 for o-suite and -0.01 for control, Table 8.2.1).

In the case of the North-Western Maghreb (see Table 8.2.1 and Saada in Figure 8.2.3b), o-suite shows slightly lower correlation coefficient (0.78) than control (0.81) although o-suite tends to enhance the overestimations observed in control (MB of 0.05 for control and 0.08 for o-suite). Over the Iberian Peninsula and the Mediterranean, both CAMS runs show correlations between 0.63 and 0.87 and slightly overestimations (MB between 0 and 0.04) except in the Iberian Peninsula and Western Mediterranean where control slightly underestimates DOD (MB of -0.01). In Western and Eastern Mediterranean is where both CAMS runs show lower correlation coefficient decreases (0.63 for Western Mediterranean and 0.64 for Eastern Mediterranean, see Table 8.2.1 and Agia Marina Xyliatou in Figure 8.2.3b).

The comparison of the 1- to 3-day forecasts shows that the prediction is stable during the forecasts in comparison with AERONET dust-filtered observations with correlation coefficients of 0.70 (0.73), 0.71 (0.72), and 0.71 (0.70) respectively for 24, 48 and 72h forecasts for all the sites, for o-suite (control).

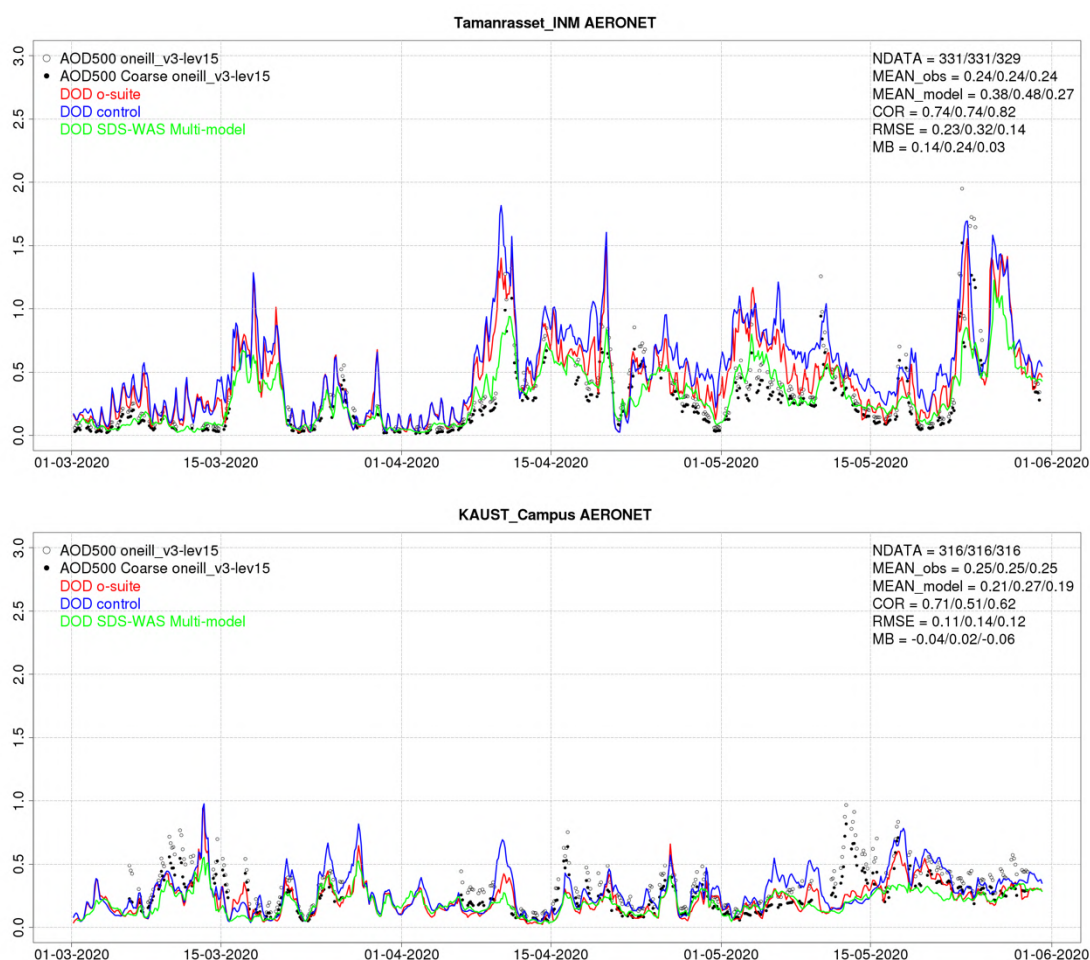


Figure 8.2.3a: AOD and Angstrom Exponent from AERONET Direct-sun (black dots), DOD o-suite (red line), DOD control (blue line) and DOD Multi-model SDS-WAS Median (green line) for the study period over Tamanrasset INM (Sahara) and Kaust Campus (Middle East). Skill scores per each site and model (o—suite/control/ SDS-WAS Multi-model) are shown in the upper right corner (NDATA: available 3-hourly values used for the calculations, MEAN observations, MEAN model, COR, RMSE, MB).

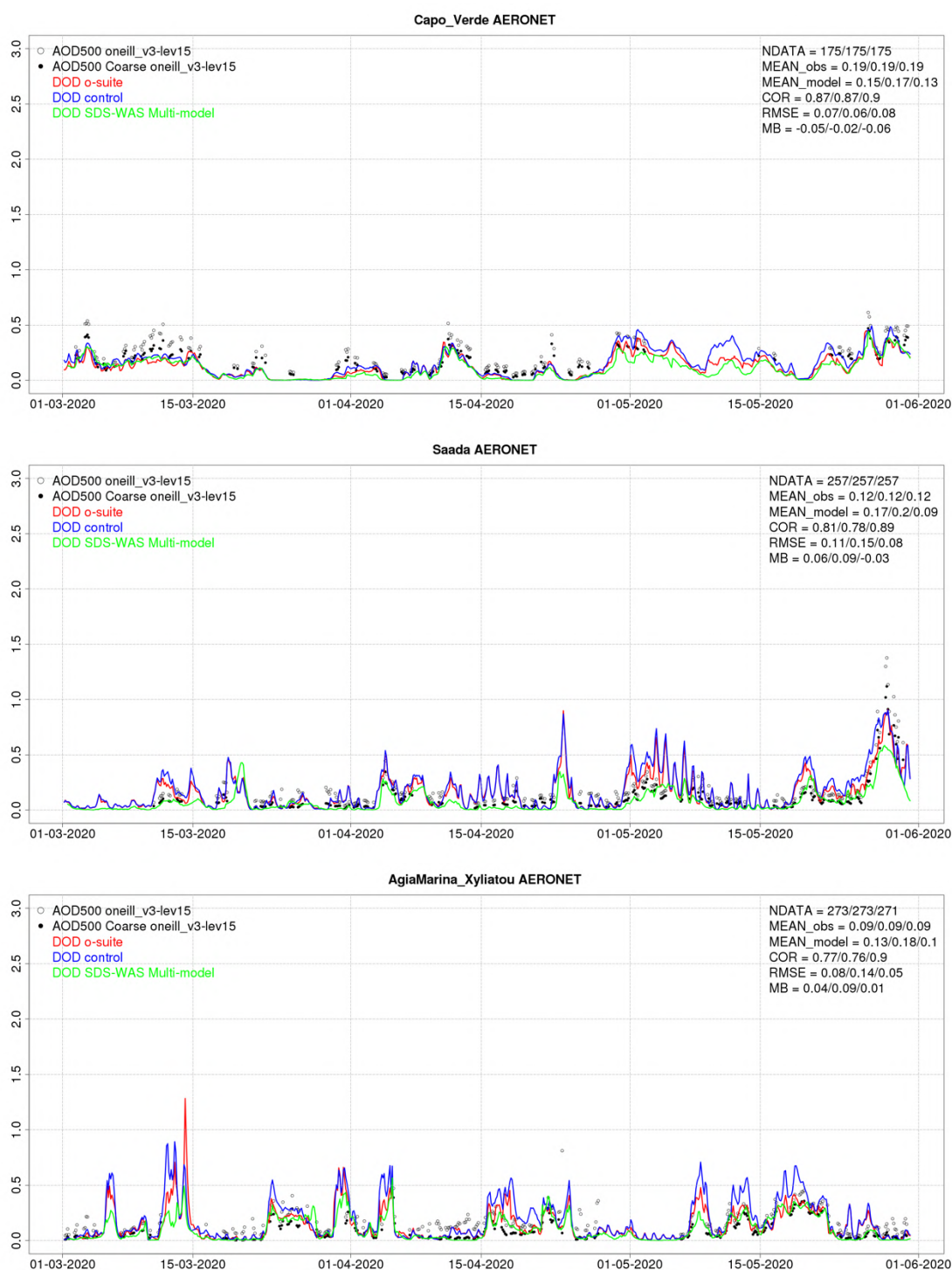


Figure 8.2.3b: AOD and AOD-coarse from AERONET SDA (black dots), DOD o-suite (red line), DOD control (blue line) and DOD Multi-model SDS-WAS Median (green line) for the study period over Capo Verde (Tropical North Atlantic), Saada (NW Maghreb) and Agia Marina Xyliatou (Eastern Mediterranean) Skill scores per each site and model (o—suite/control/SDS-WAS Multi-model) are shown in the upper right corner (NDATA: available 3-hourly values used for the calculations, MEAN observations, MEAN model, COR, RMSE, MB).

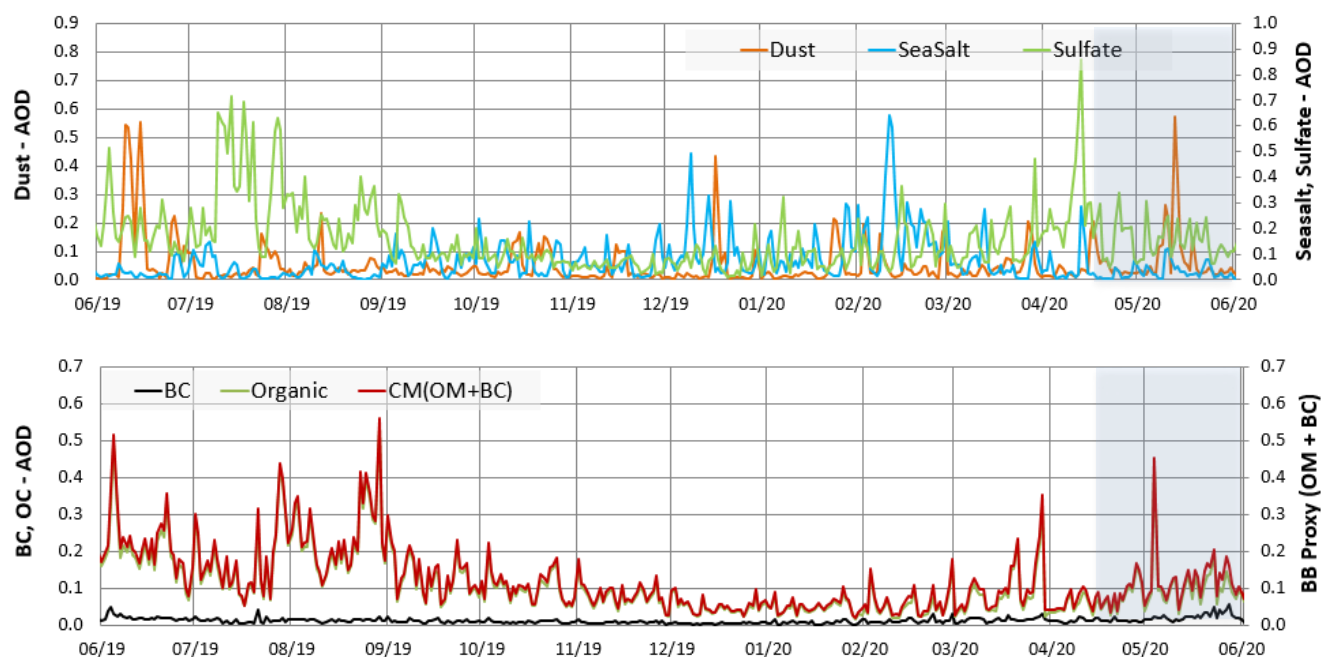


Figure 8.3.1: Maximum daily AOD over Germany for aerosols included in the IFS model from 06/2019 - 05/2020: sea salt (blue), dust (orange), sulfate (light green), black carbon (BC, black), organic matter (green), proxy for 'biomass burning' (as OC+BC - red). Note the different y-axes for the aerosol species.

8.3 Ceilometer backscatter profiles

Technical specifications of data sources, evaluated parameters and methods are described in the report CAMS-84 D8.1. In this section, the temporal and vertical variation of the backscatter coefficient (bsc) profiles are evaluated, statistically as bias, correlation, and standard deviation of o-suite '0001' and control run 'h7c4' vs ceilometers, and summarized in Taylor plots.

Period Overview

The model aerosol optical depth (AOD) and ceilometer overviews are used to select periods with significant aerosol plumes over Germany. Figure 8.3.1 showing the maximum AOD over Germany, separately for contributions of mineral dust (SD), sea salt (SS), carbonaceous matter (CM), black (BC) and organic carbon (OC), as well as sulfate (SU). The model aerosol optical depth (AOD) indicates initially higher (starting with the update on 10 July 2019) but then decreasing SO₄ concentrations, while all other components show no marked changes. During the reports time one Saharan dust events occurred in mid-May 2020. With respect to AOD, all aerosol components follow their usual seasonality.

Mean and Median profiles:

In the new IFS cycle 46r1, implemented on 10th July 2019, nitrate NO₃ and ammonia NH₄ have been added and, likewise sulfate SO₄, have been coupled w.r.t homogeneous (gas-phase) and heterogeneous (particle phase) chemical processes. They contribute roughly 10-30% of aerosol mass in the rural central European PBL, as neutralized forms NO₃NH₄ or (NH₄)₂SO₄. Simultaneously, emissions of most aerosol components were significantly upgraded.

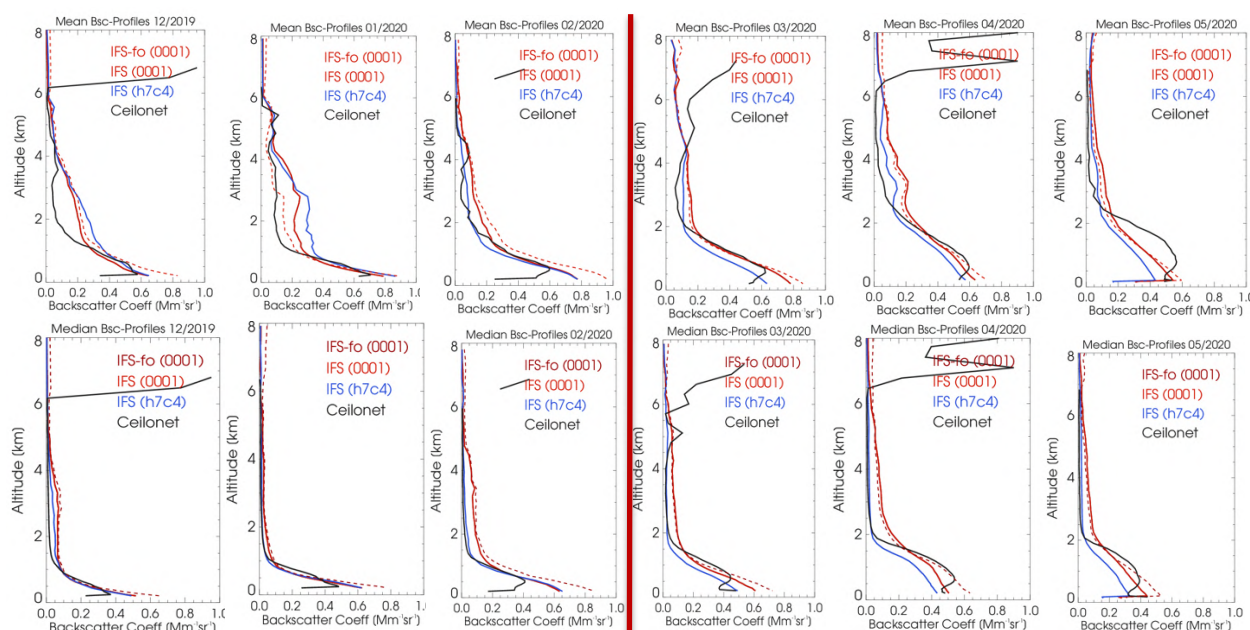


Figure 8.3.2: Monthly mean profiles (upper panel) and median profiles (lower panel) of backscatter coefficients from o-suite (red), control run (blue), and ceilometers (black) combined from 21 German stations in Dec 2019 to May 2020 (left DJF 2019/20, right MAM 2020).

The median for December to February 2020 show only minimal bias, increasing minimal in March and April 2020 with a greater amplitude in the upper troposphere (see Figure 8.3.2) due to cloud contamination.

This mean value offset is explainable by several factors. During Winter 2019/20 atmospheric conditions often produced westerly winds. This leads to relatively warm and dryer weather conditions increasing the maximal load of dust. During winter foehn situations over the alps including some transport of Saharan dust into Germany, for example January the 24th.

By comparing MAM 2019 to MAM 2020, the gap between Model and Ceilometer is closing, in comparison to last year's report (see Figure 8.3.3), especially in the lower troposphere/boundary layer. The negative bias of the model has significantly decreased from 60L to 137L model version.

Taylor Plots:

The average coefficient of correlation between modelled and observed vertical backscatter profiles ranges between $r = 0.2 - 0.8$ in MAM (Fig. 8.3.4). This is mainly due to better representation of the PBL top height. The absolute standard deviation (SD) are normalized to the SD of observations per day, as reference value at $SD \equiv 1.0$. In comparison to winter 2019/20, o-suite (red dots) and control run (blue dots), March to May 2020 both suites show a similar correlation (0.2-0.8) with the observation, but better standard deviation (SD) from 0.2-0.8 to 0.3 to 0.8. The better clustering of the data also hinting to more consistent results with fewer outliers. The o-suits even showed a stronger correlation in some cases then the control run. There is a large day-to-day and a seasonal variation of the performance. It must be noted, that small vertical displacements decrease the correlation coefficient, although the SD plumes are mostly reproduced at geographically truthful positions.

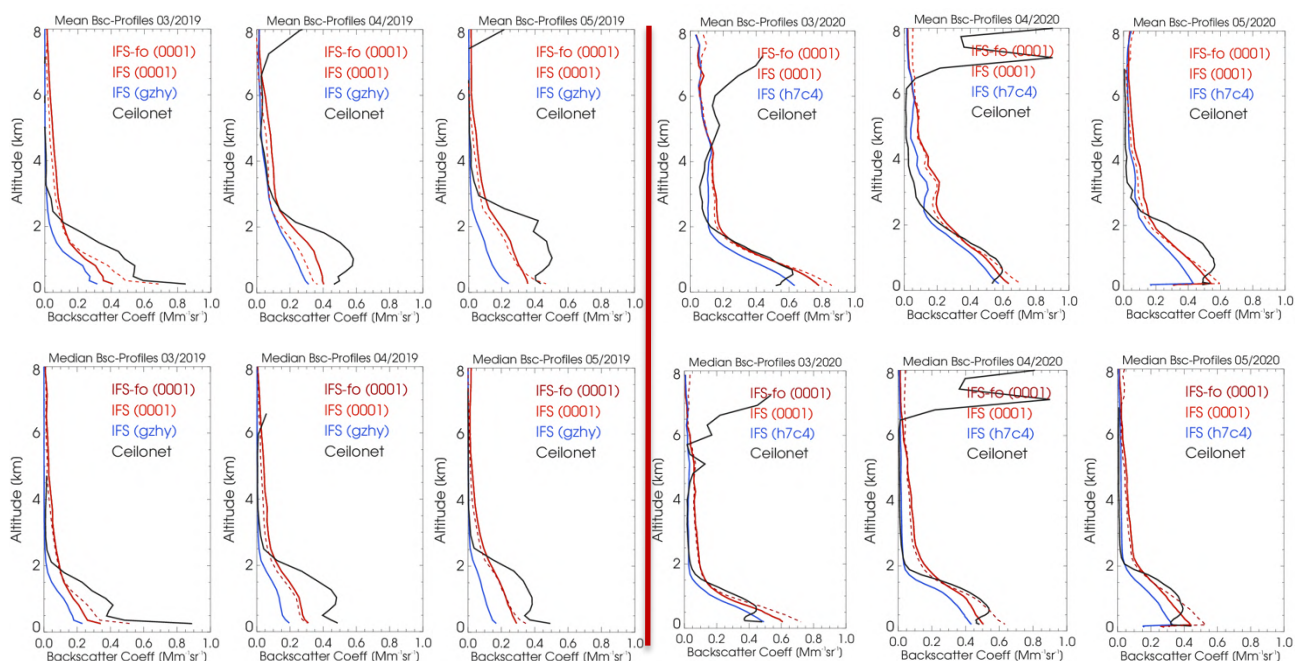


Figure 8.3.3: Comparison of monthly mean (top) and median (bottom) of backscatter coefficients from o-suite (red), control run (blue), and ceilometers (black) combined from 21 German stations for MAM 2019 (left) and MAM 2020 (right).

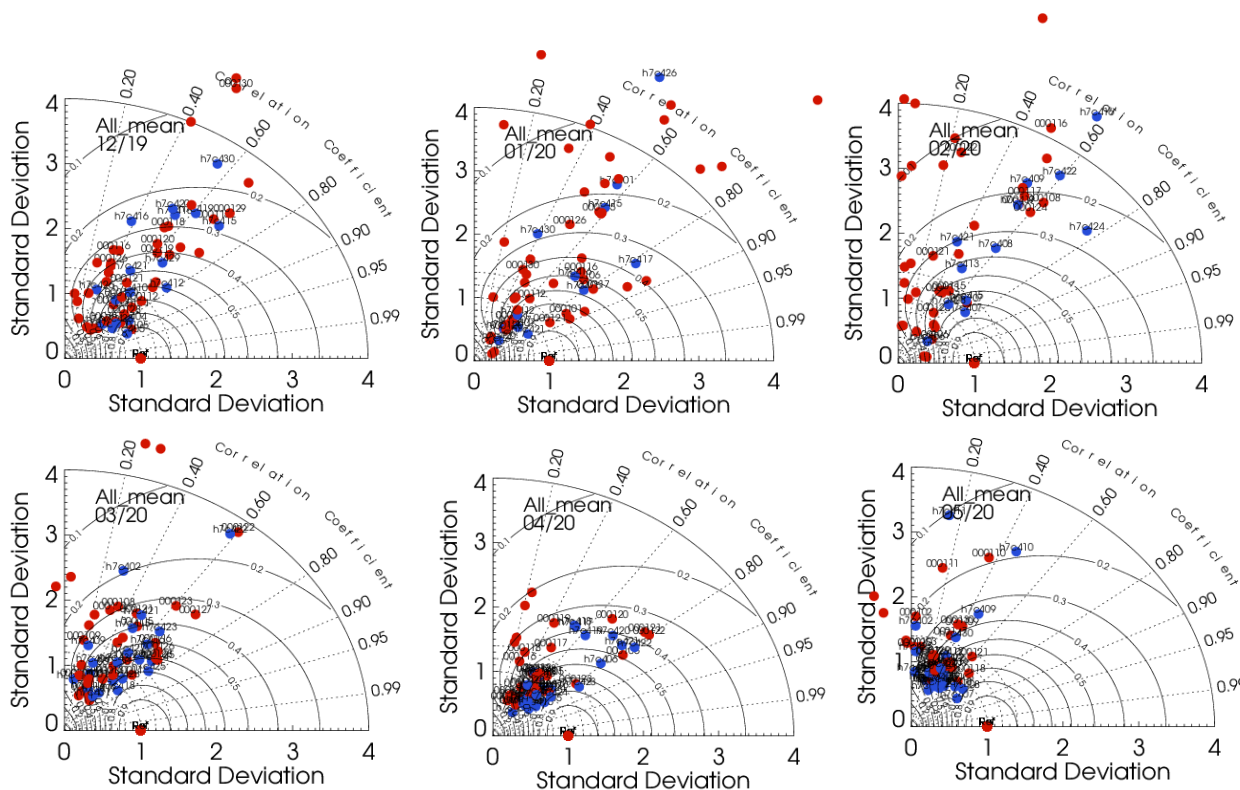


Fig. 8.3.4: Taylor polar plots with daily average standard deviation of vertical profiles vs correlation coefficient, averaged over 21 German ceilometer sites for Dec 2019 to Feb 2020 (top) and Mar2020-May 2020 (bottom). O-suite red, control blue.

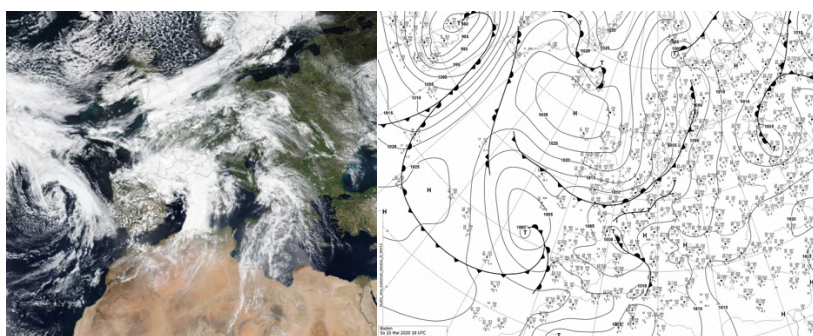


Figure 8.3.5: Meteorological situation on May 10th 2020, 18 UTC. On the right Suomi NPP VIIRS True Color Corrected Reflectance (© NASA) and on the left the surface pressure map at 18 UTC (© DWD).

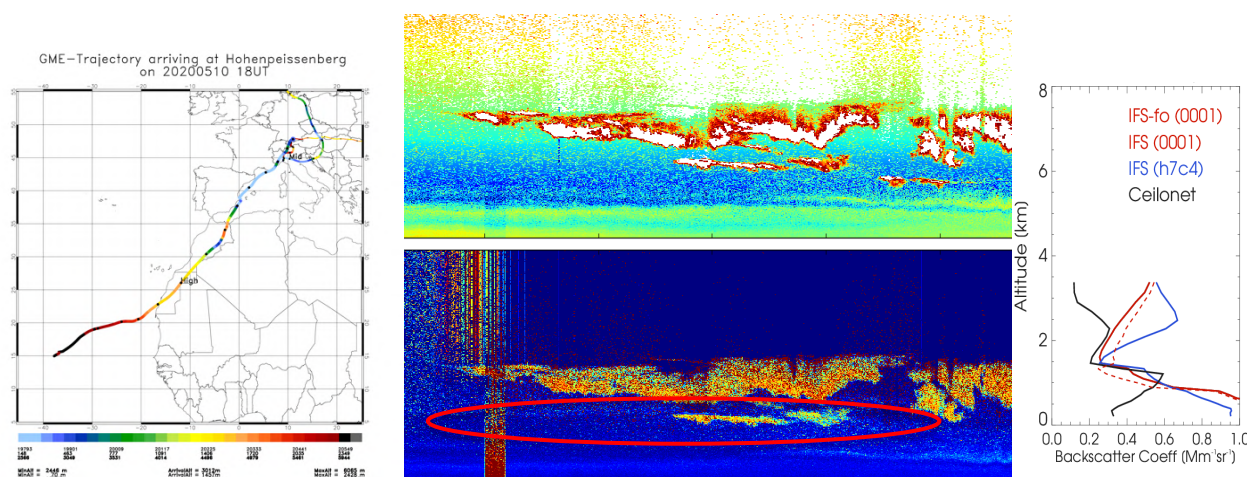


Figure 8.3.6: Dust event on May 10th 2020. Left is the Backward trajectory of the air impacting Hohenpeißenberg on that specific day. In the middle is the visualization of depolarization lidar, operated at Hohenpeißenberg, showing layers of dust transported into the area beneath some clouds. On the right the mean backscatter profile for the day.

Case study, 10.05.2020

During the time covered in this report, one event of 10th of May 2020 occurred and significantly impacts the mean profile (Figure 8.3.5 and 8.3.6). The Synoptical situation at this day shows a low over south France and high pressure over the Rhoné area (Fig. 8.3.5). This situation transported dust from North Africa over Spain and France to southern Germany (Fig. 8.3.6). The May 10th event is an example for Saharan Dust transport to Europe. Although not a very strong event, it is clearly visible in the measurements and the CAMS model.

Summary

After changes in the model upgrade of July 2019 a notable reduction of the positive bias of the model backscatter combined with higher correlations are observed. The step at the top of the PBL is captured notably better with 137 levels than with 60 levels (51L instead of 27L <8 km altitude), same for o-suite and control. The amplitude of the model vertical profile is now very close the observation (reference). Concluding 3-hly averages of Pearson's correlation coefficients the better clustering of the data also hinting to more consistent results with fewer outliers.



- Very low bias of the model backscatter coefficients during spring.
- High bias in upper troposphere can occur due to cloud contamination.
- The step at the top of the PBL is captured notably better with 137 levels than with 60 levels (51L instead of 27L <8 km altitude), same for o-suite and control.
- The amplitude of the model vertical profile is still close the observation (reference).
- Daily averages of Pearsons correlation coefficients in March/April (control run) cluster around $r = 0.3-0.6$.

8.4 Aerosol validation over Europe and the Mediterranean

Three-hourly aerosol optical depth (AOD) and surface concentration (PM₁₀ and PM_{2.5}) from the o-suite and control run have been validated against AERONET AOD direct-sun cloud-screened and EEA PM₁₀ and PM_{2.5} observations.

Aerosol optical depth over the Mediterranean

During spring, both CAMS runs do reproduce the daily variability of AERONET AOD observations, although present general overestimation in the whole Mediterranean Basin (see Figure 8.4.1). The correlation coefficient increases from (0.53, 0.63 and 0.65) for control to (0.59, 0.74 and 0.71) and MB decreases from (0.14, 0.15 and 0.11) for control to (0.09, 0.10 and 0.12) for o-suite respectively for Western, Central and Eastern Mediterranean. Overestimations are linked to an excess of dust transport over this region during this season (see Section 8.2). The highest AOD peaks of both CAMS runs (achieving maximum peaks above 1) are linked to desert dust intrusions occurring during the whole season in the whole Mediterranean Basin. This is shown in the Palma de Mallorca (Spain, Western Mediterranean), Lampedusa (Italy, Central Mediterranean) and Sede Boker (Israel, Eastern Mediterranean) AERONET sites (see Figure 8.4.2).

Surface aerosol concentrations in Europe

At surface levels, both CAMS runs show a higher correlation coefficient in Northern Europe (above 0.6) than Southern Europe (under 0.4) in comparison with the EEA PM₁₀ and PM_{2.5} observations (see Figure 8.4.3 and 8.4.4). For PM₁₀, both CAMS runs show larger underestimations in Northern Europe (MB under $-8 \mu\text{g}/\text{m}^3$) meanwhile Central and Southern Europe appear overestimated (MB above $6 \mu\text{g}/\text{m}^3$). On the contrary, both CAMS runs underestimated PM_{2.5} EEA observations with larger underestimations in northern European and North Atlantic regions (see Figure 8.4.4).

During the whole study period, both CAMS runs predict peaks above $50 \mu\text{g}/\text{m}^3$ for PM₁₀ (see Figure 8.4.5) that in most of the cases overestimated the EEA (see Figure 8.4.5). Frequent desert dust episodes were observed in Southern Europe during this season. The upgrade of the CAMS o-suite during July 2019 led to an increase of the coarse particles at the surface that increase the PM₁₀ levels in Southern Europe. In particular coastal sites in Italy and Spain (see IT2061A in Figure 8.4.5a and ES1569A in Figure 8.4.5b), CAMS runs show systematic high PM₁₀ concentrations ($25 \mu\text{g}/\text{m}^3$). This enhancement of the PM₁₀ levels is being associated with the presence of maritime aerosols.

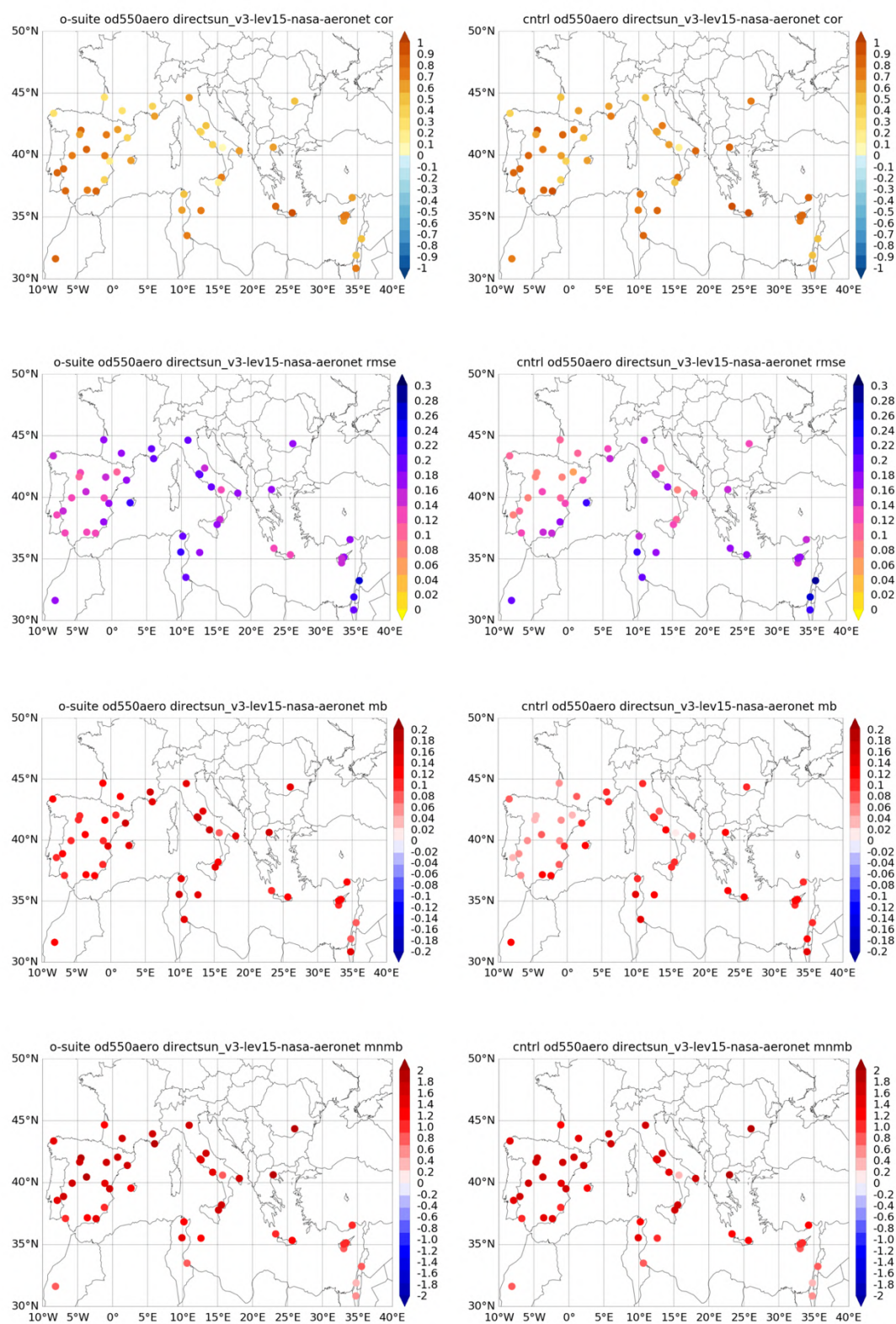


Figure 8.4.1: Skill scores (correlation coefficient, RMSE, MB and MNMB) for 24-hour forecasts of CAMS o-suite and control for the study period. AOD from AERONET direct-sun is the reference.

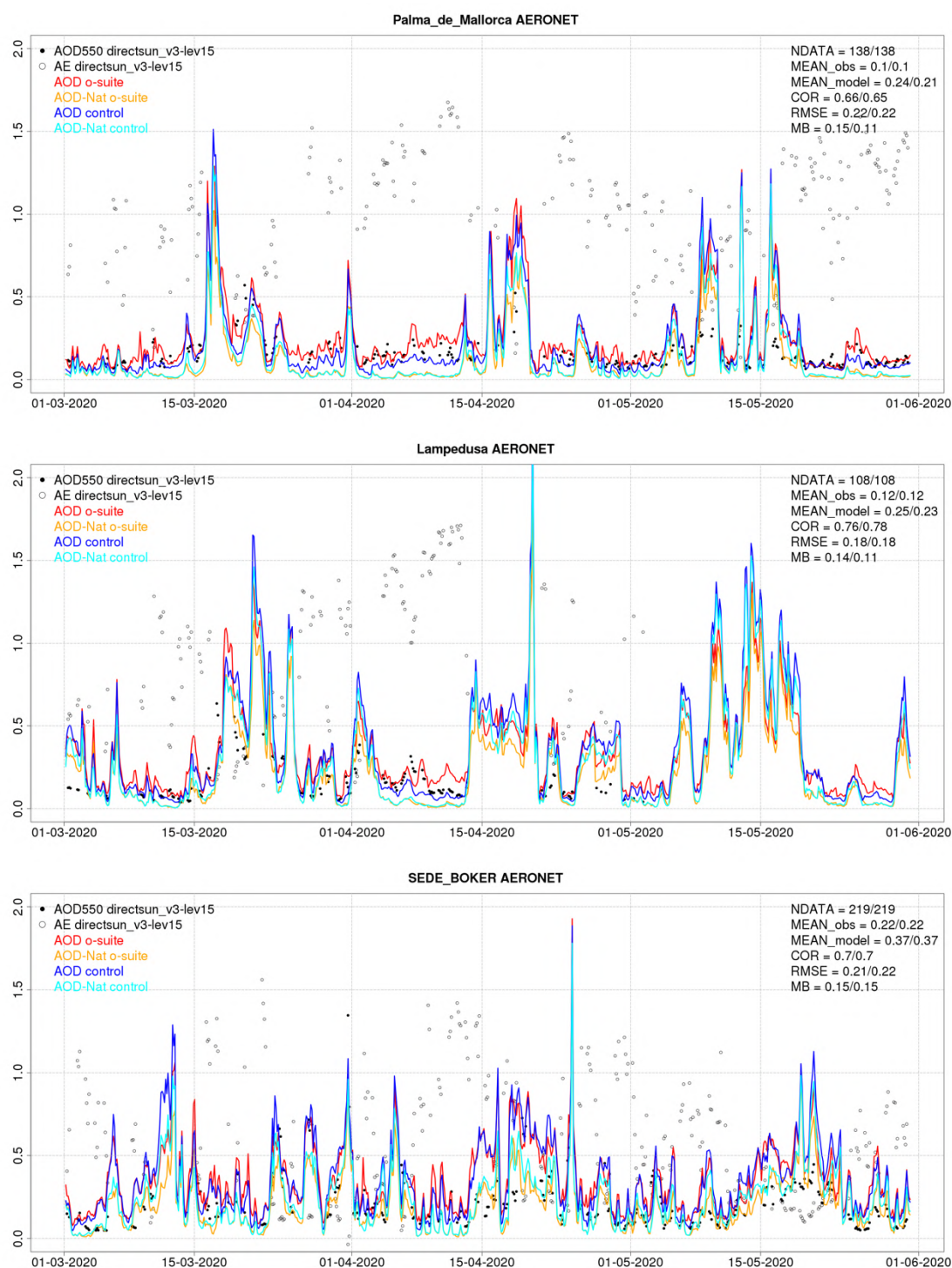


Figure 8.4.2: AOD from AERONET (black dot), AOD o-suite (red line), AOD control (blue line), AOD-Nat o-suite (orange line), AOD-Nat control (cyan line), for the study period over Palma de Mallorca (Spain), Lampedusa (Italy) and SEDE BOKER (Israel). AOD-Nat corresponds to the natural aerosol optical depth that includes dust and sea-salt. Skill scores per each site and model (o—suite/control) are shown in the upper right corner (NDATA: available 3-hourly values used for the calculations, MEAN observations, MEAN model, COR, RMSE, MB).

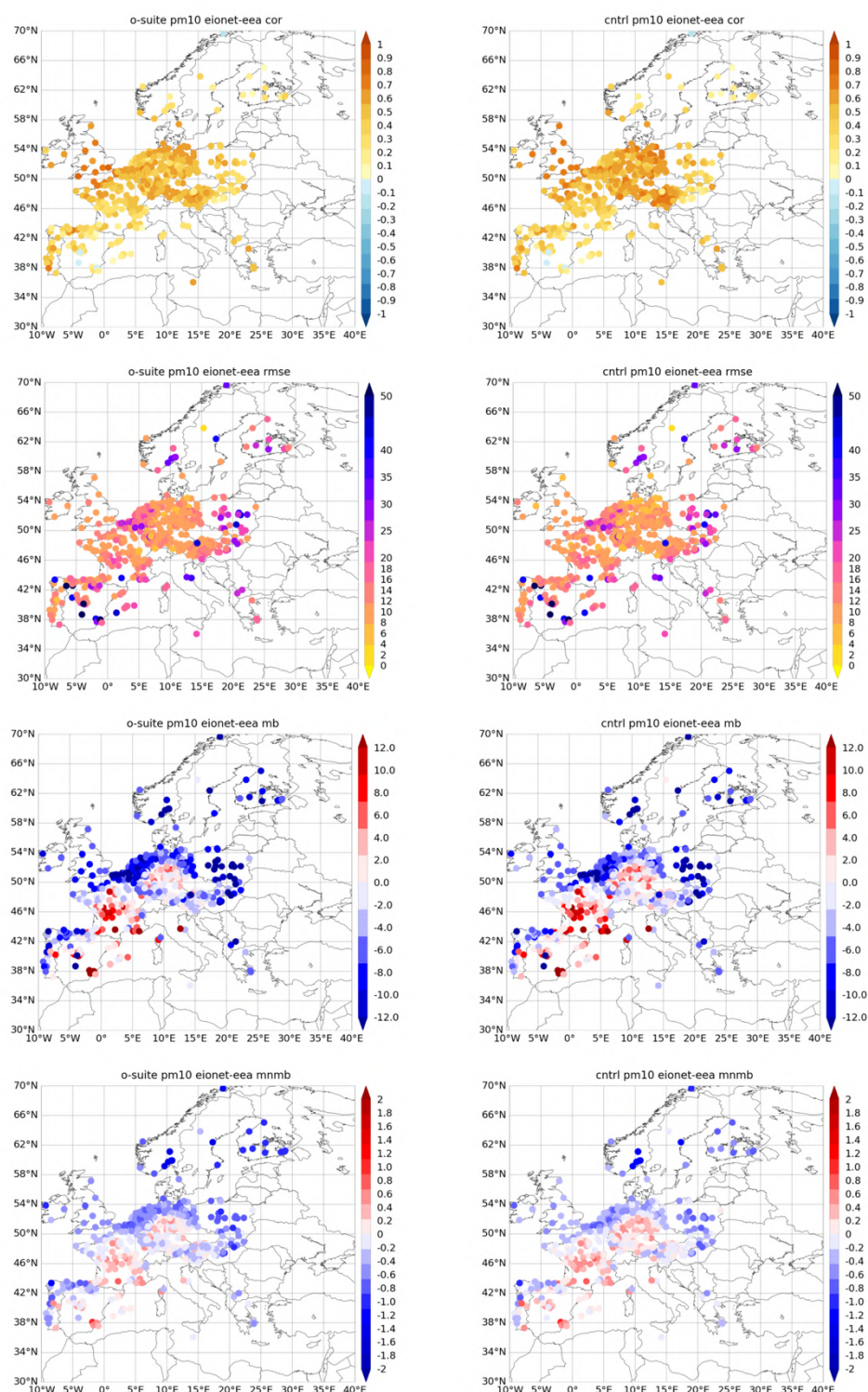


Figure 8.4.3: Skill scores (correlation coefficient, RMSE, MB and MNMB) for 24-hour forecasts (at 3-hourly basis) of CAMS o-suite and control for the study period. 3-hourly PM10 from EIONET is the reference. Only global scale representative available stations are displayed.

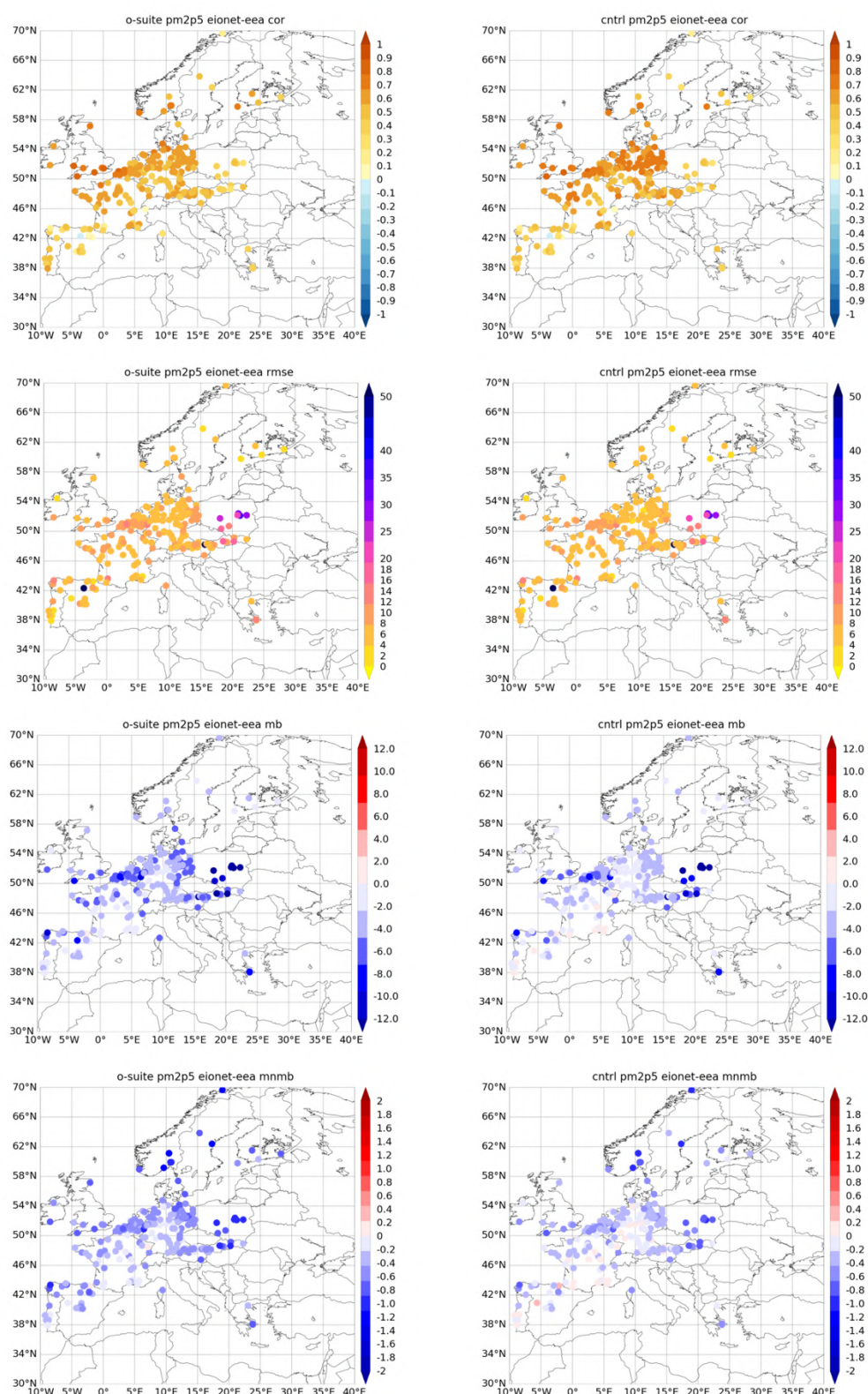


Figure 8.4.4: Skill scores (correlation coefficient, RMSE, MB and MNMB) for 24-hour forecasts (at 3-hourly basis) of CAMS o-suite and control for the study period. 3-hourly PM_{2.5} from EIONET is the reference. Only global scale representative available stations are displayed.

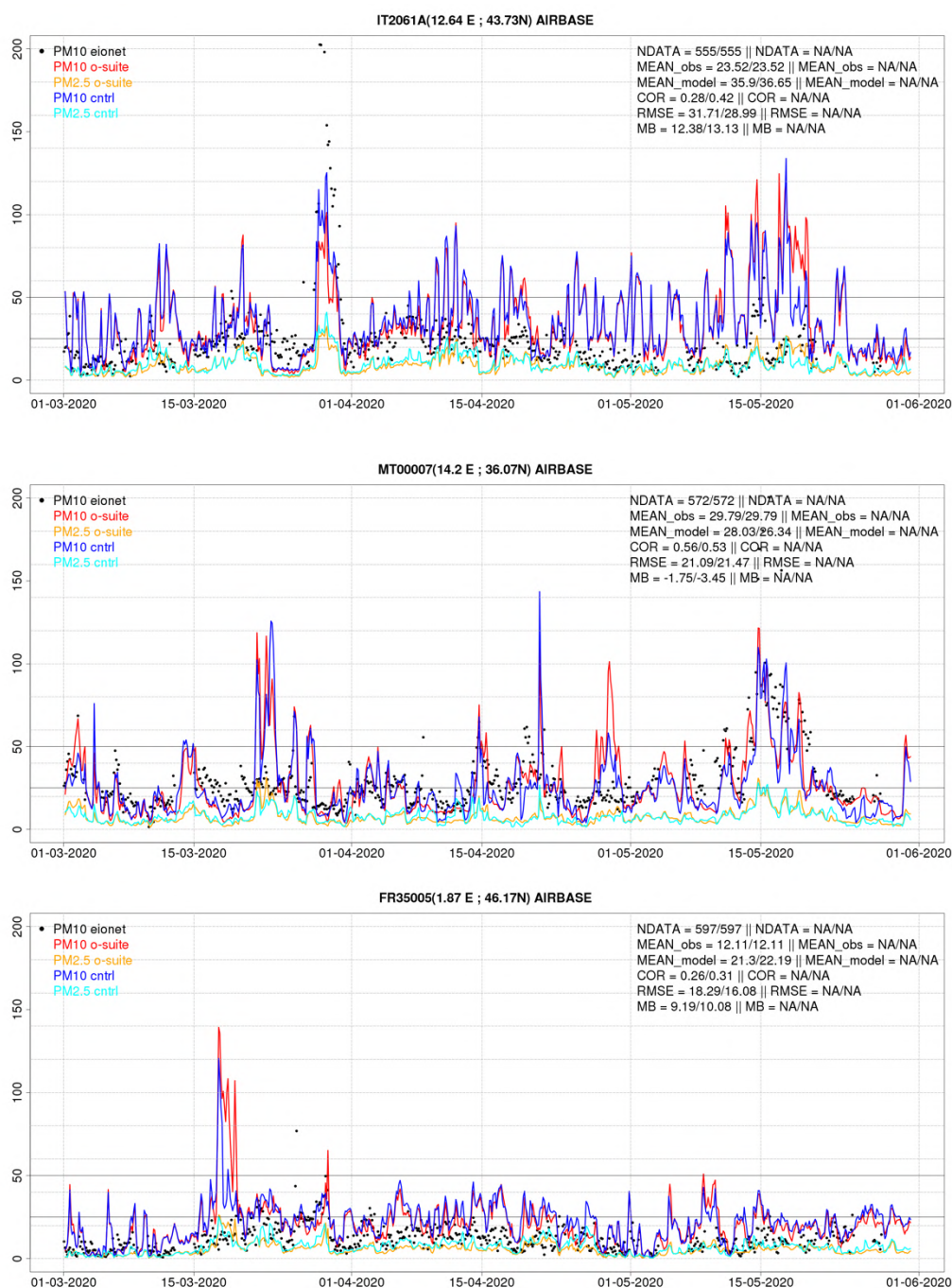


Figure 8.4.5a: PM10 and PM2.5 Airbase observations (black and grey dots, respectively), PM10 and PM2.5 o-suite (red and orange lines, respectively) and PM10 and PM2.5 control (blue and cyan lines, respectively) for the study period over IT2061A (Italy), MT00007 (Malta) and FR35005 (Central France). Skill scores per each site and model (o—suite/control) are shown in the upper right corner (NDATA: available 3-hourly values used for the calculations, MEAN observations, MEAN model, COR, RMSE, MB).

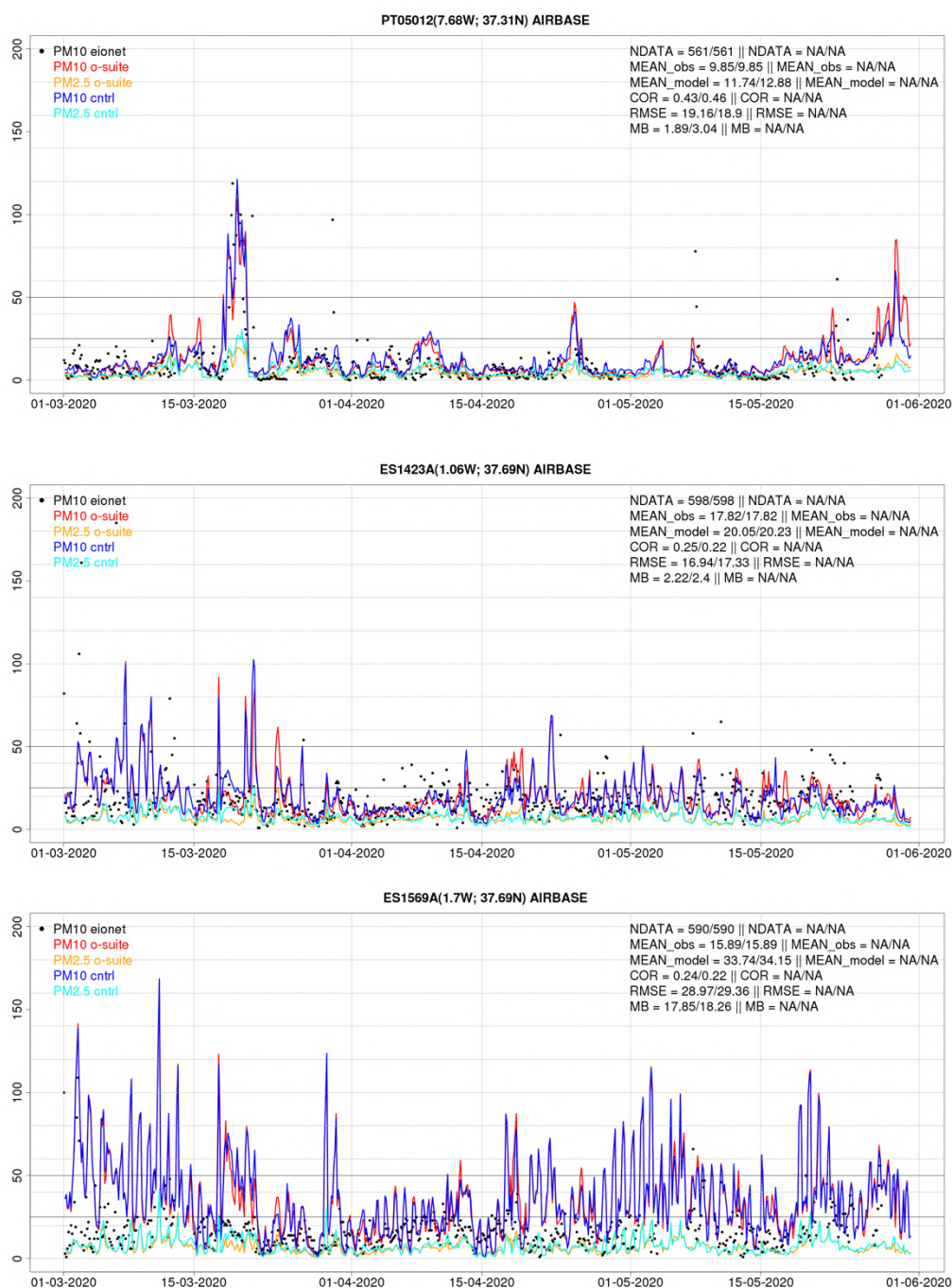


Figure 8.4.5b: PM10 and PM2.5 Airbase observations (black and grey dots, respectively), PM10 and PM2.5 o-suite (red and orange lines, respectively) and PM10 and PM2.5 control (blue and cyan lines, respectively) for the study period over PT05012 (Portugal), ES1423A and ES1569A (Spain, SE Iberian Peninsula). Skill scores per each site and model (o—suite/control) are shown in the upper right corner (NDATA: available 3-hourly values used for the calculations, MEAN observations, MEAN model, COR, RMSE, MB).

9. Stratosphere

9.1 Validation against ozone sondes

In this section, we present the results of the stratospheric ozone evaluation against ozone soundings from the NDACC, WOUDC, NILU and SHADOZ databases. The sondes have a precision of 3-5% (~10% in the troposphere for Brewer Mast) and an uncertainty of 5-10%. For further details see Cammas et al. (2009), Deshler et al. (2008) and Smit et al (2007). Model profiles of the o-suite are compared to balloon sondes measurement data of 44 stations for the period January 2013 to February 2020 (please note that towards the end of the validation period fewer soundings are available). As C-IFS-CB05 stratospheric composition products beyond O₃ in the o-suite is not useful we provide only a very limited evaluation of the control experiment. A description of the applied methodologies and a map with the sounding stations can be found in Eskes et al. (2019). Please note that recent scientific findings (<https://tropo.gsfc.nasa.gov/shadoz/Archive.html>, Thompson et al., 2017; Witte et al., 2017; 2018, Stauffer, et al. in preparation 2020) show a drop-off in Total Ozone at various global ozone stations in comparison with satellite instruments. This drop-off amounts between 5-10% for stratospheric ozone. Changes in the ECC ozone instrument are associated with the drop-off, but no single factor has been identified as cause yet.

The o-suite shows MNMBs within the range $\pm 14\%$, for all regions and months (some exceptions with MNMBs of up to $\pm 18\%$ for single months in the high latitude regions). Figure 9.1.1 shows the results for the past year.

Fig. 9.1.2 compares the averaged profiles in each region during April 2020. The vertical distribution of stratospheric ozone is quite well represented for all regions by the o-suite (MNMBs between -1.8 to 7.4% for MAM 2020). Over the Arctic, there was a big ozone hole in spring this year visible in the reduced partial pressure between 80 and 40 hPa over the Arctic in Fig.9.1.2. While the o-suite reproduces stratospheric ozone, the control run shows an overestimation of stratospheric ozone for all regions stratosphere and underestimations for Antarctica.

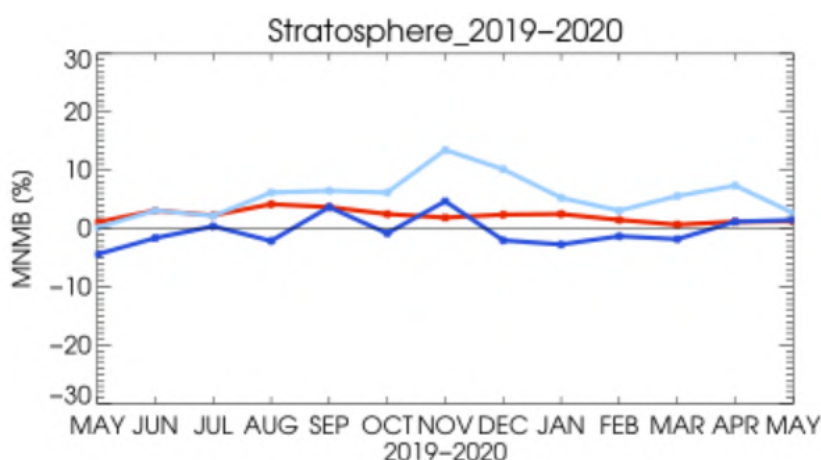


Figure 9.1.1: MNMBs (%) of ozone in the stratosphere from the o-suite against aggregated sonde data in the Arctic (light blue), Antarctic (dark blue) and northern midlatitudes (red). Period May 2019 to May 2020. The stratosphere is defined as the altitude region between 90 and 10 hPa.

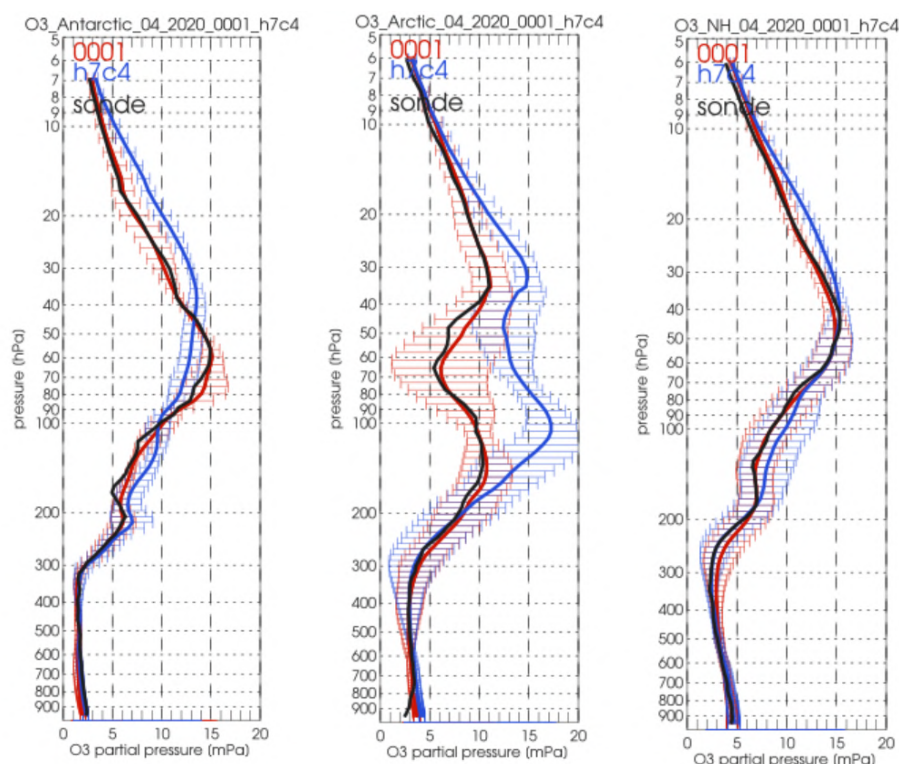


Figure 9.1.2: Comparison between mean O₃ profiles (units: mPa) of o-suite (red), and control (blue) in comparison with observed O₃ sonde profiles (black) for April 2020 for the various latitude bands: Arctic, NH-mid latitudes and Antarctic.

9.2 Validation against observations from the NDACC network

UVVIS column and FTIR stratospheric columns

Since the start of the CAMS27 project, the number of UVVIS Zenith ozone measurements have increased on NDACC. Currently 14 sites provided data in the recent quarter allowing for a representative picture on the latitude dependence of the o-suite runs.

The systematic uncertainty of the UVVIS measurements is typically 5%, hence the relative biases for most sites for both the AN and 1d FC of the o-suite are very close to each other and within the uncertainty ranges, see Figure 9.2.1. The averaged bias for the 14 UVVIS sites is comparable to the measurement uncertainty of 5%, the averaged correlation is 0.84 during this quarter and did not change compared to the previous quarter.

The correlations between the sites and o-suite are presented in the Taylor diagrams in Figure 9.2.2. Again, the o-suite AN and 1d FC perform very similarly in correlation coefficients.

Figure 9.2.3 depicts the FTIR stratospheric columns showing a discontinuity in the o-suite 1d FC for the tropical sites (Mauna Loa, Altimoni and Reunion) in the June 2016 model update. The worse performance of the tropical sites is also seen in lower correlations in Figure 9.2.2 and Table 9.2.1.

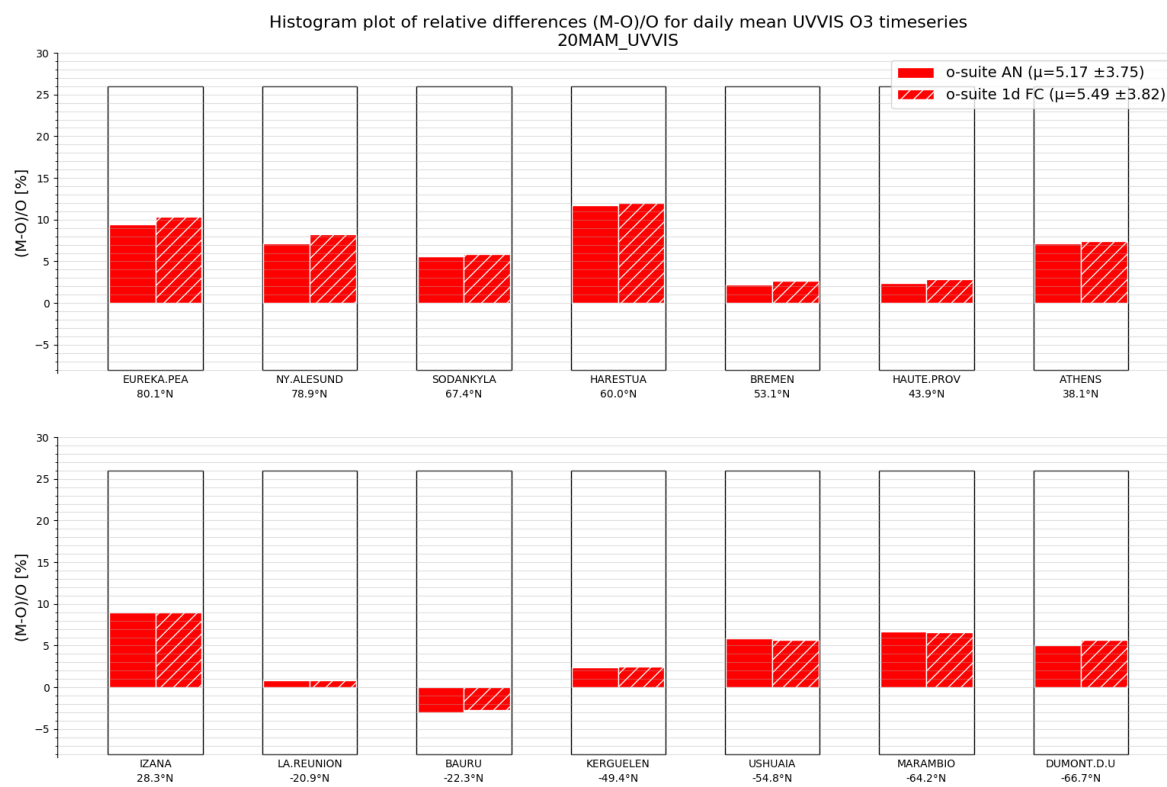


Figure 9.2.1 Relative biases during quarter MAM 2020 for 14 UVVIS stations measuring stratospheric ozone columns with ZENITH measurement geometry (stations sorted with decreasing latitude). The overall relative bias is positive for all latitudes and comparable to the typical measurement uncertainty of 5% for most of the sites.

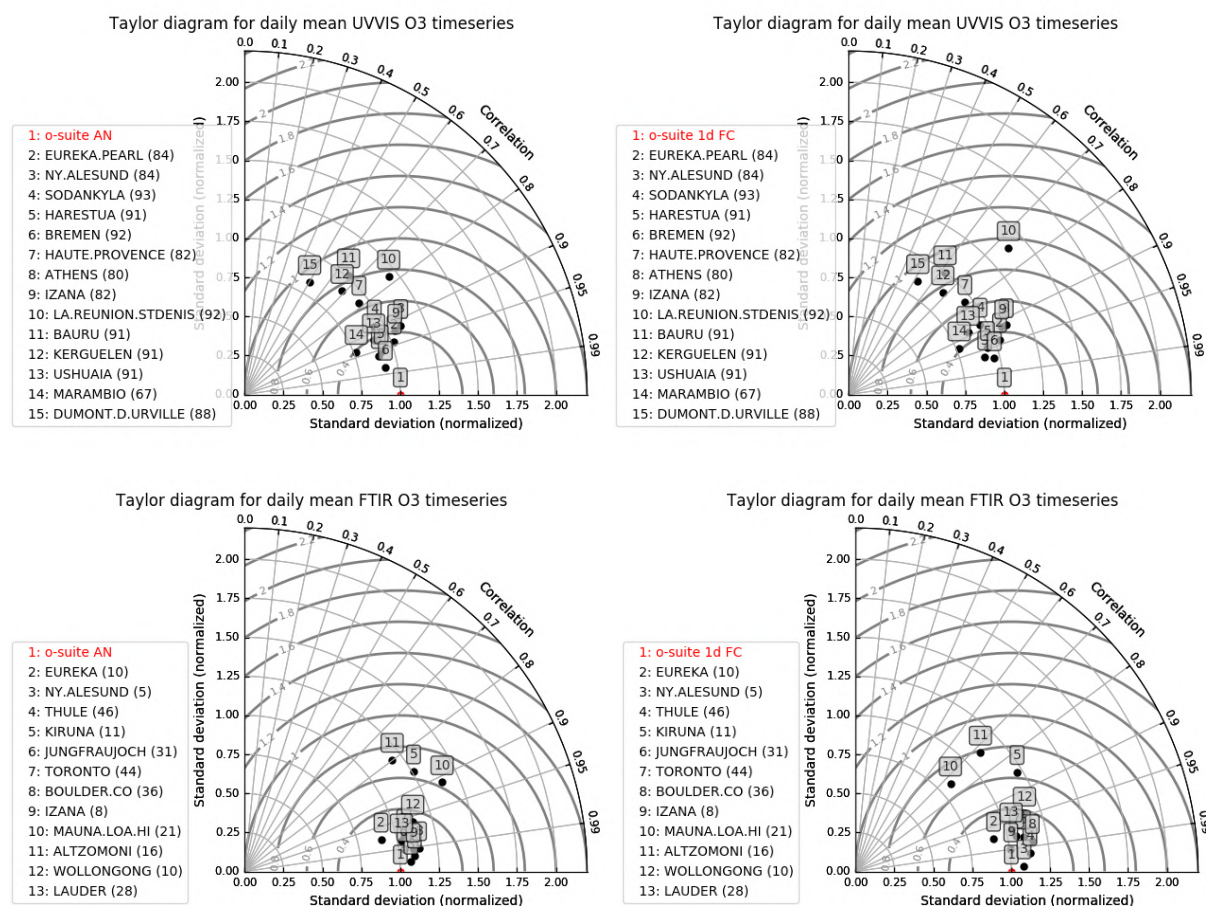


Figure 9.2.2. Taylor diagrams relating the standard deviations for the model and GB stratospheric column time series and their correlation for the time period MAM-2020. All time-series are normalized such that the standard deviation of the model is 1. The performance for the o-suite is slightly better (averaged correlation is 0.95 for FTIR and 0.84 for UVVIS) compared to the 1-day forecast (averaged correlation is 0.93 for FTIR and 0.84 for UVVIS). The correlation for the tropical sites Altzomoni and Mauna Loa are worse in the 1-day forecast compared to the analysis.



Table 9.2.1: Detailed statistics for stratospheric ozone column comparisons for UVVIS and FTIR measurements during MAM 2020. FTIR Tropical sites at Mauna Loa and Altzomoni perform worse in the o-suite 1d FC. Standard deviations (std) are relative to the std of the o-suite.

UVVIS site	o-suite AN					o-suite 1d FC					lat
	#	rel. std	corr	rel diff (%)	rel diff std(%)	#	rel. std	corr	rel diff (%)	rel diff std(%)	
EUREKA.PEARL	84	1	0.94	9.47	7.03	84	1	0.94	10.33	7.26	80.1
NY.ALESUND	84	0.9	0.96	7.13	4.88	84	0.9	0.97	8.2	4.57	78.9
SODANKYLA	93	0.9	0.89	5.6	7.64	93	1	0.88	5.84	7.69	67.4
HARESTUA	91	0.9	0.95	11.75	3.57	91	0.9	0.95	12.01	3.73	60
BREMEN	92	0.9	0.98	2.23	1.58	92	1	0.97	2.7	1.9	53.1
HAUTE.PROVENCE	82	0.9	0.78	2.35	5.11	82	1	0.78	2.88	5.05	43.9
ATHENS	80	1.1	0.92	7.11	3.67	80	1.1	0.92	7.42	3.71	38.1
IZANA	82	1	0.92	8.94	2.45	82	1.1	0.91	8.99	2.55	28.3
LA.REUNION.STDENIS	92	1.2	0.77	0.84	2.05	92	1.4	0.74	0.87	2.18	-20.9
BAURU	91	1	0.66	-3.02	1.92	91	1	0.62	-2.76	2.04	-22.3
KERGUELEN	91	0.9	0.69	2.43	7.48	91	0.9	0.68	2.46	7.68	-49.4
USHUAIA	91	0.9	0.92	5.88	2.52	91	0.9	0.89	5.68	3.12	-54.8
MARAMBIO	67	0.8	0.93	6.72	2.83	67	0.8	0.92	6.56	2.99	-64.2
DUMONT.D.URVILLE	88	0.8	0.5	5.01	7.91	88	0.9	0.52	5.69	7.66	-66.7
		1	0.84	5.17	4.33		1	0.84	5.49	4.44	

FTIR site	o-suite AN					o-suite 1d FC					lat
	#	rel. std	corr	rel diff (%)	rel diff std(%)	#	rel. std	corr	rel diff (%)	rel diff std(%)	
EUREKA	10	0.9	0.97	-2.08	2.18	10	0.9	0.97	-0.74	2.08	80.1
NY.ALESUND	5	1.1	1	-0.81	2.39	5	1.1	1	1.07	2.57	78.9
THULE	46	1.1	1	-3.64	2.05	46	1.1	0.99	-2.8	2.69	76.5
KIRUNA	11	1.3	0.86	-2.27	4.22	11	1.2	0.85	-2.36	4.31	67.8
JUNGFRAUJOCH	31	1	0.99	-4.38	1.09	31	1.1	0.98	2.18	1.83	46.6
TORONTO	44	1	0.98	-3.91	2.27	44	1.1	0.98	-4.25	2.2	43.6
BOULDER.CO	36	1.1	0.99	-4.64	1.31	36	1.2	0.99	-8.06	1.52	40
IZANA	8	1.1	0.99	-2.45	1.07	8	1	0.99	0.84	1.18	28.3
MAUNA.LOA.HI	21	1.4	0.91	-4.94	1.19	21	0.8	0.73	5.69	2.36	19.5
ALTZOMONI	16	1.2	0.8	-1.18	1.73	16	1.1	0.72	2.6	2.12	19.1
WOLLONGONG	10	1.1	0.96	1.68	1.66	10	1.1	0.95	1.47	1.84	-34.4
LAUDER	28	1	0.98	-2.59	1.2	28	1	0.97	-3.04	1.6	-45
		1.1	0.95	-2.6	1.86		1.1	0.93	-0.62	2.19	

Profile comparison using LIDAR and MWR

In this section we present a comparison between the CAMS o-suite and control products against MWR and LIDAR observations from the NDACC network. A detailed description of the instruments and applied methodologies for all NDACC instruments can be found at <http://nors.aeronomie.be>. MWR (microwave) at Ny Alesund (79°N, 12°E, Arctic station) and Bern (47°N, 7°E, northern midlatitude station). LIDAR at Observatoire Haute Provence (OHP), France (43°N, 5.7°E, altitude 650m), Hohenpeissenberg, Germany (47°N, 11°E, altitude 1km) and Mauna Loa, Hawaii (19.5°N, 204°E, altitude 3.4km)

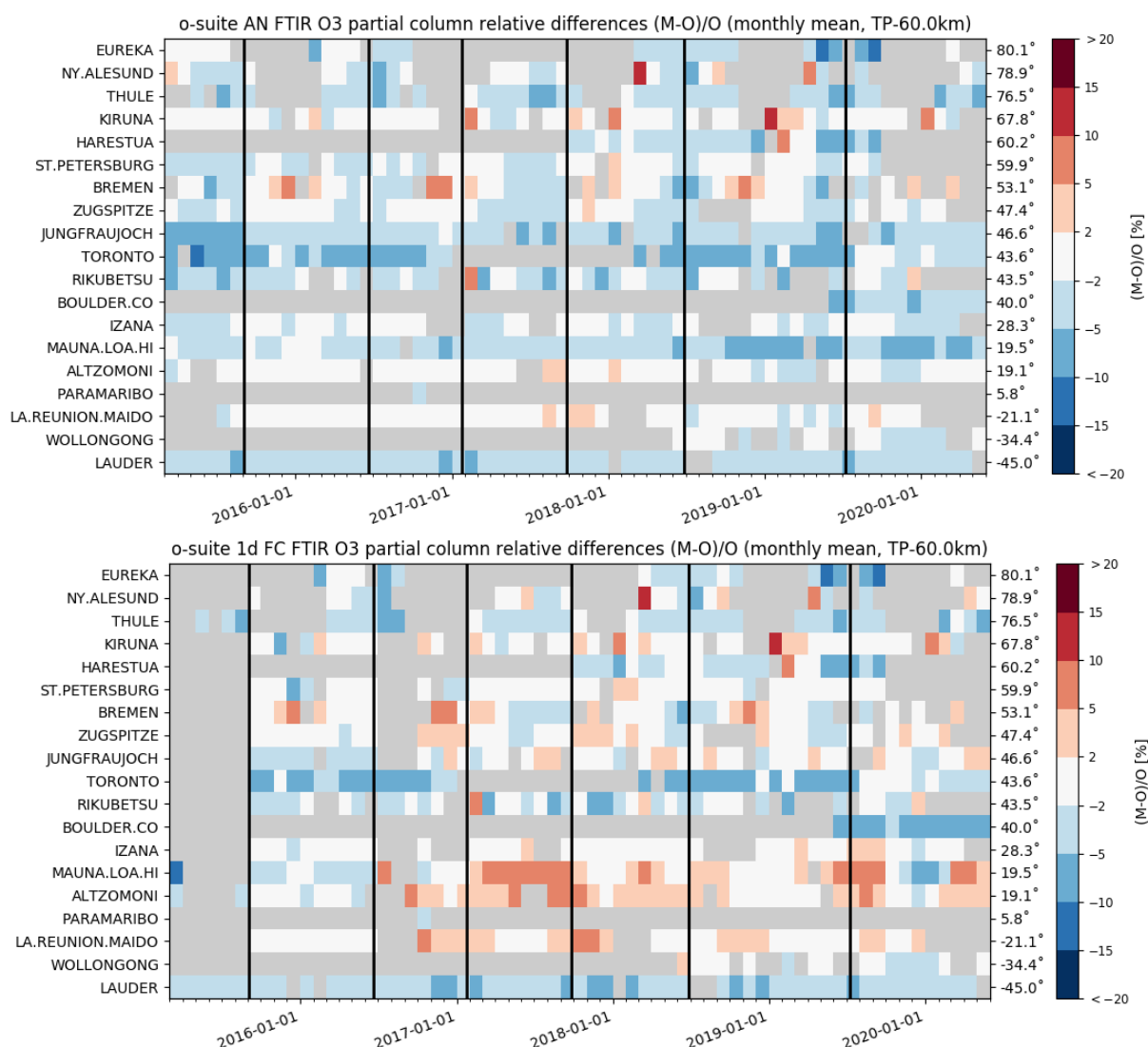
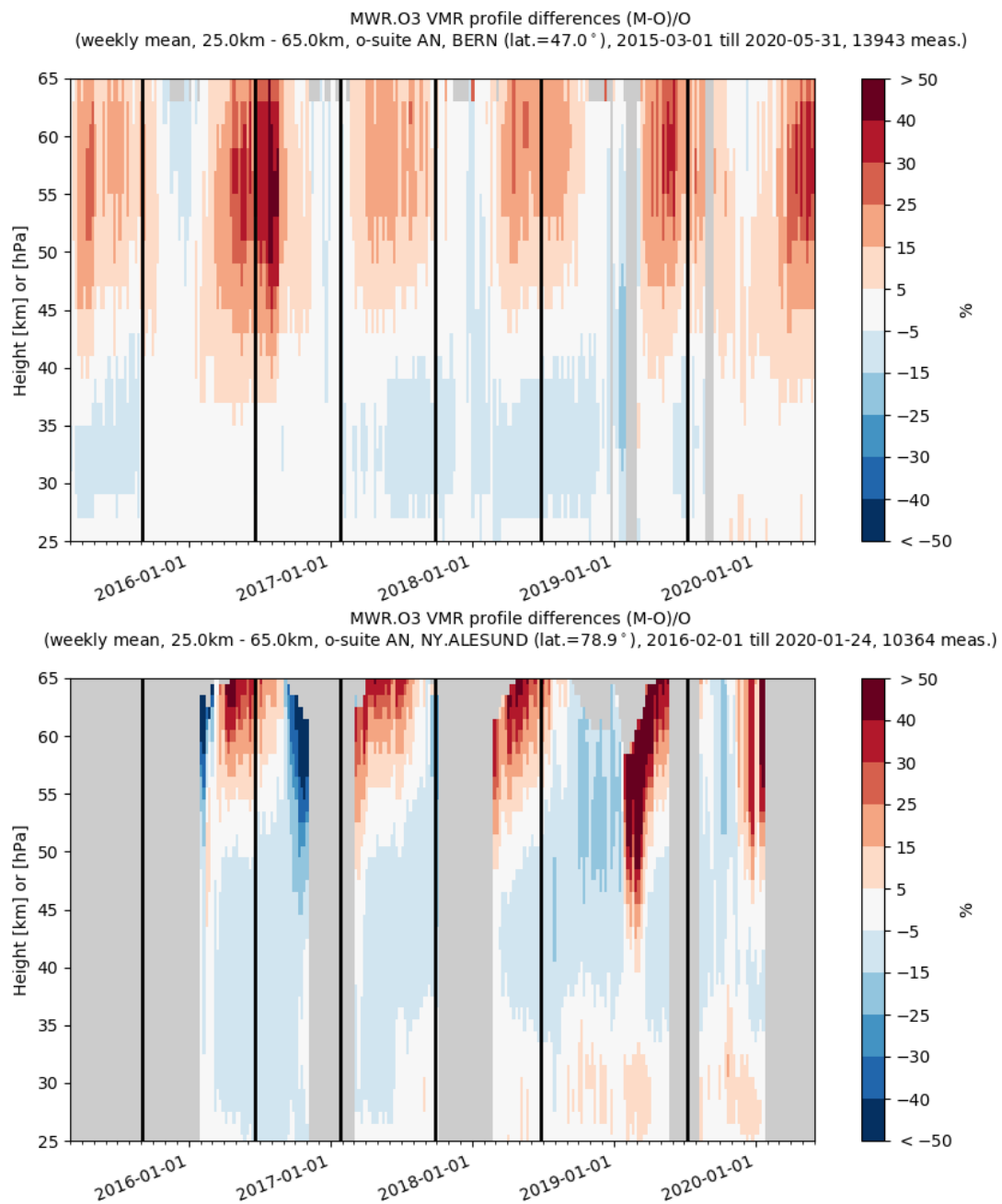


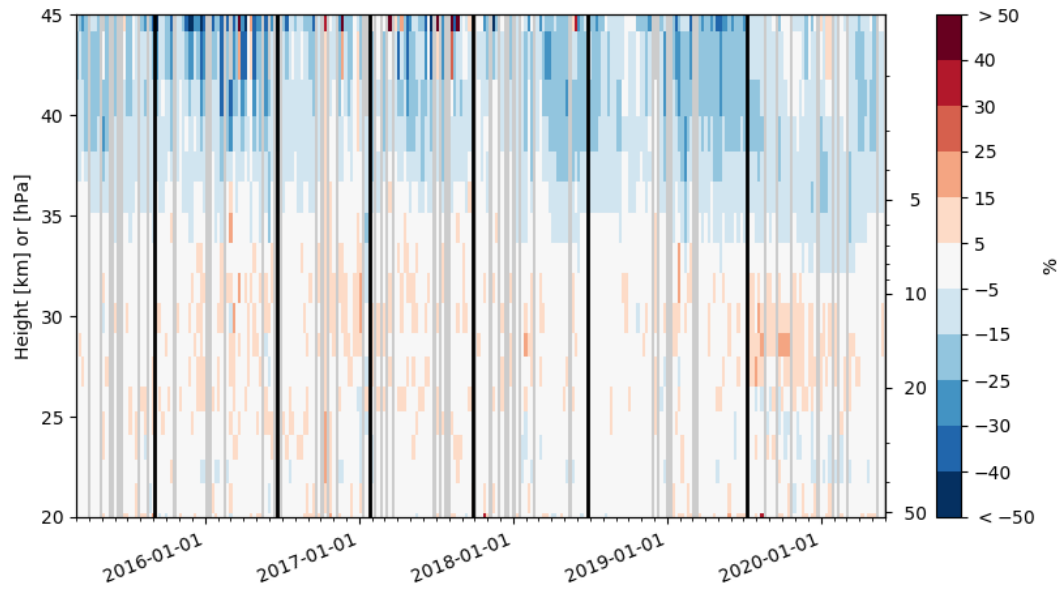
Figure 9.2.3 Time series of monthly mean relative differences for stratospheric FTIR columns along with model cycle updates (black vertical lines) (o-suite AN top, o-suite 1d FC bottom). The stratospheric FTIR columns for the tropical sites at Izana, Mauna Loa, Altimoni and Reunion show a higher overestimation for the 1dFC compared to the AN.

At OHP, Hohenpeissenberg and Mauna Loa (LIDAR, see Figure 9.2.4), the o-suite slightly overestimates the observed ozone (<10%) between 25km and 35km. The uncertainty on the LIDAR concentration increases with altitude and above 35km the observed differences are comparable to the measurement uncertainty (>10%, see http://nors.aeronomie.be/projectdir/PDF/NORS_D4.2_DUG.pdf).

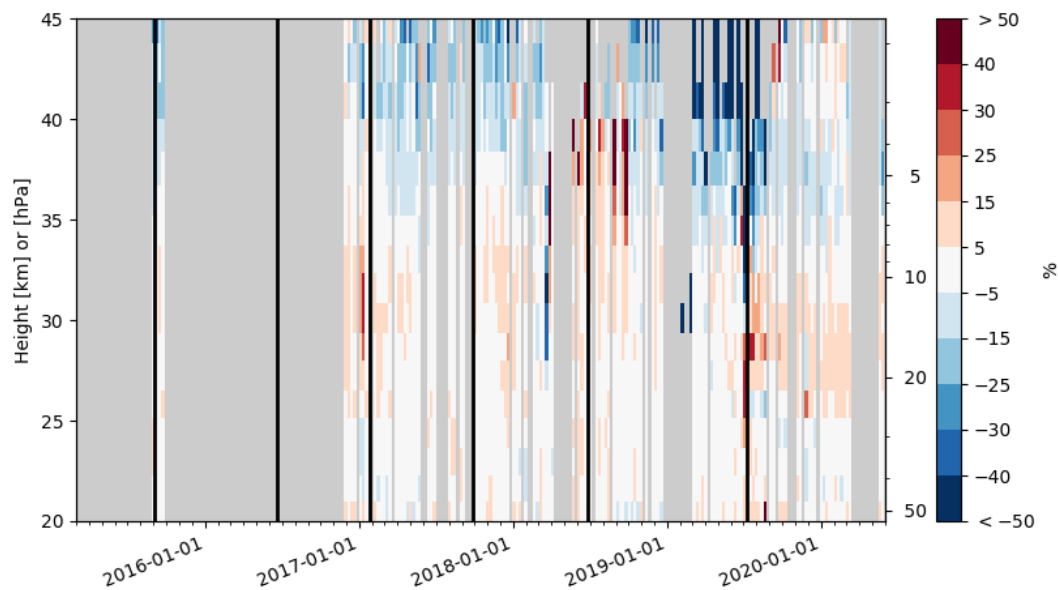


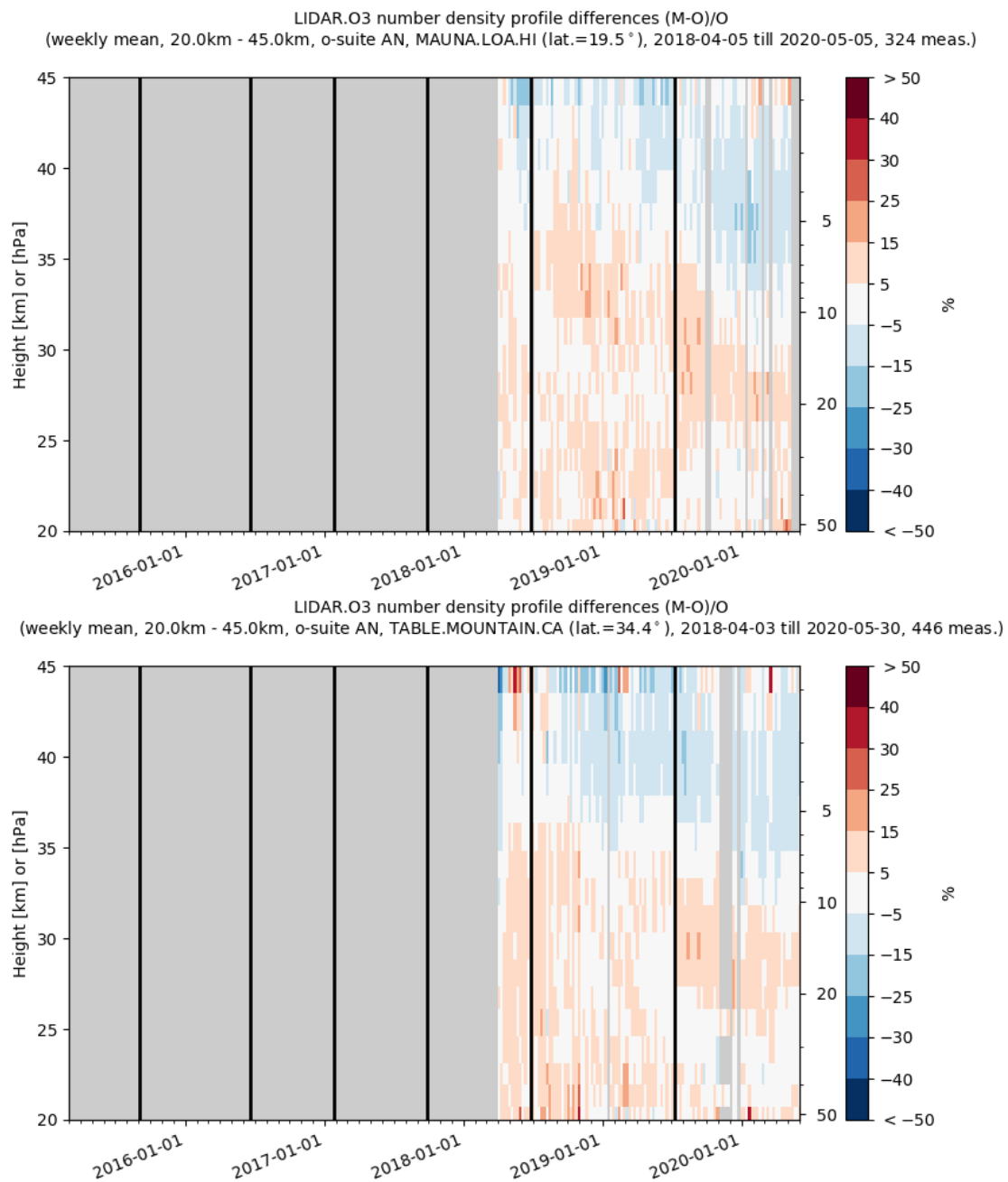


LIDAR.O3 number density profile differences (M-O)/O
(weekly mean, 20.0km - 45.0km, o-suite AN, HOHENPEISSENBERG (lat.=47.8°), 2015-03-06 till 2020-05-29, 596 meas.)



LIDAR.O3 number density profile differences (M-O)/O
(weekly mean, 20.0km - 45.0km, o-suite AN, HAUTE.PROVENCE (lat.=43.9°), 2015-09-01 till 2020-05-27, 412 meas.)





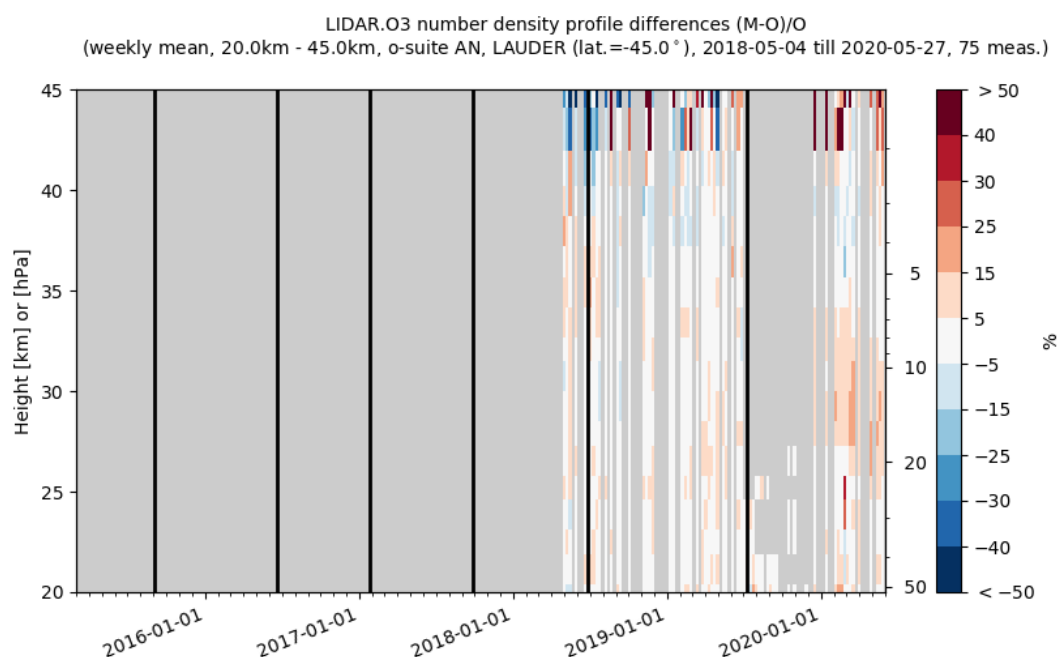


Figure 9.2.4: Comparison of the weekly mean profile bias between the O₃ mixing ratios of o-suite AN and the NDACC station at Ny Alesund, Bern, Hohenpeissenberg, OHP, Mauna Loa, Table Mountain and Lauder. For the LIDAR stations, the measurement uncertainty above 35km is comparable to the observed profile bias.

9.3 Comparison with dedicated systems and with observations by limb-scanning satellites

This section compares the output of the o-suite for the last period with observations by limb-scanning satellite instruments, using the methodology described by Lefever et al. (2015). We also include the comparisons for the o-suite 4th day forecasts (96h to 120h) of stratospheric ozone. These forecasts are represented by dotted lines in the figures.

All datasets are averaged over all longitudes and over the three most interesting latitude bands for stratospheric ozone: Antarctic (90°S-60°S), Tropics (30°S-30°N) and Arctic (60°N-90°N). In order to provide global coverage, the two mid-latitude bands (60°S-90°S and 60°N-90°N) are also included in some comparisons with satellite observations.

The level-2 data from limb scanning instrument used in this section are:

- ACE-FTS version 3.6, on board SCISAT-1
- SAGE-III version 5.1, on board the International Space Station (ISS); among the 3 different ozone profiles delivered by the solar occultation (denoted Mesospheric, MLR and AO3), we use the AO3 retrieval which is recommended by the mission science team.
- OMPS-LP version 2.5, on board NPP

For reference, we include also the BASCOE analyses which are very constrained by the AURA MLS offline profiles.

o3 relative bias against observations: 10-30hPa mean from 20170601 to 20200601

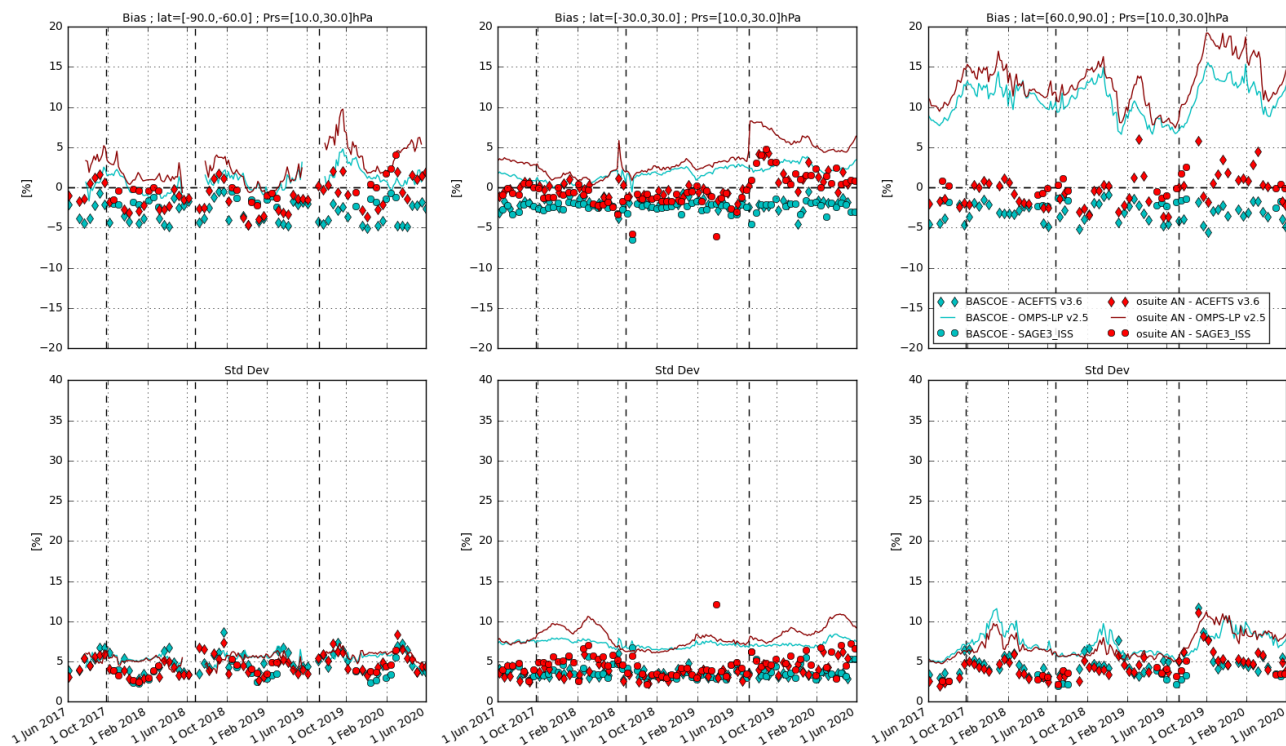


Figure 9.3.1: Time series comparing model runs to observations for the period 2017-06-01 to 2020-06-01 in the upper stratosphere (10-30hPa averages): o-suite analyses (red) and BASCOE (cyan) vs OMPS-LP (solid), ACE-FTS (diamonds) and SAGE-III (bullets). Top row, normalized mean bias (model-obs)/obs (%); bottom row, standard deviation of relative differences (%). Vertical dashed lines indicate the date of CAMS model updates.

o3 relative bias against observations: 30-70hPa mean from 20170601 to 20200601

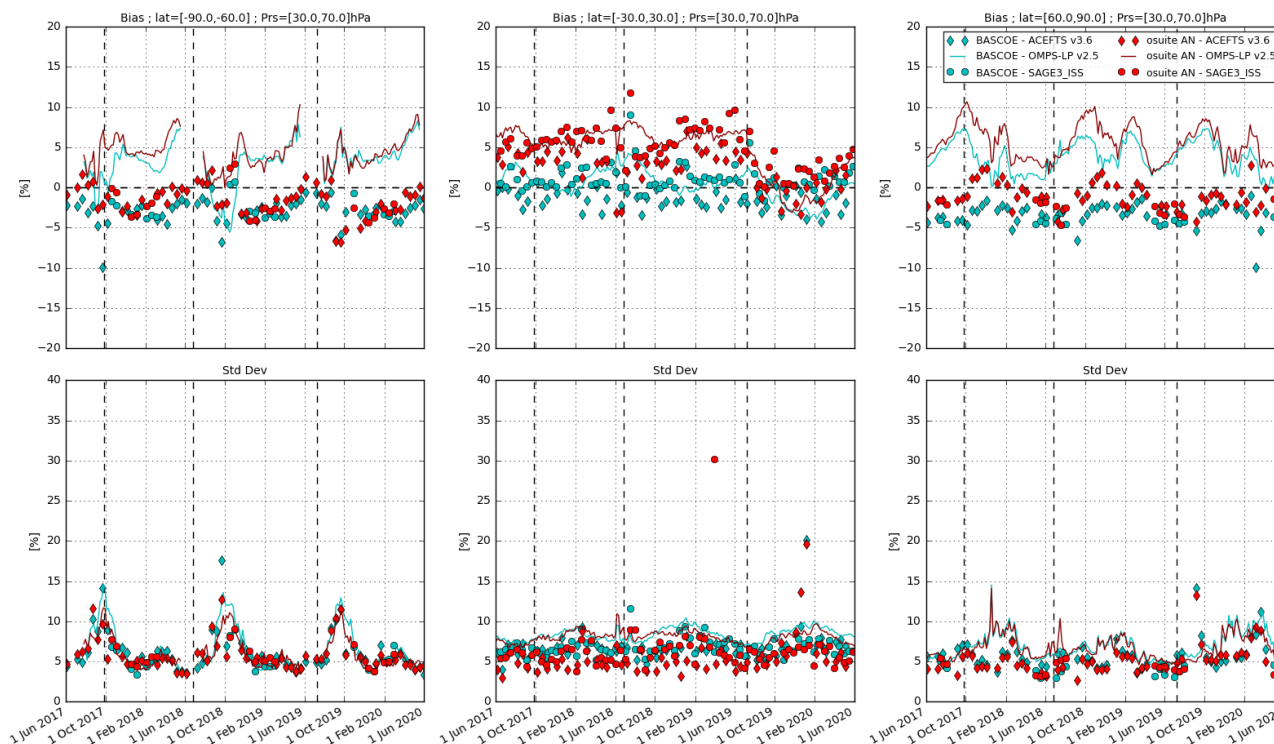


Figure 9.3.2: Time series comparing model runs to observations for the period 2017-06-01 to 2020-06-01 in the middle stratosphere (30-70hPa averages): o-suite analyses (red) and BASCOE (cyan) vs OMPs-LP (solid), ACE-FTS (diamonds) and SAGE-III (bullets). Top row, normalized mean bias (model-obs)/obs (%); bottom row, standard deviation of relative differences (%). Vertical dashed lines indicate the date of CAMS model updates.

Figure 9.3.1 to 9.3.3 present, in the upper row, the time series over the last 36 months of the bias of the o-suite against the three satellite measurements for respectively three layers of the stratosphere (10-30hPa upper, 30-70hPa middle, and 70-100hPa lower and UTLS); the bottom row of the figures shows the standard deviation of the differences and can be used to evaluate the random error in the analyses.

In the tropics for the 70-100hPa region, the comparison with all instruments is unreliable (highly scattered bias and large standard deviations)

The agreement with ACE-FTS is good: the bias is generally within $\pm 5\%$ for all regions.

The SAGE-III onboard ISS provide observations since June 2017. The latitudinal coverage is more limited than ACE-FTS; the polar regions are not covered for long periods of time (data available only in the summer). Where available, the agreement of the o-suite with SAGE-III is good, with biases similar to those observed against ACE-FTS, except in the tropics in the 30-70hPa region where they are more positive (3-13%).

o3 relative bias against observations: 70-100hPa mean from 20170601 to 20200601

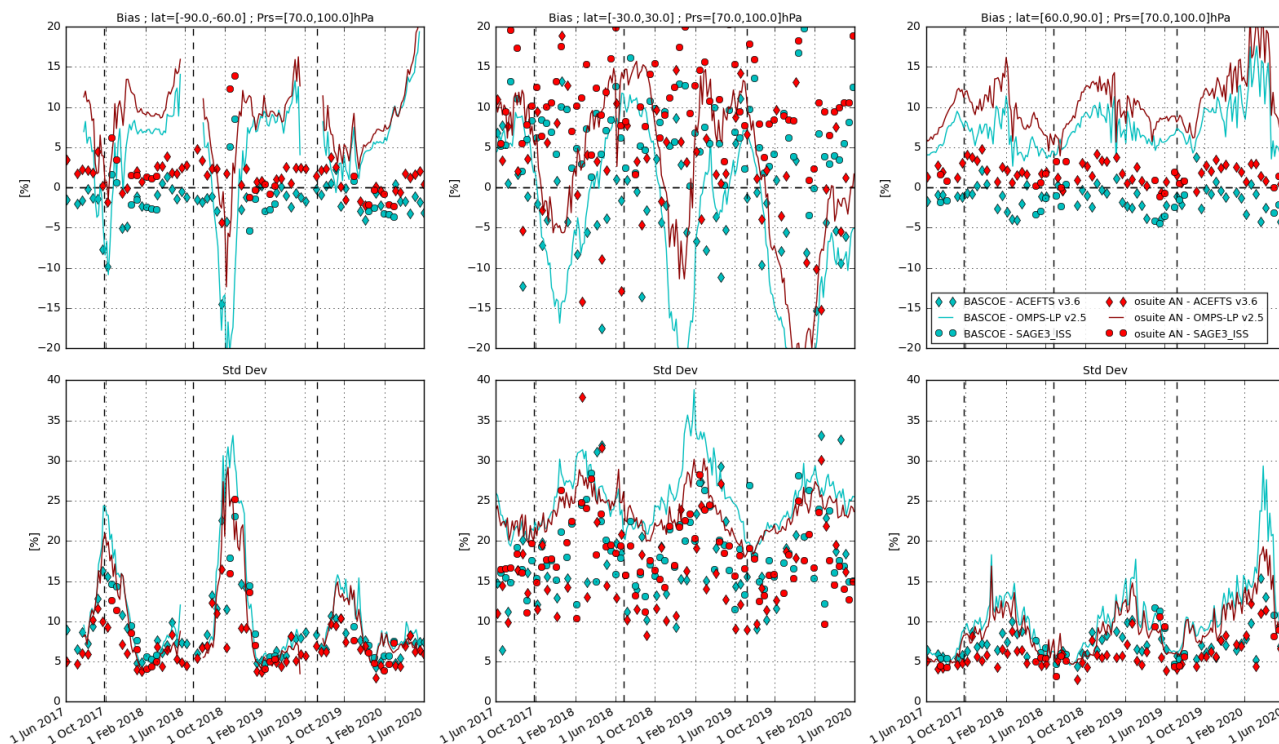


Figure 9.3.3: Time series comparing model runs to observations for the period 2017-06-01 to 2020-06-01 in the lower stratosphere (70-100hPa averages): o-suite analyses (red) and BASCOE (cyan) vs OMPS-LP (solid), ACE-FTS (diamonds) and SAGE-III (bullets). Top row, normalized mean bias (model-obs)/obs (%); bottom row, standard deviation of relative differences (%). Vertical dashed lines indicate the date of CAMS model updates.

Compared to OMPS-LP, there is an almost systematic overestimation by the o-suite; the biases are more variable and more marked than for the other instruments (10% to 15% in the north polar at 10-30hPa region, up to 10% at 30-70hPa and up to 20% at 70-100hPa), so this may in fact be a systematic underestimation by OMPS.

The bias of BASCOE against the satellite observations for the considered regions is systematically lower, but follows a similar evolution as the o-suite. Using the BASCOE bias as a reference for the evolution of the o-suite bias, the change of model settings in the o-suite in July 2019 causes an increase of ~3% in the 10-30hPa pressure range, and a decrease of ~3% in the Tropics in the 30-70hPa, which is confirmed for this period MAM 2020.

Figure 9.3.4 to 9.3.7 display vertical profiles of the relative biases between the o-suite or BASCOE and the satellite measurements. The difference is averaged over the most recent 3-month period considered in this validation report, i.e. MAM 2020.

All o-suite profiles present a common feature of a slight overestimation at around 30km, followed by a stronger underestimation at around 40km, which is evidenced in the 4th day forecast.

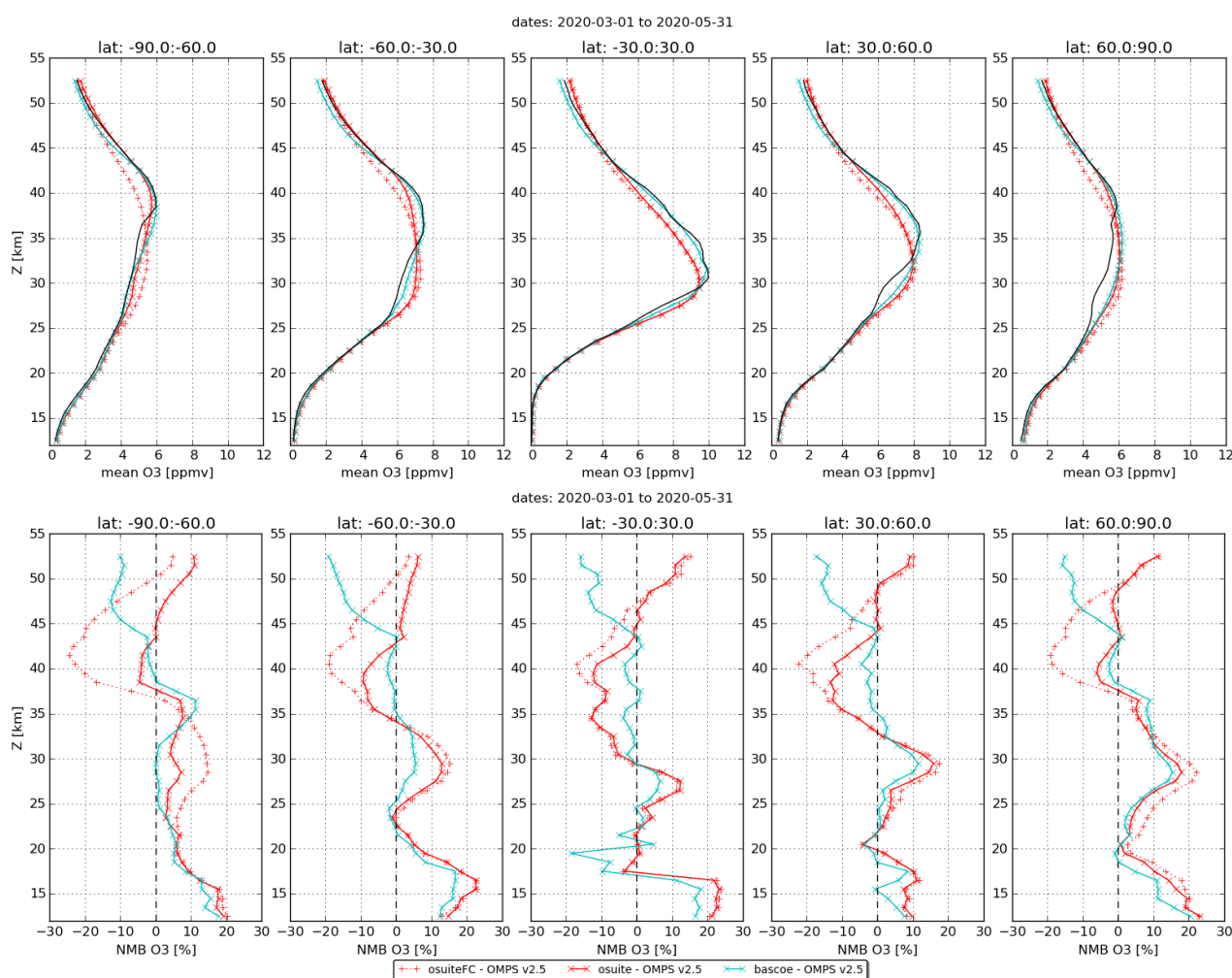


Figure 9.3.4: Mean value (top) and normalized mean bias (bottom) of the ozone profile between o-suite analyses (red, solid), o-suite forecasts 4th day (red, dotted) and BASCOE (cyan line) with OMPS-LP v2.5 observations for the period MAM 2020.

The profiles of OMPS-LP in the northern hemisphere present irregularities (mainly in the part contributed by the sensor in the visible), which are not found in the other instruments nor in the o-suite or the BASCOE models; hence they should be disregarded for this validation.

At the higher part of the north polar profiles, an overestimation of ~2 ppm is seen above 55km compared to ACE-FTS and 0.5 hPa compared to MLS. This is a typical phenomenon in the o-suite which appears systematically above the south polar region in the months of August-September and above the north polar region in February-March.

It must be noted that the different instruments have a variety of spatial and temporal coverage: for a 3 month period and over the latitude bands considered, OMPS and Aura MLS provide daily data with more than 40000 valid profiles, while ACE-FTS provides around 700 profiles in the polar region and 200 profiles in the tropics, and SAGE-III around 800 profiles in each latitude band except the south polar region (none).

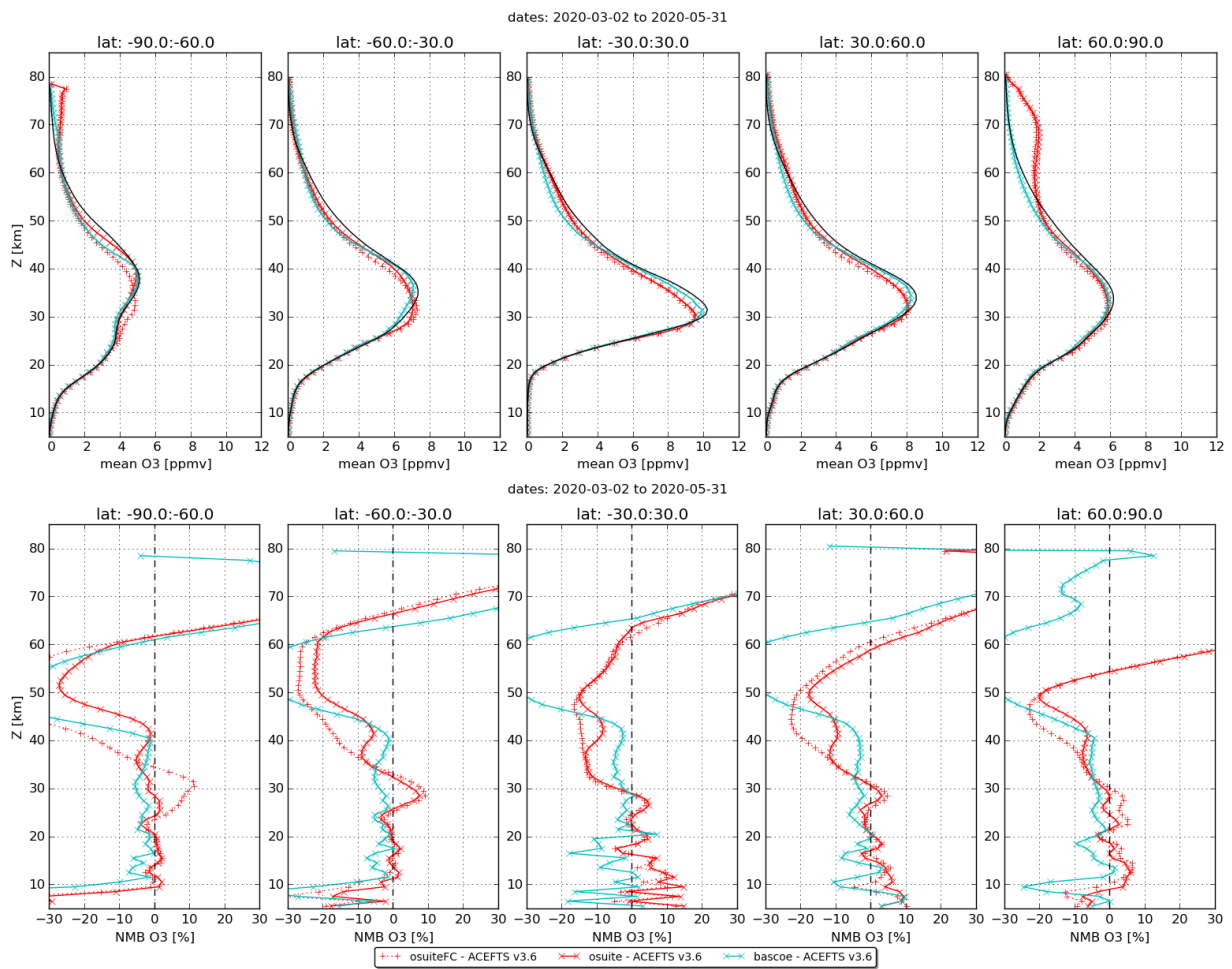


Figure 9.3.5: Mean value (top) and normalized mean bias (bottom) of the ozone profile between o-suite analyses (red, solid), o-suite forecasts 4th day (red, dotted) and BASCOE (cyan line) with ACE-FTS observations for the period MAM 2020.

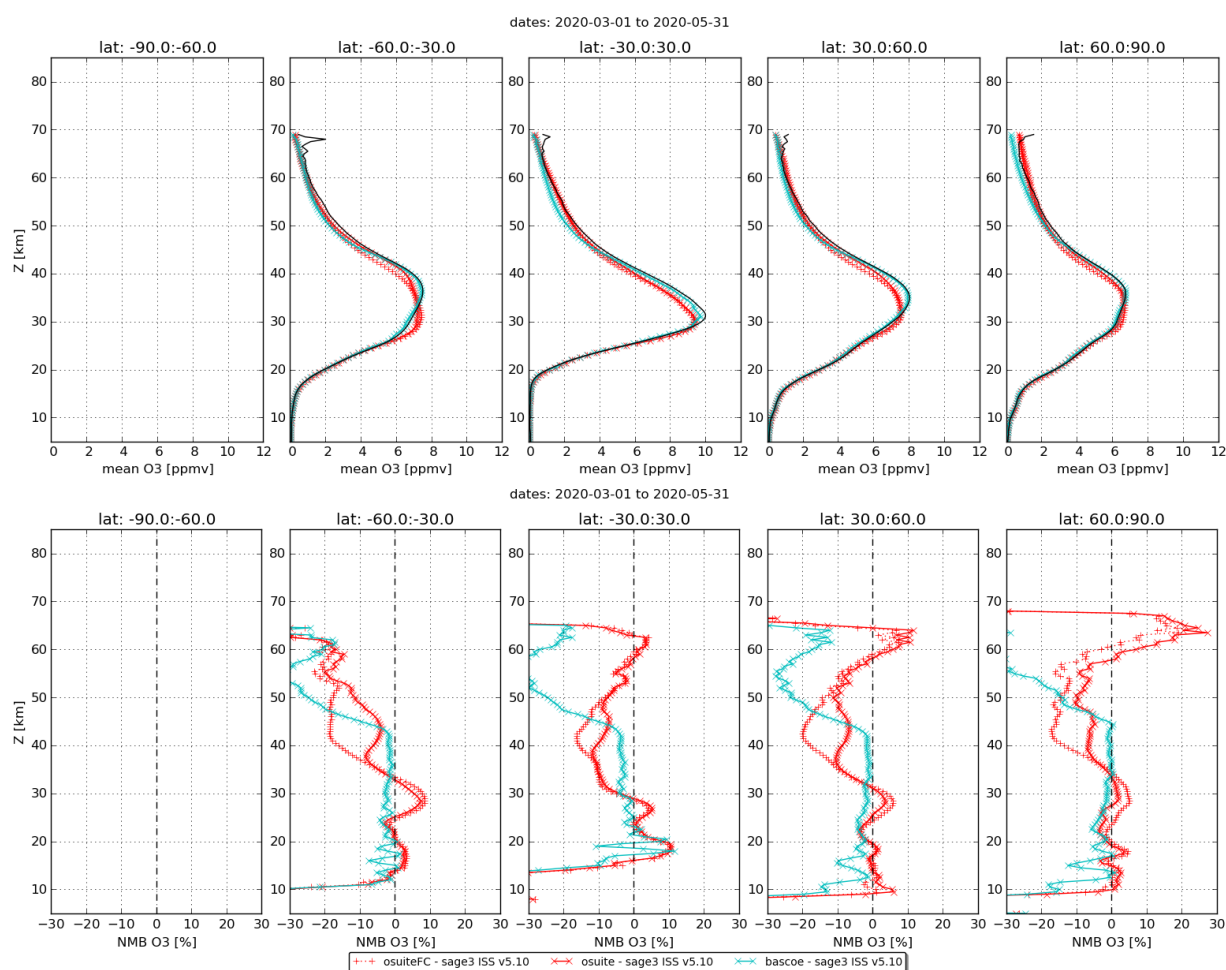


Figure 9.3.6: Mean value (top) and normalized mean bias (bottom) of the ozone profile between o-suite analyses (red, solid), o-suite forecasts 4th day (red, dotted) and BASCOE (cyan line) with SAGE-III observations for the period MAM 2020.

9.4 Stratospheric NO₂

The CAMS model uses a tropospheric chemistry scheme in combination with a parameterization for stratospheric ozone. Stratospheric ozone is also well constrained by satellite observations. Therefore, the only useful product in the stratosphere is ozone, and all other compounds, including NO₂, should not be used, as demonstrated by the validation results presented here.

In this section, nitrogen dioxide from SCIAMACHY/Envisat satellite retrievals (IUP-UB v0.7) and GOME-2/MetOp-A satellite retrievals (IUP-UB v1.0) are compared to modelled stratospheric NO₂ columns. Monthly mean stratospheric NO₂ columns from SCIAMACHY and GOME-2 have relatively small errors on the order of 20% in the tropics and in mid-latitudes in summer and even lower errors at mid-latitudes in winter. As the time resolution of the saved model files is rather coarse and NO_x photochemistry in the stratosphere has a large impact on the NO₂ columns at low sun, some uncertainty is introduced by the time interpolation at high latitudes in winter.

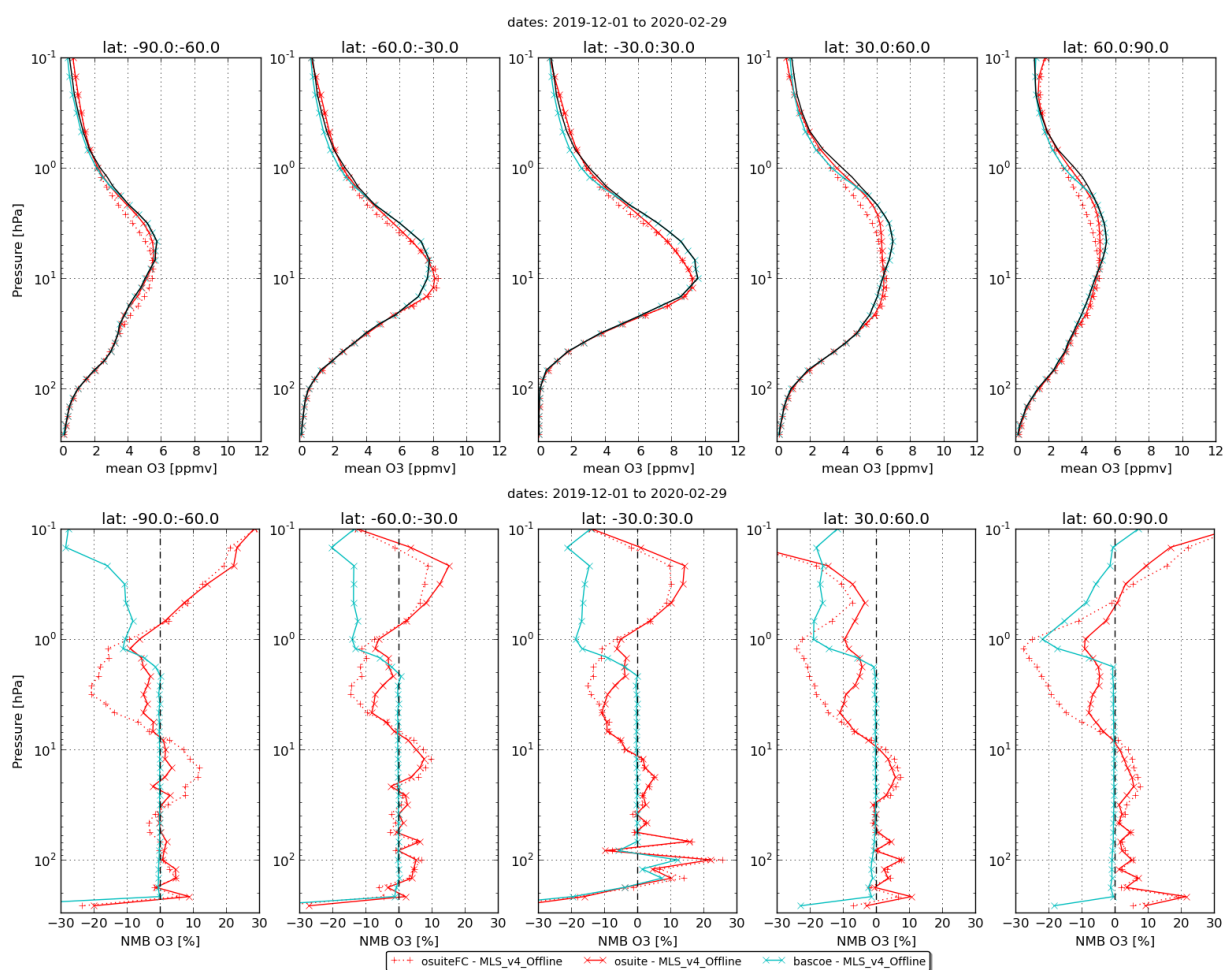


Figure 9.3.7: Mean value (top) and normalized mean bias (bottom) of the ozone profile between o-suite analyses (red, solid), o-suite forecasts 4th day (red, dotted) and BASCOE (cyan line) with MLS observations for the period MAM 2020.

As shown in Figure 9.4.1, amplitude and seasonality of satellite stratospheric NO₂ columns are poorly modelled with CB05-based chemistry runs including the more recent versions of the o-suite. The significant differences between observations and CB05 chemistry runs, i.e. a strong underestimation of satellite retrievals by models, can be explained by the missing stratospheric chemistry for these model versions. The only constraint on stratospheric NO_x is implicitly made by fixing the HNO₃/O₃ ratio at the 10 hPa level. This assumption, in combination with the changing model settings for stratospheric O₃ for control compared to MACC_CIFS_TM5, may explain some of the jumps we see in stratospheric NO₂. In any of these runs the stratospheric NO₂ is poorly constrained. It clearly indicates that stratospheric NO₂ in the latest versions of the o-suite is not a useful product and should be disregarded.

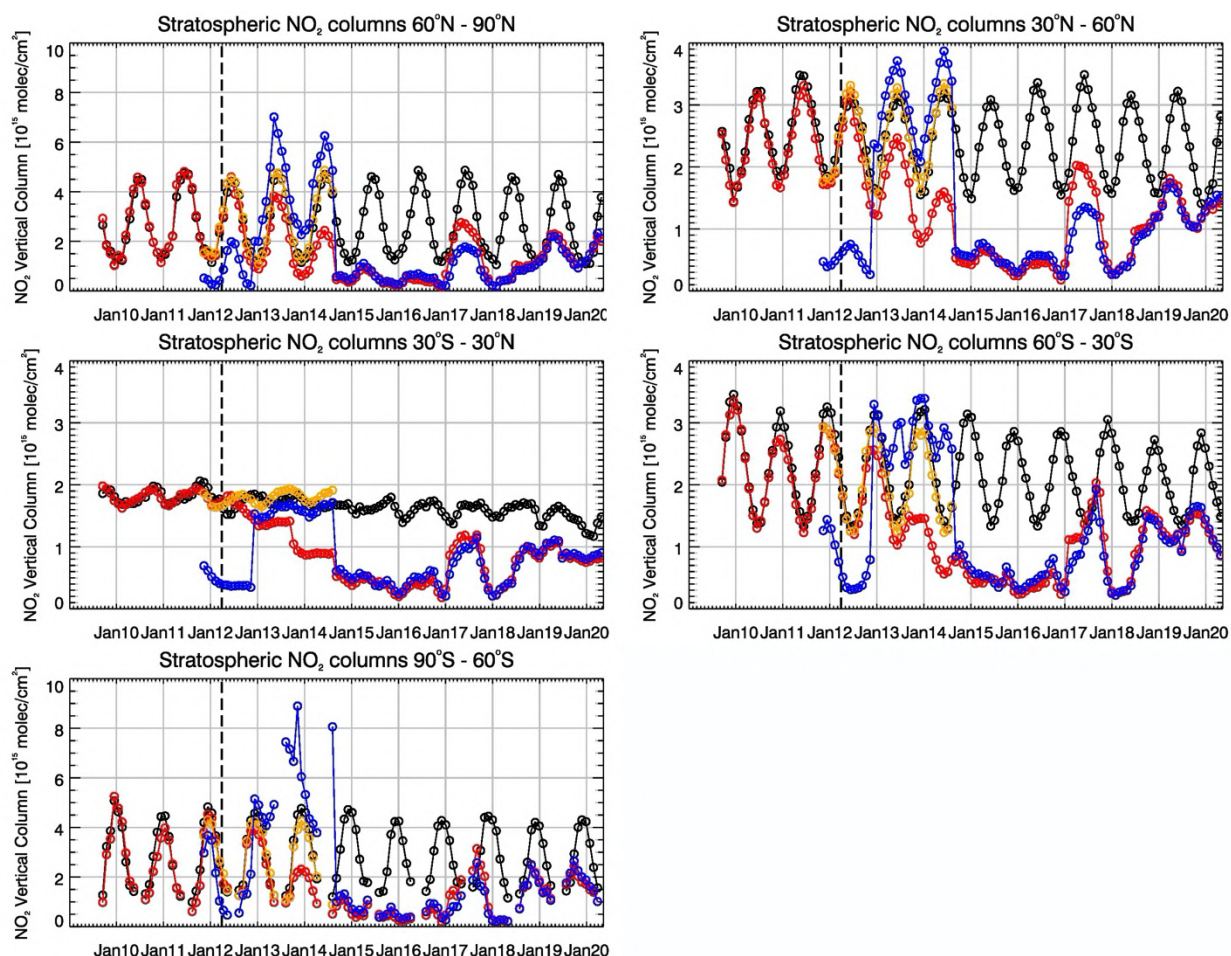


Figure 9.4.1: Time series of average stratospheric NO₂ columns [10^{15} molec cm⁻²] from SCIAMACHY (up to March 2012) and GOME-2 (from April 2012, black) compared to model results (red: o-suite, blue: MACC fcncrt TM5/MACC CIFS TM5/control, orange: MACC fcncrt MOZ) for different latitude bands. See text for details. The blue line shows MACC_fcncrt_TM5 from November 2011 to November 2012, MACC_CIFS_TM5 results from December 2012 until August 2014 and control results from September 2014 onwards (the model run without data assimilation is termed control since Sep 2014). The vertical dashed black lines mark the change from SCIAMACHY to GOME-2 based comparisons in April 2012.

Comparison of the o-suite from July 2012 until August 2014 with the other model runs and satellite observations shows that the previous version of the o-suite stratospheric NO₂ columns had a systematic low bias relative to those from MACC_fcncrt_MOZ and satellite observations for all latitude bands. For example, o-suite values are a factor of 2 smaller than satellite values between 60°S to 90°S for October 2013. Best performance was achieved with the MOZART chemistry experiments without data assimilation (MACC_fcncrt_MOZ, running until September 2014), especially northwards of 30°S. Details on the NO₂ evaluation can be found at: http://www.doas-bremen.de/macc/macc_veri_iup_home.html.



10. Validation results for greenhouse gases

This section describes the NRT validation of the pre-operational, high resolution forecast of CO₂ and CH₄ from 1st June 2019 to 1st June 2020 based on observations from 17 surface stations, located in Western Europe; 10 TCCON stations measuring XCO₂ and XCH₄ total columns, and 13 NDACC stations measuring partial and total CH₄ columns. We compare the observations to the high-resolution forecast experiments (*gznv/h9sp*, *Tco1279L137*; *9x9 km*), coupled to the analysis experiment (*gwx3/h72g*, *Tco399L137*, *25x25 km*). The *gznv/gwx3* experiments, based on IFS CY45R1, are used from 1st December 2018 to 30 November 2019. The *h9sp/h72g* experiments, based on IFS CY46R1, are used from 1st December 2019 onwards.

10.1 CH₄ and CO₂ validation against ICOS observations

The CO₂ and CH₄ simulations from the analysis and high resolution forecast have been compared to the 17 ICOS stations. The near-real time data processing of the in-situ measurements is ensured by the Atmospheric Thematic Center (Hazan et al., 2016). Among the 17 stations we can distinguish three sites located on top of mountains (PUY, JFJ, CMN), two background sites (PAL, ZEP) and 12 tall towers. For the later we consider only in this report the highest sampling levels which are at least at 100m above the ground.

Figure 10.1.1 shows the time varying biases (observations minus CAMS runs), averaged on a weekly basis, for all ICOS stations. The CO₂ biases from the previous experiments (prior to Dec.2019) were characterized by a clear seasonal cycles at most sites with maximum values in Summer/Autumn, and minimum in Winter/Spring. The new experiments, started on 1st Dec. 2019, correspond to a step change for all sites, and both in the forecast and analysis. The bias changes from positive to negative biases at all sites. Ispra (IPR), a tall tower located in the Po valley, appears as an outlier probably due to the complex orography. Two examples are detailed on Figure 10.1.2 for Jungfrauhoch (Switzerland) and Trainou tall tower (France). The first one is typical of the mountain sites, with an overestimation of the CO₂ concentration up to 2% in September 2019, decreasing down to 1% in December 2019, and close to zero at the beginning of the new experiment, but progressively increasing up to 1% in May 2020. Trainou is representative of most ICOS stations. The CO₂ bias is quite similar to JFJ with a less marked change between the two experiments in December 2019. The bias remains close to zero from December 2019 to April 2020, but the CAMS runs fails to reproduce the CO₂ decrease starting in mid-April due to the photosynthetic activity of plants in spring.

The seasonal cycle of the CO₂ bias calculated from the average of all European sites is shown on figure 10.1.4. It was ranging between 4 and 8 ppm from March 2019 to December 2019. With the new experiment started in December 2019 the mean European bias appears to be increasing from -2 to +3 ppm in May 2020. It should also be noted that the RMS are significantly higher in summer.

For CH₄ the figure 10.1.1 shows also a significant step change with the new experiments starting on December 2019, with similar feature on the high resolution forecast and the analysis. Before this date we observe two distinct patterns in the CAMS-observations differences: a seasonal and a

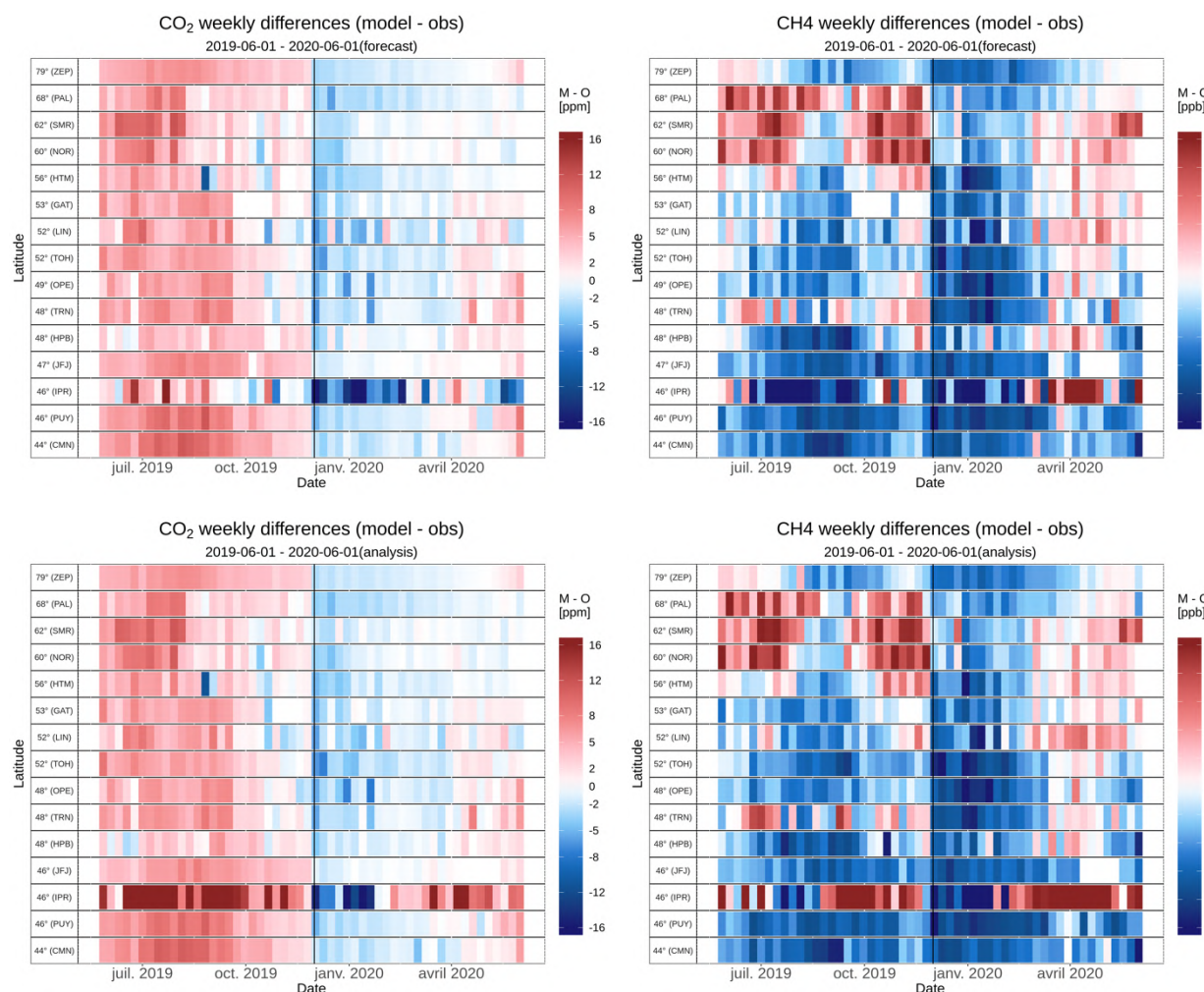


Figure 10.1.1: Mosaic plot of CO₂ (left, in ppm) and CH₄ (right, in ppb) biases of the CAMS high resolution forecast (top panel) and analysis (bottom panel), compared to surface station observations. Each vertical colored line represents a weekly mean.

latitudinal one. At the Scandinavian sites the CAMS runs overestimates (up to 50 ppb) the observations almost all along the year. The example of Norunda (Figure 10.1.3) clearly shows that both the baseline and the CH₄ spikes are overestimated by the CAMS runs, which could indicate that the wetland emissions are overestimated. There is only a period in August/September 2019 when the observations are greater than the simulated values (Figure 10.1.3). The more we go at lower latitudes, the more we observe negative biases. In Germany and North France the bias is negative in Summer/Autumn. Negative biases are observed all year long for the mountain sites of Puy de dome. Then from December to March 2019 we observe negative biases at all sites, ranging from 0 to -50 ppb. When considering the average signal from 15 European sites (Figure 10.1.4), we observe a mean positive bias up 20 ppb until May 2019, and negative bias (0 to -20 ppb) from June to November 2019. The new experiment did not improve the mean European bias which was about -30 ppb from December 2019 to February 2020, but it is close to zero since March 2020 (Figure 10.1.4).

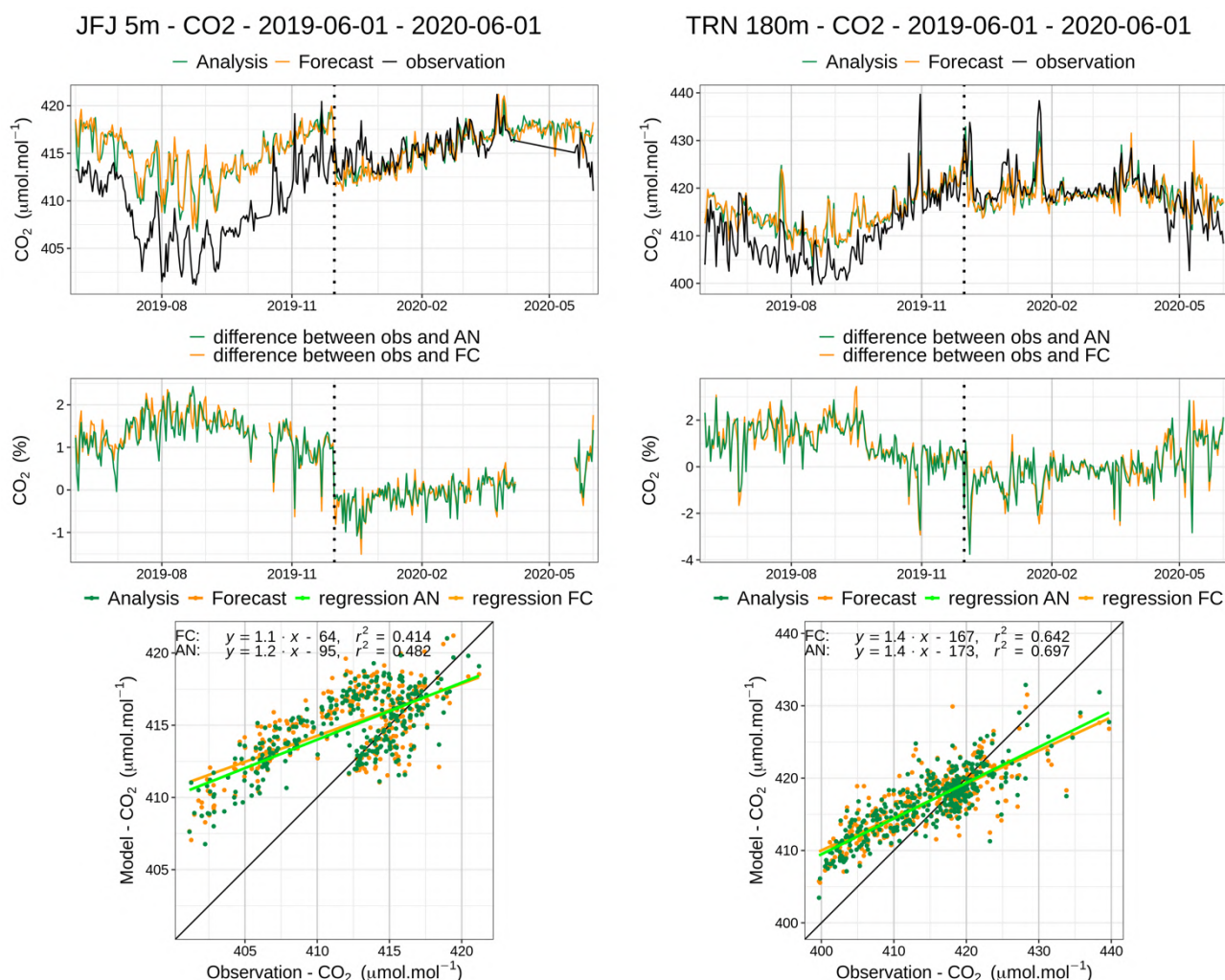


Figure 10.1.2: Comparison of CO₂ daily means observed (black) with the analysis run (green) and the high-resolution forecast (orange) at Jungfrau (left) and Trainou (right). Middle: differences of the observations minus the simulations. Below: Linear fit between observations and simulations. The dashed vertical line represents the change of experiments in December 2019.

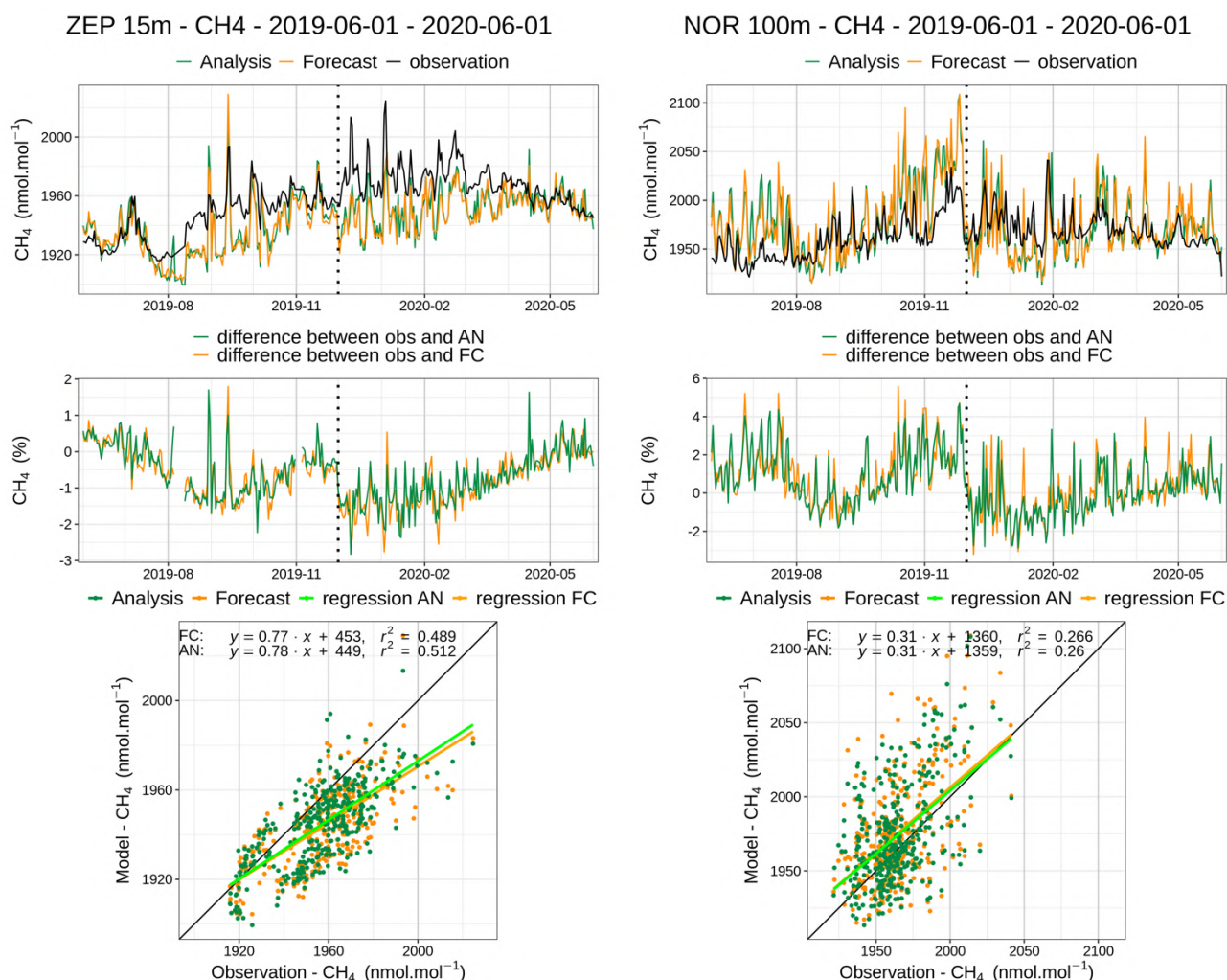


Figure 10.1.3: Comparison of CH₄ daily means observed (black) with the analysis run (green) and the high-resolution forecast (orange) at Zeppelin (left) and Norunda (right). Middle: differences of the observations minus the simulations. Below: Linear fit between observations and simulations. The dashed vertical line represents the change of experiments in December 2019.

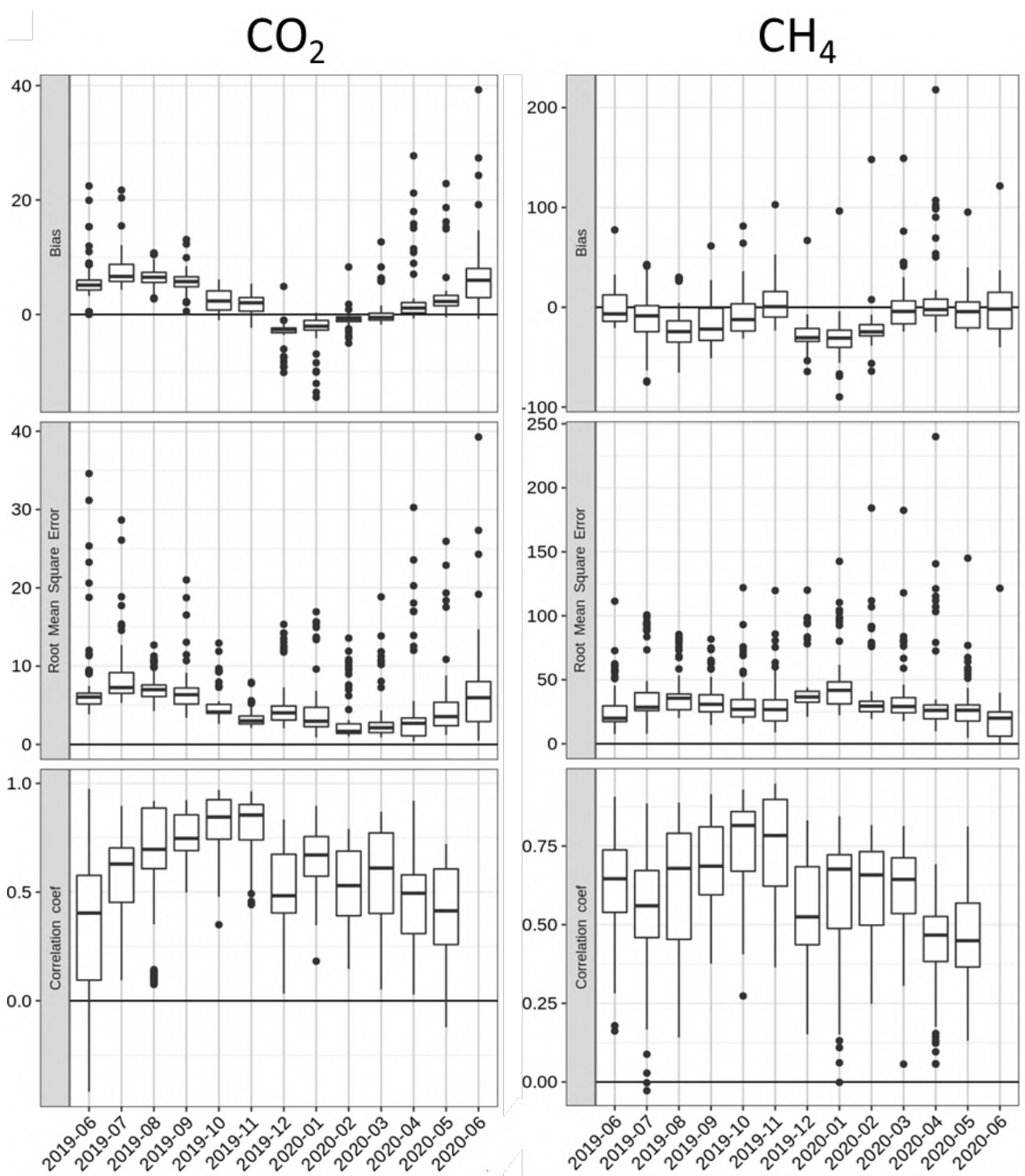


Figure 10.1.4: Monthly statistics (bias, RMSE, correlation coefficients) of the high resolution forecast experiment compared to CO₂ (left) and CH₄ (right) surface measurements at ICOS sites. The results obtained for all European sites (CMN, GAT, HPB, HTM, IPR, JFJ, LIN, NOR, OPE, PAL, PUY, SMR, TOH, TRN, ZEP) are averaged. September 2019 is not representative, since using only one day.

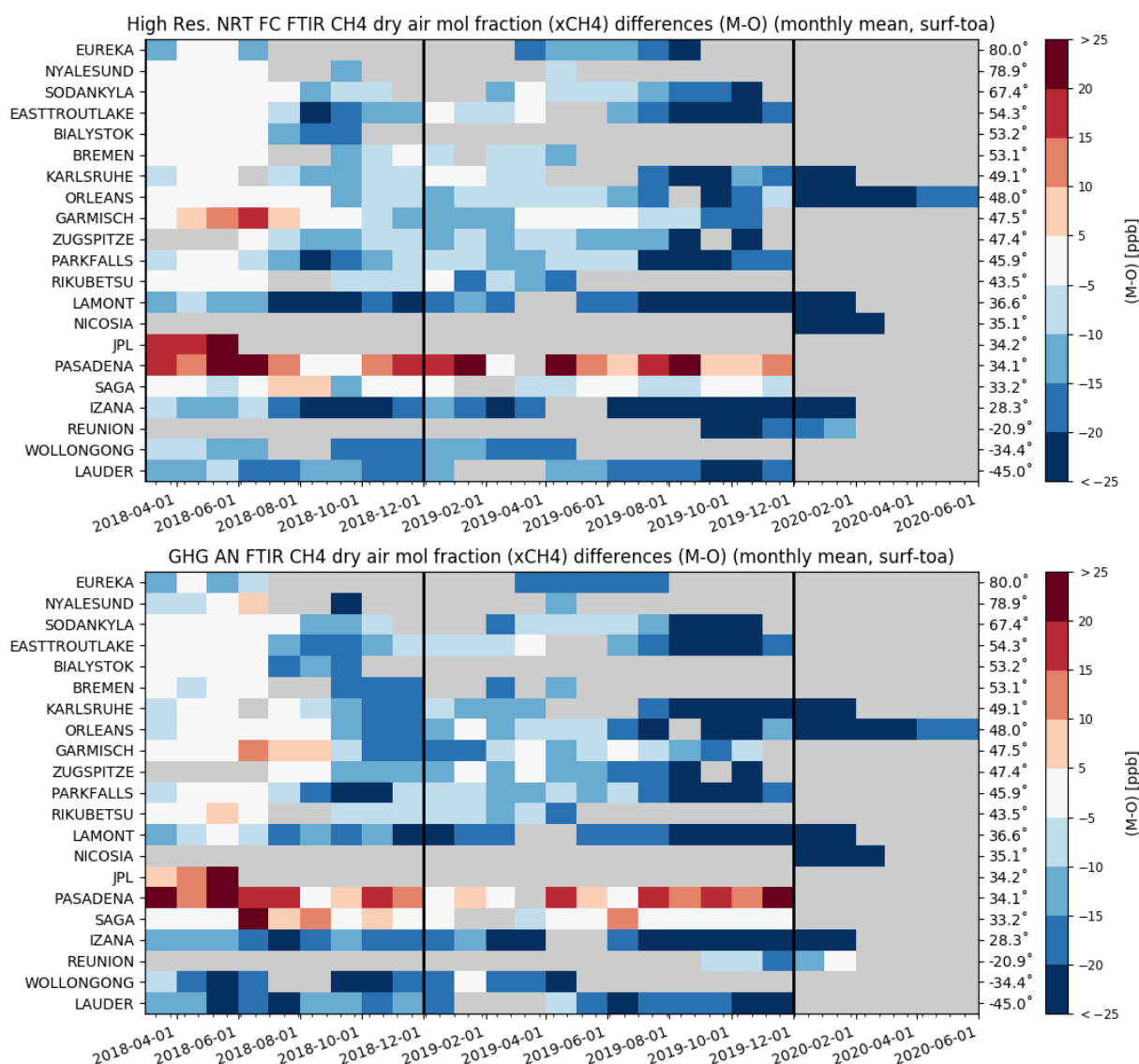


Figure 10.2.1: Monthly differences for the last 2.5 years (upper plot: high res NRT, lower plot: GHG AN). The stations are sorted by latitude (northern to southern hemisphere).

10.2 CH₄ and CO₂ validation against TCCON observations

For the validation column averaged mole fractions of CO₂ and CH₄ (denoted as XCO₂ and XCH₄) from the Total Carbon Column Observing Network (TCCON) are used. Column averaged mole fractions provide different information than the in situ measurements and are therefore complementary to the in situ data. The validation routines used for TCCON data are the same as used for the NDACC network and are documented in Langerock et al. (2015). In this section, we compare column averaged mole fractions of CH₄ and CO₂ of the CAMS runs with TCCON retrievals. Data from the following TCCON sites has been used: Izaña (Blumenstock et al., 2017), Reunion (De Mazière et al., 2017), Bialystok (Deutscher et al., 2017), Manaus (Dubey et al., 2017), Four Corners (Dubey et al., 2017), Ascension (Feist et al., 2017), Anmeyondo (Goo et al., 2017), Darwin (Griffith et al., 2017), Wollongong (Griffith et al., 2017),

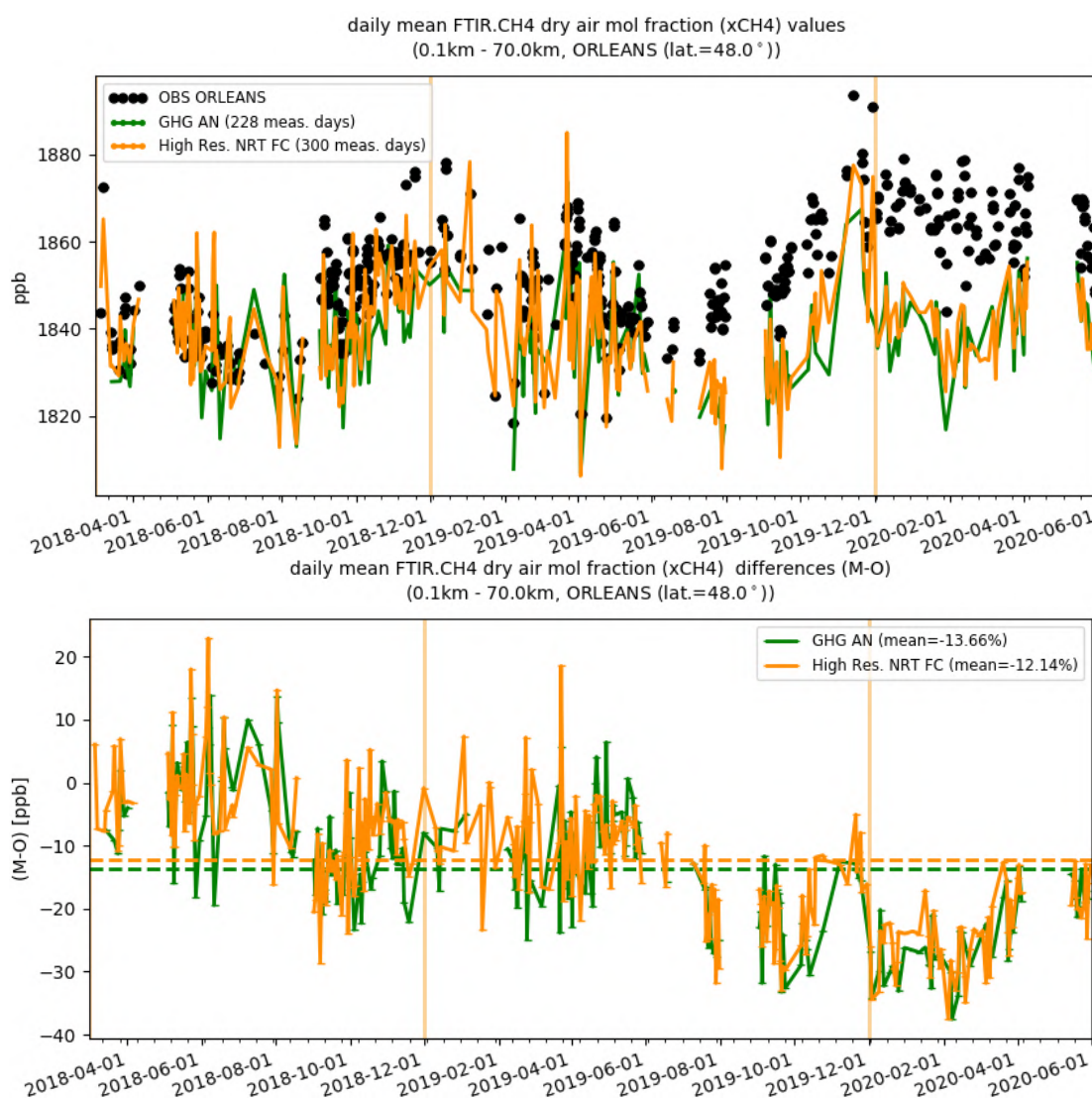


Figure 10.2.2: Comparison of the CH₄ CAMS runs with TCCON CH₄ at Orleans.

Karlsruhe (Hase et al., 2017), Edwards (Iraci et al., 2017), Indianapolis (Iraci et al., 2017), Saga (Kawakami et al., 2017), Sodankyla (Kivi et al., 2017), Hefei (Liu et al., 2018), Tsukuba (Morino et al., 2017), Burgos (Morino et al., 2018), Rikubetsu (Morino et al., 2017), Bremen (Notholt et al., 2017), Spitsbergen (Notholt et al., 2017), Lauder (Sherlock et al., 2017, Pollard et al., 2019), Eureka (Strong et al., 2018), Garmisch (Sussmann et al., 2017), Zugspitze (Sussmann et al., 2018), Paris (Te et al., 2017), Orleans (Warneke et al., 2017), Park Falls (Wennberg et al., 2017), Caltech (Wennberg et al., 2017), Lamont (Wennberg et al., 2017), Jet Propulsion Laboratory (Wennberg et al., 2017), East Trout Lake (Wunch et al., 2017), Nicosia (Petri et al., 2020)

For the validation of the CAMS runs in March, April and May TCCON data was available only from the site Orleans. The data from Nicosia (Cyprus) was delayed due to a retrieval problem but will be available in a rapid mode again for the next report.

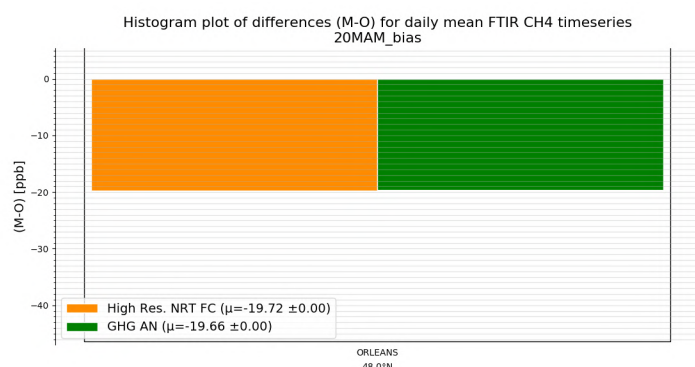
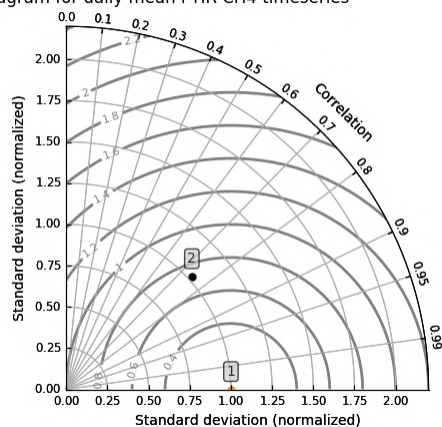
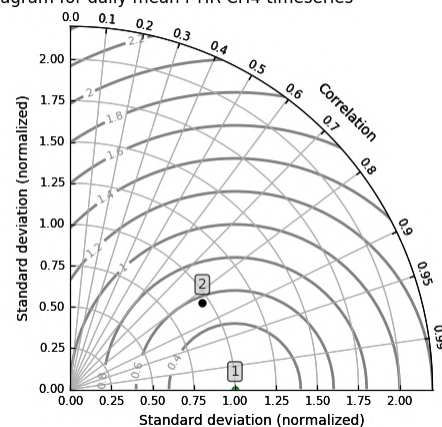
Taylor diagram for daily mean FTIR CH₄ timeseriesTaylor diagram for daily mean FTIR CH₄ timeseries

Figure 10.2.3: Differences during the reporting period and Taylor diagrams for the site that cover the whole reporting period

Methane (CH₄)

Figure 10.2.1 shows the data for the last 2.5 years. The only data for the reporting period is from Orleans (Fig. 10.2.2). The data from this station shows that the CAMS runs continues to underestimate the CH₄ for these stations by 15-20 ppb.

Carbon dioxide (CO₂)

Figure 10.2.4 shows the comparisons for the last 2.5 years. The only data for the reporting period is from Orleans. The data from this station shows that for the reporting period the CAMS runs agrees very well, with an overestimation of the CO₂ by about 1 ppm.

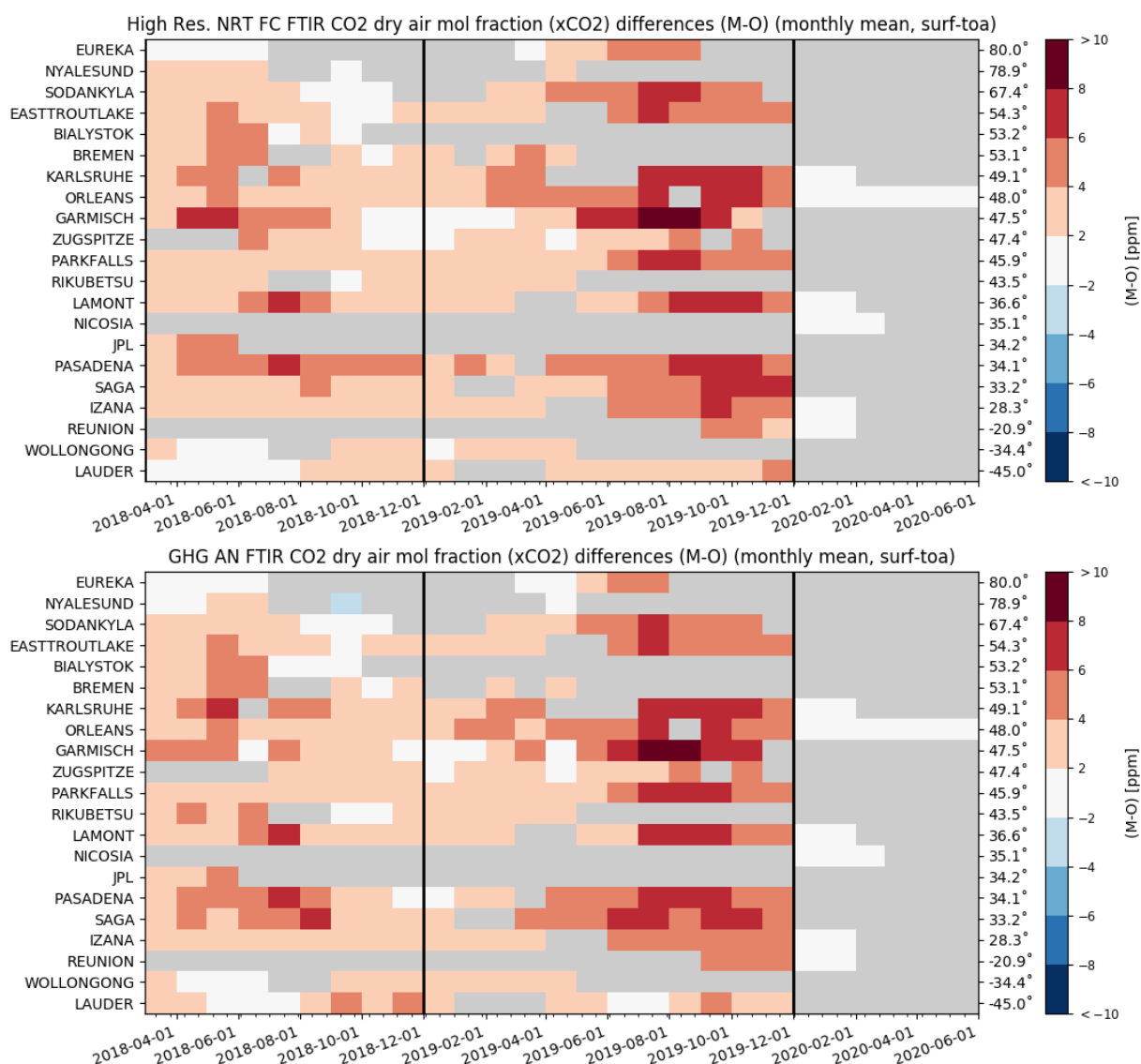


Figure 10.2.4: Monthly differences for the last 4 years (upper plot: high res NRT, lower plot: GHG AN). The stations are sorted by latitude (northern to southern hemisphere).

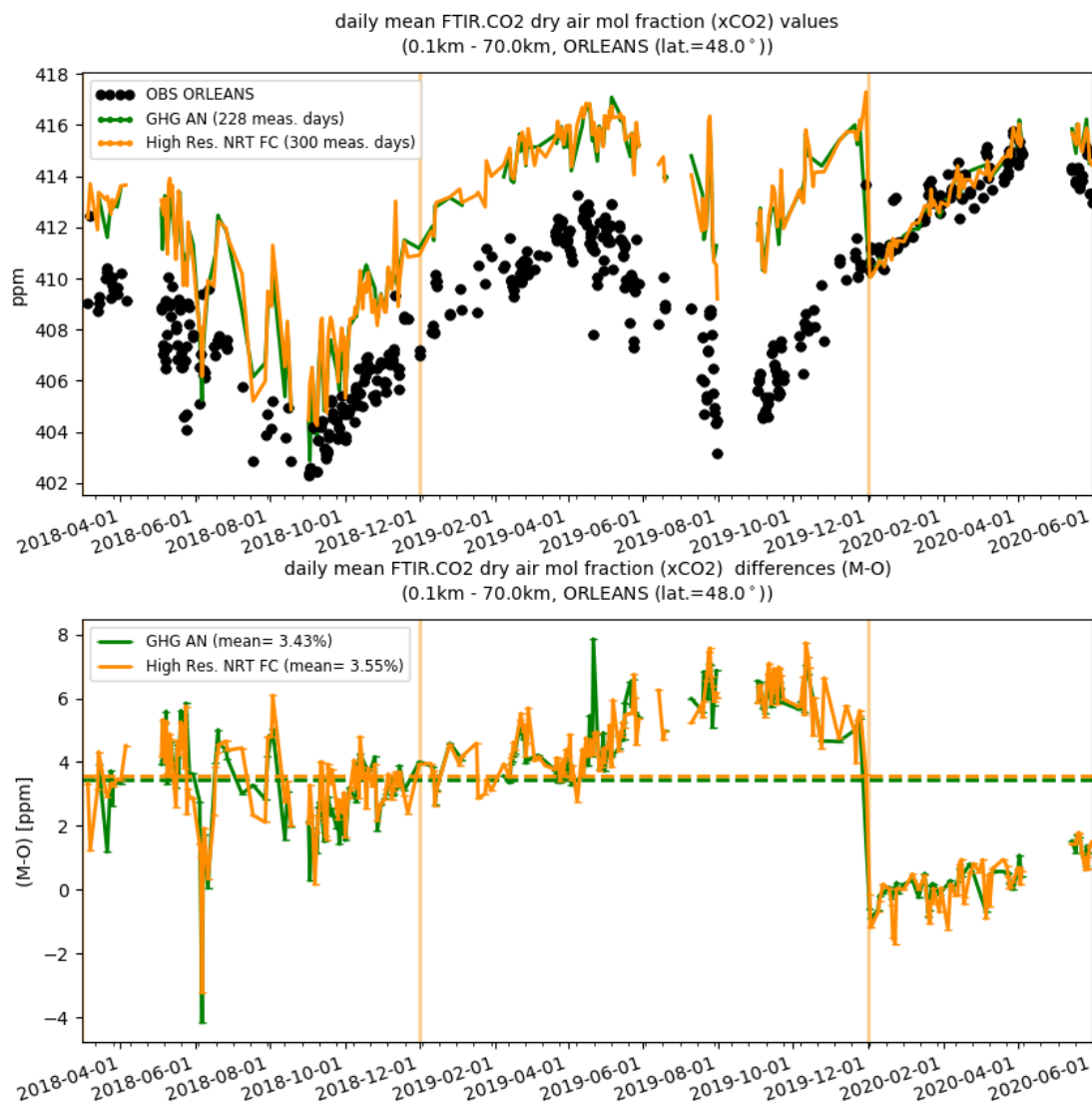


Figure 10.2.5: Comparison of the CO₂ CAMS runs with TCCON CO₂ at Orleans.

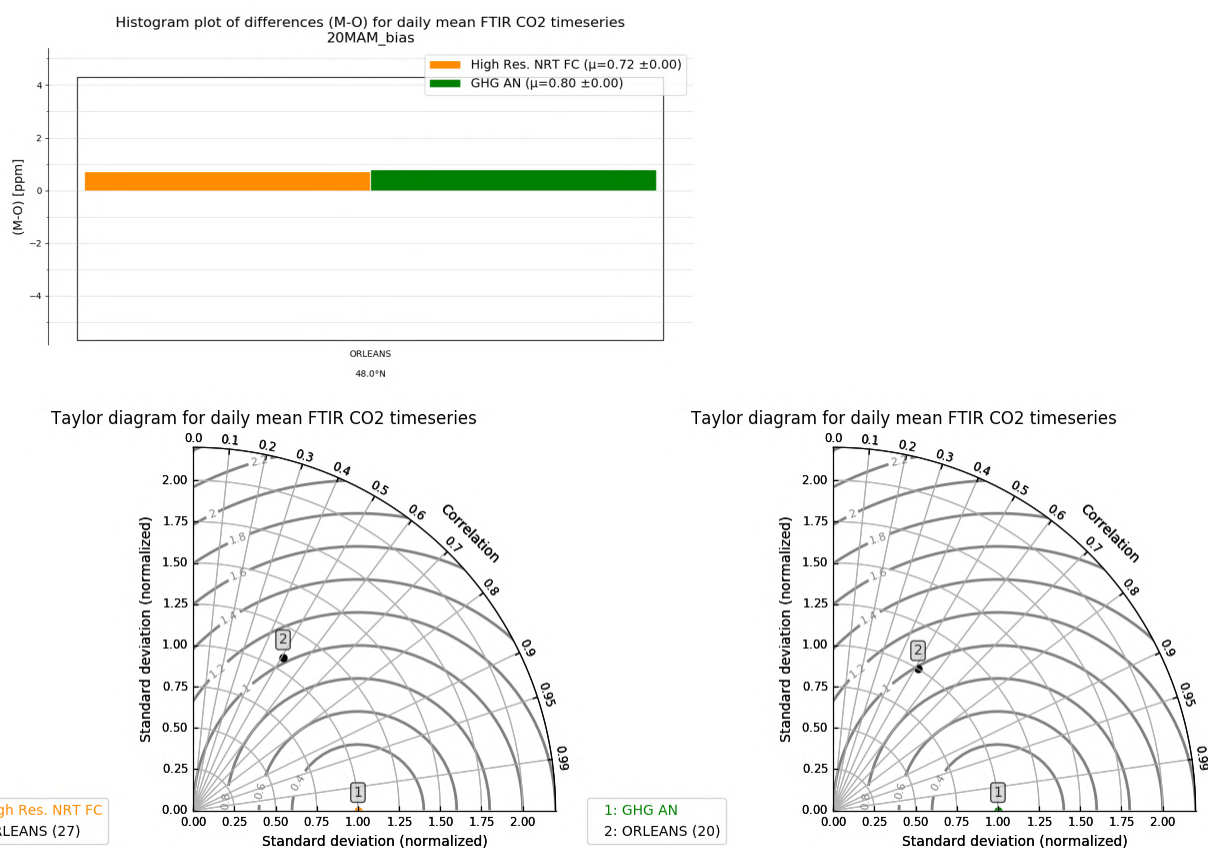


Figure 10.2.6: Differences during the reporting period and Taylor diagrams for the site that covers the whole reporting period

10.3 Validation against FTIR observations from the NDACC network

In this section, we compare the CH₄ profiles of the CAMS GHG products with FTIR measurements at different FTIR stations within the NDACC network. These ground-based, remote-sensing instruments are sensitive to the CH₄ abundance in the troposphere and lower stratosphere, i.e. between the surface and up to 25 km altitude. Tropospheric and stratospheric CH₄ columns are calculated from the FTIR profile data and used to validate corresponding columns obtained from the CAMS runs. A description of the instruments and applied methodologies can be found at <http://nors.aeronomie.be>. The typical uncertainty on the FTIR tropospheric column is 2%, while the uncertainty on the stratospheric column is 7.5%, adding together to a 3% uncertainty on the total column. The systematic uncertainty is large for the NDACC methane product mostly due to higher spectroscopic uncertainties.

Figure 10.3.1 (middle row) shows that the tropospheric columns of CH₄ agree well and only small differences appear between the analysis and the high resolution forecast. In comparison with the measurement uncertainty, a slight underestimation is observed in the tropospheric columns which is in agreement with the TCCON results. The Paramaribo measurements have reduced sensitivity and the tropospheric/stratospheric split is not valid in this case and the Toronto FTIR time series suffers from too low outliers.

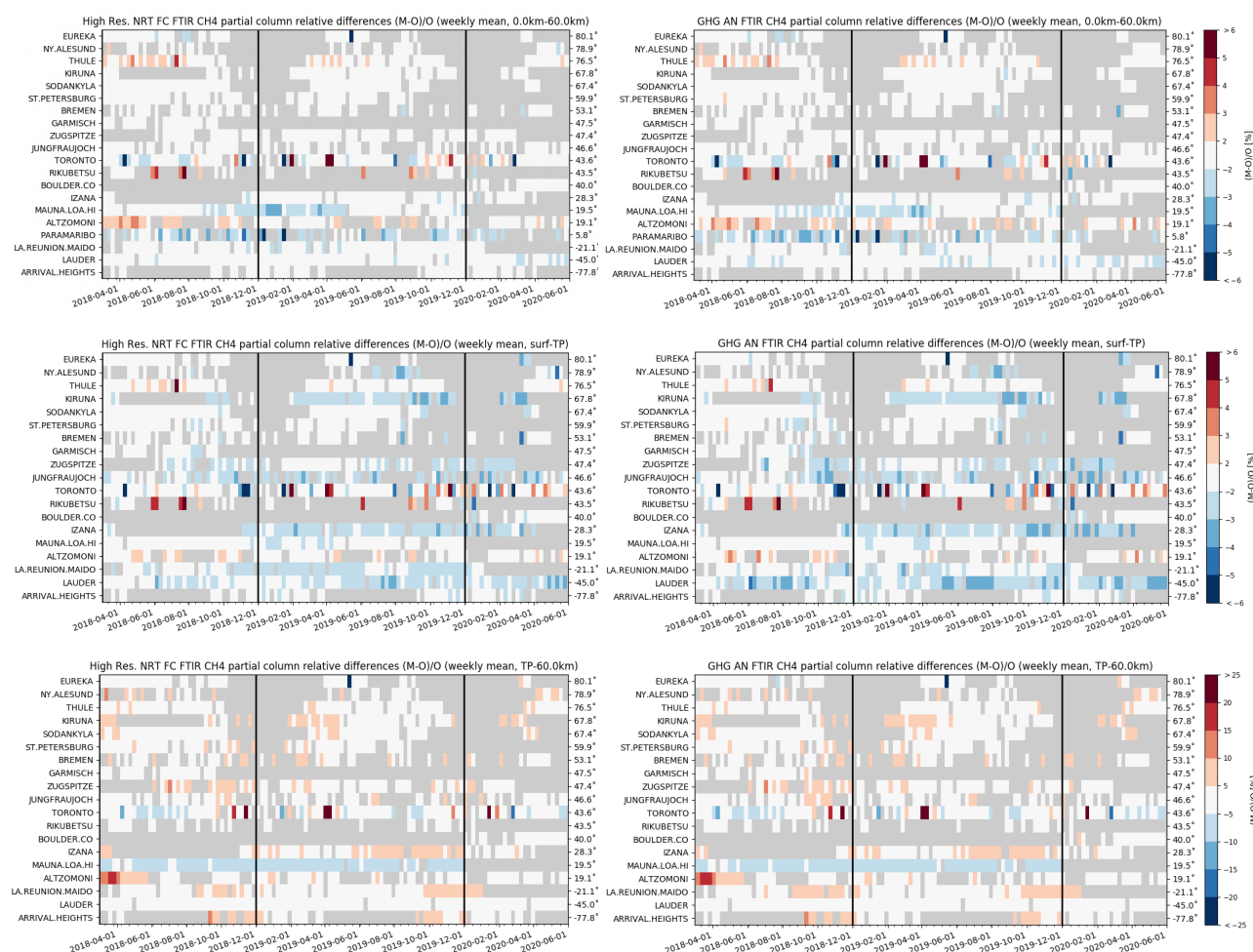


Figure 10.3.1: Weekly mean relative bias for total (top row), tropospheric (middle row) and stratospheric CH_4 columns (bottom row) for the period March 2018 – May 2020 for high resolution forecast (left) and the analysis (right). The overall uncertainty for the CH_4 total column measurements is approximately 4%. The overall uncertainty for the CH_4 total/tropospheric column measurements is approximately 2%, while the stratospheric uncertainty is 7.5% (the colour scale for the mosaic plots follows the uncertainty scale)

The stratospheric columns (Figure 10.3.1, bottom row) show a slight overestimation compared to the measurement uncertainty.

At some sites a seasonal change is observed in either the tropospheric or stratospheric concentrations. Due to the short time period, it is unclear if this is a recurring seasonal dependent performance of the CAMS runs. In Figure 10.3.2 the tropospheric and stratospheric relative difference time series are plotted at Thule and St. Petersburg.

Figure 10.3.3 shows Taylor diagrams for the MAM time period and for a selected number of sites: some stations have limited observations and should be treated with care. Assimilation has a small effect on the correlation coefficients for most sites: the average correlation for 11 stations is 0.84 for the analysis and 0.88 for the high-resolution forecast. Table 10.3.1 contains detailed statistics per site.

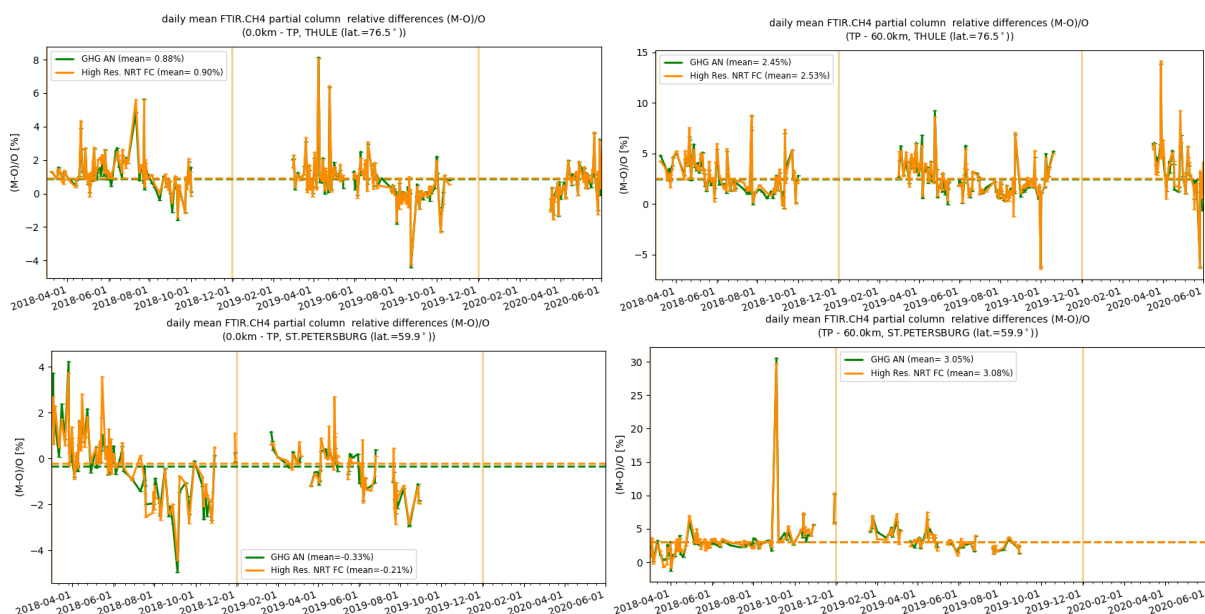


Figure 10.3.2: Daily mean of relative differences for tropospheric CH₄ columns (left) and stratospheric CH₄ columns (right) at Thule (top) and St. Petersburg (bottom). At Thule the stratospheric column shows a reduced bias during the summer months, while at St. Petersburg the tropospheric column performs worse during June-October.

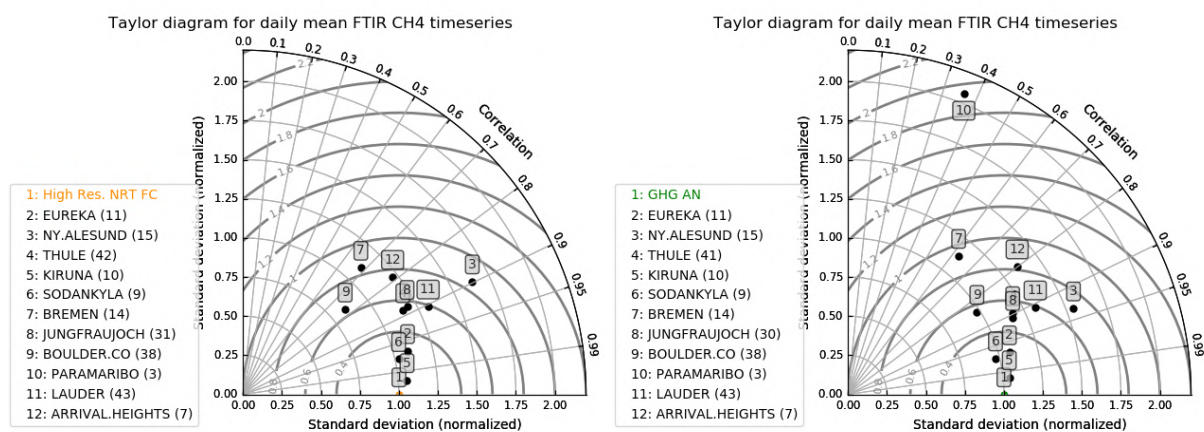


Figure 10.3.3: Taylor diagrams relating the standard deviations for the CAMS runs /GB time series of total CH₄ column data and their correlation for the period MAM 2020 (the stations with a limited number of measurements should be ignored). All time-series are normalized such that the standard deviation of the CAMS runs column time series is 1.



Table 10.3.1: Detailed statistics for total CH₄ column comparisons against FTIR measurements during MAM 2020. Both analysis and highres forecast behave similar.

FTIR site	Highres Forecast total column					ghg AN total column					lat
	#	rel. std	corr	rel diff (%)	rel diff std(%)	#	rel. std	corr	rel diff (%)	rel diff std(%)	
EUREKA	11	1.1	0.97	-1.5	0.36	11	1.1	0.97	-1.47	0.36	80.1
NY.ALESUND	15	1.6	0.9	-0.07	1.11	15	1.5	0.93	-0.09	1.04	78.9
THULE	42	1.2	0.89	1.22	1.03	41	1.2	0.9	1.16	0.99	76.5
KIRUNA	10	1.1	1	-0.95	0.15	10	1	0.99	-0.93	0.17	67.8
SODANKYLA	9	1	0.98	-0.41	0.39	9	1	0.97	-0.34	0.43	67.4
BREMEN	14	1.1	0.68	0.17	1	14	1.1	0.63	0.12	1.08	53.1
JUNGFRAUJOCH	31	1.2	0.88	-0.88	0.64	30	1.2	0.91	-0.94	0.55	46.6
BOULDER.CO	38	0.9	0.77	0.21	0.58	38	1	0.84	0.08	0.47	40
PARAMARIBO	3	3.5	0.98	-1.83	0.73	3	2.1	0.36	-1.85	0.96	5.8
LAUDER	43	1.3	0.9	-1.71	0.79	43	1.3	0.91	-1.89	0.79	-45
ARRIVAL.HEIGHTS	7	1.2	0.79	-0.41	0.62	7	1.4	0.8	-0.39	0.61	-77.8
		1.4	0.88	-0.56	0.67		1.3	0.84	-0.59	0.68	

11. Event studies

11.1 Ozone hole over the Arctic in spring 2020

We are used to ozone holes appearing over Antarctica every year during Antarctic spring time, related to the accumulation of human-made chemicals including chlorine and bromine inside the strong polar vortex that develops over the Antarctic every winter. When temperatures are very low over a longer period, Polar Stratospheric Clouds (PSCs) can form, which play an important role in chemical reactions that lead to ozone depletion once sunlight is back in this polar region.

Ozone holes over the Arctic are an unusual event however, as the polar vortex over the Arctic is usually weaker and more perturbed than over the Antarctic, and temperatures are normally not low enough for the formation of PSCs. This year's spring, an exceptionally strong and stable polar vortex and cold temperatures in the Arctic stratosphere lasted several months, enabling the formation of PSCs and resulting in large ozone losses over the Arctic. The Copernicus Atmosphere Monitoring Service tracked this "ozone hole" in near-real time (<https://atmosphere.copernicus.eu/cams-tracks-record-breaking-arctic-ozone-hole>).

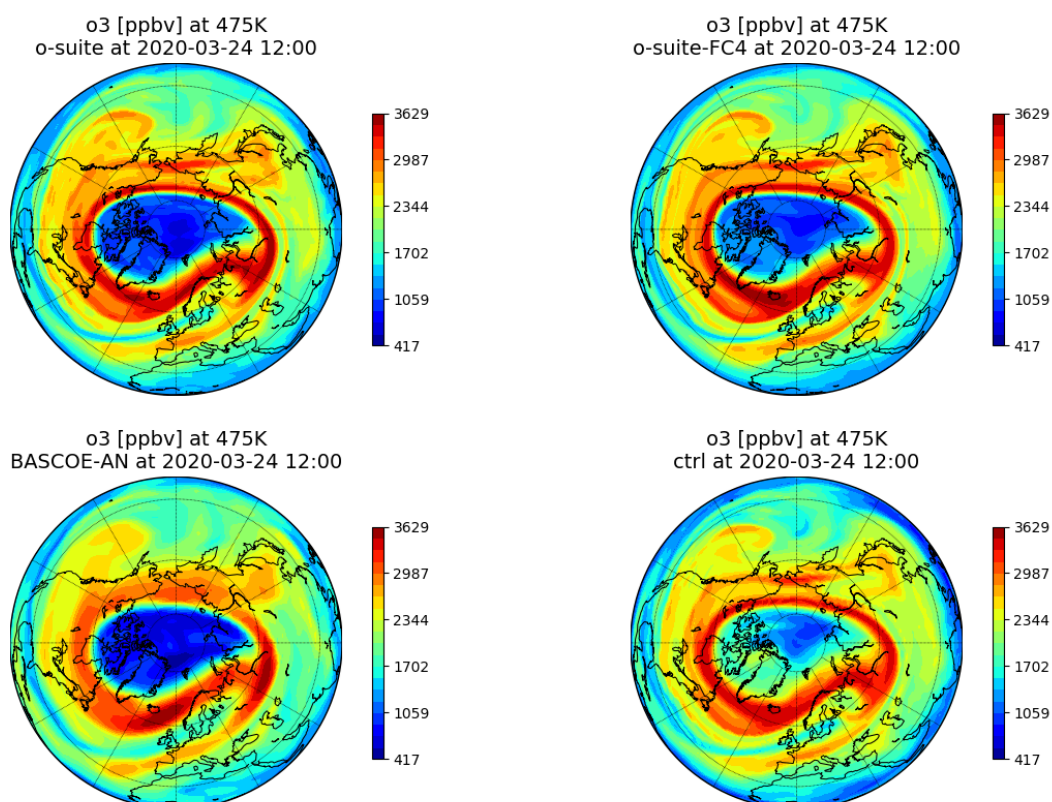


Figure 11.1.1: Map of ozone volume mixing ratio (ppbv) at the level of 475K at March 24. Upper left: o-suite, upper right: o-suite 4 day forecast, lower left: BASCOE and lower right: control run.

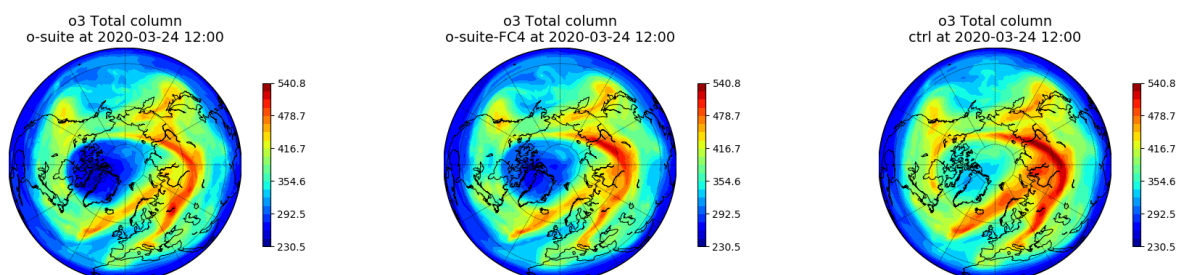


Figure 11.1.2: Map of total column ozone (DU) at March 24. Left: o-suite, middle: o-suite 4-day forecast, right: control run.

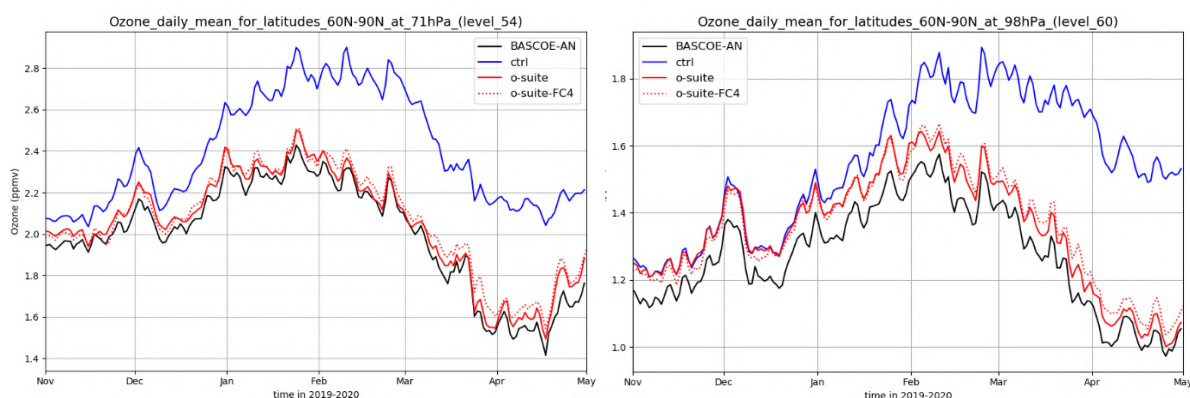


Figure 11.1.3: Time series of zonal mean of ozone in the north polar region (60° to 90°) at 98hPa (left) and 71hPa (right). Black: BASCOE, red: o-suite, red-dashed: o-suite 4-day forecast, blue: control run.

Figure 11.1.1 shows the spatial extent of the Arctic ozone hole at the isentropic level 475 K (i.e. in the lower stratosphere where ozone concentration is usually maximum) on at 24th March for the o-suite (upper left), the o-suite 4 day forecast (upper right), the independent assimilation system BASCOE (lower left) and the control run (lower right). The size and shape of the ozone hole is similar in all model outputs because it is determined by the polar vortex which is identically represented in all systems. Yet the ozone depletion is much weaker for the control run without chemical data assimilation, as can likewise be seen for the total column ozone on the same date (Fig. 11.1.2).

The development of the Arctic ozone hole is displayed in the timeseries plots at 98 hPa (left) and 71 hPa (right) in Fig. 11.1.3. The o-suite analyses (red solid lines) and o-suite forecast runs with 4 days lead time (red dashed lines) reproduce the decrease in ozone from March 2020 onwards correctly, whereas the control run (blue, without assimilated ozone data) shows large positive offsets. The monthly mean vertical profiles in Fig. 11.1.4 likewise illustrate the good agreement of o-suite analyses and 4-day forecasts with the Aura-MLS analyses delivered by the external BASCOE system. Data assimilation plays an essential role, as can be seen in the results for the control run, which overestimates ozone partial pressures in the profiles.

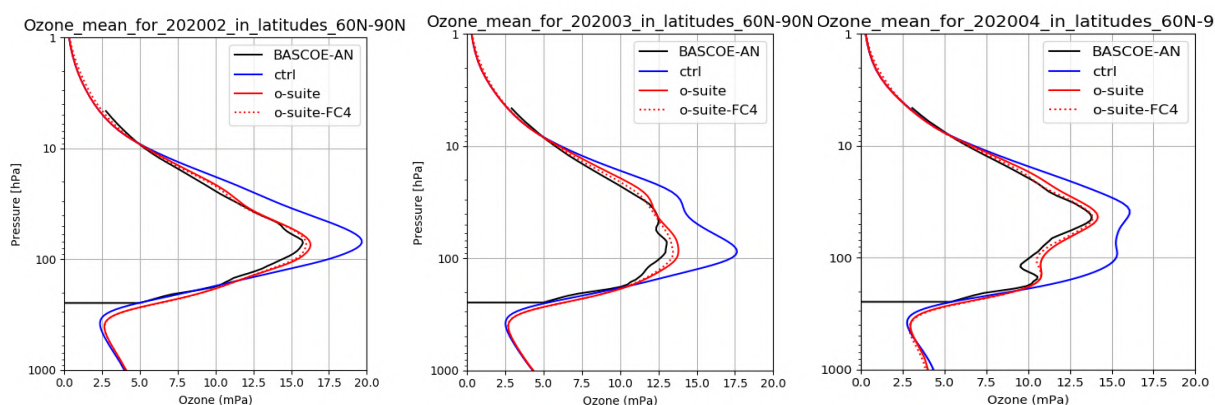


Figure 11.1.4: Mean monthly vertical profiles of ozone in the Arctic polar region (60° to 90°) for the months of February, March and April 2020. Black: BASCOE, red: o-suite, red-dashed: o-suite 4 day forecast, blue: control run.

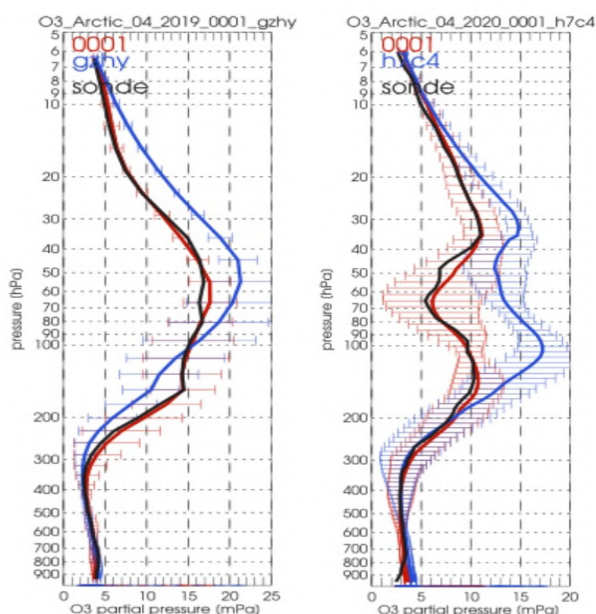
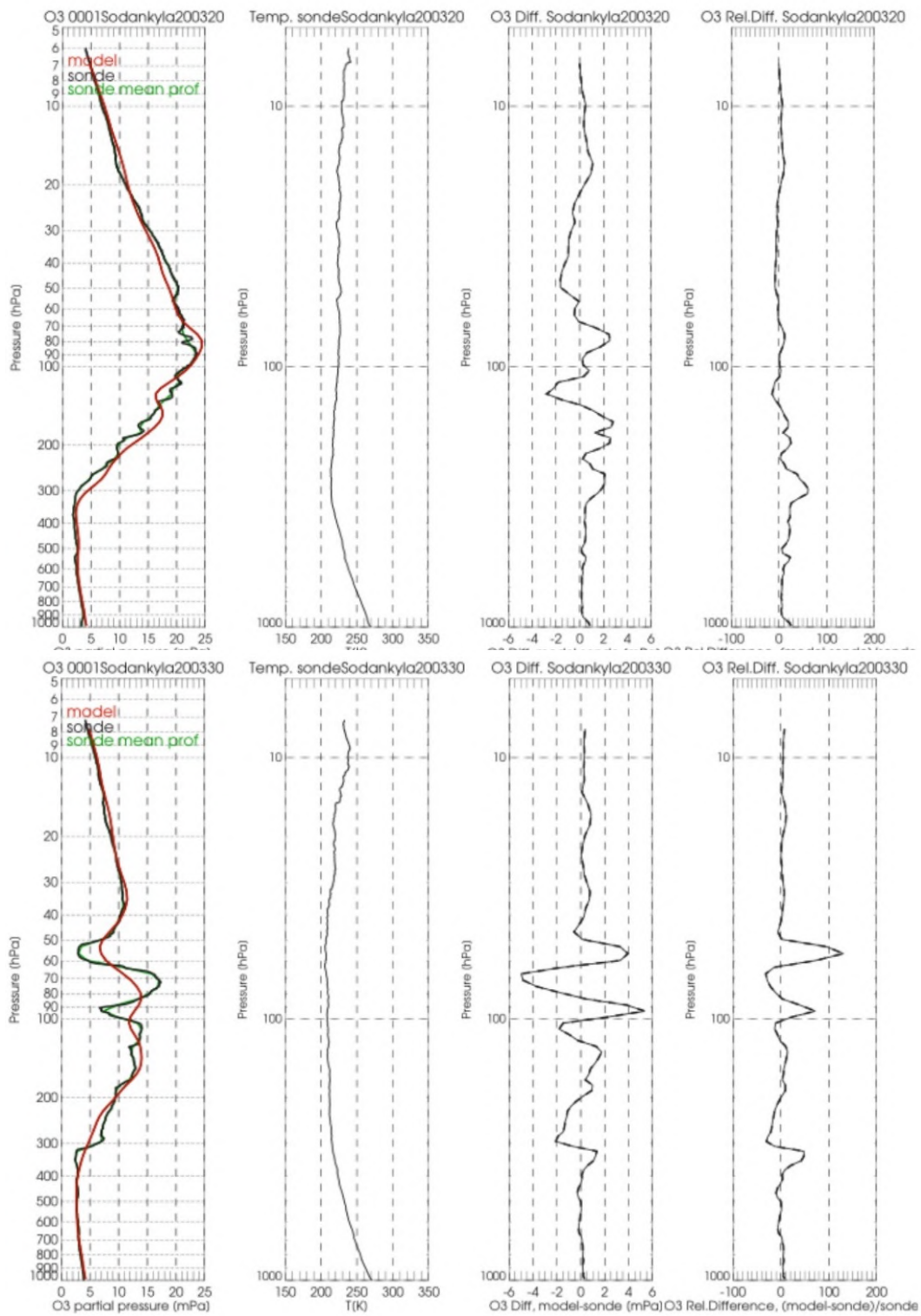
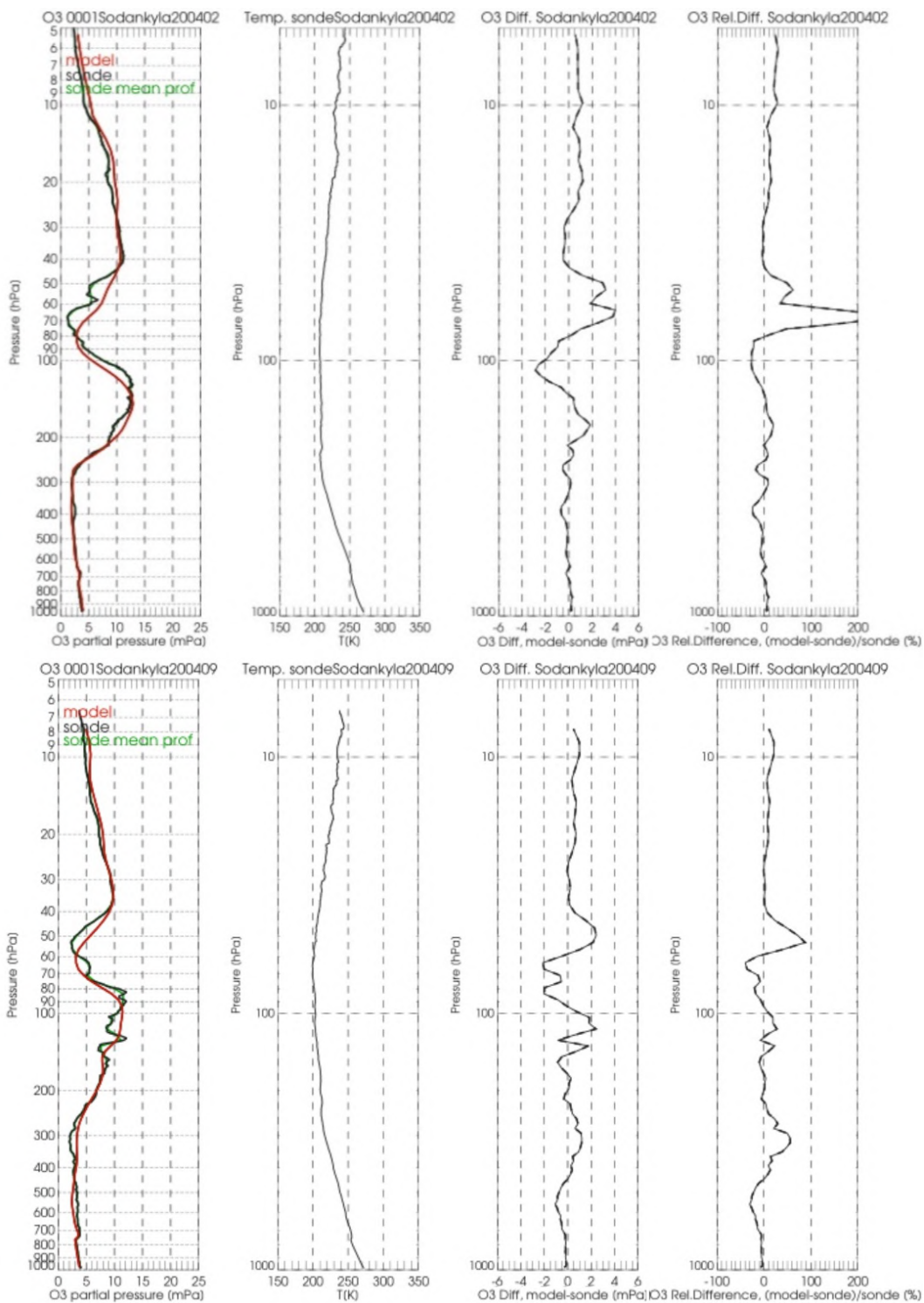


Figure 11.1.5: Comparison of mean ozone and model profiles over the Arctic in April 2019 (left panel) and April 2020 (right panel). Black: sonde profile, red: o-suite, blue: control run.

Figure 11.1.5 shows the comparison of mean Arctic ozone profiles with ozonesonde (balloon) observations for April in the years 2019 (no ozone hole) and 2020 (ozone hole). Differences in ozone between the two years can be clearly seen between 100 and 40 hPa, where ozone partial pressure strongly decreases in 2020. The vertical resolution of the model recently increased from 60 to 137 vertical levels, which allows a more detailed investigation of ozone vertical distribution. The CAMS o-suite is reproducing the observed profile very well.

Figure 11.1.6 shows the temporal evolution of the Arctic ozone hole between March and April 2020 above the Sodankylä station. The example displays how well the CAMS o-suite was able to reproduce the formation and break-up of the ozone hole in the Arctic stratosphere for this location during the two respective months.





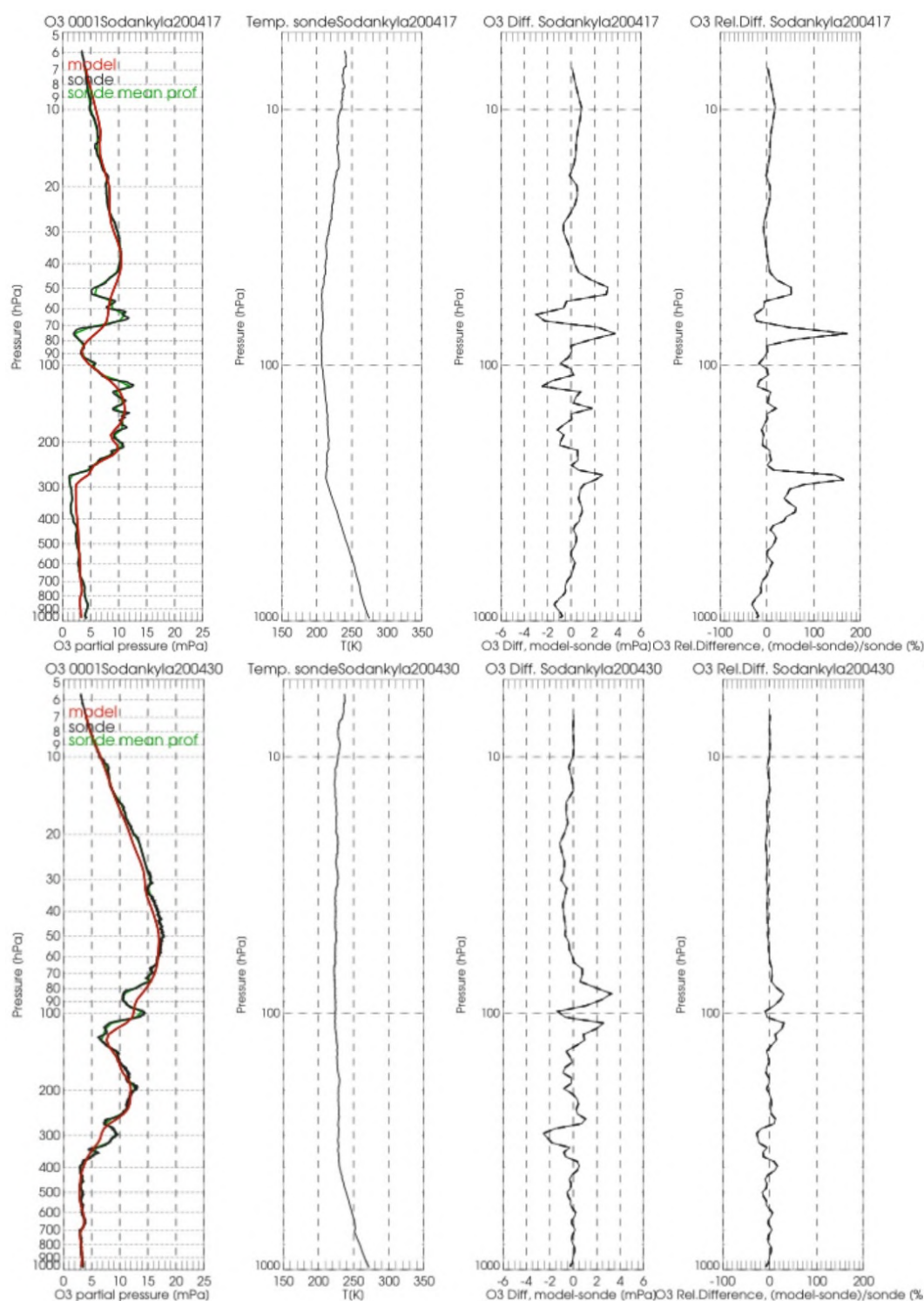


Figure 11.1.6: Ozone sonde (black) and model profiles (red) (first column), temperature profiles (second column), difference between model and sonde in mPa and rel. difference in % (third and fourth column, respectively) above the Sodankylä station in March (first two panels) and April (last four panels) 2020.

11.2 Dust event in the Eastern Mediterranean in May 2020

From early May, satellites and ground-based observations detected several African dust outbreaks into Europe (see Section 9.4). One of the most intense events (with hourly $\text{PM}_{10} > 50 \mu\text{g}/\text{m}^3$) was observed in south-eastern Europe and the Eastern Mediterranean between 14th and 20th May. Particularly, in Cyprus, Saharan dust intrusion occurred during some local fires (see Figure 11.2.1).

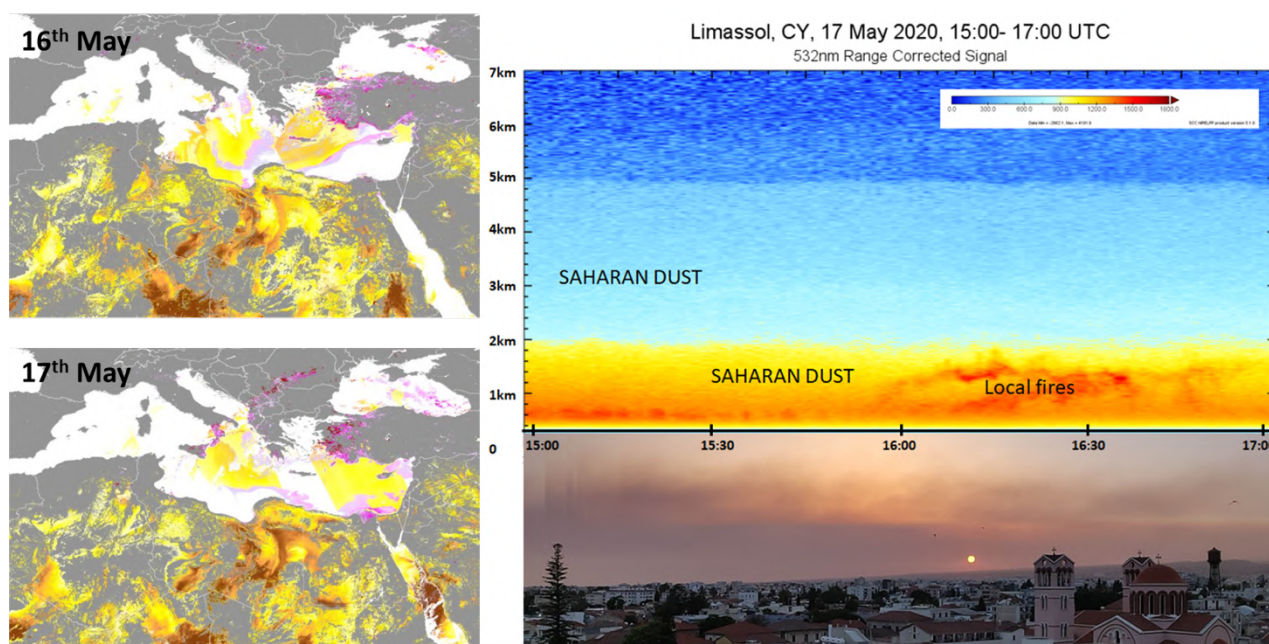


Figure 11.2.1: Left: VIIRS aerosol detection product on board of SNPP and NOAA20 on 16-17 May. The blowing dust (yellow/brown shading) moved across the Mediterranean Sea into southern Europe (Source: NOAA's JSTAR Mapper website, Twitter @AerosolWatch) Right: Smoke from local fires as captured over Limassol in Cyprus by ACTRIS-EARLINET lidar (Source: Twitter @SIROCCO_RESTART).

Predicted AOD values above 0.7 and PM_{10} values above $100 \mu\text{g}/\text{m}^3$ are observed in the whole Mediterranean with maximum values up to $700 \mu\text{g}/\text{m}^3$ in Sardinia on 17th May. The comparison in the Eastern Mediterranean with AERONET DOD (see Finokalia FKT in Figure 12.2) and with EEA PM_{10} and $\text{PM}_{2.5}$ observations (see GR0039A in Greece in Figure 12.3) show how o-suite did timely reproduce the spatial distribution of the two dust plumes despite the model tending to overestimate the observed maximum values.

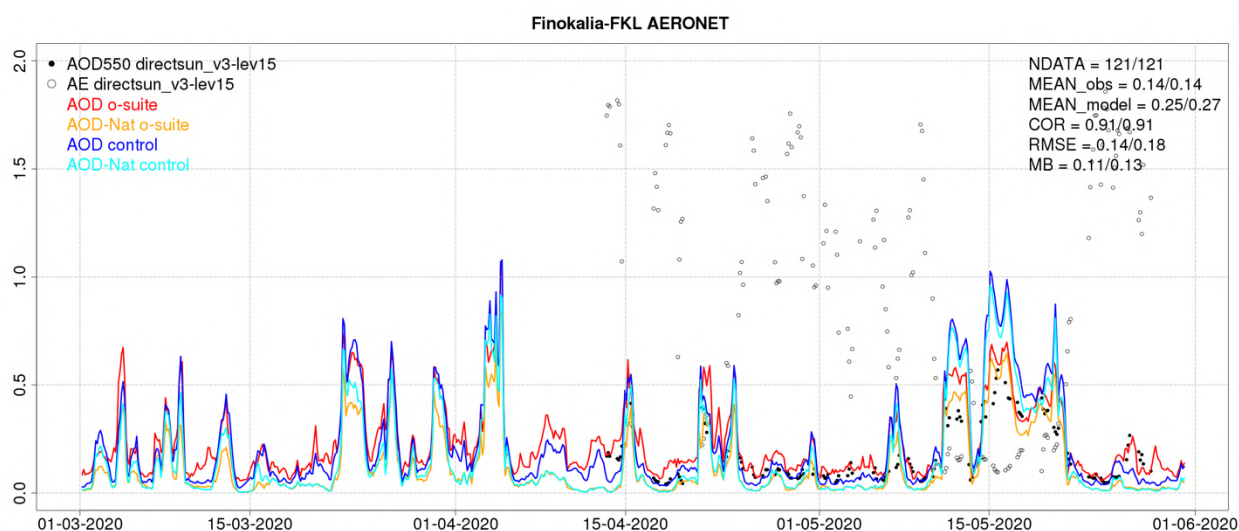


Figure 11.2.2: AOD from AERONET (black dot), AOD o-suite (red line), AOD control (blue line), AOD-Nat o-suite (orange line), AOD-Nat control (cyan line), for the study period over Finokalia FKL (Cyprus). AOD-Nat corresponds to the natural aerosol optical depth that includes dust and sea-salt. Skill scores per each site and model (o—suite/control) are shown in the upper right corner (NDATA: available 3-hourly values used for the calculations, MEAN observations, MEAN model, COR, RMSE, MB).

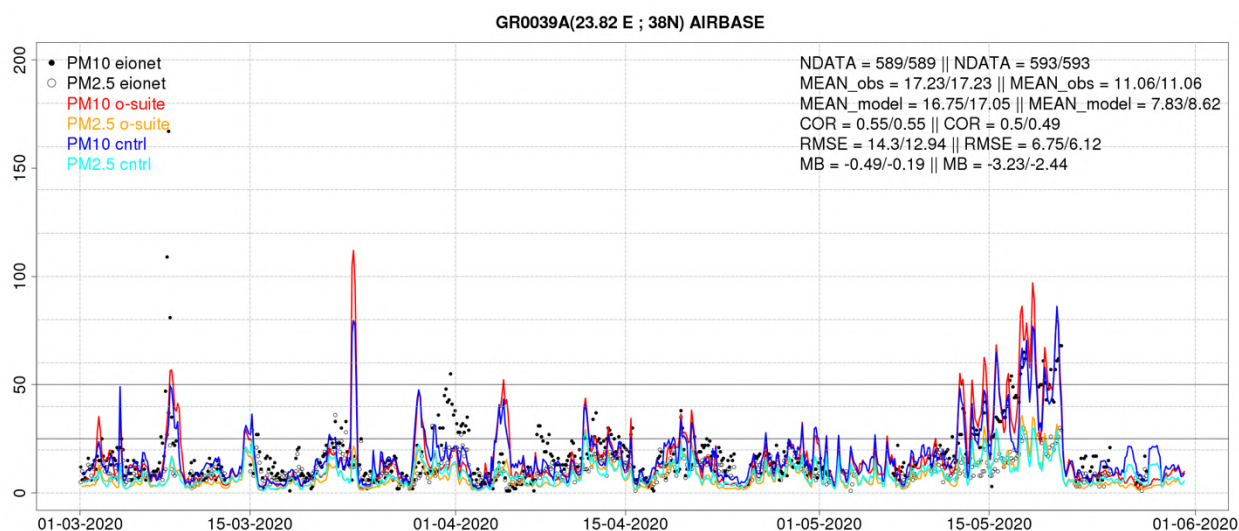


Figure 11.2.3: PM10 and PM2.5 Airbase observations (black and grey dots, respectively), PM10 and PM2.5 o-suite (red and orange lines, respectively) and PM10 and PM2.5 control (blue and cyan lines, respectively) for the study period over GR0039A (Greece). Skill scores per each individual site and model (o—suite/control) are shown in the upper right corner (NDATA: available 3-hourly values used for the calculations, MEAN observations, MEAN model, COR, RMSE, MB).

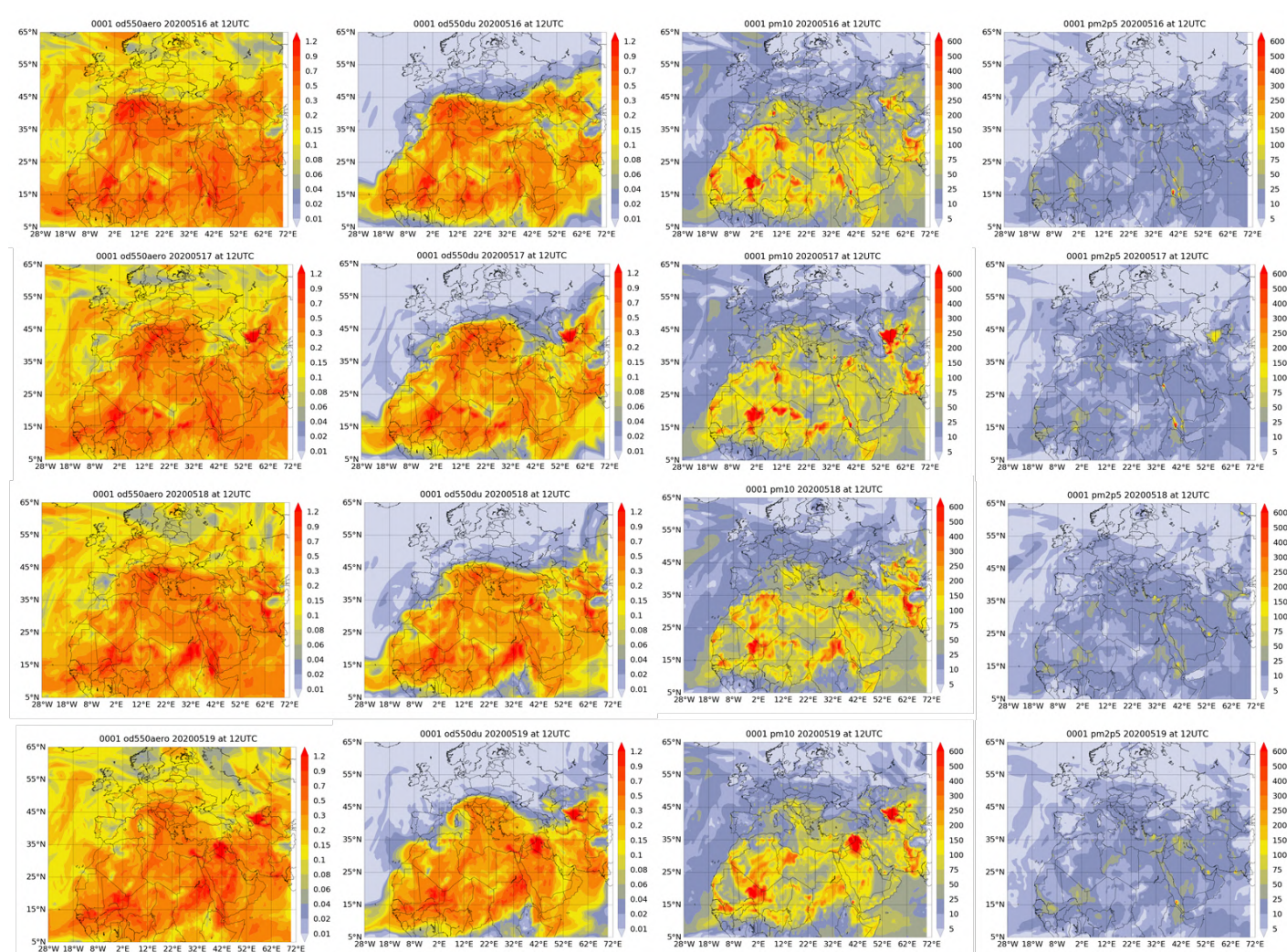


Figure 11.2.4: AOD, DOD, PM10 (in $\mu\text{g}/\text{m}^3$) and PM2.5 (in $\mu\text{g}/\text{m}^3$) at 12UTC from o-suite for 16-19 May 2020.

11.3 Impact of COVID-19 on tropospheric NO_2

In this section, the ability of the model simulations to reproduce observed tropospheric NO_2 columns during time periods with COVID-19 lockdown is investigated based on GOME-2/MetOp-A (IUP-UB v1.0) [Richter et al., 2011] and TROPOMI/Sentinel-5P data (IUP-UB v0.9, preliminary) satellite retrievals (see section 5 for a description of the validation method and datasets).

The impact of the COVID-19 lockdowns on air pollutions has been a special subject of study within CAMS, see e.g. <https://atmosphere.copernicus.eu/copernicus-provides-vital-information-advance-covid-19-research>. In the comparisons below we present direct ratios of observations in 2019 and 2020. It should be noted that the interpretation of such results is complicated: in part the signal may be attributed to COVID-19 measures, but also the differences in meteorological conditions will play an important role. Furthermore, the extensive upgrade of the model versions in July 2019 complicates the comparison of the two years. The same kind of analysis should be applied to the CAMS reanalysis, to at least rule out differences resulting from different model versions.

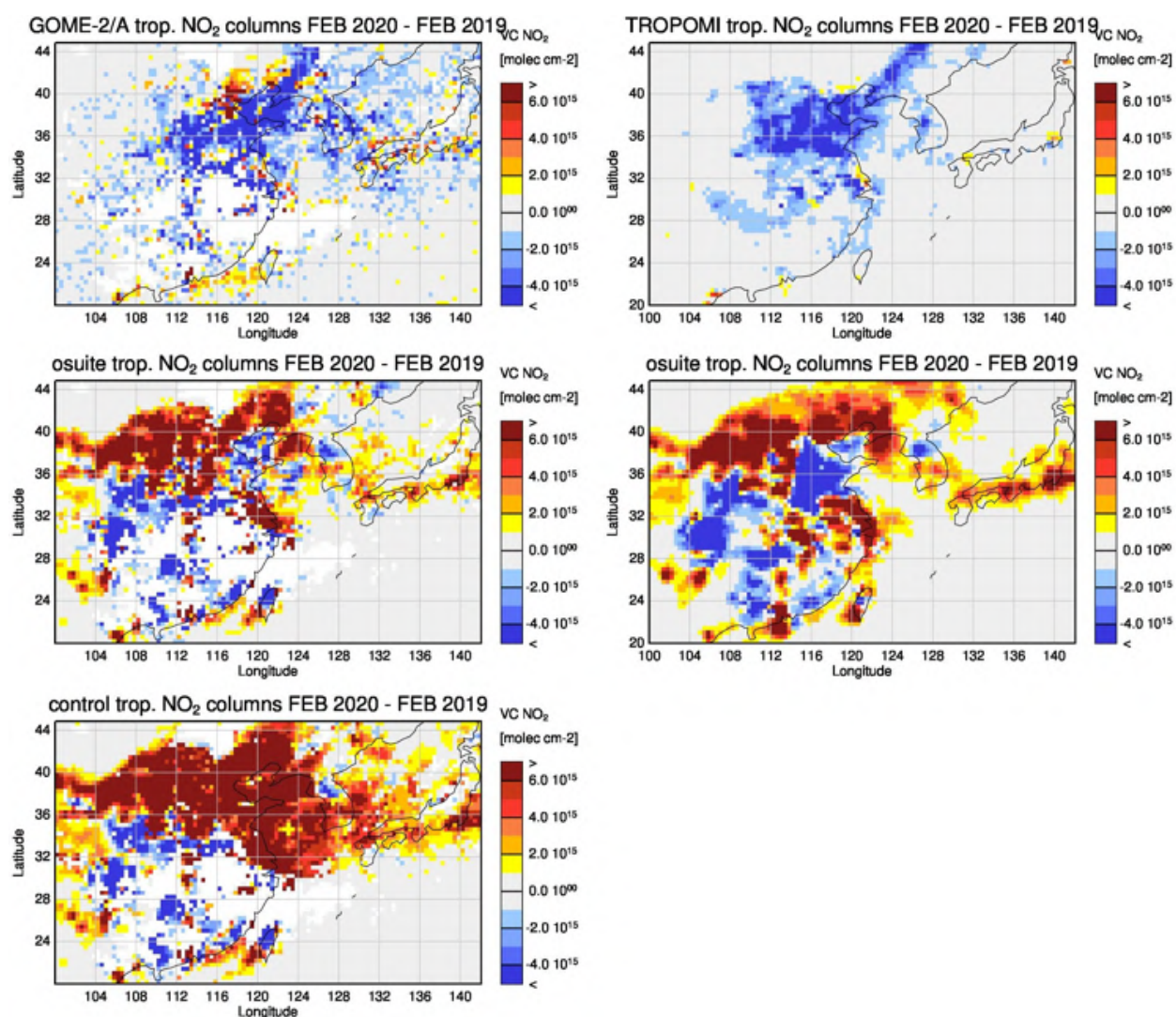


Figure 11.3.1a: Differences of monthly averaged tropospheric NO₂ columns [molecules cm⁻²] over East-Asia for 2020-2019 during months with COVID-19 lockdown: results for February. The top row shows differences based on satellite observations (see section 5 for a description of the satellite retrievals), the middle row differences for the o-suite at the orbit of the corresponding satellite sensor and the bottom row differences for the control at the orbit of the corresponding satellite sensor. The satellite data were gridded to model resolution (i.e. 0.4° x 0.4° degree). The CAMS o-suite was used as a-priori in the TROPOMI retrievals. Model data at GOME-2A orbit were treated using the same stratospheric correction method as applied to the GOME-2A satellite data.

Figure 11.3.1 shows differences between February 2020 and February 2019 as well as March 2020 and March 2019 over China. Reductions in tropospheric NO₂ are seen in widespread areas over China in the satellite retrievals. The observed differences are not well reproduced by the model simulations, showing in contrast to the observations also large areas with positive differences. Compared to the control run, simulated tropospheric NO₂ columns are generally closer to the satellite observed differences for the o-suite, but the impact of the data assimilation is not large enough to match the satellite observed differences between 2020 and 2019.

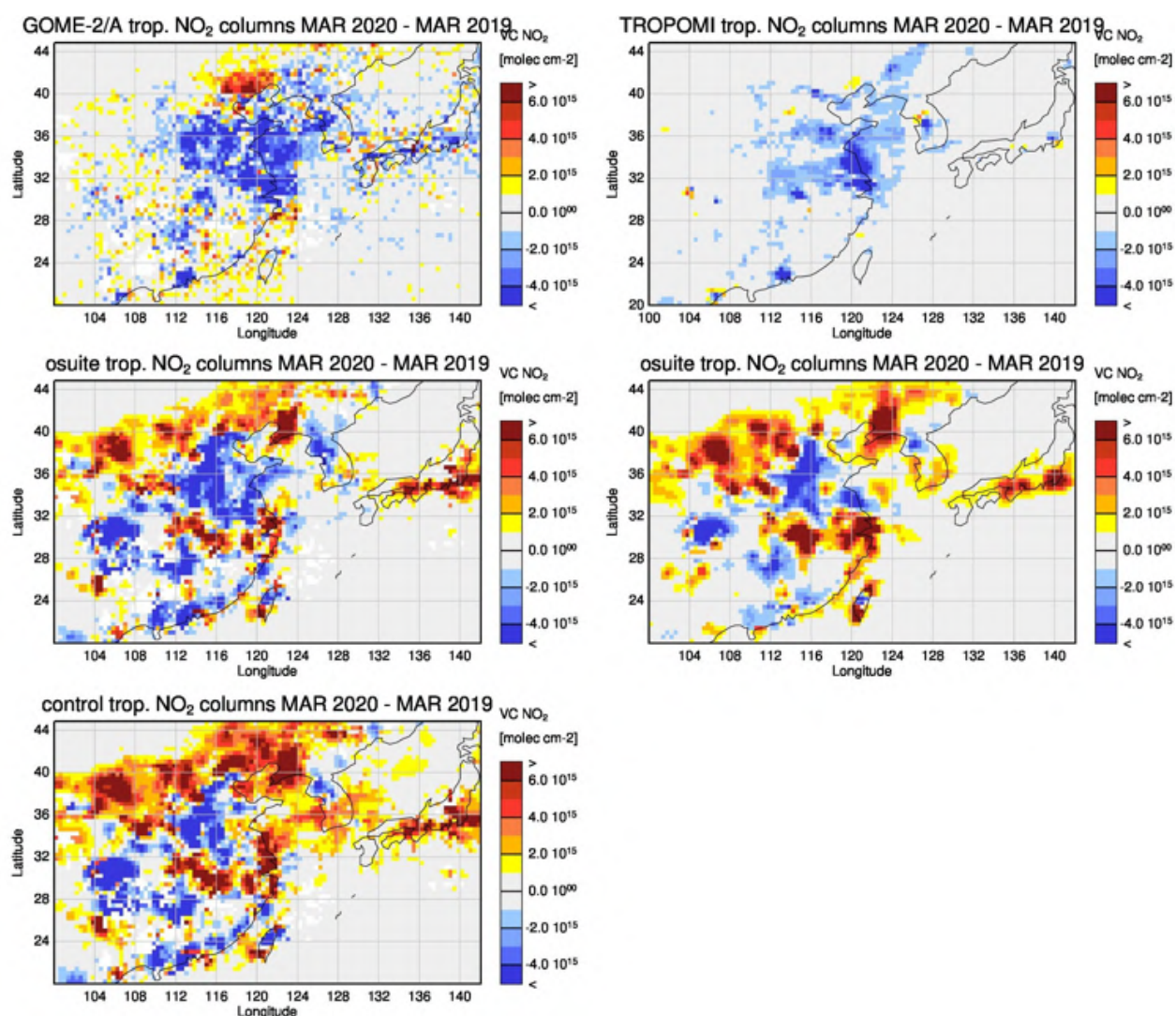


Figure 11.3.1b: Same as figure 11.3.1a, but results for March.

Differences for March 2020 and March 2019 as well as April 2020 and March 2020 over Europe are shown in Figure 11.3.2. Large areas of negative differences are observed, with the exception of GOME-2A retrievals for March. The models also show areas with negative differences, but partly in different locations than the satellite observations. There are minor differences between the o-suite and the control run.

Figure 11.3.3 shows differences for March 2020 and March 2019 as well as April 2020 and March 2020 over South Asia. In contrast to the satellite observed differences, the model simulations show rather large areas with positive differences. Differences between results for the o-suite and the control are minor.

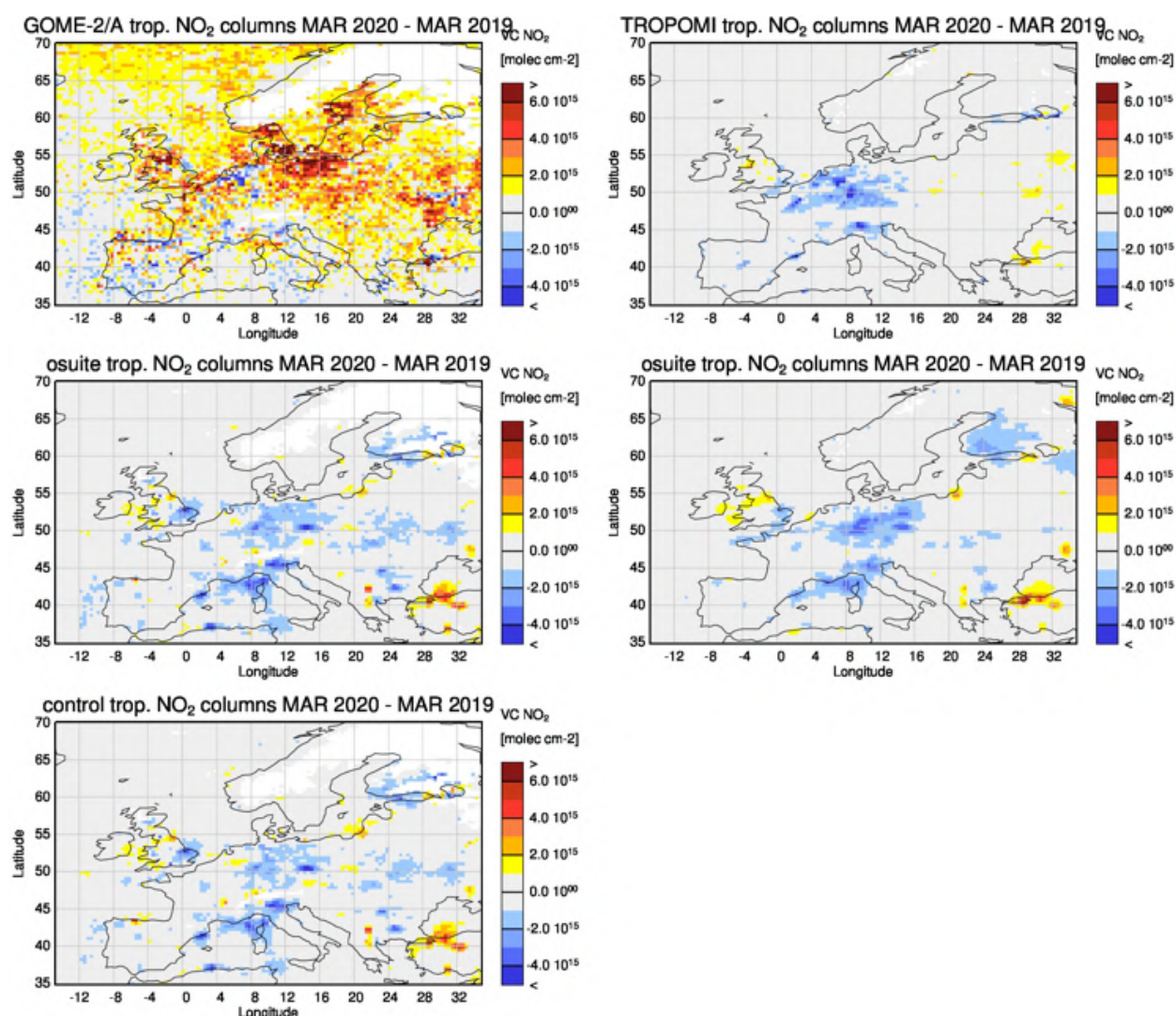


Figure 11.3.2a: As in Figure 11.3.1 but for months with COVID-19 lockdown over Europe: March.

With respect to months affected by COVID-19 lockdown time periods, the o-suite generally fails to reproduce observed reductions in tropospheric NO₂ for large areas over China and South Asia, but performs better for Europe. The results described above are however not easy to interpret. In general one would expect to see a reduction in observed and simulated tropospheric NO₂ columns for 2020 lockdown months compared to 2019 as a result of reduced emissions. Results for the o-suite would be expected to match the satellite observations better than the control as a result of data assimilation.

In summary the results show that the use of tropospheric column NO₂ data in the analysis to modify the initial conditions is not very effective for short lived species like NO₂. The resulting analysis is strongly influenced by the used NO_x emissions, which over China use a constant trend in 2019/2020 and do not capture any reduction due to Covid restrictions.

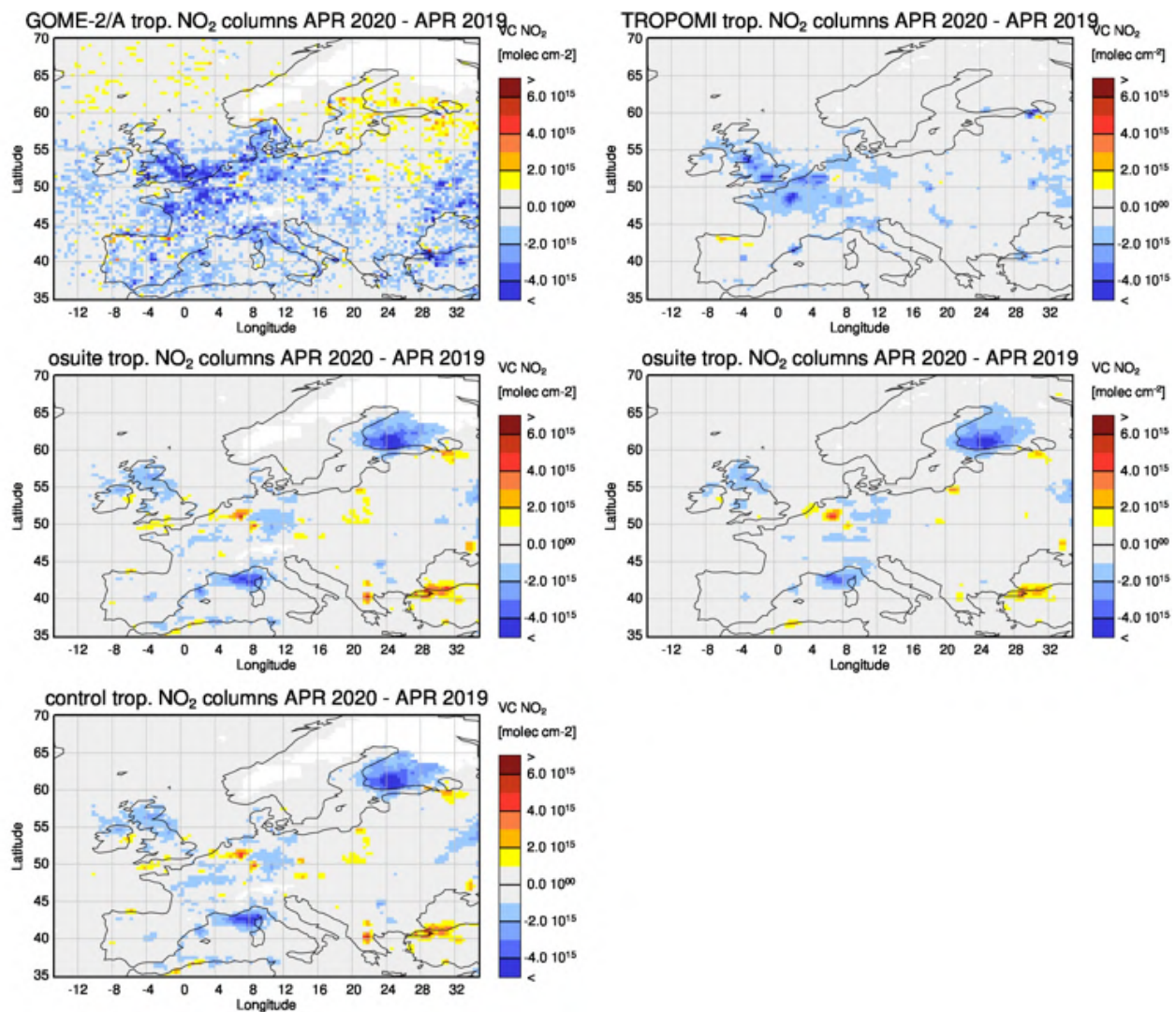


Figure 11.3.2b: As in Figure 11.3.1 but for months with COVID-19 lockdown over Europe: April.

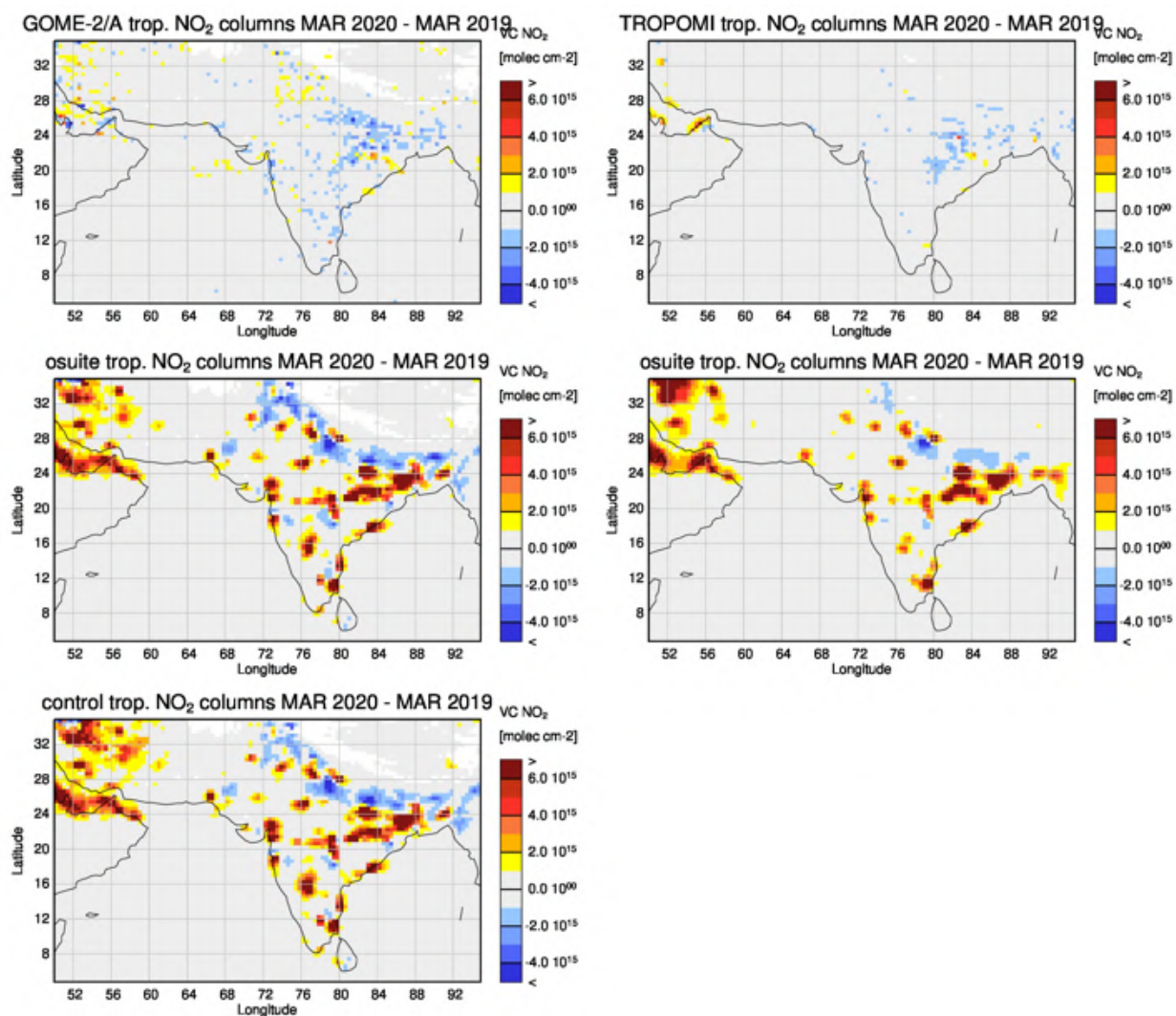


Figure 11.3.3a: As in Figure 11.3.1 but for months with COVID-19 lockdown over South Asia: March.

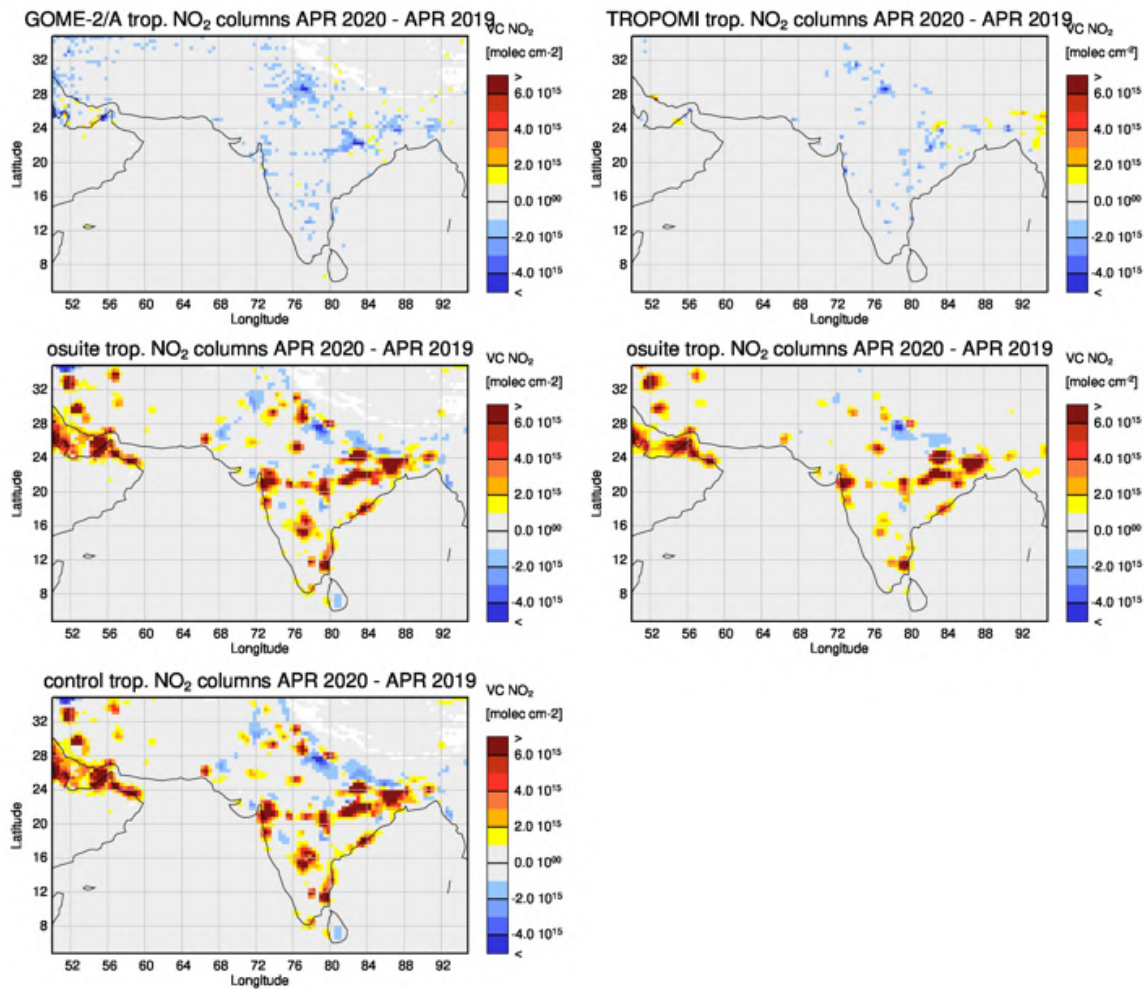


Figure 11.3.3b: As in Figure 11.3.1 but for months with COVID-19 lockdown over South Asia: April.



12. References

- Agusti-Panareda, A., *Monitoring upgrades of analysis/forecast system, MACC-III Deliverable D44.04*, June 2015.
- Basart, S, A. Benedictow, Y. Bennouna, A.-M. Blechschmidt, S. Chabrillat, Y. Christophe, E. Cuevas, H. J. Eskes, K. M. Hansen, O. Jorba, J. Kapsomenakis, B. Langerock, T. Pay, A. Richter, N. Sudarchikova, M. Schulz, A. Wagner, C. Zerefos, *Upgrade verification note for the CAMS near-real time global atmospheric composition service: Evaluation of the e-suite for the CAMS upgrade of July 2019*, Copernicus Atmosphere Monitoring Service (CAMS) report, CAMS84_2018SC1_D3.2.1-201907_esuite_v1.pdf, July 2019.
- Beirle, S., Hörmann, C., Jöckel, P., Liu, S., Penning de Vries, M., Pozzer, A., Sihler, H., Valks, P., and Wagner, T.: *The STRatospheric Estimation Algorithm from Mainz (STREAM): estimating stratospheric NO₂ from nadir-viewing satellites by weighted convolution*, *Atmos. Meas. Tech.*, 9, 2753–2779, <https://doi.org/10.5194/amt-9-2753-2016>, 2016.
- Bergamaschi, P., Frankenberg, C., Meirink, J. F., Krol, M., Villani, M. G., Houweling, S., Dentener, F., Dlugokencky, E. J., Miller, J. B., Gatti, L. V., Engel, A., and Levin, I.: *Inverse modeling of global and regional CH₄ emissions using SCIAMACHY satellite retrievals*, *J. Geophys. Res.*, 114, D22301, doi:10.1029/2009JD012287, 2009.
- Benedetti, A., J.-J. Morcrette, O. Boucher, A. Dethof, R. J. Engelen, M. Fisher, H. Flentjes, N. Huneus, L. Jones, J. W. Kaiser, S. Kinne, A. Mangold, M. Razinger, A. J. Simmons, M. Suttie, and the GEMS-AER team: *Aerosol analysis and forecast in the ECMWF Integrated Forecast System. Part II : Data assimilation*, *J. Geophys. Res.*, 114, D13205, doi:10.1029/2008JD011115, 2009.
- Birmili, W., Schepanski, K., Ansmann, A., Spindler, G., Tegen, I., Wehner, B., Nowak, A., Reimer, E., Mattis, I., Müller, K., Brüggemann, E., Gnauk, T., Herrmann, H., Wiedensohler, A., Althausen, D., Schladitz, A., Tuch, T., and Löschau, G.: *A case of extreme particulate matter concentrations over Central Europe caused by dust emitted over the southern Ukraine*, *Atmos. Chem. Phys.*, 8, 997–1016, <https://doi.org/10.5194/acp-8-997-2008>, 2008.
- Boussetta, S., Balsamo, G., Beljaars, A., Agusti-Panareda, A., Calvet, J.-C., Jacobs, C., van den Hurk, B., Viterbo, P., Lafont, S., Dutra, E., Jarlan, L., Balzarolo, M., Papale, D., and van der Werf, G.: *Natural carbon dioxide exchanges in the ECMWF Integrated Forecasting System: implementation and offline validation*, *J. Geophys. Res.-Atmos.*, 118, 1–24, doi: 10.1002/jgrd.50488, 2013.
- Braathen, WMO Arctic Ozone Bulletin No 1/2016, DOI:10.13140/RG.2.1.4929.6403, 2016.
- Cammas, J.P., Brioude J., Chaboureaud J.-P., Duron J., Mari C., Mascart P., Nédélec P., Smit H., Pätz H.-W., Volz-Thomas A., Stohl A., and Fromm M., *Injection in the lower stratosphere of biomass fire emissions followed by long-range transport: a MOZAIC case study*, *Atmos. Chem. Phys.*, 9, 5829–5846, 2009
- Cariolle, D. and Teyssède, H.: *A revised linear ozone photochemistry parameterization for use in transport and general circulation models: multi-annual simulations*, *Atmos. Chem. Phys.*, 7, 2183–2196, doi:10.5194/acp-7-2183-2007, 2007.
- Dee, D. P. and S. Uppala, *Variational bias correction of satellite radiance data in the ERA-Interim reanalysis*, *Quart. J. Roy. Meteor. Soc.*, 135, 1830–1841, 2009.
- Deeter, M. N., Emmons, L. K., Edwards, D. P., Gille, J. C., and Drummond, J. R.: *Vertical resolution and information content of CO profiles retrieved by MOPITT*, *Geophys. Res. Lett.*, 31, L15112, doi:10.1029/2004GL020235, 2004.



- Deeter, M. N., et al. (2010), *The MOPITT version 4 CO product: Algorithm enhancements, validation, and long-term stability*, *J. Geophys. Res.*, 115, D07306, doi:10.1029/2009JD013005.
- Dentener, F., et al., 2006: *Emissions of primary aerosol and precursor gases in the years 2000 and 1750 prescribed data-sets for AeroCom*, *Atmos. Chem. Phys.*, 6, 4321 – 4344.
- Deshler, T., J.L. Mercer, H.G.J. Smit, R. Stubi, G. Levrat, B.J. Johnson, S.J. Oltmans, R. Kivi, A.M. Thompson, J. Witte, J. Davies, F.J. Schmidlin, G. Brothers, T. Sasaki (2008) *Atmospheric comparison of electrochemical cell ozonesondes from different manufacturers, and with different cathode solution strengths: The Balloon Experiment on Standards for Ozonesondes*. *J. Geophys. Res.* 113, D04307, doi:10.1029/2007JD008975
- Dupuy, E., et al.: *Validation of ozone measurements from the Atmospheric Chemistry Experiment (ACE)*, *Atmos. Chem. Phys.*, 9, 287–343, doi:10.5194/acp-9-287-2009, 2009.
- Elbern, H., Schwinger, J., Botchorishvili, R.: *Chemical state estimation for the middle atmosphere by four-dimensional variational data assimilation: System configuration*. *Journal of Geophysical Research (Atmospheres)* 115, 6302, 2010.
- Emmons, L. K., D. P. Edwards, M. N. Deeter, J. C. Gille, T. Campos, P. Nédélec, P. Novelli, and G. Sachse, *Measurements of Pollution In The Troposphere (MOPITT) validation through 2006* *Atmos. Chem. Phys.*, 9, 1795–1803, 2009
- Errera, Q., Daerden, F., Chabrilat, S., Lambert, J. C., Lahoz, W. A., Viscardy, S., Bonjean, S., and Fonteyn, D., *4D-Var Assimilation of MIPAS chemical observations: ozone and nitrogen dioxide analyses*, *Atmos. Chem. Phys.*, 8, 6169–6187, 2008.
- Errera, Q. and Ménard, R.: *Technical Note: Spectral representation of spatial correlations in variational assimilation with grid point models and application to the belgian assimilation system for chemical observations (BASCOE)*, *Atmos. Chem. Phys. Discuss.*, 12, 16763–16809, doi:10.5194/acpd-12-16763-2012, 2012.
- Eskes, H.J., S. Basart, A. Benedictow, Y. Bennouna, A.-M. Blechschmidt, S. Chabrilat, Y. Christophe, E. Cuevas, H. Flentje, K. M. Hansen, J. Kapsomenakis, B. Langerock, M. Ramonet, A. Richter, M. Schulz, N. Sudarchikova, A. Wagner, T. Warneke, C. Zerefos, *Observation characterisation and validation methods document*, Copernicus Atmosphere Monitoring Service (CAMS) report, December 2019, doi: 10.24380/0nsd-wb26. Available from: <http://atmosphere.copernicus.eu/user-support/validation/verification-global-services>
- Eskes, H. J., S. Basart, A. Benedictow, Y. Bennouna, A.-M. Blechschmidt, S. Chabrilat, Y. Christophe, H. Clark, E. Cuevas, K. M. Hansen, U. Im, J. Kapsomenakis, B. Langerock, K. Petersen, M. Schulz, A. Wagner, C. Zerefos, *Upgrade verification note for the CAMS near-real time global atmospheric composition service*, Copernicus Atmosphere Monitoring Service (CAMS) report, CAMS84_2015SC3_D84.3.1.5_201802_esuite_v1.pdf, February 2018 (2018b)
- Eskes et al., *Upgrade verification note for the CAMS near-real time global atmospheric composition service*, Addendum July 2018, CAMS84_2015SC3_D84.3.1.5_201802_esuite_v1.pdf (2018c).
- Flemming, J., Huijnen, V., Arteta, J., Bechtold, P., Beljaars, A., Blechschmidt, A.-M., Diamantakis, M., Engelen, R. J., Gaudel, A., Inness, A., Jones, L., Josse, B., Katragkou, E., Marecal, V., Peuch, V.-H., Richter, A., Schultz, M. G., Stein, O., and Tsikerdekis, A.: *Tropospheric chemistry in the Integrated Forecasting System of ECMWF*, *Geosci. Model Dev.*, 8, 975–1003, doi:10.5194/gmd-8-975-2015, 2015.
- Flemming, J., Benedetti, A., Inness, A., Engelen, R. J., Jones, L., Huijnen, V., Remy, S., Parrington, M., Suttie, M., Bozzo, A., Peuch, V.-H., Akritidis, D., and Katragkou, E.: *The CAMS interim Reanalysis of Carbon Monoxide, Ozone and Aerosol for 2003–2015*, *Atmos. Chem. Phys.*, 17, 1945–1983, doi:10.5194/acp-17-1945-2017, 2017.

- Franco, B., et al., Retrievals of formaldehyde from ground-based FTIR and MAX-DOAS observations at the Jungfraujoch station and comparisons with GEOS-Chem and IMAGES model simulations, *Atmos. Meas. Tech.*, 8, 1733-1756, 2015
- Gielen, C., Van Roozendael, M., Hendrick, F., Pinardi, G., Vlemmix, T., De Bock, V., De Backer, H., Fayt, C., Hermans, C., Gillotay, D., and Wang, P.: A simple and versatile cloud-screening method for MAX-DOAS retrievals, *Atmos. Meas. Tech.*, 7, 3509-3527, doi:10.5194/amt-7-3509-2014, 2014.
- Granier, C. et al.: Evolution of anthropogenic and biomass burning emissions of air pollutants at global and regional scales during the 1980–2010 period. *Climatic Change* (109), 2011
- Holben, B. N., Eck, T. F., Slutsker, I., Tanré, D., Buis, J. P., Setzer, A., Vermote, E., Reagan, J. A., Kaufman, Y. J., Nakajima, T., Lavenu, F., Jankowiak, I., and Smirnov A.: AERONET – a federated instrument network and data archive for aerosol characterization, *Remote Sens. Environ.*, 66, 1–16, 5529, 5533, 5537, 5544, 1998.
- Hommel, R., Eichmann, K.-U., Aschmann, J., Bramstedt, K., Weber, M., von Savigny, C., Richter, A., Rozanov, A., Wittrock, F., Khosrawi, F., Bauer, R., and Burrows, J. P.: Chemical ozone loss and ozone mini-hole event during the Arctic winter 2010/2011 as observed by SCIAMACHY and GOME-2, *Atmos. Chem. Phys.*, 14, 3247-3276, doi:10.5194/acp-14-3247-2014, 2014.
- Huijnen, V., et al.: The global chemistry transport model TM5: description and evaluation of the tropospheric chemistry version 3.0, *Geosci. Model Dev.*, 3, 445-473, doi:10.5194/gmd-3-445-2010, 2010.
- Inness, A., Blechschmidt, A.-M., Bouarar, I., Chabrillat, S., Crepulja, M., Engelen, R. J., Eskes, H., Flemming, J., Gaudel, A., Hendrick, F., Huijnen, V., Jones, L., Kapsomenakis, J., Katragkou, E., Keppens, A., Langerock, B., de Mazière, M., Melas, D., Parrington, M., Peuch, V. H., Razinger, M., Richter, A., Schultz, M. G., Suttie, M., Thouret, V., Vrekoussis, M., Wagner, A., and Zerefos, C.: Data assimilation of satellite-retrieved ozone, carbon monoxide and nitrogen dioxide with ECMWF's Composition-IFS, *Atmos. Chem. Phys.*, 15, 5275-5303, doi:10.5194/acp-15-5275-2015, 2015.
- Janssens-Maenhout, G., Dentener, F., Aardenne, J. V., Monni, S., Pagliari, V., Orlandini, L., Klimont, Z., Kurokawa, J., Akimoto, H., Ohara, T., Wankmueller, R., Battye, B., Grano, D., Zuber, A., and Keating, T.: EDGAR-HTAP: a Harmonized Gridded Air Pollution Emission Dataset Based on National Inventories, JRC68434, EUR report No EUR 25 299–2012, ISBN 978-92-79- 23122-0, ISSN 1831-9424, European Commission Publications Office, Ispra (Italy), 2012.
- Jaross, G., Bhartia, P.K., Chen, G., Kowitt, M., Haken, M., Chen, Z., Xu, Ph., Warner, J., Kelly, T. : OMPS Limb Profiler instrument performance assessment, *J. Geophys. Res. Atmos* 119, 2169-8996, 2014.
- Joly, M. and Peuch, V. H., Objective classification of air quality monitoring sites over Europe, *Atmospheric Environment*, 47, 111-123, 2012.
- Kaiser, J. W., Heil, A., Andreae, M. O., Benedetti, A., Chubarova, N., Jones, L., Morcrette, J.-J., Razinger, M., Schultz, M. G., Suttie, M., and van der Werf, G. R.: Biomass burning emissions estimated with a global fire assimilation system based on observed fire radiative power, *Biogeosciences*, 9, 527-554, doi:10.5194/bg-9-527-2012, 2012.
- Kramarova, N. A., Nash, E. R., Newman, P. A., Bhartia, P. K., McPeters, R. D., Rault, D. F., Seftor, C. J., Xu, P. Q., and Labow, G. J.: Measuring the Antarctic ozone hole with the new Ozone Mapping and Profiler Suite (OMPS), *Atmos. Chem. Phys.*, 14, 2353-2361, doi:10.5194/acp-14-2353-2014, 2014.
- Lahoz, W. A., Errera, Q., Viscardi, S., and Manney G. L., The 2009 stratospheric major warming described from synergistic use of BASCOE water vapour analyses and MLS observations, *Atmos. Chem. Phys.* 11, 4689-4703, 2011



- Lambert, A, et al., *Aura Microwave Limb Sounder Version 3.4 Level-2 near real-time data user guide*, <http://disc.sci.gsfc.nasa.gov/Aura/data-holdings/MLS/documents/NRT-user-guide-v34.pdf>
- Langerock, B., De Mazière, M., Hendrick, F., Vigouroux, C., Desmet, F., Dils, B., and Niemeijer, S.: *Description of algorithms for co-locating and comparing gridded model data with remote-sensing observations*, *Geosci. Model Dev.*, 8, 911-921, doi:10.5194/gmd-8-911-2015, 2015.
- Lefever, K., van der A, R., Baier, F., Christophe, Y., Errera, Q., Eskes, H., Flemming, J., Inness, A., Jones, L., Lambert, J.-C., Langerock, B., Schultz, M. G., Stein, O., Wagner, A., and Chabrillat, S.: *Copernicus stratospheric ozone service, 2009–2012: validation, system intercomparison and roles of input data sets*, *Atmos. Chem. Phys.*, 15, 2269-2293, doi:10.5194/acp-15-2269-2015, 2015.
- Liu, Z., et al., *Exploring the missing source of glyoxal (CHOCHO) over China*, *Geophys. Res. Lett.*, 39, L10812, doi: 10.1029/2012GL051645, 2012
- Massart, S., Flemming, J., Cariolle, D., Jones, L., *High resolution CO tracer forecasts*, MACC-III Deliverable D22.04, May 2015, available from <http://www.gmes-atmosphere.eu/documents/macciii/deliverables/grg>
- Morcrette, J.-J., O. Boucher, L. Jones, D. Salmond, P. Bechtold, A. Beljaars, A. Benedetti, A. Bonet, J. W. Kaiser, M. Razinger, M. Schulz, S. Serrar, A. J. Simmons, M. Sofiev, M. Suttie, A. M. Tompkins, and A. Untch: *Aerosol analysis and forecast in the ECMWF Integrated Forecast System. Part I: Forward modelling*, *J. Geophys. Res.*, 114, D06206, doi:10.1029/2008JD011235, 2009.
- Rémy, S., Kipling, Z., Flemming, J., Boucher, O., Nabat, P., Michou, M., Bozzo, A., Ades, M., Huijnen, V., Benedetti, A., Engelen, R., Peuch, V.-H., and Morcrette, J.-J.: *Description and evaluation of the tropospheric aerosol scheme in the European Centre for Medium-Range Weather Forecasts (ECMWF) Integrated Forecasting System (IFS-AER, cycle 45R1)*, *Geosci. Model Dev.*, 12, 4627–4659, <https://doi.org/10.5194/gmd-12-4627-2019>, 2019.
- Richter, A., Burrows, J. P., Nüß, H., Granier, C., Niemeier, U.: *Increase in tropospheric nitrogen dioxide over China observed from space*, *Nature*, 437, 129-132, doi: 10.1038/nature04092, 2005
- Richter, A., Begoin, M., Hilboll, A., and Burrows, J. P.: *An improved NO₂ retrieval for the GOME-2 satellite instrument*, *Atmos. Meas. Tech.*, 4, 1147-1159, doi:10.5194/amt-4-1147-2011, 2011
- Schulz, M., Y. Christophe, M. Ramonet, Wagner, A., H. J. Eskes, S. Basart, A. Benedictow, Y. Bennouna, A.-M. Blechschmidt, S. Chabrillat, E. Cuevas, A. El-Yazidi, H. Flentje, P. Fritzsche, K.M. Hansen, U. Im, J. Kapsomenakis, B. Langerock, A. Richter, N. Sudarchikova, V. Thouret, T. Warneke, C. Zerefos, *Validation report of the CAMS near-real-time global atmospheric composition service: Period December 2019 – February 2020*, Copernicus Atmosphere Monitoring Service (CAMS) report, CAMS84_2018SC2_D1.1.1_DJF2020.pdf, June 2020.
- Sindelarova, K., Granier, C., Bouarar, I., Guenther, A., Tilmes, S., Stavrou, T., Müller, J.-F., Kuhn, U., Stefani, P., and Knorr, W.: *Global data set of biogenic VOC emissions calculated by the MEGAN model over the last 30 years*, *Atmos. Chem. Phys.*, 14, 9317-9341, doi:10.5194/acp-14-9317-2014, 2014.
- Smit, H.G.J., W. Straeter, B.J. Johnson, S.J. Oltmans, J. Davies, D.W. Tarasick, B. Hoegger, R. Stubi, F.J. Schmidlin, T. Northam, A.M. Thompson, J.C. Witte, I. Boyd: *Assessment of the performance of ECC-ozone sondes under quasi-flight conditions in the environmental simulation chamber: Insights from the Juelich Ozone Sonde Intercomparison Experiment (JOSIE)*, *J. Geophys. Res.* 112, D19306, doi:10.1029/2006JD007308, 2007.
- Solomon, S., Haskins, J., Ivy, D. J. and Min, F.: *Fundamental differences between Arctic and Antarctic ozone depletion*, *PNAS* 2014 111 (17) 6220-6225, doi:10.1073/pnas.1319307111, 2014.



- Stauffer, R. M., Thompson, A. M., Kollonige, D. E., Witte, J. C., Tarasick, D. W., and Davies, J., Voemel, H., Morris, G. A., VanMalderen, R., Johnson, B. J. J., Querel, R.R., Selkirk, H.B., Stübi, R., Smit, H.G.J.: A Post-2013 Drop-off in Total Ozone at Half of Global Ozone Sonde Stations: ECC Instrument Artifacts? *Earth and Space Science Open Archive JF M310.1002/essoar.10501543.1*, 2020.
- Stavrakou, T., First space-based derivation of the global atmospheric methanol fluxes, *Atm. Chem. Phys.*, **11**, 4873–4898, 2013.
- Strahan, S.E., A.R. Douglass, and P.A. Newman, The contributions of chemistry and transport to low arctic ozone in March 2011 derived from Aura MLS observations, *J. Geophys. Res. Atmos.*, **118**, 1563–1576, doi:10.1002/jgrd.50181, 2013.
- Taha, G.; Jaross, G. R.; Bhartia, P. K.: Validation of OMPS LP Ozone Profiles Version 2.0 with MLS, Ozone Sondes and Lidar Measurements, American Geophysical Union, Fall Meeting 2014, abstract #A33J-3322, 2014.
- Taylor, K.E.: Summarizing multiple aspects of model performance in a single diagram. *J. Geophys. Res.*, **106**, 7183–7192, 2001.
- Thompson, A. M., Witte, J. C., Sterling, C., Jordan, A., Johnson, B. J., Oltmans, S. J., Thiongo, K. (2017). First reprocessing of Southern Hemisphere Additional Ozone sondes (SHADOZ) ozone profiles (1998–2016): 2. Comparisons with satellites and ground-based instruments. *Journal of Geophysical Research: Atmospheres*, **122**, 13,000–13,025. <https://doi.org/10.1002/2017JD027406>, 2017.
- van der A, R. J., M. A. F. Allaart, and H. J. Eskes, Multi sensor reanalysis of total ozone, *Atmos. Chem. Phys.*, **10**, 11277–11294, doi:10.5194/acp-10-11277-2010, www.atmos-chem-phys.net/10/11277/2010/, 2010
- van der A, R., M. Allaart, H. Eskes, K. Lefever, Validation report of the MACC 30-year multi-sensor reanalysis of ozone columns Period 1979–2008, MACC-II report, Jan 2013, MACCII_VAL_DEL_D_83.3_OzoneMSRv1_20130130.docx/pdf.
- van der A, R. J., Allaart, M. A. F., and Eskes, H. J.: Extended and refined multi sensor reanalysis of total ozone for the period 1970–2012, *Atmos. Meas. Tech.*, **8**, 3021–3035, doi:10.5194/amt-8-3021-2015, 2015.
- van Geffen, J., Boersma, K. F., Eskes, H., Sneep, M., ter Linden, M., Zara, M., and Veefkind, J. P.: S5P TROPOMI NO₂ slant column retrieval: method, stability, uncertainties and comparisons with OMI, *Atmos. Meas. Tech.*, **13**, 1315–1335, <https://doi.org/10.5194/amt-13-1315-2020>, 2020.
- Vrekoussis, M., Wittrock, F., Richter, A., and Burrows, J. P.: GOME-2 observations of oxygenated VOCs: what can we learn from the ratio glyoxal to formaldehyde on a global scale?, *Atmos. Chem. Phys.*, **10**, 10145–10160, doi:10.5194/acp-10-10145-2010, 2010
- Wennberg, P. O., Mui, W., Wunch, D., Kort, E. A., Blake, D. R., Atlas, E. L., Santoni, G. W., Wofsy, S. C., Diskin, G. S., Jeong, S., and Fischer, M. L.: On the sources of methane to the Los Angeles atmosphere, *Environ. Sci. Technol.*, **46**, 9282–9289, <https://doi.org/10.1021/es301138y>, 2012
- Wittrock, F., A. Richter, H. Oetjen, J. P. Burrows, M. Kanakidou, S. Myriokefalitakis, R. Volkamer, S. Beirle, U. Platt, and T. Wagner, Simultaneous global observations of glyoxal and formaldehyde from space, *Geophys. Res. Lett.*, **33**, L16804, doi:10.1029/2006GL026310, 2006
- Witte, J. C., Thompson, A. M., Smit, H. G. J., Vömel, H., Posny, F., & Stübi, R. : First reprocessing of Southern Hemisphere Additional Ozone sondes profile records: 3. Uncertainty in ozone profile and total column. *Journal of Geophysical Research: Atmospheres*, **123**, 3243–3268. <https://doi.org/10.1002/2017JD027791>, 2018.
- WMO (2010), Guidelines for the Measurement of Atmospheric Carbon Monoxide, GAW Report No. 192, World Meteorological Organization, Geneva, Switzerland, 2010.



WMO (2013), Guidelines for the Continuous Measurements of Ozone in the Troposphere, GAW Report No. 209, World Meteorological Organization, Geneva, Switzerland, 2013.

Wunch, D., Wennberg, P. O., Toon, G. C., Keppel-Aleks, G., and Yavin, Y. G.: Emissions of greenhouse gases from a North American megacity, Geophys. Res. Lett., 36, 1–5, <https://doi.org/10.1029/2009GL039825>, 2009.



Annex 1: Acknowledgements

Listed below are the authors contributing to the sections in this report. The authors contributing to the model description are also provided, as well as acknowledgements to the validation datasets.

Tropospheric reactive gases reactive gases

Annette Wagner, MPG (editor, O₃ sondes, GAW data)
Yasmine Bennouna, Valerie Thouret, CNRS-LA (IAGOS)
Harald Flentje, DWD (O₃ sondes, GAW data)
Anne Blechschmidt and Andreas Richter, IUB Bremen (GOME-2 NO₂, HCHO)
John Kapsomenakis, Christos Zerefos, AA (ESRL)
Natalia Sudarchikova, satellite IR observations (MPG)
Kaj Hansen, Ulas Im, AU (Arctic theme)
Bavo Langerock, BIRA (NDACC)

Tropospheric aerosol

Michael Schulz, MetNo (editor, Aerocom, Aeronet)
Anna Benedictow, Jan Griesfeller, MetNo (Aerocom, Aeronet)
Sara Basart, MTeresa Pay, Oriol Jorba, BSC-CNS (Aeronet, MODIS, AirBase, SDS-WAS NAMEE RC)
Emilio Cuevas, AEMET (Aeronet, MODIS, AirBase, SDS-WAS NAMEE RC)
Harald Flentje, DWD (Backscatter profiles)

Stratospheric reactive gases

Yves Christophe, BIRA (editor, model-satellite intercomparisons)
Simon Chabrillat, BIRA (model intercomparisons)
Annette Wagner, MPI-M (O₃ sondes)
Bavo Langerock, BIRA (NDACC FTIR, MWR, UVVIS DOAS, LIDAR)
Anne Blechschmidt and Andreas Richter, IUB-UB Bremen (SCIAMACHY/GOME-2 NO₂)

Greenhouse gases

Michel Ramonet, IPSL (ICOS)
Abdelhadi El-Yazidi and Leonard Rivier, LSCE (ICOS)
Thorsten Warneke, UBC (TCCON)
Bavo Langerock, BIRA (TCCON)

Reactive gases and aerosol modeling

Johannes Flemming (ECMWF), Antje Inness (ECMWF), Angela Benedetti (ECMWF), Sebastien Massart (ECMWF), Anna Agusti-Panareda (ECMWF), Johannes Kaiser (KCL/MPIC/ECMWF), Samuel Remy (LMD), Olivier Boucher (LMD), Vincent Huijnen (KNMI), Richard Engelen (ECMWF)



Acknowledgements for the validation datasets used

We wish to acknowledge the provision of NRT GAW observational data by: Institute of Atmospheric Sciences and Climate (ISAC) of the Italian National Research Council (CNR), South African Weather Service, National Centre for Atmospheric Science (NCAS, Cape Verde), National Air Pollution Monitoring Network (NABEL) (Federal Office for the Environment FOEN and Swiss Federal Laboratories for Materials Testing and Research EMPA), Atmospheric Environment Division Global Environment and Marine Department Japan Meteorological Agency, Chinese Academy of Meteorological Sciences (CAMS), Alfred Wegener Institut, Umweltbundesamt (Austria), National Meteorological Service (Argentina), Umweltbundesamt (UBA, Germany)

We are grateful to the numerous operators of the Aeronet network and to the central data processing facility at NASA Goddard Space Flight Center for providing the NRT sun photometer data, especially Ilya Slutsker and Brent Holben for sending the data.

The authors thank to all researchers, data providers and collaborators of the World Meteorological Organization's Sand and Dust Storm Warning Advisory and Assessment System (WMO SDS-WAS) for Northern Africa, Middle East and Europe (NAMEE) Regional Node. Also special thank to Canary Government as well as AERONET, MODIS, U.K. Met Office MSG, MSG Eumetsat and EOSDIS World Viewer principal investigators and scientists for establishing and maintaining data used in the activities of the WMO SDS-WAS NAMEE Regional Center (<http://sds-was.aemet.es/>).

We wish to acknowledge the provision of ozone sonde data by the World Ozone and Ultraviolet Radiation Data Centre established at EC in Toronto (<http://woudc.org>), by the Data Host Facility of the Network for the Detection of Atmospheric Composition Change established at NOAA (<http://ndacc.org>), by the Norwegian Institute for Air Research and by the National Aeronautics and Space Administration (NASA).

We wish to thank the NDACC investigators for the provision of observations at Ny Alesund, Bern, Jungfraujoch, Izaña, Xianghe, Harestua, Reunion Mado, Uccle, Hohenpeissen, Mauna Loa, Lauder and Haute Provence.

The authors acknowledge the NOAA Earth System Research Laboratory (ESRL) Global Monitoring Division (GMD) for the provision of ground-based ozone concentrations.

The MOPITT CO data were obtained from the NASA Langley Research Center ASDC. We acknowledge the LATMOS IASI group for providing IASI CO data.

SCIAMACHY lv1 radiances were provided to IUP-UB by ESA through DLR/DFD.

GOME-2 lv1 radiances were provided to IUP-UB by EUMETSAT.

S5P lv1 radiances and NO₂ operational were provided by EU Copernicus.

The authors acknowledge Environment and Climate Change Canada for the provision of Alert ozone data and Sara Crepinsek – NOAA for the provision of Tiksi ozone data. Surface ozone data from the Zeppelin Mountain, Svalbard are from www.luftkvalitet.info. Surface ozone data from the Villum Research Station, Station Nord (VRS) were financially supported by "The Danish Environmental Protection Agency" with means from the MIKA/DANCEA funds for Environmental Support to the



Arctic Region. The Villum Foundation is acknowledged for the large grant making it possible to build VRS in North Greenland.

We acknowledge the National Aeronautics and Space Administration (NASA), USA for providing the OMPS limb sounder data (<http://npp.gsfc.nasa.gov/omps.html>), the SAGE III-ISS ozone data https://eosweb.larc.nasa.gov/project/sageiii-iss/sageiii-iss_table and the Aura-MLS offline data (<http://mls.jpl.nasa.gov/index-eos-mls.php>).

We thank the Canadian Space Agency and ACE science team for providing level 2 data retrieved from ACE-FTS on the Canadian satellite SCISAT-1.

The European Environment Information and Observation Network (Eionet) Air Quality portal provides details relevant for the reporting of air quality information from EU Member States and other EEA member and co-operating countries. This information is submitted according to Directives 2004/107/EC and 2008/50/EC of the European Parliament and of the Council.

We are grateful to the IAGOS operators from the various institutes which are members of IAGOS-AISBL (<http://www.iagos.org>). The authors also acknowledge the strong support of the European Commission, Airbus, and the airlines (Lufthansa, Air France, Austrian, Air Namibia, Cathay Pacific, Iberia, China Airlines and Hawaiian Airlines so far) which have carried the MOZAIC or IAGOS equipment and undertaken maintenance since 1994. In the last 10 years of operation, MOZAIC has been funded by INSU-CNRS (France), Météo-France, Université Paul Sabatier (Toulouse, France) and Research Center Jülich (FZJ, Jülich, Germany). IAGOS has been additionally funded by the EU projects IAGOS-DS and IAGOS-ERI. The MOZAIC-IAGOS database (<http://www.iagos-data.fr>) is supported by AERIS (CNES and INSU-CNRS). Data are also available via AERIS web site www.aeris-data.fr.

We acknowledge the contribution of the ICOS Atmospheric Thematic Center (Lynn Hazan, Amara Abbaris, and Leonard Rivier) for the near real time data processing of surface CO₂ and CH₄ concentrations. The ICOS monitoring sites are maintained by the national networks: ICOS-Czech Rep. (Michal Marek, Katerina Komínková, Gabriela Vítková), ICOS-Finland (Olli Peltola, Janne Levula, Tuomas Laurila), ICOS-France (Michel Ramonet, Marc Delmotte, Sebastien Conil, Morgan Lopez, Victor Kazan, Aurélie Colomb, Jean Marc Pichon, Roxanne Jacob, Julie Helle, Olivier Laurent), ICOS-Germany (Matthias Lindauer, Dagmar Kubistin, Christian Plass-Duelmer, Dietmar Weyrauch, Marcus Schumacher), ICOS-Italy (Paolo Cristofanelli, Michela Maione, Francesco Apadula), ICOS-Norway (Cathrine Lund Myhre, Ove Hermansen), ICOS-Sweden (Jutta Holst, Michal Heliasz, Meelis Molder, Mikael Ottosson Lofvenius, Anders Lindroth, Per Marklund), ICOS-Switzerland (Martin Steinbacher, Simon Wyss), European Commission, Joint Research Centre, Directorate for Energy, Transport and Climate (Peter Bergamaschi, Giovanni Manca).

The TCCON site at Orleans is operated by the University of Bremen and the RAMCES team at LSCE (Gif-sur-Yvette, France). The TCCON site at Bialystok is operated by the University of Bremen. Funding for the two sites was provided by the EU-project ICOS-INWIRE and the University of Bremen. The TCCON site at Réunion is operated by BIRA-IASB, in cooperation with UReunion and is funded by BELSPO in the framework of the Belgian ICOS program.

TCCON references:



- Blumenstock, T., F. Hase, M. Schneider, O. E. García, and E. Sepúlveda. 2017. "TCCON data from Izana (ES), Release GGG2014.R1." CaltechDATA. doi:10.14291/tcon.ggg2014.izana01.r1.
- De Mazière, M., M. K. Sha, F. Desmet, C. Hermans, F. Scolas, N. Kumps, J.-M. Metzger, V. Dufлот, and J.-P. Cammas. 2017. "TCCON data from Réunion Island (RE), Release GGG2014.R1." CaltechDATA. doi:10.14291/tcon.ggg2014.reunion01.r1.
- Deutscher, N. M., J. Notholt, J. Messerschmidt, C. Weinzierl, T. Warneke, C. Petri, and P. Grupe. 2017. "TCCON data from Bialystok (PL), Release GGG2014.R1." CaltechDATA. doi:10.14291/tcon.ggg2014.bialystok01.r1/1183984.
- Dubey, M. K., B. G. Henderson, D. Green, Z. T. Butterfield, G. Keppel-Aleks, N. T. Allen, J.-F. Blavier, C. M. Roehl, D. Wunch, and R. Lindenmaier. 2017. "TCCON data from Manaus (BR), Release GGG2014.R0." CaltechDATA. doi:10.14291/tcon.ggg2014.manaus01.r0/1149274.
- Dubey, M. K., R. Lindenmaier, B. G. Henderson, D. Green, N. T. Allen, C. M. Roehl, J.-F. Blavier, et al. 2017. "TCCON data from Four Corners (US), Release GGG2014.R0." CaltechDATA. doi:10.14291/tcon.ggg2014.fourcorners01.r0/1149272.
- Feist, D. G., S. G. Arnold, N. John, and M. C. Geibel. 2017. "TCCON data from Ascension Island (SH), Release GGG2014.R0." CaltechDATA. doi:10.14291/tcon.ggg2014.ascension01.r0/1149285.
- Goo, T.-Y., Y.-S. Oh, and V. A. Velazco. 2017. "TCCON data from Anmeyondo (KR), Release GGG2014.R0." CaltechDATA. doi:10.14291/tcon.ggg2014.anmeyondo01.r0/1149284.
- Griffith, D. W. T., N. M. Deutscher, V. A. Velazco, P. O. Wennberg, Y. Yavin, G. Keppel-Aleks, R. A. Washenfelder, et al. 2017. "TCCON data from Darwin (AU), Release GGG2014.R0." CaltechDATA. doi:10.14291/tcon.ggg2014.darwin01.r0/1149290.
- Griffith, D. W. T., V. A. Velazco, N. M. Deutscher, C. Paton-Walsh, N. B. Jones, S. R. Wilson, R. C. Macatangay, G. C. Kettlewell, R. R. Buchholz, and M. O. Rigenbach. 2017. "TCCON data from Wollongong (AU), Release GGG2014.R0." CaltechDATA. doi:10.14291/tcon.ggg2014.wollongong01.r0/1149291.
- Hase, F., T. Blumenstock, S. Dohe, J. Groß, and M.ä. Kiel. 2017. "TCCON data from Karlsruhe (DE), Release GGG2014.R1." CaltechDATA. doi:10.14291/tcon.ggg2014.karlsruhe01.r1/1182416.
- Iraci, L. T., J. R. Podolske, P. W. Hillyard, C. Roehl, P. O. Wennberg, J.-F. Blavier, J. Landeros, et al. 2017. "TCCON data from Edwards (US), Release GGG2014.R1." CaltechDATA. doi:10.14291/tcon.ggg2014.edwards01.r1/1255068.
- . 2017. "TCCON data from Indianapolis (US), Release GGG2014.R1." CaltechDATA. doi:10.14291/tcon.ggg2014.indianapolis01.r1/1330094.
- Kawakami, S., H. Ohshima, K. Arai, H. Okumura, C. Taura, T. Fukamachi, and M. Sakashita. 2017. "TCCON data from Saga (JP), Release GGG2014.R0." CaltechDATA. doi:10.14291/tcon.ggg2014.saga01.r0/1149283.
- Kivi, R., P. Heikkinen, and E. Kyrö. 2017. "TCCON data from Sodankylä (FI), Release GGG2014.R0." CaltechDATA. doi:10.14291/tcon.ggg2014.sodankyla01.r0/1149280.
- Liu, Cheng, Wei Wang, and Youwen Sun. 2018. "TCCON data from Hefei (PRC), Release GGG2014.R0." CaltechDATA. doi:10.14291/tcon.ggg2014.hefei01.r0.
- Morino, I., N. Yokozeki, T. Matsuzaki, and M. Horikawa. 2017. "TCCON data from Rikubetsu (JP), Release GGG2014.R2." CaltechDATA. doi:10.14291/tcon.ggg2014.rikubetsu01.r2.
- Morino, I., T. Matsuzaki, and M. Horikawa. 2017. "TCCON data from Tsukuba (JP), 125HR, Release GGG2014.R2." CaltechDATA. doi:10.14291/tcon.ggg2014.tsukuba02.r2.
- Morino, Isamu, Voltaire A. Velazco, Akihiro Hori, Osamu Uchino, and David W. T. Griffith. 2018. "TCCON data from Burgos, Ilocos Norte (PH), Release GGG2014.R0." CaltechDATA. doi:10.14291/tcon.ggg2014.burgos01.r0.



- Notholt, J., C. Petri, T. Warneke, N. M. Deutscher, M. Palm, M. Buschmann, C. Weinzierl, R. C. Macatangay, and P. Grupe. 2017. "TCCON data from Bremen (DE), Release GGG2014.R0." CaltechDATA. doi:10.14291/tccon.ggg2014.bremen01.r0/1149275.
- Notholt, J., T. Warneke, C. Petri, N. M. Deutscher, C. Weinzierl, M. Palm, and M. Buschmann. 2017. "TCCON data from Ny Ålesund, Spitsbergen (NO), Release GGG2014.R0." CaltechDATA. doi:10.14291/tccon.ggg2014.nyalesund01.r0/1149278.
- Pollard, David Frank, John Robinson, and Hisako Shiona. 2019. "TCCON data from Lauder (NZ), Release GGG2014.R0." CaltechDATA. doi:10.14291/tccon.ggg2014.lauder03.r0.
- Sherlock, V., B. Connor, J. Robinson, H. Shiona, D. Smale, and D. F. Pollard. 2017. "TCCON data from Lauder (NZ), 120HR, Release GGG2014.R0." CaltechDATA. doi:10.14291/tccon.ggg2014.lauder01.r0/1149293.
- . 2017. "TCCON data from Lauder (NZ), 125HR, Release GGG2014.R0." CaltechDATA. doi:10.14291/tccon.ggg2014.lauder02.r0/1149298.
- Strong, K., S. Roche, J. E. Franklin, J. Mendonca, E. Lutsch, D. Weaver, P. F. Fogal, J. R. Drummond, R. Batchelor, and R. Lindenmaier. 2018. "TCCON data from Eureka (CA), Release GGG2014.R3." CaltechDATA. doi:10.14291/tccon.ggg2014.eureka01.r3.
- Sussmann, R., and M. Rettinger. 2017. "TCCON data from Garmisch (DE), Release GGG2014.R2." CaltechDATA. doi:10.14291/tccon.ggg2014.garmisch01.r2.
- . 2018. "TCCON data from Zugspitze (DE), Release GGG2014.R1." CaltechDATA. doi:10.14291/tccon.ggg2014.zugspitze01.r1.
- Té, Y., P. Jeseck, and C. Janssen. 2017. "TCCON data from Paris (FR), Release GGG2014.R0." CaltechDATA. doi:10.14291/tccon.ggg2014.paris01.r0/1149279.
- Warneke, T., J. Messerschmidt, J. Notholt, C. Weinzierl, N. M. Deutscher, C. Petri, and P. Grupe. 2017. "TCCON data from Orléans (FR), Release GGG2014.R0." CaltechDATA. doi:10.14291/tccon.ggg2014.orleans01.r0/1149276.
- Wennberg, P. O., C. M. Roehl, D. Wunch, G. C. Toon, J.-F. Blavier, R. Washenfelter, G. Keppel-Aleks, N. T. Allen, and J. Ayers. 2017. "TCCON data from Park Falls (US), Release GGG2014.R1." CaltechDATA. doi:10.14291/tccon.ggg2014.parkfalls01.r1.
- Wennberg, P. O., C. M. Roehl, J.-F. Blavier, D. Wunch, and N. T. Allen. 2017. "TCCON data from Jet Propulsion Laboratory (US), 2011, Release GGG2014.R1." CaltechDATA. doi:10.14291/tccon.ggg2014.jpl02.r1/1330096.
- Wennberg, P. O., D. Wunch, C. M. Roehl, J.-F. Blavier, G. C. Toon, and N. T. Allen. 2017. "TCCON data from Caltech (US), Release GGG2014.R1." CaltechDATA. doi:10.14291/tccon.ggg2014.pasadena01.r1/1182415.
- . 2017. "TCCON data from Lamont (US), Release GGG2014.R1." CaltechDATA. doi:10.14291/tccon.ggg2014.lamont01.r1/1255070.
- Wennberg, P. O., D. Wunch, Y. Yavin, G. C. Toon, J.-F. Blavier, N. T. Allen, and G. Keppel-Aleks. 2017. "TCCON data from Jet Propulsion Laboratory (US), 2007, Release GGG2014.R0." CaltechDATA. doi:10.14291/tccon.ggg2014.jpl01.r0/1149163.
- Wunch, D., J. Mendonca, O. Colebatch, N. T. Allen, J.-F. Blavier, S. Roche, J. Hedelius, et al. 2017. "TCCON data from East Trout Lake, SK (CA), Release GGG2014.R1." CaltechDATA. doi:10.14291/tccon.ggg2014.easttroutlake01.r1.



Wunch, D., Toon, G. C., Sherlock, V., Deutscher, N. M., Liu, C., Feist, D. G., & Wennberg, P. O. (2015). The Total Carbon Column Observing Network's GGG2014 Data Version. Tech. rep., California Institute of Technology, Pasadena. doi:10.14291/tccon.ggg2014.documentation.R0/1221662

